Wound healing, a multidisciplinary approach: combining mathematical models and biological experiments

Elizabeth Jane Gothard

Doctor of Philosophy

University of York

Biology

December 2016

Abstract

Cutaneous wound repair occurs as a continuous process in both space and time; however, studies of healing mechanisms and outcomes frequently generate spatially and temporally sparse datasets. We propose a range of techniques that allow the size, cellular processes and scar tissue properties of wounds to be measured and predicted at high spatial and temporal resolution. A non-invasive wound imaging system is shown to provide reliable measurements of wound diameter, perimeter and surface area, but is less reliable in producing 3D metrics such as volume and depth. Wound size and time post healing have a combined effect on reliability, with more reliable measurements obtained at earlier timepoints. A semi-automated pipeline is found to be appropriate for determining the cellular composition of the wound space, but cannot be applied to areas of healthy epidermis due to the close packing of keratinocytes. A range of mathematical models are employed to predict cell numbers within the wound space. An extended domain, partial differential equation model with spatial control of cell proliferation and migration is found to best recapitulate the cellular dynamics observed *in vivo*. However, if epidermal stratification is to be incorporated, an agent-based description may be preferable. Finally, we formulate a model system that can predict the alignment of collagen fibres and fibroblasts over continuous orientation space. Parameter sets that include large shear forces (which may result from elongated wound geometries or interventions such as suturing) can produce skewed distributions of orientation that cannot be established using discontinuous approaches. Together, this suite of computational approaches provides a powerful set of tools with which the mechanisms of cutaneous wound healing can be investigated, quantified and elucidated.

Contents

List of Tables

List of Figures

Acknowledgements

I would like to dedicate this thesis to my parents: to Will who nurtured my curiosity, helped me start my first lab book, and has always been on hand to provide reassurance; and to Jeeva, whose unwavering support and encouragement has given me the confidence to take on great challenges.

Multi-disciplinary science is truly a team pursuit, and I am indebted to numerous colleagues for their input and support. I am grateful to my supervisors, Professor Mark Coles and Professor Martin Bees, for their guidance and advice over the course of this project. I would like to thank Professor Jenny Southgate and Professor Jon Timmis who, as members of my training advisory panel, have been generous with their support and feedback during the past three years. I would also like to acknowledge the invaluable help provided by staff from both the Technology Facility and the Biological Services Facility at York.

Having arrived at the CII as a complete novice in biomedical science, I was afforded the opportunity to learn experimental techniques and conduct wet-lab experiments. This would not have been possible without the support of colleagues who were willing to let me shadow them in the lab, to spend time helping me learn even the most basic of skills, and to answer any question, no matter how obtuse. The patience displayed by those who supported me during my first 6 months in the lab is truly astounding, and something for which I am incredibly grateful.

This piece of research was made possible by funding from the Wellcome Trust, for which I am very thankful.

Finally, I would like to thank my friends and family, both in York and further afield, whose encouragement has been invaluable not only in enabling me to reach the end of my studies, but to do so having thoroughly enjoyed the journey.

Declaration

I declare that this thesis is a presentation of original work and I am the sole author. This work has not previously been presented for an award at this, or any other, University. All sources are acknowledged as References.

The research in this thesis was supervised by Professor Martin Bees and Professor Mark Coles, and was produced as a result of the following collaborations:

Chapter 2

Dr Zhi Li performed surgical procedures, assisted by Elizabeth Gothard. Dr Zhi Li contributed to the collection of 3D images, and their analysis for the quantification of inter-operator variation. Jennifer Coles contributed to the analysis of 3D images to ascertain the effect of the region of interest.

Adaptations of Figures 2.1 and 2.11 are published in:

Li, Z, Hodgkinson, T, Gothard, E. J, Boroumand, S, Lamb, R, Cummins, I, Narang, P, Sawtell, A, Coles, J, Leonov, G, Reboldi, A, Buckley, C. D, Cupedo, T, Siebel, C, Bayat, A, Coles, M. C, and Ambler, C. A. Epidermal Notch1 recruits ROR+ group 3 innate lymphoid cells to orchestrate normal skin repair. *Nature Communications*, 7:11394, 2016.

Chapter 3

The material in this chapter has been submitted for publication and is currently in review. The text was researched and written by Elizabeth Gothard, with input from co-authors:

Gothard, E. J, Bayat, A, Ambler, C. A, Coles, M. C, Bees, M. A. Epidermal wound healing: do mathematical models tell us anything new? *Wound Repair and Regeneration.*

Chapter 4

Dr Zhi Li performed surgical procedures, assisted by Elizabeth Gothard. Jennifer Coles contributed to conducting manual cell counts. The discrete model of epidermal healing was formulated in collaboration with, and implemented by, Simon Jarrett, Jason Cosgrove and Thomas Pennington.

Chapter 1

Introduction

The ability to heal wounds after damage to the skin is crucial for the survival and quality of life of a mammal. Skin forms an interface between the body and the outside world, acting both as a physical barrier to infection and an immuno-protective organ that actively defends the body's internal tissues [1]. Damage to the skin disrupts its mechanical and immunologic barrier functions so, after cutaneous trauma, rapid and efficient wound healing is paramount to successful recovery. Under normal circumstances wounded skin will undergo a tightly regulated cascade of processes to restore its structural and functional integrity [2]; however, chronic wounds (for example diabetic foot ulcers) may fail to heal even over long periods of time [3]. Aberrant healing may alternatively result in fibroproliferative disorders such as keloids and hypertrophic scars that, despite forming an intact cutaneous barrier, are nonetheless debilitating [4]. Despite the significant costs – to both the economy and patients' quality of life – associated with chronic wounds and scarring abnormalities, there are still no effective treatments for many healing impairments.

1.1 The clinical implications of aberrant wound healing

Although most cutaneous wounds heal without significant intervention and do not result in lasting adverse effects, a small but significant proportion of the population suffer from chronic wounds or scarring abnormalities. Chronic wounds are defined as those that do not heal within an expected time frame (usually 3 months) and fail to follow the orderly process of events associated with successful healing (see Sections 1.3-1.4) [5]. These wounds vary in origin but exhibit common characteristics, including elevated cytokine levels, increased cellular activity and sustained immune cell influx, that are associated with the inflammatory

stage of healing [6]. A study based in Hull, UK estimated an overall prevalence of patients with wounds (in hospital, primary care and residential care settings) at 3.73 per 1000 population [7]. Whilst the median healing duration at the time of survey was 6-12 weeks, 24% of patients reported a duration of 6 months or more, and 16% of patients reported a wound that had remained unhealed for a year or longer. Leg and foot ulcers, which are commonly associated with comorbidities such as diabetes, were the most commonly reported chronic wound type; a systematic review of prevalence studies found that 0.12-1.1% of the population suffered from an open leg ulcer, increasing to 1.8% when healed ulcers were also included [8]. The studies reviewed were all based in developed countries: quantifying the prevalence of chronic wounds and comorbidities in lower-income countries is challenging and is yet to be systematically conducted.

By contrast, fibroproliferative disorders result from a failure to regulate and subsequently inhibit the healing process, leading to excessive scar tissue deposition [9]. A hypertrophic scar is defined as excessive scar tissue raised above the normal surface of the skin but limited by the wound boundaries, which is likely to regress over time, whereas keloids are similar growths that extend beyond the boundaries of the inciting injury [4]. Both are caused by full-thickness cutaneous injury, commonly piercings, cuts and burns [10, 11]; however, hypertrophic scars are most commonly associated with burns and surgery (with an incidence of 40-70% in post-operative patients) [9], whereas there is evidence of genetic predisposition to keloids, which have an incidence of 6-16% in populations of African origin [12, 9]. Although benign, fibroproliferative disorders can cause major functional impairment – reducing mobility and inducing pruritus and pain – and are aesthetically disfiguring, leading to emotional and psychological distress [13].

Infection can be considered as both a cause and consequence of aberrant healing. *Pseudomonas aeruginosa* and *Staphylococcus aureus* are commonly isolated from chronic wounds, and appear to delay and disrupt their healing process [14, 15]. Chronic wounds also predispose patients to infection, as breaks in the skin weaken its defence against pathogens, and conditions such as diabetes may increase the risk of both chronic wounds and infections [16]. Infection rates are particularly high in wounds resulting from surgery and trauma, and are more common in hospital patients than those receiving treatment in a primary care or residential setting [7]. Fibroproliferative disorders are less strongly linked to infection; however, the associated alterations to dermal collagen composition, and disruption or destruction of skin appendages, may render the local area immuno-compromised [13].

Management of non-healing wounds represents a significant portion of healthcare expendi-

ture worldwide. A study of wound prevalence and treatment in the UK conducted in 2005 estimated the cost of wound care to be between £2.5 million and £3.1 million per 100,000 population [7]. This represented 2-3% of the total local healthcare expenditure [17]. In EU-27 countries, it has been estimated that €4-6 billion and €6.5 billion are spent treating diabetic foot ulcers and venous leg ulcers respectively, each year [17]. The majority of these costs are associated with the nurse time spent on wound management and the cost of dressings [17, 18], reflecting the fact that wound dressing and ongoing management is more common than active treatment of chronic wounds. The lack of effective treatment strategies can in part be attributed to limitations in our understanding of the causes and mediators of chronic wound phenotypes.

Although direct healthcare costs comprise a significant economic implication of impaired wound healing, other factors are also involved. In particular, chronic wounds and scarring disorders are long-lasting conditions, often afflicting patients for months to years [3, 4]. Whilst it is difficult to quantify their effects, symptoms including pain, poor sleep, loss of mobility, and psychological factors (such as embarrassment about a wound or keloid's appearance) cause both a lack of economic productivity and a reduced quality of life of the patients whom they afflict [19, 20, 21, 22].

Despite the benefits associated with improving wound outcomes, the underlying mechanisms responsible for the healing process are still relatively poorly understood. Where mechanistic knowledge is available, it is often not easily related to clinically important factors or outcomes due to limited knowledge of higher-level behaviours. A systems-level analysis of the healing response may help to remedy this situation by providing insight into the complex, multi-scale processes involved.

1.2 Approaches for investigating cutaneous wound healing

1.2.1 Clinical studies

Studying the molecular, cellular and biophysical mechanisms of wound healing provides a scientific basis for improving outcomes for human patients; clinical studies, either analysing the progression of pre-existing wounds or conducting trials in which experimental wounds are created uniformly under controlled conditions, are important in achieving this.

Studies of pre-existing wounds commonly involve taking a biopsy from the edge of a chronic

wound and comparing the gene expression, protein expression and skin morphology to either that of unwounded skin [23], or to an acute wound created at a separate site [24]. Tissue resulting from hyperproliferative disorders can be surgically excised for analysis; for example, samples of keloids have been compared to normal skin and scars, finding increased numbers of T cells, B cells and mast cells [25]. Although these study designs can provide valuable insights into the mechanisms underpinning aberrant healing, they are not always the most appropriate approach. For example, it may be infeasible and unethical to create surgical wounds in at-risk patients, such as those who suffer from comorbidities to chronic wounds or are genetically predisposed to scarring disorders. Additionally, follow up periods may not be long enough to capture the full repair process.

An alternative study design involves creating experimental wounds on participants, commonly patients undergoing other surgical procedures or healthy volunteers [26]. Benefits of this approach include the ability to create wounds of a standardised size and at a predetermined location, using techniques including tape stripping [27], suction blisters [28], surgical abrasion [29], split thickness wounding [30, 31, 32] and full thickness punch biopsies [25, 33, 34]. Partial thickness wounds are often created at donor sites for skin grafts, and biopsies may be taken after the initial excision for further analysis [35, 31]; however, whilst their pathology and physiology is representative of acute wounds, such samples cannot provide insights into healing disorders.

Another key limitation of these approaches is that taking multiple biopsies is generally infeasible, so observations can only be made at a single timepoint; constructing timecourses with biopsies from multiple participants is possible, but the inevitable heterogeneity of patients and wounds may introduce confounding factors. This can be overcome using non-invasive techniques, such as: spectrophotometric intracutaneous analysis, which measures the concentration and distribution of haemoglobin, melanin and collagen; full-field laser perfusion imaging, which measures blood flow; and three-dimensional imaging, which can quantify wound metrics including diameter, perimeter, surface area and volume [33].

Although recent technological advances allow non-invasive measurements of a variety of features of wounds, the most common method of observation is measurement of wound size [36]. Quantifying wound size is important both for determining patients to be included in an observational study and for monitoring all types of wounds as a study progresses. Additionally, the trajectory of wound sizes during cutaneous repair has been proposed as a determinant of the overall healing outcome [37], but implementing this as a clinical predictor will require routine accurate wound measurement. In acute wounds – for which wound size is

often unrepresentative of healing progression, as sutures are commonly used to achieve initial closure – the tensile strength of the wound and surrounding skin may be an appropriate metric for repair [38]. Other frequently employed methods of wound observation include recording wound appearance, for example its colour and shape, and monitoring the condition of tissue in the wound bed [39]; however, the subjectivity inherent in these methods has been proposed as a significant limitation [40].

Another important goal of clinical studies is to identify agents that accelerate or modify healing outcomes. An early clinical study assessed the impact of treatment with topical hydrocolloids on partial thickness healing [41]; although a treatment effect was previously observed in mice, this was not recapitulated in human participants, highlighting the need to for the results of animal studies to be clinically validated. A subsequent study of epidermal wounds investigated the healing properties of various dressings, finding that hydrocolloid and polyurethane plasters were most effective [29]. The disparities in these results may be due to differing modes of delivery, an effect that was observed when treatment with tyrothricin gel was compared to the use of its vehicle: both expedited the onset of healing compared to untreated wounds, suggesting that the vehicle rather than the supposed active ingredient was responsible for the effect [42]. A similar study found polymeric films to be more efficient at delivering aloe vera and vitamin E (common treatments to relieve the symptoms of burns) to the stratum corneum than standard creams [43].

The effects of electrical stimulation have been tested using full thickness punch biopsies, and found to reduce wound size and increase blood flow and angiogenic markers in healthy volunteers [33]. However, many such treatments are designed to improve chronic wound healing, so results from the acute wounds on which they are tested may not be directly relevant. Some treatments, for example the use of heat radiation, have been tested on post-operative patients; the results of such studies give a good indication of treatment efficacy post-surgery, but may be confounded by common post-operative features, meaning that the conclusions are not necessarily generalisable to other types of wounds [44]. Additionally, many such studies involve very small sample sizes, for example involving as few as five healthy volunteers, making it difficult to achieve the power required for robust and translational results [45].

Another limitation of clinical studies is that they are often observational in nature, thus do not investigate the cellular and molecular mechanisms underlying the healing process. For example, a study of punch biopsies obtained following breast surgery carefully characterised angiogenesis and dermal constitution during and after healing, but provided limited insight

into the processes involved [46]. One exception is a study that used full thickness punch biopsies to investigate the mechanism by which platelet-derived growth factor (PDFG) expedites wound closure; the increase of granulation tissue observed in the wound space led to the hypothesis that PDGF limits wound contraction but increases the rate of granulation tissue deposition [47]. More recently, the genes associated with healing processes, such as epithelialisation, have been investigated using genome-wide microarrays of biopsies from graft donor sites [48] and following burns [32]; however, the translational relevance of these findings are yet to be realised.

In general, whilst clinical studies are valuable in understanding specific human wound pathologies and the effects of nascent treatments, they are less amenable to provide robust insights into the mechanisms of healing. This may be attributed to the different areas of interest and expertise of those conducting the studies, but the logistical and financial constraints of clinical experiments should not be overlooked. For these reasons, wound healing models using animals, cultured cells and tissue, and *in silico* experiments also have important roles to play in furthering our understanding of healthy and pathological wound healing.

1.2.2 Animal studies

Animal models are widely used in the study of mammalian wound repair, and have been successful in overcoming some of the logistical difficulties associated with clinical studies. Lower organisms, including Drosophila and zebrafish, have been used to study barrier repair in epithelial surfaces, providing important insights into the processes involved [49, 50]. Mice, rats and pigs are the most commonly used animals in the study of wound healing, with the majority of experiments conducted in mice [51]. Mice are inexpensive compared with human subjects, and both incisional and excisional wounding surgeries can be performed with relative ease [52]. Murine wound studies may also be considered more reproducible and controllable, as the housing and care of mice can be standardised in ways that are rarely achievable with human participants.

Another advantage to this model system is the ease with which genetically modified strains (including knockouts, knockins and transgenic animals) may be generated, allowing the roles of specific genes in the healing cascade to be elucidated [53, 54]. For example, the role of interleukin-6 (IL-6) in healing has been studied by assessing cutaneous repair in IL-6 deficient mice, and those lacking its receptor; IL-6 deficiency caused delays in macrophage

infiltration, fibrin clearance, wound contraction and overall healing that were not observed in mice lacking only the receptor IL-6Rα [55]. Conversely, deficiency in keratinocyte growth factor (KGF) production was found not to impair murine wound healing, and mice deficient in both KGF and transforming growth factor-α (TGF-α) did not exhibit healing abnormalities [56]; whereas, in FGFR2-IIb (KGF receptor) deficient mice re-epithelialisation was delayed, an effect that was attributed to reduced keratinocyte proliferation [57]. Together these findings imply a level of redundancy in the KGF/FGF signalling cascade and suggest that investigating the effects of receptor expression and combinations of growth factors and cytokines is just as important as considering individual ligands: a challenge that murine models are well placed to address.

Mice can also be used as a model for patients with comorbidities that preclude inclusion in clinical studies due to known associated healing impairments. For example, a diabetic phenotype can be chemotherapeutically induced *in vivo*; comparisons of diabetic and wild type animals have helped to characterise the roles of cells (such as dendritic epidermal T cells) and growth factors (such as granulocyte macrophage colony-stimulating factor (GM-CFS)), in chronic wounds [58, 59]. Mice with a spontaneous diabetes mutation, termed db/db mice, are also routinely used in healing studies either as a model of diabetic skin repair [60] or as a broader model for chronic wounds in general [61]. Other species may also be used to model chronic wounds, for example ischemia may be induced by severing blood vessels close to wounds in rabbits and pigs, and porcine models of wound infection have also been developed [52]. However, whilst these model systems can be instructive, none provide completely analogous healing deficits to those found in human wound pathologies.

Rodent models have been used to investigate the efficacy and mode of action of a range of putative healing aids, including dermal substitutes [62], topical therapies [63] and dressings [64]. However, their utility for preclinical evaluation of treatment strategies is limited due to differences in the healing mechanisms and wound management of rodents compared to humans. This is partly due to structural differences between murine and human epidermis (see Figure 1.1): hair follicles occur more frequently in mice, whereas human skin has a greater proportion of interfollicular epidermis; the human epidermis is thicker than that of mice, caused both by larger keratinocytes and more cell layers; ridges at the dermal-epidermal junction are found in humans but not mice; and immune cell populations differ, with a population of dendritic epidermal T cells found in murine but not human epidermis [65]. In the dermis, rodents have a more rudimentary vasculature, whereas human skin is highly vascularised [66]. Additionally, the human subcutaneous adipose layer is much thicker than that of mice and rats; whereas rodents have a layer of subcutaneous muscle, the pannicu-

lus carnosus, that allows large skin movements and causes a loose-skinned appearance [66]. This difference causes a key contrast in the modes of healing between rodents and humans: full thickness murine wounds heal primarily by contraction, whereas this effect is relatively small in humans [67].

Porcine skin is an alternative material used to study wound healing that is more similar to human skin in both structure and healing mechanism than that of mice. Porcine epidermis is of similar thickness to that of humans and adherent to its underlying fascia, although the upper stratum corneum layer is denser in pigs [66]. Pigs also have ridges at the dermal-epidermal junction that are similar to rete ridges in humans [68], a similarly structured but less dense dermal vasculature [66], and their hair follicle density is much lower than that of mice and rats [69].

Porcine models have been used to investigate the effect of TGF-β on collagen fibre orientation [70], FGF on epidermal healing [71] and more recently the efficacy of skin micrografts [72] hydrogel burn treatments [73] and novel dressings [74]. However, pigs are less frequently employed than rodents in studies of cutaneous healing, which may be attributed to the lack of genetic tools, increased costs, more complex housing requirements and unfamiliarity with handling and conducting surgery associated with porcine experiments. Local ethics regulations may also limit or prohibit their use.

Whilst both animal and clinical studies have been successfully used to elucidate the overall mechanisms and outcomes of wound healing, it can be difficult to analyse individual mechanisms and cellular processes in isolation. For example, although the origin and eventual location of individual cells can be established *in vivo* [75], the migration of individual cells cannot be tracked at a high temporal resolution in human or animal wounds. Additionally, *in vivo* studies provide limited insight into the cellular processes underpinning successful migration: an area in which *in vitro* experiments have made a significant contribution to our understanding.

1.2.3 *In vitro* studies

A commonly used *in vitro* technique for studying wound healing is the scratch assay, in which a confluent monolayer of cells is scratched to form an artificial gap, and cells are observed as they migrate and proliferate to close the defect [76]. It is relatively straightforward to assess the effect of therapeutic compounds, endogenous biochemicals and genetic alterations on the behaviour of the monolayer [77]. However, whilst these experiments are generally

less time consuming than their *in vivo* equivalents (for example, the process of transfecting cells is usually less complex than that of genetically modifying mice), cell monolayers are often considered unrepresentative of healing processes in humans and can have higher levels of operator based experimental variation [51, 78]. Nevertheless, time lapse microscopy of scratch assays represents a convenient method to investigate cellular processes, the results of which may be used as the basis of subsequent studies.

It is now known that the behaviour of cells in a monolayer is not a good representation of processes within an organism [79]. This is in part because cells *in vivo* exist in a three-dimensional physiological environment that is not recapitulated by monolayers, and because the environment with which skin cells interact *in vivo* (including extracellular matrix components, blood vessels and other cell types) is very different from the plastic on which they are routinely cultured [77]. The latter shortcoming may be overcome using 3D culture techniques.

Commercially available skin substitutes have been developed to enable *in vitro* experiments to be conducted in a 3D environment that mimics the structure of human skin [80]. Materials developed for use as clinical skin grafts can be repurposed to mimic human tissue, most of which consist of separate layers comprising dermal and epidermal components. The dermis is simulated using a hydrogel, for example collagen, populated with dermal fibroblasts, over which layers of keratinocytes are cultured [77]. Whilst this is a more complex model than cell monolayers, the effects of immune cells and blood vessels are still excluded. Following wounding with a scalpel or punch biopsy, time lapse microscopy, histological analysis or PCR may be conducted to investigate closure rates, cell and tissue morphology, and gene expression.

Skin substitutes may be used to assess the toxicology or mode of action of a range of topical treatments, however they are limited in their ability to assess responses to novel dressings or other delivery modes [80]. Basic cellular processes, such as the secretion of biochemicals that regulate wound healing, may also be elucidated using this experimental approach [81]; however, limited ability to culture skin substitutes over a long period of time may hinder their use in studying the later phases of cutaneous healing [51]. Methods have been developed to overcome this limitation: culturing samples of human skin *ex vivo* has been shown to allow experiments to be conducted over longer periods of time, for example in the study of keloid disease [25].

1.2.4 Theoretical studies

Mathematical models have been widely used to study the dynamics and outcomes of cutaneous wound healing in both the dermis and epidermis [82], and are reviewed in detail in Chapters 3 and 5. Models can be used to investigate unconventional hypotheses [83], to make predictions that may then be experimentally tested [84], or to add value to sparse experimental data by predicting system behaviour at a higher temporal or spatial resolution [75]. However, the majority of theoretical studies of wound healing have been conducted in isolation from experimental work, which can lead to models incorporating inappropriate biological assumptions or just replicating known experimental results. Combining modelling with experiments in an iterative process will allows each to inform the design and execution of the other, and is more likely to yield novel and clinically relevant results.

1.3 The epidermal healing process

The epidermis, which constitutes the uppermost layer of skin, is an important physical barrier to external influences. As such, restoration of epidermal integrity (or re-epithelialisation) is an essential feature of successful healing, regardless of whether a wound affects only the epidermis or the full thickness of skin. Re-epithelialisation requires cells of the epidermis (keratinocytes) to undergo two processes – migration and proliferation – in order to recover the wounded area. It has previously been proposed that migration is the most limiting step in epidermal re-epithelialisation, as defects in this aspect of the healing response have been implicated in the clinical phenotype of chronic, non-healing wounds [85, 23]. However, theoretical studies suggest an essential link between keratinocyte migration and proliferation during the healing response, with each process enabling the other through a positive feedback mechanism [86, 87]. As such, deficiencies in the migratory response may in fact be underpinned by a lack of proliferation in the epidermis. Further study of the dynamics and interactions between these two processes are therefore vital to elucidate mechanistic differences between normal and aberrant healing.

1.3.1 Structure of the epidermis

In mammalian epidermis, keratinocytes are the predominant cell type comprising 95% of epidermal cells; Langerhans cells (antigen-presenting dendritic cells), Merkel cells (receptor cells that contribute to touch discrimination of fine detail) and melanocytes (melanin-

producing cells) are also present [88]. Mammalian epidermis is made up of hair follicles interspersed with interfollicular epidermis (IFE) that consists of several layers of cells, each performing distinct functions in the maintenance of the epithelial barrier. The epidermal layer closest to the dermis is termed the stratum basale, or basal layer, followed by the stratum spinosum (spinous layer), stratum granulosum (granular layer), stratum lucidum and stratum corneum [89]. Whilst murine, porcine and human epidermis all follow this structure, the depths of the cell layers differ between species (Figure 1.1).

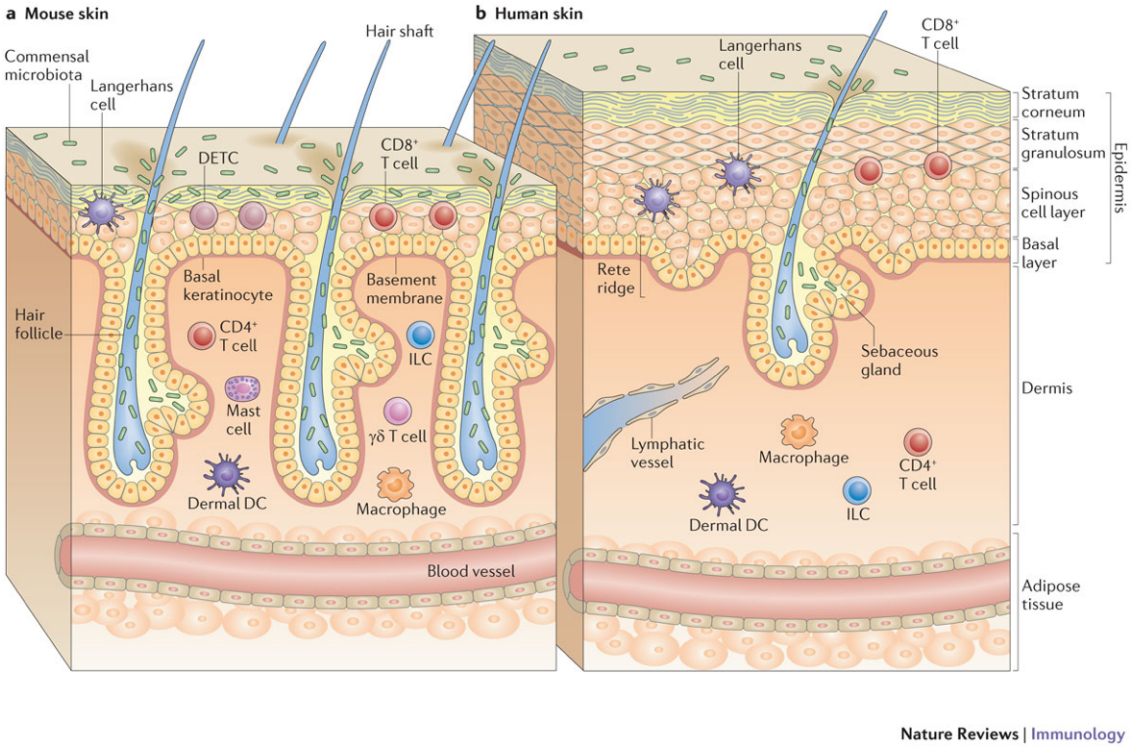

Figure 1.1: **Comparison of the structure and cellular components of mouse and human skin.** Reprinted by permission from Macmillan Publishers Ltd: Nature Reviews Immunology [65], copyright 2014.

Keratinocytes in the hair follicles and basal layer of the IFE undergo mitosis at a slow rate to ensure continuous renewal of the cells in their niche [90]. Whilst relatively large numbers of epidermal stem cells reside in the hair follicles, only 15% of cells in the basal layer of the human IFE are constantly involved in proliferation, with the remaining cells found in a resting or quiescent state [91]. This can be attributed to the existence of proliferating epidermal progenitor cells (EPCs), which in mouse tail epidermis have been found to undergo asymmetric cell division: producing either one cycling and one non-cycling daughter cell, two cycling cells or two non-cycling cells [92]. Apoptosis is rarely observed in the basal

keratinocytes of mammalian epidermis; instead, keratinocytes exit the cell cycle, migrate upwards through the suprabasal layers, and undergo cornification before being shed [93].

The spinous layer is located above the basal layer and consists of viable keratinocytes that do not undergo mitosis. Cells in the basal and spinous layers form numerous intracellular connections: desmosomes connect epidermal cells to their neighbours [90] and hemidesmosomes attach basal keratinocytes to the extracellular matrix of the basal laminar beneath them [94]. Desquamation of the skin (shedding the outer layers) occurs when keratinocytes undergo differentiation, first shedding desmosomes and forming keratohyalin granules in the granular layer, then transforming into flattened, non-viable cornercytes of the stratum lucidum and stratum corneum, having lost their nuclei and organelles [95]. In healthy human skin the balance between basal layer proliferation and desquamation from the stratum corneum achieves tissue homeostasis [96].

1.3.2 Keratinocyte migration

Wounding disrupts the careful balance between keratinocyte proliferation and loss, as well as altering the structural properties of the epidermal layers. After a wound occurs, hemidemosomal and desmosomal attachments are dissolved from viable keratinocytes adjacent to the wound edge, whilst leading edge keratinocytes become flattened and express new integrins to facilitate migration [97]. The precise stimuli for this phenotypic change are incompletely understood [98], however pro-inflammatory cytokines released by degranulating platelets, neutrophils and macrophages at the wound site are thought to be responsible [99]. A loss of contact inhibition among keratinocytes and exposure to constituents of the extracellular matrix (for example fibronectin) are also proposed to play a role [100]. An epithelial tongue then encroaches on the wound space, migrating over granulation tissue and remnants of the basal membrane. In addition, hair follicle stem cells migrate into the IFE after wounding, providing a rapid increase in cell numbers close to the wound site [101]; this is most notable in large wounds where extensive re-epithelialisation is required [102]. Whilst the process of keratinocyte migration is common to both mice and human epidermis, the onset of migration occurs at different timepoints. In murine skin, migrating epidermal tongues are observed at 12 hours post wounding (hpw) [103]; whereas human keratinocyte migration has been observed at 48 hpw, with an epithelial tongue visible by 72 hours [45].

1.3.3 Keratinocyte hyperproliferation and epidermal hyperplasia

Epidermal wounding causes fixed basal keratinocytes close to the wound periphery to increase their rate of mitosis, providing a pool of extra cells to facilitate migration and repair [104]. Whilst basal cells are primarily responsible for the increased keratinocyte proliferation rate, hyperproliferative cells have also been observed in suprabasal layers [105]. More details on the locations and dynamics of the increased keratinocyte mitosis can be found in Chapter 4. In addition to increasing proliferation rates, it has been shown *in vitro* that keratinocytes responding to a scratch wound produce an excess of cycling cells compared to differentiated daughters, thus producing an 'expanding' population to restore tissue integrity [106].

Hyperproliferation is induced and maintained by the release of growth factors and cytokines that are produced by eosinophils, macrophages and damaged fibroblasts and keratinocytes at the wound edge (see Chapter 4 for more details) [107]. It has recently been shown in mouse models that innate lymphoid cells (ILCs) have some role in regulating epidermal proliferation at the periphery of a wound [34]. Keratinocyte hyperproliferation causes a degree of hyperplasia, resulting in a characteristic ridge around the edge of a healing wound [102].

1.3.4 Keratinocyte differentiation

In the days following wounding, keratinocyte differentiation is suppressed close to the wound edge, allowing a larger population of cells to undergo mitosis than in unwounded skin; Notch and Vimentin have been implicated in this process [108, 109]. Once new epidermis has covered the wounded area, keratinocytes revert to a non-migratory phenotype [86], becoming either proliferative or terminally differentiated depending on the migratory mechanism proposed [102]. It is unclear as to the cause of this change in phenotype; however, the re-emergence of contact inhibition, which occurs when cells from the opposite sides of the wound meet, is likely to be involved [110].

1.3.5 Promoting and regulating epidermal healing: the role of immune cells and growth factors

In addition to the resident epidermal cells that participate in wound healing, a large number of infiltrating cell types are also required to stimulate and regulate successful repair. Cytokines and chemokines, predominantly TGF-β1 and PDGF, are released by degranulating platelets in the wound space and recruit neutrophils, macrophages and lymphocytes to the wound and surrounding dermis [111, 112]. Immune cells, in particular macrophages, display a degree of plasticity as healing progresses. During the early stages macrophages take on a pro-inflammatory phenotype, producing cytokines and growth factors that recruit additional immune cells to carry out debridement and phagocytosis [113]. Subsequently, macrophages contribute to the promotion and regulation of keratinocyte proliferation, and may also be responsible for certain migratory cues [114].

One of the most important ligands for keratinocyte migration is TGF-β1, which is produced by platelets and macrophages, and stimulates changes to keratinocyte integrin expression that facilitates cell migration [113]. Regulation of hyperproliferation occurs through the epidermal growth factor (EGF) receptor on keratinocytes, which can be bound by a range of ligands including EGF, TGF-α, KGF and heparin-binding EGF (HB-EGF) [113]. These growth factors may be produced by macrophages, fibroblasts, and keratinocytes adjacent to the wound [112]. Additionally, a role for FGF7, which is produced by fibroblasts and can bind to the receptor FGFR2IIIb on keratinocytes, in regulating re-epithelialisation has been proposed but not fully elucidated [112].

Studies of murine wounds have highlighted significant redundancies in the regulation of keratinocyte hyperproliferation. For example, blocking FGFR2IIIb (the receptor to KGF) in basal keratinocytes at murine wound sites caused a reduction in cell proliferation leading to defective and delayed re-epithlialisation [57]; however, mice lacking KGF did not exhibit healing defects, suggesting the lack of KGF is compensated for by other KGF receptor ligands [56]. FGF-10 has been proposed as most likely to be providing this compensatory effect [53]. Additionally, wounds in KGF receptor deficient mice did eventually heal, although on a significantly delayed timecourse, suggesting that other epithelial mitogens also enable healing [53]. Similarly, no significant healing abnormalities were observed in TGF-α deficient mice [115, 116] and incisional wound healing appeared normal in mice deficient in both TGF-α and KGF, suggesting further growth factors are involved [56].

Other growth factors have been identified as essential for successful healing. For example,

mice lacking FGF-2 exhibit delayed healing, including retardation of re-epithelialisation, that does not appear to be compensated for by other molecules [117, 53]. TGF-β requirements also appear to be very specific, as both over- and under-expression of the molecule have been associated with healing impediments [53].

1.3.6 Open questions in the study of epidermal repair

Although epidermal repair is recognised as an integral stage of healing in both partial and full thickness wounds, with key implications in controlling infection and maintaining a microenvironment conducive to subsequent dermal healing, the process is yet to be fully characterised and understood. One open question is that of the mechanism by which keratinocyte migration proceeds. Early work postulated that a single layer of basal cells undergoes migration into the wound and, once the gap is bridged, migrating cells revert to their normal morphology (becoming more columnar in shape), firmly attach to the basal membrane and begin to undergo mitosis; cells produced by this proliferation then form suprabasal layers of the epidermis until eventually the whole surface is keratinised [118, 100]. Subsequently it was proposed that suprabasal cells in fact contribute to migration by rolling over leading edge basal cells and de-differentiating to form new leaders: the "leapfrog" or "rolling" mechanism [103, 119, 120]. Another alternative is the "tractor-tread" or "sliding" mechanism, whereby only basal keratinocytes actively migrate over the wound surface; however, the entire epidermis is observed to advance in a block, as suprabasal cells are passively dragged along due to the strong desmosomal attachments between them and migrating basal cells [86].

Recent work has suggested that collectively migrating cells continuously build a multilayered epithelial tongue by migrating from unwounded regions and lifting preceding migratory cells to form an "extending epithelial shield" [75]. One reason for the controversy surrounding mechanisms of migration may be the use of various models of the healing process: it is unsurprising that cell monolayers, 3D cultures, animal models, human skin and *ex vivo* cultures exhibit different migratory processes. However, even when considering only a single model system, efforts to elucidate the migratory mechanism have been inconclusive, so further investigation in this area is required. Furthermore, the temporal dynamics of the processes have not been comprehensively examined so require systematic study.

The role of epidermal stem cells that originate in the hair follicle bulge is also incompletely understood. It is known that hair follicle stem cells migrate rapidly into the IFE to increase

the pool of cells available for re-epithelialisation to take place; however, the fate of these cells – in particular whether they retain their stem cell phenotype to contribute to hyper-proliferation, or whether they behave like differentiated cells with a migratory phenotype – is unknown [121]. Models that investigate the dynamics of re-epithelialisation may be able to shed light on this, by identifying whether model predictions without the contribution of hair follicle stem cell proliferation can match observed healing dynamics.

1.4 The dermal healing process

1.4.1 Structure of the dermis

The dermis is thicker and considerably less cellular than the epidermis; its key functions include cushioning underlying organs from mechanical injury and providing nutrients to the epidermis and its appendages. The main structural component of the dermis is the extracellular matrix (ECM): a network of fibres – predominantly collagen but also containing elastin – embedded in a gel-like matrix of polysaccharides. Collagen fibres, which constitute approximately 30% of the dermal volume in mice, strengthen the ECM by forming an organised structure cross-linked by covalent bonds; the coiled structure of elastin, which represents 1% of dermal volume, provides a degree of skin elasticity [122]. Whilst the ECM is key for dermal structure, it is not simply an inert scaffolding: the behaviour of its resident cells can be regulated by ECM components, either by acting as a reservoir for biochemical signalling molecules, or through fibre-facilitated contact guidance. Additionally, the aqueous phase of the polysaccharide gel allows nutrients, metabolites and hormones to diffuse between blood and tissue cells [122].

In healthy skin the ECM is primarily populated by fibroblasts, which are responsible for secreting dermal constituents such as collagen and can produce contractile forces during healing; fibroblasts are most commonly found in close proximity to collagen fibres [123]. Mast cells and macrophages are also found in dermal tissue, and lymphocytes are present in small numbers [124, 125].

Additionally, dermal tissue contains follicles and glands, including sebaceous glands, sweat glands and hair follicles, which are in fact epidermal structures that protrude into the dermis (Figure 1.1). Arteries, veins and lymphatic vessels enter the lowest cutaneous layers, supplying the network of capillaries that provides a blood supply to the rest of the skin. The skin also provides information about an organism's surroundings by detecting pressure,

temperature and vibrations, and transmitting signals to the central nervous system via a large number of cutaneous nerves.

When damage occurs to the dermis, a complex, multistep healing process is initiated. The stages of dermal healing are briefly outlined in the following sections, with additional details provided in Section 5.1.

1.4.2 Haemostasis

Cutaneous trauma routinely results in damage to dermal blood vessels, due to the abundance of capillaries found in the skin. To prevent excessive blood loss, vessels rapidly constrict and platelets aggregate to form a blood clot, composed of proteins including fibrin, fibronectin, vitronectin, trombospondin and cells such as erythrocytes and platelets [126, 127]. This clot acts to inhibit bleeding, protect underlying tissue and attract immune cells towards the wound [128].

1.4.3 Dermal inflammation

After clot formation, the release of histamine causes blood vessels close to the wound to dilate and become more permeable, which facilitates delivery of immune cells through rapid changes to blood flow around the wound site [129]. The expression of inflammatory chemokines on the lumen of the blood vessel, localised chemokine production as a result of cytokine production, and localised prostaglandin and leukotriene production leads to specific immune cell recruitment to the wound site. This process is additionally modulated through production of PDGF and TGF-β1 in the clot. Once at the wound site, immune cells initially defend against pathogens: neutrophils remove foreign particles and bacteria from the site, macrophages later clear senescent cells and other wound eschar, phagocytose pathogens and present antigens to T-cells [130]. Macrophages involved in clearance undergo apoptosis, and those that remain in the wound space take on other regulatory roles during the tissue repair phase of healing [131]. The length of the inflammatory phase depends predominantly on the level of infection or presence of foreign bodies in the wound, but may be extended by immune complications [132].

1.4.4 Dermal collagen deposition

Dermal volume is initially increased by the production of granulation tissue: between 3 and 5 days post wounding (dpw), fibroblasts and myofibroblasts begin to produce new ECM components which are necessary to support further cell infiltration and angiogenesis [133]. In particular, collagen is laid down as the main structural component of the nascent ECM, along with fibrin and glycoproteins that enable cell adhesion [134, 135]. Specific details of this process are described in Section 5.1.

1.4.5 Angiogenesis

As granulation tissue and the basement membrane in the wound space begin to degrade, endothelial cells migrate into the wound space. They are attracted by growth factors – including TGF-β, FGF, vascular endothelial growth factor (VEGF) and angiopoietins – that are produced by immune cells and fibroblasts [136]. VEGF also stimulates endothelial cell proliferation, further increasing the pool of cells available to enable angiogenic sprouting of dermal capillaries, thus vascularising the wound bed [137].

1.4.6 Contraction

Wound contraction acts to reduce the size of an injury without the need to synthesise new skin components; as described in Section 1.2.2, this occurs to a greater extent in rodent skin than in humans and pigs. The primary cell types implicated in dermal contraction are fibroblasts and myofibroblasts, which differentiate from fibroblasts in response to the presence of growth factors (such as TGF-β1) and mechanical forces generated by the ECM as, for example, it resists initial wound edge retraction [138, 139, 140]. Myofibroblasts take on phenotypic characteristics of smooth muscle cells to facilitate force generation; application of these forces to the collagen and elastin fibres with which myofibroblasts have contact results in contraction of the ECM [141]. Recently, it has been shown that both myofibroblasts and fibroblasts contribute to ECM contraction, with myofibroblast-deficient wounds still exhibiting contraction [142].

1.4.7 Resolution of tissue inflammation and remodelling

Tissue remodelling is by far the longest phase of dermal healing, lasting from months to years [143]. The rate of cell proliferation in the wound space decreases, regulated by macrophage-derived growth factors, and endothelial cells, macrophages and myofibroblasts apoptose or exit the wound site [144]. This causes a reduction in the rate of production of ECM components, and helps to promote remodelling: a process through which existing collagen is either degraded or restructured into larger, more organised bundles, restoring dermal tissue to an architecture closer to that of unwounded skin [143].

1.5 The need for continuous observation, description and prediction of normal and pathological healing

Characterising the progression of normal wound repair is an important step in understanding the causes and consequences of pathological healing. Although normal cutaneous wound healing is commonly described as a series of discrete steps, in fact there is significant overlap of the cellular, molecular and mechanical processes involved. Even when studying an individual aspect of the healing process, the ability to make observations and take measurements at high spatial and temporal resolution is hugely beneficial. Whilst this is relatively easy to implement using *in vitro* systems, experiments involving animal models or human participants typically collect sparse data sets that characterise healing at discrete positions in space and time. Given the financial costs and ethical considerations associated with *in vivo* studies, it is important to glean as much information from each experiment as possible.

A range of techniques may be implemented either to collect data at high temporal resolution or to exploit sparse datasets to provide additional insights. Non-invasive imaging is a technique commonly used in the clinic to assess wound size at regular intervals during healing, whereas histology is most widely used in murine studies [33, 145]. In Chapter 2 we evaluate one such non-invasive technology in the context of murine experimental wounds, to establish whether a 3D imaging approach is suitable to make repeated measurements of mouse wounds. Mathematical models of epidermal healing, which may be used to interpolate between sparse observational data points, providing additional insight into intermediate healing dynamics, are reviewed in Chapter 3. Whilst both continuous and discrete computational representations of cutaneous healing have been implemented to study a range of repair processes, rigorous comparison of different computational systems has not been undertaken.

Therefore, in Chapter 4 we present three relatively simple models of normal epidermal repair, and investigate some of their key assumptions in detail. The use of sparse histological data to inform model formulation and parameterisation is also explored, and a novel technique for capturing a wider temporal region in a single histology image is assessed. In Chapter 5 the importance of continuous representation of not only cell and biochemical concentrations, but their orientations in the dermis, is illustrated in a continuous model of scar tissue formation. Finally, the potential of using these three key approaches – non-invasive imaging, histological observation and mathematical modelling (Figure 1.2) – in combination to radically enhance our understanding of mammalian cutaneous healing is evaluated, and the next steps required to achieve this, are presented in Chapter 6.

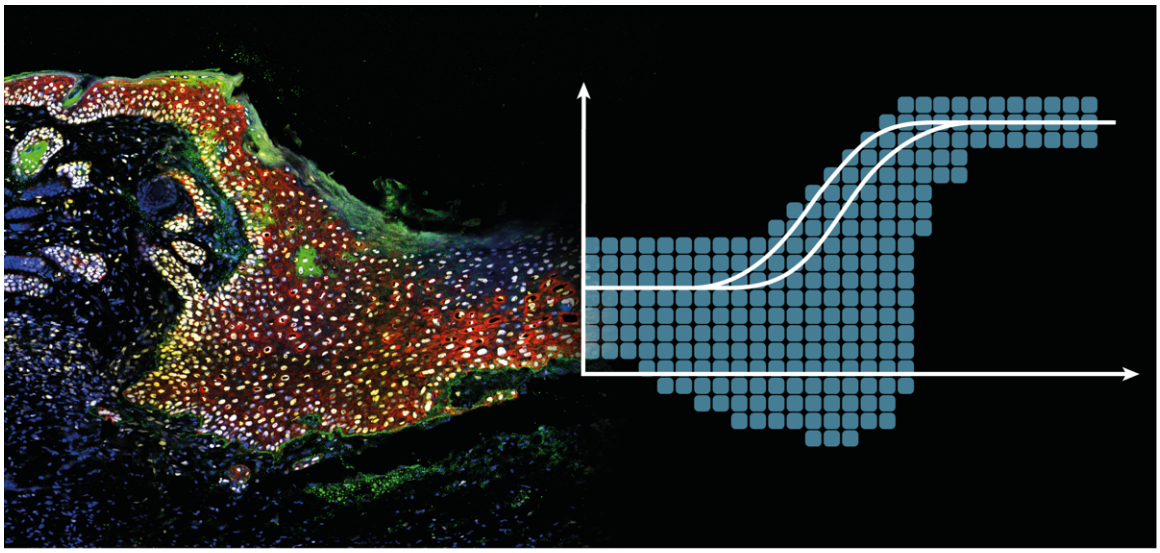

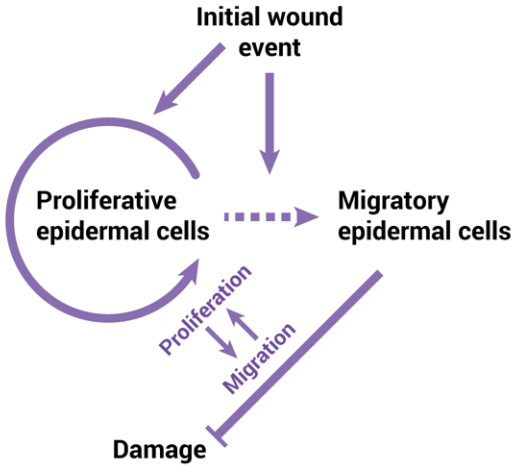

$$\frac{\partial n}{\partial t} = \nabla \cdot [D n^p \nabla n] + n(1-n)$$

Figure 1.2: **An illustration of modelling approaches to wound healing.** Top left: Cross section through a murine wound at 5 days post wounding; blue - DAPI; yellow - tet histone GFP; green - integrin-α6; red - Plet 1. Top right: Describing the system with either an agent or differential equation based approach. Bottom left: A schematic of the principal biological interactions. Bottom right: A typical partial differential equation description of the density of epidermal cells.

Chapter 2

An evaluation of a novel method for murine cutaneous wound measurement

2.1 Introduction

Characterising how wound size changes over time is a prerequisite for understanding normal skin repair and healing disorders. Wound measurement is considered a key part of clinical wound evaluation, and studies suggest that the wound healing trajectory (changes to wound size over time) may be used to monitor and predict progression towards healing, as well as to predict the effectiveness of therapeutic agents [40, 36, 37]. Research has therefore been undertaken to evaluate the wound measurement techniques available, finding that non-invasive, objective measurement strategies are preferable in clinical practice [36]. Many clinical and biomedical studies of wound healing involve creating surgical wounds of known initial size that are monitored over a time course [146, 147, 148, 34, 149, 150, 151, 33]. Objective wound measurements would therefore also be beneficial in these fields; however, limited work has been undertaken to assess the suitability of the various clinical techniques when applied to experimental wounds.

When measuring wounds, be they clinical or experimental, it is advantageous if the method employed is non-invasive, convenient, reliable and accurate [152]. For carefully controlled experiments using standardised wound sizes, non-invasiveness is particularly important so as not to disrupt the process of normal healing. Methods must be convenient so that large

cohorts of patients or experimental subjects can be analysed rapidly; for murine models in which wounds heal quickly, measurements may need to be taken daily or more frequently, necessitating a technique that is not too time consuming. Reliability requires that the method used is well-defined, produces consistent results when applied repeatedly, and that inter-operator variation is low. Finally, a successful wound measurement technique must be accurate in quantifying the size of the wound.

The sizes of experimental wounds are commonly measured using calipers [146, 147, 148, 149, 150, 151]. Whilst convenient, this technique can disrupt the wound, particularly if depth measurements are required. Two-dimensional estimations are also problematic as wound size is frequently calculated by multiplying length by width, which does not take irregular wound shapes into account [36]. This issue may be overcome by tracing the wound border onto acetate and quantifying its area by counting squares on a pre-printed grid (manual planimetry), or using digital planimetry whereby measurement of the tracing is automated [153]. Whilst more amenable to two-dimensional measurements than callipers or rulers, the planimetry technique may disrupt the wound bed during tracing. Planimetry may also be less effective for smaller wounds and highly curved surfaces, such as those found in mouse models or small experimental wounds created on human arms [152, 154].

Recently, a 3D camera system known as LifeViz was developed and tested in the contexts of pre-operative breast measurement [155], quantification of facial and dental measurements [156], assessment of skin legions and carcinomas [157], monitoring paediatric burns [158] and the measurement of experimental wounds in human trial subjects [33]. Another assessment of the agreement between measurement using the LifeViz system and digital planimetry applied the technology to paediatric burn wounds; however, these are much larger than murine experimental wounds and the study did not investigate whether measurements are replicable [159]. The clinical study used the LifeViz camera to measure excisional wounds in human trial participants, an application that is similar to murine experiments; however, data was presented describing changes to wound size over time with no investigation of the accuracy or reliability of the technique [33]. Additionally, although many wound healing experiments are conducted on human patients or trial subjects, there is a large body of work using animal models to investigate healing phenomena, particularly using mice [146, 147, 148, 34, 149, 150, 54, 151]. Key differences between murine studies and clinical investigations include the smaller size of subjects and wounds, faster healing rates and additional considerations of handling when working with mice. It is therefore important that new technologies for healing assessment are assessed in the context of murine wound healing if they are to be applied to this area. This study evaluates the 3D camera system as a tool

specifically for quantifying murine wound healing, systematically assessing its invasiveness, convenience, reliability and accuracy.

2.2 Methods

2.2.1 Creation of surgical wounds

At 1 day prior to wounding, each mouse was given unique identifiers by cage numbering and ear notching. Genotype, sex and age were recorded. The mice were aged between 6 and 9 weeks as this is the resting phase of hair growth, which minimises the effect of hair follicle stem cells on wound healing [160]. The dorsum of each mouse was shaved using clippers; this was carried out 1 day prior to wounding to reduce the effect of any resulting micro-abrasions on the healing of experimental wounds [161].

On the day of wounding each mouse was injected subcutaneously with analgesic Vetgesic (Alstoe Animal Health) at 0.05 mg/kg and anaesthetised using inhaled isofluorane. The dorsal skin was washed with sterile water and then sterilised with iodine Providine (Ecolab). Two, 4 mm punch wounds were made to full thickness on each mouse using a sterile biopsy punch (Stiefel) (wounding surgery was carried out by Dr Zhi Li). Top-bottom wounds were located along the dorsal midline. Each mouse was measured from base of ears to base of tail; wounds were made at 0.4× and 0.67× this distance, ensuring that wounds were at least 1 cm apart (Figure 2.1a). Left-right wounds were located on either side of the dorsal midline, with the centre of each wound at approximately 0.8 cm to the left or right of the midline. Mice were monitored during recovery, after which they were housed in cages of up to 5 same-sex littermates and given free access to food and water.

2.2.2 Collection of stereo images using 3D LifeViz Micro camera (Quantificare)

Each mouse was stabilised by allowing it to grip the horizontal cage-top bars whilst holding it firmly by the tail. Gentle pressure was applied (pulling the tail away from the head) to present the wound, whilst avoiding stretching the skin beyond its normal tension. The camera's dual beam red light pointers were projected onto the wound and the camera was positioned such that the beams were entirely overlapping and circular (as opposed to elliptic). This ensured that the picture was taken from the correct distance and angle

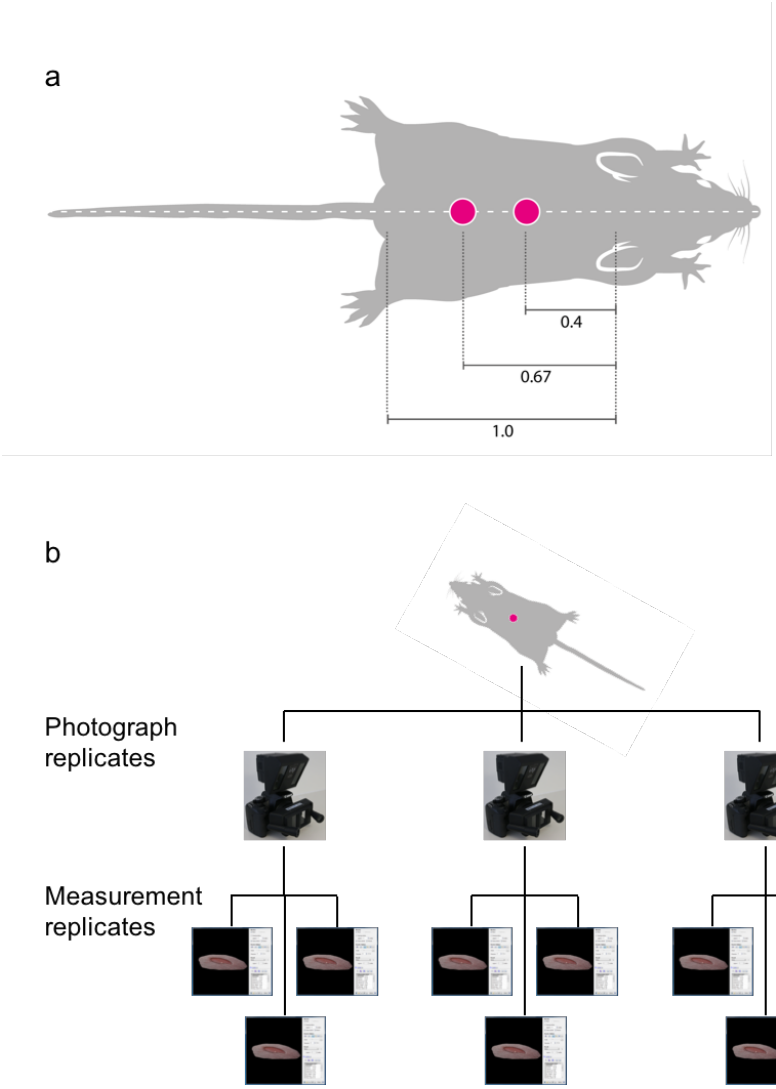

Figure 2.1: **Experimental design.** (a) The location of top-bottom wounds relative to mouse size. (b) The replication strategy employed: each wound was photographed three times, and each photograph analysed three times.

to the wound. Three photographs of each wound site were taken, repositioning the camera between pictures if necessary; the replication strategy is shown in Figure 2.1b. Images with excessive reflective glare in the wound area were discarded, and a soft box flash diffuser was used when this was a persistent problem. The procedure was repeated for each wound.

Photographs were uploaded, securely stored and each was assigned a unique, random number identifier (generated in the software R [162]). A master list of the photographs' random number identifiers and associated information (genotype, mouse identifier, wound location, wound position, wound size, photograph replicate number, time post wounding and chronological order number) was retained separately. Photographs were then renamed with their random number identifier to enable blind analysis.

2.2.3 Quantification of wound size using the Dermapix image analysis platform (Quantificare)

Photographs were imported into Dermapix software and added to an appropriate *Gallery*. In the *Visualisation* tab, a region of interest was drawn on the right hand image to include the wound and surrounding skin (Figure 2.2a). The diameter of the region was set to approximately twice that of the wound. The software was used to create a *3D mesh reconstruction* of the region of interest (Figure 2.2b). In the *3D analysis mode*, a contour was drawn by the operator around the wound edge of a 2D image, using the colour and texture of the image to guide the choice of boundary (Figure 2.2c). The contour was then checked using the 3D visualisation.

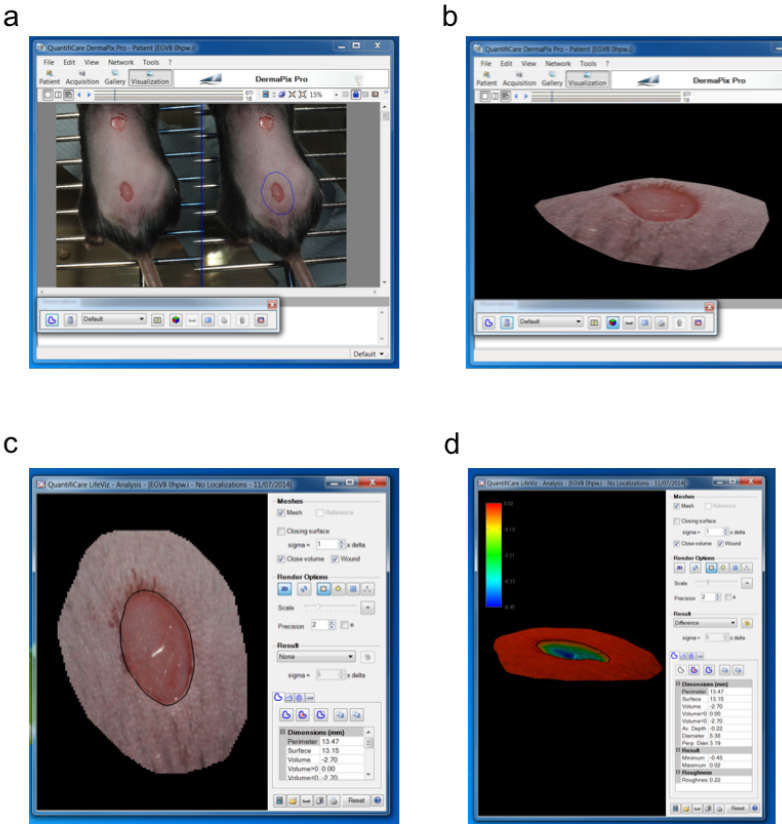

Figure 2.2: **Using Dermapix software used to quantify wound size.** (a) a region of interest of approximately twice the wound diameter was identified; (b) a 3D mesh reconstruction of the region of interest was created; (c) a contour was drawn around the wound edge in the 3D analysis mode; (d) wound metrics were obtained and exported using the settings shown.

Wound metrics were obtained using the following settings: in *Meshes*, *close volume* and *wound* were selected, and *sigma* was set to 1; in *Result* the drop-down menu was set to *Difference* (Figure 2.2d). Wound metrics were exported and saved with the corresponding random number identifier. Each photograph was analysed three times (non-sequentially) to provide technical replicates, as shown in Figure 2.1b. After all of the images were analysed, the results were unblinded by referring to the master list of identifiers; this process was automated using the software R [162].

2.3 Results

2.3.1 The feasibility of 3D imaging as a method for measuring murine cutaneous wounds

In total, 14 female mice aged between 6 and 8 weeks were wounded on the upper and lower dorsum. All mice were C57/Bl6: 4 were wild type (WT); 4 were $ROR^{+/-}$ (Het); 6 were $ROR^{-/-}$ (Hom). $ROR^{-/-}$ mice are deficient in a population of ILCs, which are hypothesised to regulate wound healing. The 28 wounds were each photographed three times at two different timepoints (0 dpw and 5 dpw); additionally, 14 wounds (from 7 mice) were photographed at 8 dpw.

The process of stabilising a mouse for photography can disrupt the wound somewhat, as it may be briefly deformed whilst the mouse is moved into position. However, the effect was not prolonged and at no point did any equipment come into contact with the wound surface. An advantage to the system is that mice did not need to be anaesthetised each time a wound measurement was obtained (as would be the case for acetate methods), so data could be collected at more frequent timepoints.

Photographing a cohort of 14 mice, each with 2 wounds to be imaged 3 times, took approximately 45 minutes, which is comparable to the time required to take three calliper measurements of the same set of wounds. However, whereas calliper measurements produce an immediate quantification, analysing the stereo images takes an experienced user approximately 3 minutes per photograph. For the replication strategy employed in this experiment ((Figure 2.1b)), applied to 14 mice each with 2 wounds, there were 252 images to analyse at each timepoint. Given the considerable cost of the equipment and time-consuming analysis process, it is therefore important to systematically assess the reliability and accuracy of 3D imaging as a tool to measure murine wound size.

2.3.2 Consistency of wound measurements

To analyse the consistency of wound measurements, 70 unique photographs (the first photograph replicate for each wound at each timepoint) were each analysed three times, giving three measurement replicates for each of the wound metrics (perimeter, surface area, volume, average depth). The coefficient of variation of each of the sets of three measurement replicates was calculated (standard deviation divided by mean), and is shown in Figure 2.3a. The median coefficient of variation for perimeter and surface area are 0.03 and 0.06 respectively, whereas volume and average depth had median coefficients of variation of 0.18 and 0.16; thus, metrics that incorporate depth were less consistent.

The sample included mice of three different genotypes although all were on the same background. Figure 2.3b shows that coefficients of variation are very similar across the genotypes; therefore, mice will not be separated by genotype in subsequent analyses.

2.3.3 The effects of healing time and wound size on measurement consistency

The 70 photographs included in the analysis from Section 2.3.2 were taken at three different timepoints; a plot of the coefficients of variation grouped by the number of days post wounding at which the photograph was taken is shown in Figure 2.4a. For both perimeter and surface area, the median coefficient of variation and their spread are greater at later timepoints. Neither volume nor average depth have enough data points to draw conclusions at 8 dpw; this is because fewer wounds were photographed at 8 dpw and wound depth is generally measured as negligible at this timepoint, so coefficients of variation are not applicable due to dividing by a mean of zero. At 5 dpw the median and interquartile range of the coefficients of variation were greater than those at 0 dpw, suggesting that measurements were less consistent at later times. Together, these results suggest that measurement consistency decreases with time post-wounding. Images of the same wound photographed at 0 dpw, 5 dpw and 8 dpw are presented in Figure 2.4b, showing that the wound is larger, and the wound edge more clearly defined, at earlier timepoints.

To evaluate whether wound size has an effect on measurement consistency, the coefficients of variation calculated previously are plotted against the mean of the three measurement replicates (Figure 2.5a). A moderate negative correlation is observed, with stronger correlations associated with perimeter and surface area; this suggests that measurements may

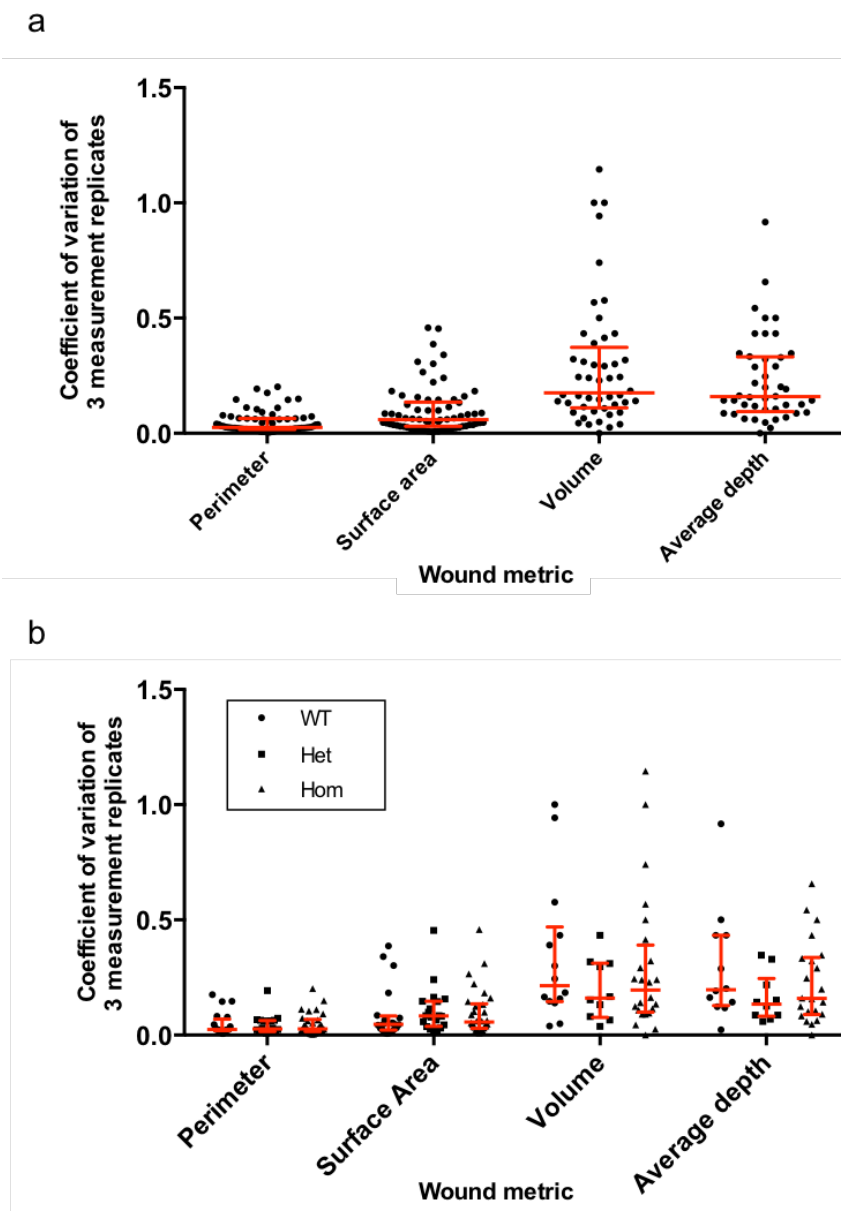

Figure 2.3: **Effects of metric and genotype on wound measurement consistency.** (a) Coefficients of variation for three measurements of 70 photographs for each wound metric. Metrics that do not involve wound depth (perimeter and surface area) have smaller coefficients of variation than those which do (volume and average depth). (b) Coefficients of variation are not significantly different across mice of different genotypes for any of the wound metrics investigated. (a-b) Coefficients of variation are set to NA when two values are equal and the other zero, when two values are zero, and when the mean is zero. Therefore, the number of values plotted are: perimeter n=70; surface area n=70; volume n=48; average depth n=44. Error bars show median and interquartile range.

be slightly more consistent for larger wounds, and that this effect is more pronounced for metrics that do not involve depth. However, it is yet to be shown whether the mean of

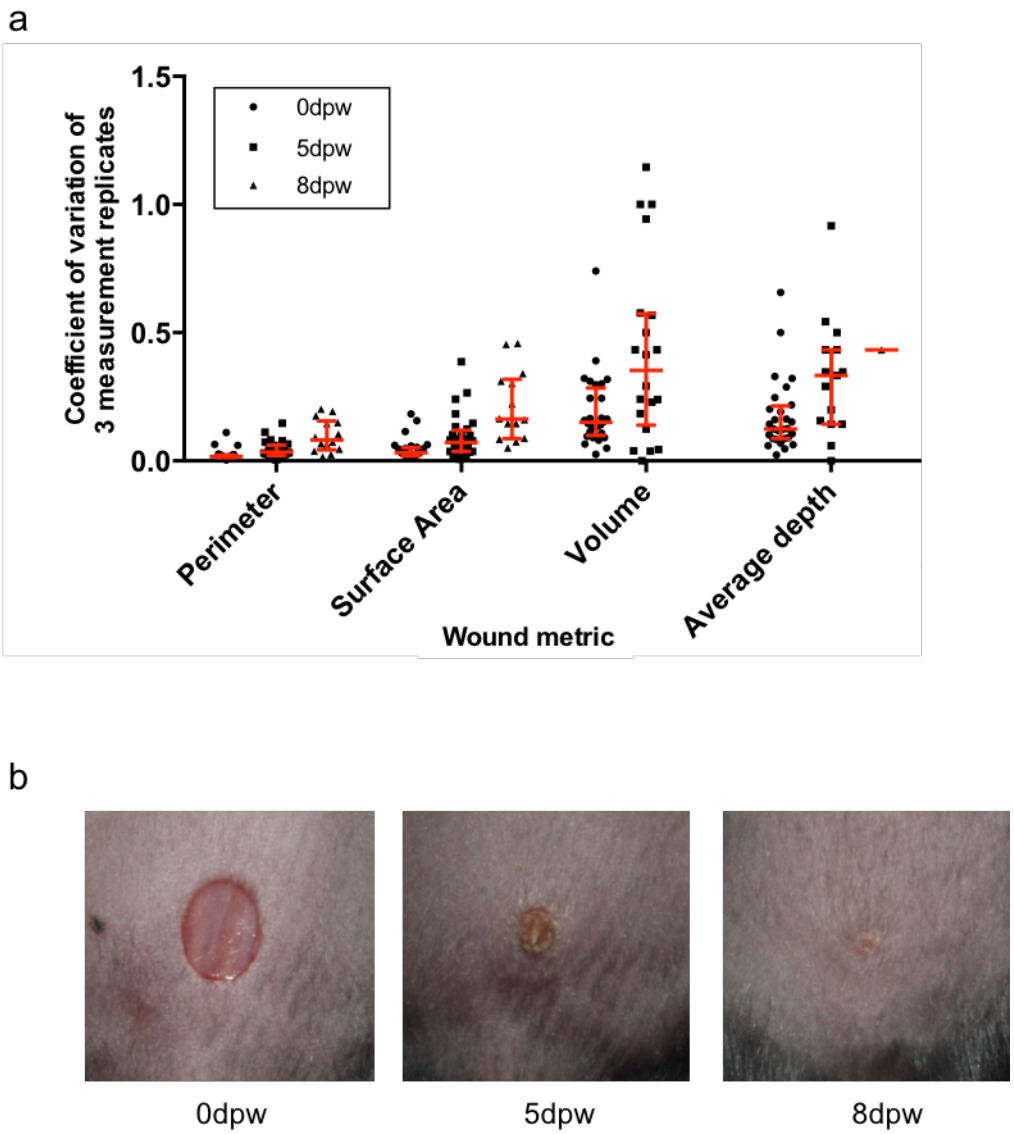

Figure 2.4: **Consistency of multiple measurements of the same photograph.** (a) Coefficients of variation taken from Figure 2.3a, grouped by time post wounding at which the photograph was taken. Consistency of measurements decreases at later timepoints. As before, coefficients of variation are set to NA when two values are equal and the other zero, when two values are zero, and when the mean is zero; this affects the majority of data points for metrics involving depth at 8 dpw. Error bars represent median and interquartile range. (b) Photographs of a wound at 0 dpw, 5 dpw and 8 dpw showing that wound size decreases the wound edge is less defined at later times.

the three measurement replicates gives an accurate representation of wound size, and data points are not available across the whole spectrum of wound sizes, particularly for perimeter and surface area, so this finding is not conclusive. Additionally, smaller wounds have less well defined edges and there is less contrast between the colours of wounded and unwounded

tissue, so effects due to healing time could be having a greater effect than size.

As an alternative test for whether measurement consistency increases with wound size, 6 mice (females, 9 weeks old) were wounded on either side of the dorsal midline, with a wound of 2 mm diameter on one side and 4 mm on the other. Photographs were taken at 0 dpw and 3 dpw (the 5 dpw and 8 dpw timepoints from the previous experiment were inappropriate in this case as wounds of 2 mm diameter would already be healed) and each was analysed 3 times as before. Figure 2.5b shows the coefficients of variation calculated for each triplicate: no notable difference was found between the consistency of measurements of wounds of different initial diameters, suggesting that size alone is not responsible for the decrease in consistency observed at later timepoints in Figure 2.4a.

It was found that, for all of the metrics investigated, wounds with a diameter of 2 mm (at 0 dpw) were of a similar size to wounds with an initial diameter of 4 mm that had been left to heal for 3 days (Figure 2.6a). Comparison of the coefficients of variation for the two sets of wounds showed no significant difference (Figure 2.6b), indicating that healing time does not affect measurement consistency when wound size is held constant. Collectively, these data suggest that measurement replicates are less consistent at later timepoints, but that this effect cannot be attributed to either wound size or time post wounding in isolation: it may be that these factors act in combination to produce the differences shown in Figure 2.4a, or that another factor is responsible. However, it should be noted that the results in Figure 2.5b and Figure 2.6 are based on data from 0 dpw and 3 dpw, whereas the original effect was observed at later timepoints. 3 dpw was chosen because a wound with an initial diameter of 2 mm would be completely healed at later timepoints; conducting a similar analysis on larger wounds for longer times may provide more conclusive evidence as to the reason for changes to measurement consistency with time post wounding.

2.3.4 Inter-operator variability

Two operators each analysed the same 20 unique photographs of wounds at 0 dpw to test for inter-operator consistency. A strong positive correlation was found between single measurements of each photograph between the two operators (Figure 2.7, column 1), suggesting a good level of consistency for all four wound metrics. However, when each operator analysed each photograph three times and the measurements were averaged, the correlation increased for all metrics (Figure 2.7, column 2). This suggests that taking multiple measurements of the same photo increases reliability, which may be advantageous despite the additional time

required.

2.3.5 The effect of the choice of region of interest on measurement consistency

When using the Dermapix software, the operator must designate a region of interest to be reconstructed in three dimensions and then measured. To test whether the size of this region affects the measurement estimates returned, three photographs of wounds taken at 2 dpw were analysed using three different region of interest sizes, taking measurements three times for each (data was collected by Jennifer Coles, undergraduate project student).

Figure 2.8 shows that the size of the region of interest did not explain a significant amount of variation in wound perimeter ($r^2 = 0.13$) or wound volume ($r^2 = 0.00$), where the coefficient of determination is calculated from the means of the three measurement replicates. Therefore, whilst we suggest that the region of interest chosen should be approximately twice the diameter of the wound for convenience of 3D reconstruction, this need not be implemented more formally or deviations controlled for.

Together, the data in Sections 2.3.1 to 2.3.5 suggest that the Dermapix analysis software produces consistent measurements of individual photographs, particularly for perimeter and surface area. Measurements are more consistent at earlier timepoints; however, there is insufficient evidence to attribute this to either wound size or healing time independently. Agreement between different operators performing the same analysis is good, and is further improved when the results of three independent analyses of each photograph are averaged. Therefore, whilst individual measurements may be sufficient, averaging over several measurements is preferable especially when multiple operators collaboratively analyse a large dataset. The size of the region of interest chosen does not appear to affect wound size estimation.

2.3.6 Consistency of measurements from multiple photographs of the same wound

Although the camera system includes light projections to guide the position from which the photograph is taken, small movements cannot be completely controlled for when photographing live mice. To investigate the effect of slight deviations in camera and mouse position on the reliability of wound size estimation, each of the 28 wounds described in

Section 2.3.1 were photographed three times at each timepoint. Each photograph was measured three times using the Dermapix software, and the mean average of the measurements calculated for each photograph replicate (see Figure 2.1b for a schematic of the replication strategy).

Coefficients of variation were calculated for each triple of photograph replicates, and are shown in Figure 2.9a. As with the measurement replicates, the metrics of perimeter and surface area are more consistent than the measures of volume and average depth, both of which involve estimating the depth of the wound. Subdividing the plot by the timepoint at which the photograph was taken (Figure 2.9b) shows similar consistency at 0 dpw and 5 dpw, except for the measure of wound depth, which is more consistent at 5 dpw. One reason for this increase in consistency at 5 dpw could be the texture of the wound: at 0 dpw the wound surface is shiny and this can cause flash glare in some photographs, potentially leading to inconsistent depth measurements if some photographs have glare and others do not (see Figure 2.9c for an example); however, at 5 dpw the wound surface is more matt, which allays the problem. At 8 dpw coefficients of variation are slightly increased and have a larger spread; however, for all metrics there are fewer data points at this time due to the experimental design, and for volume and average depth there are fewer still as the coefficient of variation is not applicable when the mean size is reported as zero.

2.3.7 Assessing the accuracy of wound measurements

Although imaging live experimental subjects is instructive in investigating the consistency of measurements and identifying limitations of the camera system in context, measurement accuracy cannot be quantified as the actual wound sizes are unknown. 3D-printed indents of known volume in surfaces of different curvatures were produced to investigate measurement accuracy (Figure 2.10a-c). Two different printing materials were used to create the constructs, and each indent was photographed three times, with each photograph analysed three times, thus following the replication strategy used in the mouse experiments (Figure 2.1b). The indents made in the shinier of the two materials were imaged both with and without a flashbox. Indents in a curved surface were analysed using the *wound* option in the DermaPix software, which is reported to apply a correction for curved surfaces; indents in flat surfaces were analysed with the *wound* option unchecked.

The LifeViz system consistently underestimated wound volume, with the greatest inaccuracies associated with the cylindrical indents (Figure 2.10d). Murine wounds are likely to

be closest to cylindrical immediately after the wound is made, with wounds becoming more concave in shape as healing progresses. Therefore, whilst the camera measurements were found to be most consistent at early timepoints (Figure 2.4a), it is likely that there is also a greater degree of underestimation of volume when photographing wounds that have been recently created. This may be particularly detrimental when subsequent wound measurements are normalised to initial wound size; however, this study took initial wound measurements at 3 hours post wounding to allow the mice time to recover from anaesthesia, at which time the wounds are likely to have become more concave due to initial edge retraction. More analysis may be necessary to determine whether 3 hours is sufficient for wounds to be suitably concave, and this effect must be balanced with ensuring that initial measurements are taken before the onset of healing. Assuming that initial and subsequent wounds are concave when measured, the 3D camera analysis appears to systematically underestimate wound size; therefore the inaccuracy may be of less concern in the majority of murine wound experiments (which compare closure rates under different conditions or in mice of different genotypes) as comparisons between groups should not be affected.

2.3.8 Using the LifeViz system to assess murine wound closure

To demonstrate the potential of LifeViz as a technique for *in vivo* wound measurement, proposed differences in healing between wildtype mice, $ROR^{+/-}$ mice and $ROR^{-/-}$ mice that are deficient ILC3s, an immune cell population that is hypothesised to play a role in the promotion and regulation of epidermal healing, were investigated. Perimeter, surface area, average depth and volume were used as measures of wound size, and each was normalised to the corresponding initial size of the wound. Figure 2.11 shows that, for wounds with an initial diameter of 4 mm, there is no difference in wound size between the three genotypes studied at either 5 dpw or 8 dpw.

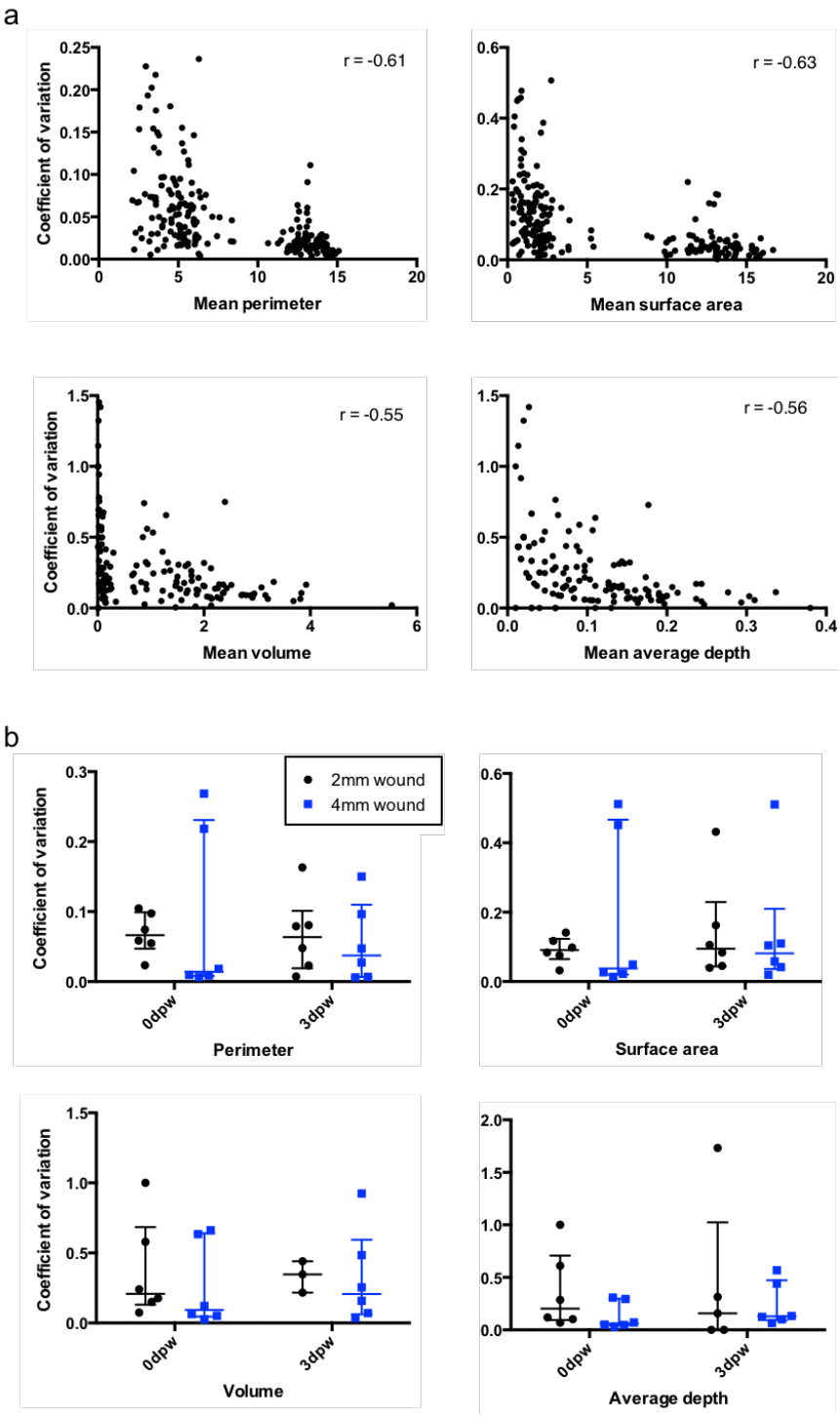

Figure 2.5: **Correlation of measurement consistency with wound size.** (a) Coefficient of variation (a measure of consistency) is moderately negatively correlated with mean wound size, suggesting that larger wounds give more consistent measurements. However, larger wounds are from earlier timepoints, so healing time is a confounding factor. r denotes Spearmans Rank correlation coefficient. (b) Smaller wounds (initial diameter 2mm) give similarly consistent measurements to larger wounds (initial diameter 4mm) when compared at the same timepoint, suggesting that size alone does not affect measurement consistency. Error bars show median and interquartile range.

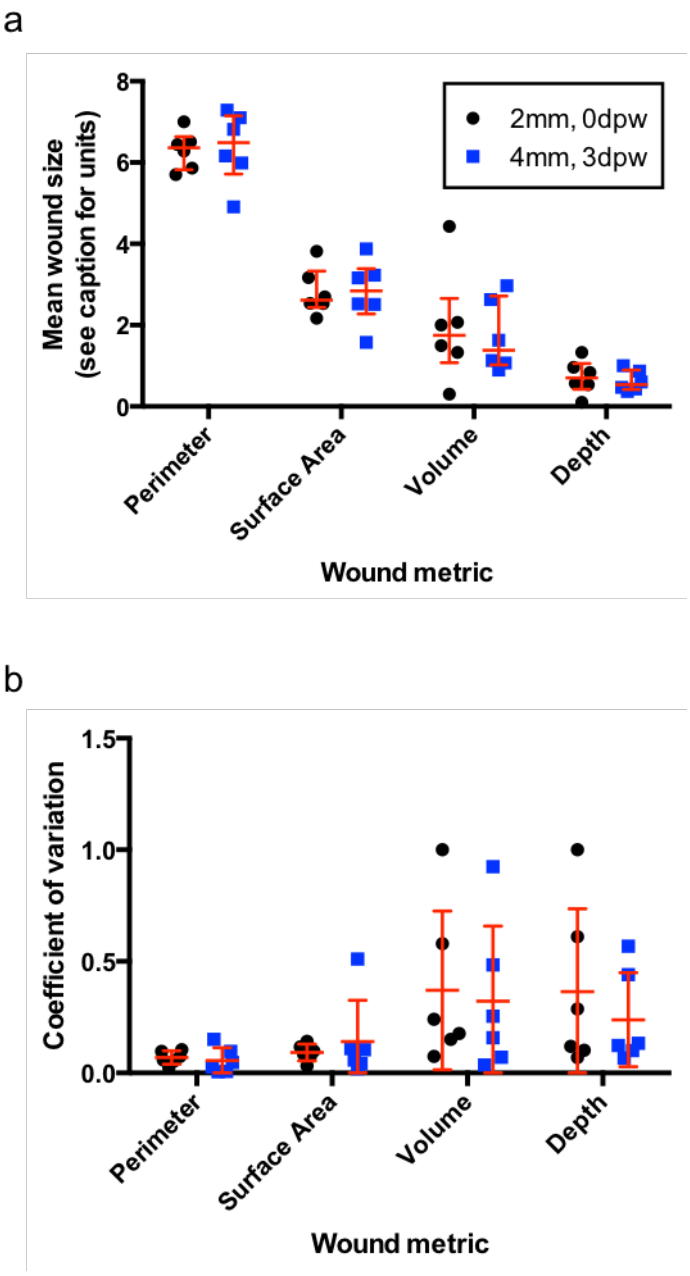

Figure 2.6: **Consistency of measurement replicates is similar for wounds of the same size but different stages of healing.** (a) Wounds of 2 mm diameter (at 0 dpw) are a similar size as wounds of 4 mm initial diameter at 3dpw. Units are: perimeter, mm; surface area, mm^2; volume, mm^{-3}; diameter, mm^{-1}. (b) Measurement consistency does not differ between wounds of the same size at different timepoints post wounding. (a-b) Error bars show median and interquartile range.

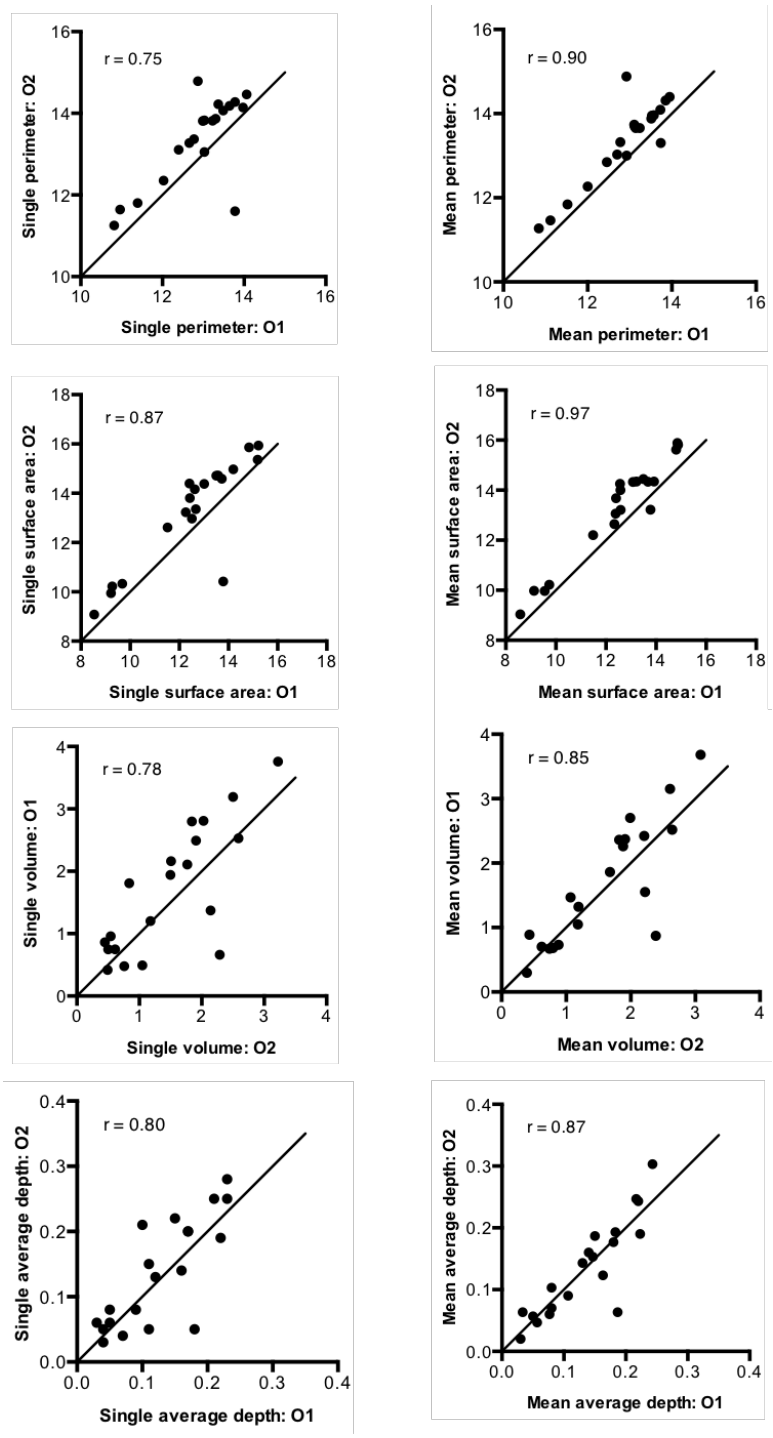

Figure 2.7: **Inter-operator variation for single measurements of each photograph, and the average of three measurements.** Wound measurements determined by operator 1 (O1) and operator 2 (O2) from the same set of photographs show a strong positive correlation was when single measurements were made of each photograph (column 1). The correlation is stronger when the mean of three separate measurements are averaged (column 2). Solid lines depict perfect agreement between operators; r denotes Pearsons correlation coefficient.

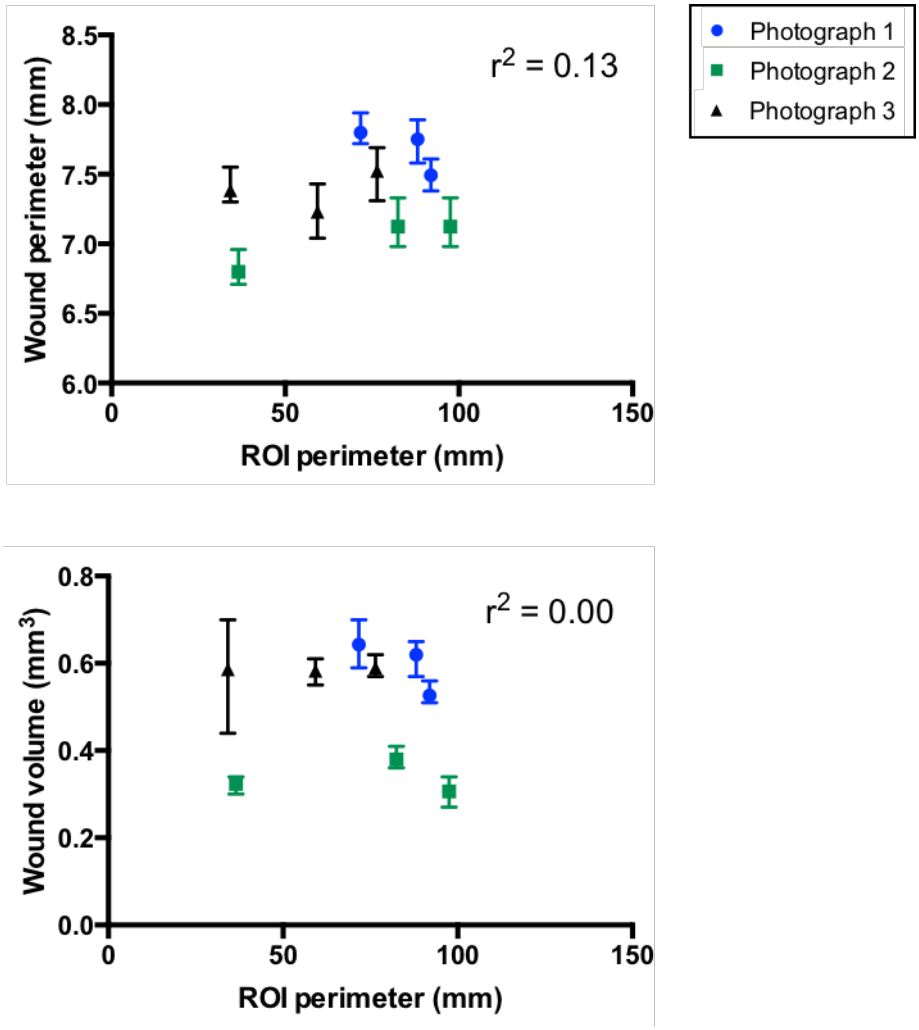

Figure 2.8: **Effect of the size of the region of interest on estimates of wound size.** Wound perimeter and volume were measured for three photographs at three different region of interest sizes. Regression analysis showed no effect of region of interest size on the measurement obtained. Error bars show mean and range (of three measurement replicates); r^2 denotes the coefficient of determination.

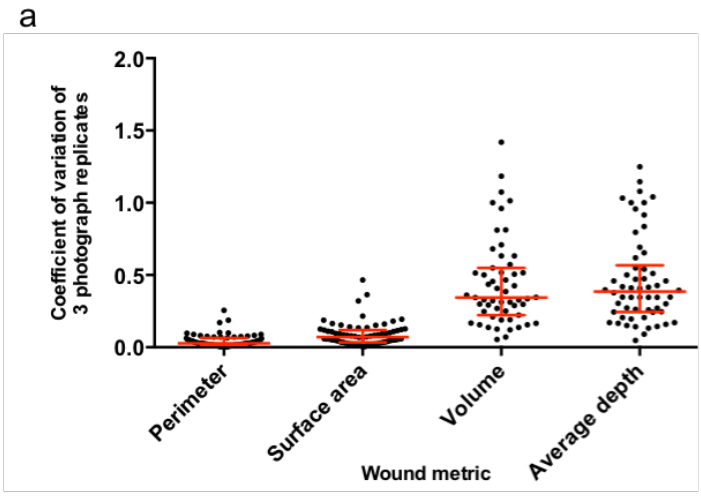

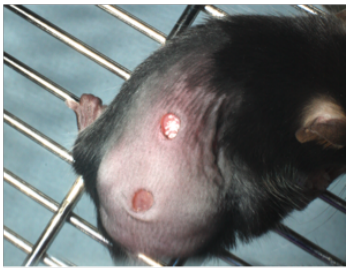

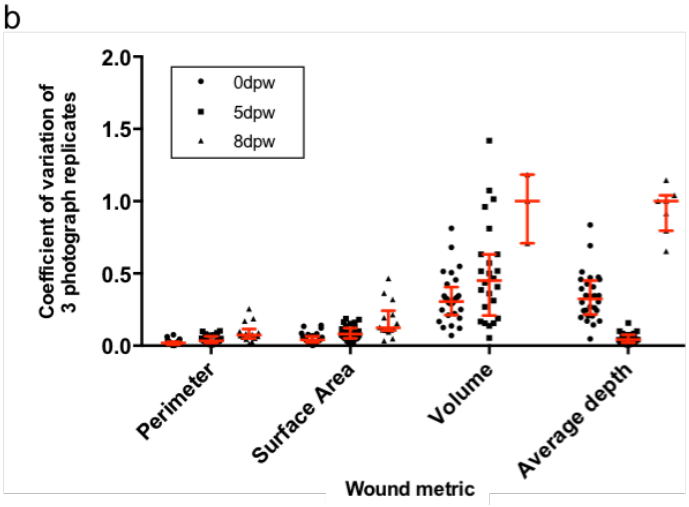

Figure 2.9: **Consistency of measurements taken from multiple photographs of the same wound.** (a) Coefficients of variation for each triple of photograph replicates show that metrics that involve depth (volume and average depth) are less consistent than perimeter and surface area. Overall levels of consistency are similar to those of measurement replicates. (b) Consistency is similar at all timepoints for perimeter and surface area. Consistency of volume measurements is similar at 0 dpw and 5 dpw, but consistency of average depth measurements reduces at 5 dpw. Consistency appears higher at 8 dpw for volume and average depth, but this may be due to non-applicable coefficients of variation where the mean was zero (as in Figure 2.4). Error bars denote median and interquartile range. (c) Flash glare on wounds from early timepoints may be responsible for less consistent depth measurements at 0 dpw.

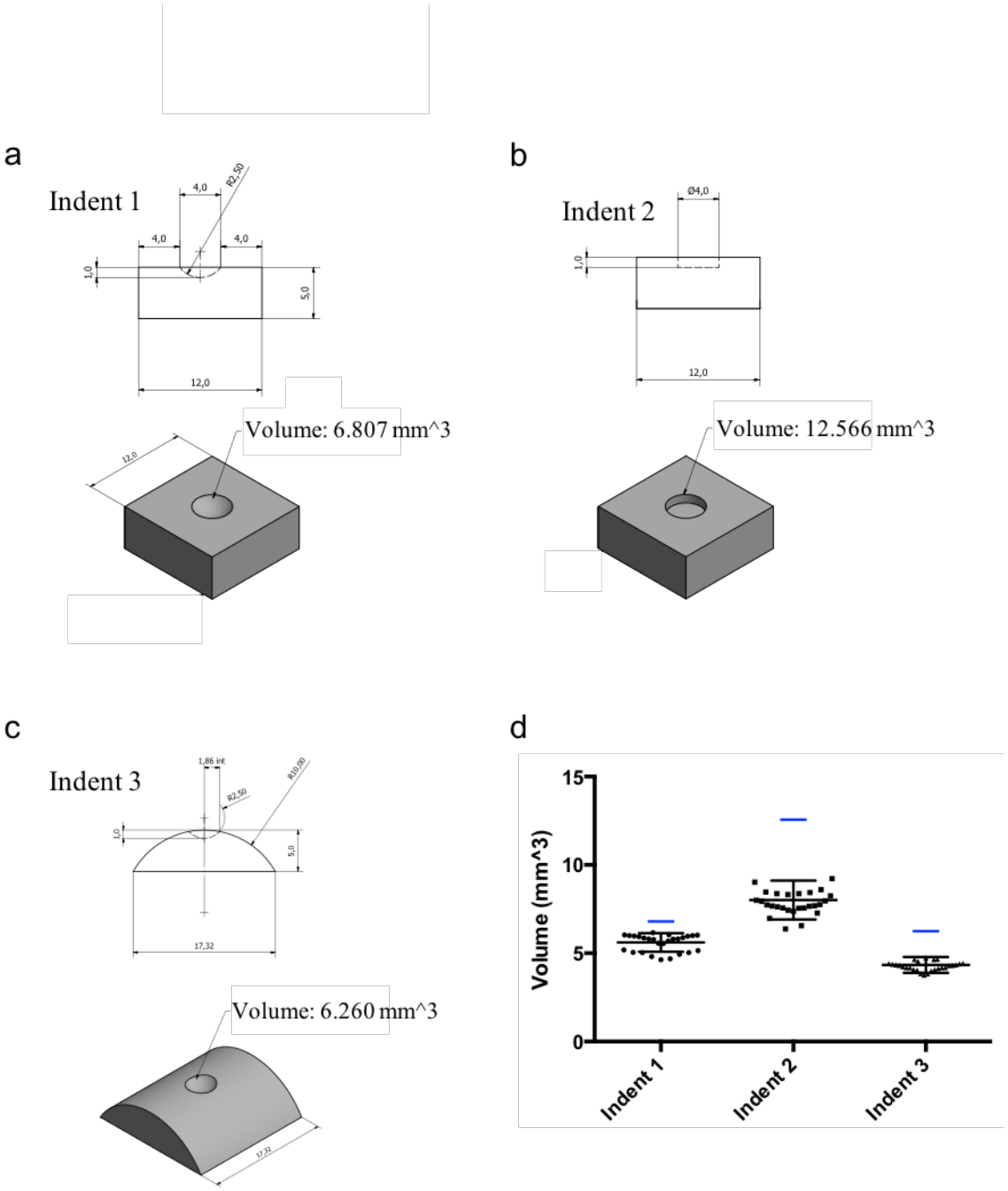

Figure 2.10: **Assessment of the accuracy of camera measurements using indents of known volume.** (a-c) 3D-printed indents of known volume were photographed to assess the accuracy of the LifeViz system. (Figures produced by Mark Bentley, biology mechanical workshops.) (a) A concave indent in a flat surface. (b) A cylindrical indent in a flat surface. (c) A concave indent in a curved surface, replicating the relative curvature of a murine dorsum. (d) 3D camera measurements of each of the three indents consistently underestimated wound volume compared to the true value (shown by blue lines.) Error bars denote mean and standard deviation.

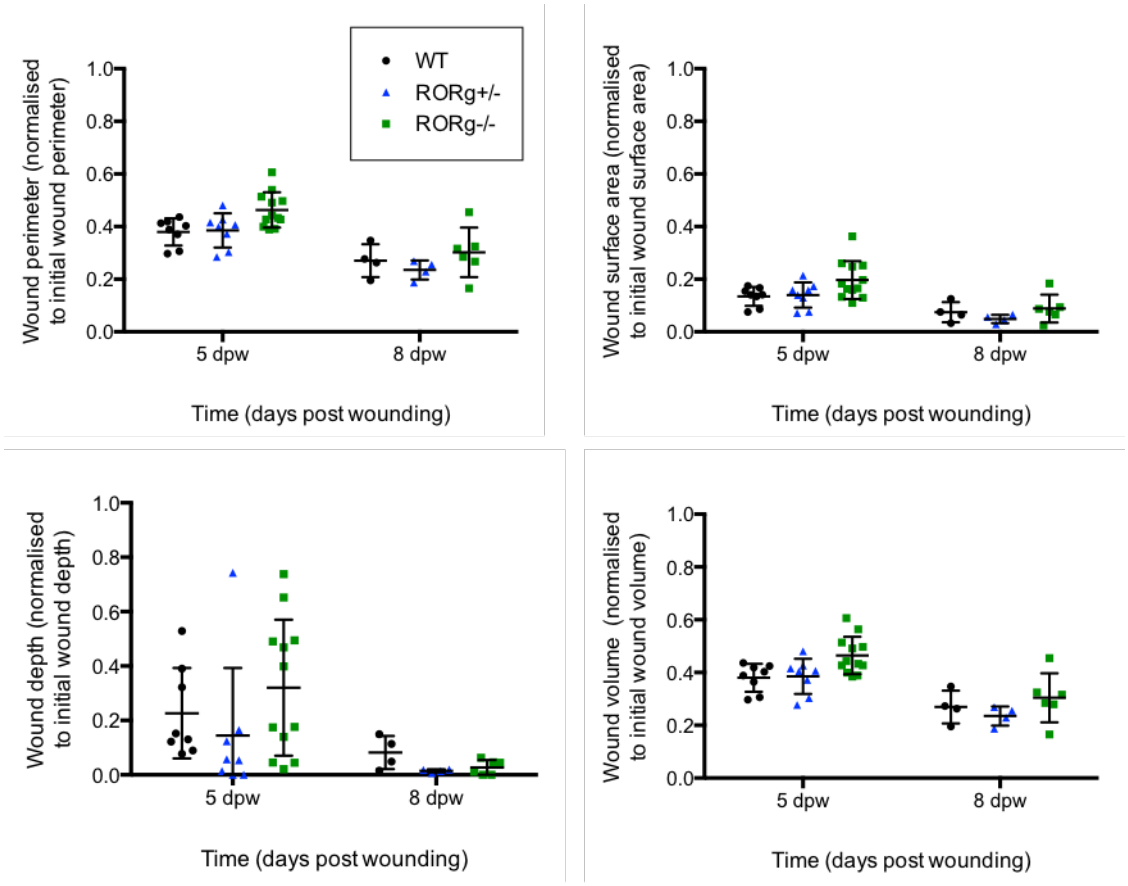

Figure 2.11: **Using the LifeViz system to assess murine wound closure in different genotypes.** Perimeter, surface area, average depth and volume of wounds with an initial diameter of 4 mm in mice of three genotypes. There is no difference in wound size between the three genotypes studied at either 5 dpw or 8 dpw. Error bars denote mean and standard deviation.

2.4 Discussion

A recent systematic review has highlighted the need for robust assessments of the accuracy, agreement, reliability and feasibility of techniques for wound measurement in the clinic [152]. This study contributes to that body of work by presenting a comprehensive analysis of the application of a wound measurement technique in murine *in vivo* wound experiments. Given the large number of studies using mouse models to investigate cutaneous healing under various conditions [54, 146, 147, 148, 149, 150, 151], and their requirement to objectively assess changes to wound size over time [145], it is important that novel and nascent technologies are not only evaluated in a clinical setting, but also undergo rigorous assessment for use in murine experiments.

Callipers are frequently used to measure murine wounds, and are equivalent to the "simple ruler method" for assessing clinical wounds. Clinical studies routinely multiply the greatest length and width of the wound to determine surface area; this technique has been found to overestimate wound size by 41% when compared to digital planimetry [163] and 29-43% when compared to manual planimetry [164]. Caliper measurements to assess wound area can be improved by assuming that wounds are elliptical rather than rectangular, finding the product of π, the longest and shortest radii of the wound. This method has been found to be reasonably accurate and reliable for clinical wounds smaller than 40 cm^2 [165, 166]. However, such measurement strategies are unreliable and inaccurate for wounds of irregular shape; whilst this is a common problem in the clinic, experimental wounds are fairly close to elliptical, especially at early timepoints, so these methods may be more applicable. Calipers are low cost but, whilst the simple ruler method for clinical wound assessment is considered easy to implement, it may be argued that the handling skills required to complete a caliper measurement on a mouse are more advanced than those used during 3D photography.

Planimetric measurement is inappropriate for the assessment of murine wounds for several reasons. Firstly, planimetric approaches perform best when applied to wounds larger than those routinely included in murine studies; one such measurement system was found to be most reliable on wounds larger than 25 mm^2 [154]. Another drawback of planimetry is the need for contact with the wound: a transparent film is first placed on the wound and the margin traced with a pen, increasing the risk of disrupting the wound or causing contamination [152]. This may be less detrimental in the assessment of clinical wounds, when measurements are commonly taken at weekly intervals and can be timed to coincide with other management procedures such as redressing [167]; however, murine studies commonly

take daily measurements over the course of a week [147, 34, 149, 151]. If carried out using planimetry, taking measurements this frequently would lead to potentially unacceptable levels of disruption to the wound bed. Finally, planimetry is time consuming [168] and requires the experimental subject to be immobile for the time taken to trace the wound. Whilst this is straightforward to achieve in the clinic, applying the method to mice would require the animals to be anaesthetised each time a measurement was to be taken. Compared to non-contact methods, this would reduce the frequency at which measurements could be taken; experimental results might also be affected due to deformations of the wound as body shape changes under anaesthesia, and any anaesthesia-induced changes to the natural healing process. As such, planimetry has not to our knowledge been successfully applied to murine healing studies.

This study has not included direct comparison of the Dermapix system to an alternative method of wound measurement; however, a clinical study found that a different method of stereophotographic imaging was more accurate than both the simple ruler method and manual planimetry for measuring wounds using 2D metrics [169]. Instead we have assessed the accuracy of the technique by photographing indents of known volume that are a similar size to those in murine studies, allowing an evaluation of accuracy that is not commonly presented in assessments of measurement techniques in a clinical setting [152].

Accurate determination of wound boundaries can be problematic regardless of the measurement technique employed [152]. Calliper measurements are well known to be somewhat subjective, as the operator is required to determine the position of the wound edge while the measurement is being taken [170, 171]. Although the Dermapix system also requires manual delineation of the wound edge, this occurs after the wound has been photographed. Separating the data collection step from the measurement process is particularly useful in murine studies as, once the relatively quick and straightforward process of photographing wounds has been carried out, the measurement analysis can be undertaken without disturbing the mice. This reduces the time pressure that is often associated with taking calliper measurements, and allows wounds to be analysed multiple times and by multiple operators if necessary.

Localisation of wounds on curved surfaces of the body (for example the heel) is known to affect the accuracy of wound measurement [152]; this is also a consideration for experimental wounds in mice, as the murine dorsum is a curved surface. Our data suggest that the correction employed by the LifeViz camera system enables the volume of indents in curved surfaces to be measured with an accuracy that is not significantly different from that of

indents in flat surfaces (Figure 2.9). However, the shape of the indent does affect the accuracy: volumetric measurements of cylindrical indents are less accurate than those of their concave counterparts. The problem would be compounded for wounds that are extensively undermined [152]; however, this is more likely to occur in a clinical rather than experimental setting.

By careful evaluation of the LifeViz 3D imaging system in the context of murine wound healing experiments, we have found the technology to be reliable, with a particularly high level of inter-operator agreement. The technique is convenient for use in experimental studies owing to its non-invasive nature and simple photographic approach; however, the time required to analyse the images is a limitation for large datasets. Finally, whilst the 3D camera system underestimates wound size the inaccuracy is fairly consistent, suggesting that it may be most suitable for the comparative studies that make up most of the murine wound healing literature. Although it would be advantageous for future studies to assess the LifeViz system in direct comparison with other wound measurement procedures, our data suggest that the technique has great potential to facilitate objective measurement of murine wounds.

Chapter 3

Epidermal wound healing: do mathematical models tell us anything new?

3.1 Introduction

Mathematical models are increasingly used to describe biomedical systems; however, their ability to address novel biological or clinical questions has largely gone unscrutinised. Epidermal wound healing is one such system, whereby complex interactions between epidermal cells (predominantly keratinocytes), immune cells and signalling molecules facilitate rapid restoration of the epidermal barrier through a process known as re-epithelialisation. Keratinocytes within and surrounding a wound undergo processes of migration, proliferation and differentiation, which are tightly regulated temporally and spatially to achieve successful epidermal healing [98]. A wide range of growth factors and cytokines, secreted by skin, blood and immune cells in and around the wound, control these processes [112].

Re-epithelialisation of the epidermis begins when keratinocytes in a layer close to, but not adjacent with, the wound edge increase their rate of mitosis, providing a pool of extra cells to facilitate repair and causing a thickening of the epidermis close to the wound edge [98]. Undamaged cells in a layer immediately adjacent to the wound undergo dissolution of their desmosomes (cell-cell contacts) and hemidesmosomes (cell-substratum contacts); cells then become flattened and express new integrins which facilitate their migration across the granulation tissue [172, 173, 99, 98]. Finally upon complete epithelialisation of the injury

site, keratinocytes gradually re-adopt the characteristics of those in unwounded skin [98]. The ability of the healing epidermis to restore its functionality is a rare regenerative outcome that is not observed in most other mammalian tissues.

In contrast to epidermal regeneration, healing of deep dermal wounds leads to the formation of scar tissue, which does not restore full functionality to the dermis. To achieve dermal healing, the processes of haemostasis, inflammation, angiogenesis, dermal collagen deposition, contraction, resolution of inflammation and tissue remodelling are undergone [174, 175]. Although dermal healing is initiated at a similar time point to epidermal repair, and there is some feedback between the systems, the two compartments can be considered distinct and are often studied individually. *In vivo* and mathematical studies that address epidermal healing in isolation can be instructive in understanding healing mechanisms and pathologies: in particular, the epidermis has been implicated in healing disorders despite the relative simplicity of this compartment. For example, chronic wounds (those that do not heal within the usual timeframe: a disorder that costs between 1 and 2% of the healthcare budget in developed countries [176, 17, 177]) exhibit a characteristic piled up and hyperproliferative epidermal edge, implying that aberrant epidermal healing is involved in the wound pathology [52]. Additionally, the rate of epidermal repair may be indicative of the progress of more complex dermal healing processes, so determining the epidermal healing trajectory could form an important diagnostic tool.

In order for mathematical modelling to make a significant contribution to cutaneous wound healing research, models must go further than quantitatively describing known aspects of the processes involved. Whilst the seminal mathematical models of epidermal healing have been reviewed extensively, little consideration was initially given to the scientific advancements or clinical implications that result [82]. More recently, focus moved from mathematical descriptions of normal repair to investigations of impaired healing and models that are developed to inform treatment design; however, reviews assessing the benefits of such studies focused mainly on models of the dermis [178, 179].

This review seeks to assess whether mathematical models have advanced beyond replicating known healing dynamics in the adult epidermis to providing additional information to that obtained experimentally. We first discuss areas in the study of epidermal repair where mathematical models have the potential to advance our biological or clinical understanding. The process of mathematical modelling is then described, and examples of extensions and combinations of pre-existing models are presented. The ability of mathematical models to provide novel insights into the scientific understanding and clinical management of epidermal

wounds is evaluated, and finally the importance of interaction between experiments and theoretical studies is highlighted.

Models of *in vivo* epidermal wound healing are discussed, including those that simulate both dermal and epidermal processes. Models of *in vitro* systems, including those investigating wounding in cell monolayers, and models of epithelial dynamics in tissue homeostasis are beyond the scope of this review, but are described in detail in works by Smallwood (2009) [180] and Maclaren et al. (2015) [181]. Given that models are often developed incrementally, with current approaches based heavily on simpler work published many years previously, this review considers both seminal and contemporary studies. A summary of the models included is presented in Table 3.1.

Table 3.1: **Computational models of epidermal healing reviewed in this chapter.**

Study	**Context**	**Category**	**Modelling approach**	**Populations and processes**	**Based on**
Adam (1999) [182]	Bone and epidermis	Descriptive	ODE	Growth factor concentration; wound edge.	Sherratt and Murray (1990) [87]
Arnold and Adam (1999) [183]	Bone	Descriptive	ODE	Growth factor concentration; wound edge.	Adam (1999) [182]
Bowden et al. (2014) [184]	Dermis and epidermis	Clinically relevant	ODE	Epidermal tissue; dermal tissue; forces acting on wound.	- - -
Denman et al. (2007) [185]	Epidermis	Clinically relevant	PDE	Epidermal stem cells; epidermal transit amplifying cells recently progressed from stem cells; transit amplifying cells; quiescent cells.	Sherratt and Murray (1990) [87]; Maini et at. (2004) [186]
Javierre et al. (2009) [187]	Dermis	Mechanistic	PDE	Growth factor concentration; wound edge.	Arnold and Adam (1999) [182]

Jones et al. (2004) [188]	Skin in general	Clinically relevant	Geometric	Area of wound; area of slough (dead tissue).	- - -
Jung et al. (2015) [167]	Healing prognosis	Clinically relevant	Statistical	Wound dimensions; clinical characteristics.	- - -
Maggelakis (2003) [189]	Dermis	Descriptive	PDE	Oxygen concentration; MDGF concentration; capillary density.	- - -
Safferling et al. (2013) [75]	Epidermis	Mechanistic	ABM	Keratinocytes.	- - -
Sherratt and Murray (1990) [87]	Epidermis	Descriptive	PDE	Keratinocyte concentration; concentration of biochemical auto-regulator of mitosis.	- - -
Sherratt and Murray (1992) [190]	Epidermis	Mechanistic	PDE	Keratinocyte concentration; concentration of biochemical auto-regulator of mitosis.	Sherratt and Murray (1990) [87]
Sherratt and Murray (1992) [191]	Epidermis	Clinically relevant	PDE	Keratinocyte concentration; concentration of biochemical auto-regulator of mitosis; topical biochemical regulator of mitosis.	Sherratt and Murray (1990) [87]
Sun et al. (2009) [192]	Epidermis and dermis	Mechanistic	ABM	Keratinocytes; TGF-β1; extracellular matrix.	Sun et al. (2007) [193]

Vermolen and Adam (2007) [194]	Dermis and epidermis	Descriptive	PDE	Keratinocyte concentration; concentration of biochemical auto-regulator of mitosis; oxygen concentration; MDGF concentration; capillary density.	Sherratt and Murray (1990) [87]; Gaffney et al. (2002) [195]; Maggelakis (2003) [189]
Zahouani et al. (1992) [196]	Skin in general	Clinically relevant	Geometric	Position of wound edge.	- - -

3.2 Areas in which mathematics can advance knowledge and treatment of wounds

Although *in vivo* studies have provided a good understanding of wound healing at discrete locations and times, financial and ethical constraints have limited their ability to incorporate the spatial and temporal resolution required to draw translational conclusions [197, 52]. For example, semi-quantitative data from images of tissue sections have shown that proportions of keratinocytes undergoing mitosis or migration change over time; but robust quantitative measurements, which may enable identification of methods to expedite epidermal healing without promoting over- or under-proliferation, are not available. The influence of hair follicles and other epidermal appendages in balancing mitotic and migratory populations represents further complexity that could be investigated using a mathematical approach. Additionally, the chemical and mechanical stimulation and regulation of epidermal healing are difficult to investigate using purely *in vivo* methods. Mathematical models, based on sparse experimental findings, can assimilate data from multiple studies and produce solutions over continuous scales that may overcome experimental limitations [197].

The dynamic impact of immune cells on epidermal healing is another widely accepted, but poorly understood, aspect of cutaneous repair. Whilst some evidence exists for the roles played by individual immune cell populations in initiating and regulating healing, there is limited systematic understanding of the factors they produce and the mechanisms underlying their observed effects. The reciprocal relationship between immune cells and keratinocytes is poorly understood, as are the dynamics of immune cell recruitment to, and efflux from, the wound site. Mathematical models of these aspects may lead to insights that experimental studies have thus far failed to produce, for example by identifying which immune cell dynamics are essential for successful healing, and by suggesting how systems deficient in these processes may be altered to avoid or reverse chronic wound phenotypes [198, 199].

More broadly, understanding the timing of key events in the wound healing cascade would be advantageous, as identification of therapeutic windows of opportunity could lead to healing deficiencies being corrected in a timely manner. The timepoint and position at which the process of cutaneous repair stalls, leading to the formation of a chronic wound, is yet to be established; identifying the tipping point at which a normally healing wound may become pathological would be of benefit [52]. Mathematical models, such as that developed by Jung et al. (2015), can also be used to assess whether cellular and signalling processes are

proceeding as expected, thus providing a prognostic marker for whether healing is likely to be successful [167].

Models can only inform treatment decisions if their quantitative output relates to relevant aspects of the understanding or clinical management of healing. As such it is important to ensure that models are designed to investigate areas of current uncertainty; close collaboration with scientists and clinicians will help facilitate this. Parameters and variables should also relate to aspects of healing that are measurable in the lab and clinic. The equivalence need not be direct, but a clear designation of the relationships, including possible transformations, between values in the model and features of tissue repair in patients or experiments is necessary for theoretical studies to provide impact.

3.3 The mathematical modelling process

Mathematical modelling is a multi-stage process that begins with the selection of a modelling approach appropriate to the nature of the biological system in question. Key considerations underpinning the choice of approach are detailed later in this section. The biological and chemical components (e.g. keratinocytes, immune cells or signalling molecules) involved in the system must then be identified, which determines the dependent variables to be considered in the model. It is then necessary to select the components that are relevant to the biological or clinical question to be investigated, as complex models that attempt to describe the entire biomedical system may be limited by the noise and uncertainty associated with large numbers of potentially irrelevant equations and parameters. The processes (e.g. migration, proliferation or differentiation) undertaken by the components should then be identified, leading to formulation of model equations or computer simulations that best represent the known dynamics of the biological processes. If appropriate, models may then be further simplified to reduce the number of dependent variables or model parameters included; this is necessary to make complex models tractable, but can also be a valuable approach when analysing competing biological processes in simpler models. Parameter estimation based on experimental data or model fitting should then be undertaken, before generating solutions and comparing model output with biological findings.

Three key modelling approaches have been previously employed in the study of epidermal healing: ordinary differential equations (ODEs), which calculate changes to cell population sizes over time; partial differential equations (PDEs), which consider both space and time; and agent-based models (ABMs), in which cells are modelled as individual entities (rather

than overall populations) whose behaviour is governed by a predetermined set of rules that permit the incorporation of individual stochasticity. It is also possible to develop hybrid models that combine more than one of these techniques (see Section 3.4). In general, models predict the number of keratinocytes in the wound area and, with the exception of ODEs, also their spatial distribution. More complex models, for example those developed by Maggelakis (2003) [189] and Bowden et al. (2014) [184], also include growth factors, other signalling molecules or aspects of the underlying dermis, such as extracellular matrix (ECM) composition and angiogenesis. Whilst the broad steps of the modelling process described previously are fairly ubiquitous, the specific requirements at each step will vary depending on the modelling approach employed. A seminal PDE model of epidermal healing developed by Sherratt and Murray (1990) [87] is presented in Table 3.2 and Figure 3.1, illustrating how differential equations may be formulated to describe how keratinocyte concentration changes during repair. This approach is in contrast to the more recent ABM developed by Safferling et al. (2013) [75], which considers cells as individual agents following a set of rules (Table 3.3).

Table 3.2: **A description of the stages and implementation of a PDE modelling approach [87].**

Stage of the modelling process	**Implementation in Sherratt and Murray, 1990** [87]
Selection of modelling approach based on the nature of the biological system	Epidermal wound closure is a spatially-dependent process, with the location of cells determining which areas of tissue are 'healed', so a non-spatial ODE model was not considered appropriate. Both PDEs and ABMs can represent spatial properties of a wound, but a PDE was chosen as it is a less computationally expensive approach.
Identification of the populations and processes	Populations: keratinocytes. Processes: cell migration; mitotic generation.
Formulation of model equations or computer simulations that best represent the known dynamics of the biological processes	A reaction-diffusion equation was used to describe the dynamics of a population of keratinocytes, measured in number per unit area and represented by the variable n: $$\frac{\partial n}{\partial t} = D\boldsymbol{\nabla} \cdot \left[\left(\frac{n}{n_0} \right)^p \boldsymbol{\nabla} n \right] + sn \left(1 - \frac{n}{n_0} \right) . \quad (3.1)$$ Cell migration takes the form of a diffusion term, whereby cells move from areas of high concentration to low concentration. D is a constant diffusivity. The concept of contact inhibition is incorporated by making the diffusion term non-linear (when $p > 0$), this reduces the diffusion rate when cell concentration is low to model individual cells remaining in contact with their neighbours. Mitosis is described using a logistic growth term, whereby the proliferation of cells is slow in areas of high and low cell concentration, but fast in regions of moderate concentration. The maximum concentration of cells is given by n_0 and the overall rate of cell division is controlled by s.

Model simplification to reduce the number of parameters	The dimensional parameters D and s may be combined into a single non-dimensional parameter $D^* = \frac{D}{sL^2}$ that denotes the ratio of diffusion rate to mitosis rate, where is the initial wound radius. Non-dimensionalising n and space leads to the dimensionless equation $$\frac{\partial n}{\partial t} = D^* \boldsymbol{\nabla} \cdot [n^p \boldsymbol{\nabla} n] + n(1-n) \, , \qquad (3.2)$$ in which the number of parameters has been reduced from three to two (D^* and p).
Parameter estimation based on experimental data or model fitting	Due to a lack of experimental data available to directly inform choices of D^* and p, a best-fit analysis was conducted. Model output (relative wound radius) was compared to wound radius data from experiments for various choices of parameter values. The parameters that gave the best fit to the data were identified and, after checking that the values were biologically reasonable, included in the model.
Comparison of model output with biological findings	Cell densities were converted to wound radii by considering an area 'healed' when keratinocytes reached 80% of their unwounded cell concentration. The speed of healing was calculated and was consistent with experimental findings. However, the solutions failed to replicate an experimentally observed initial lag phase, where healing progresses slowly at early timepoints, which motivated model extensions incorporating biochemical regulation.

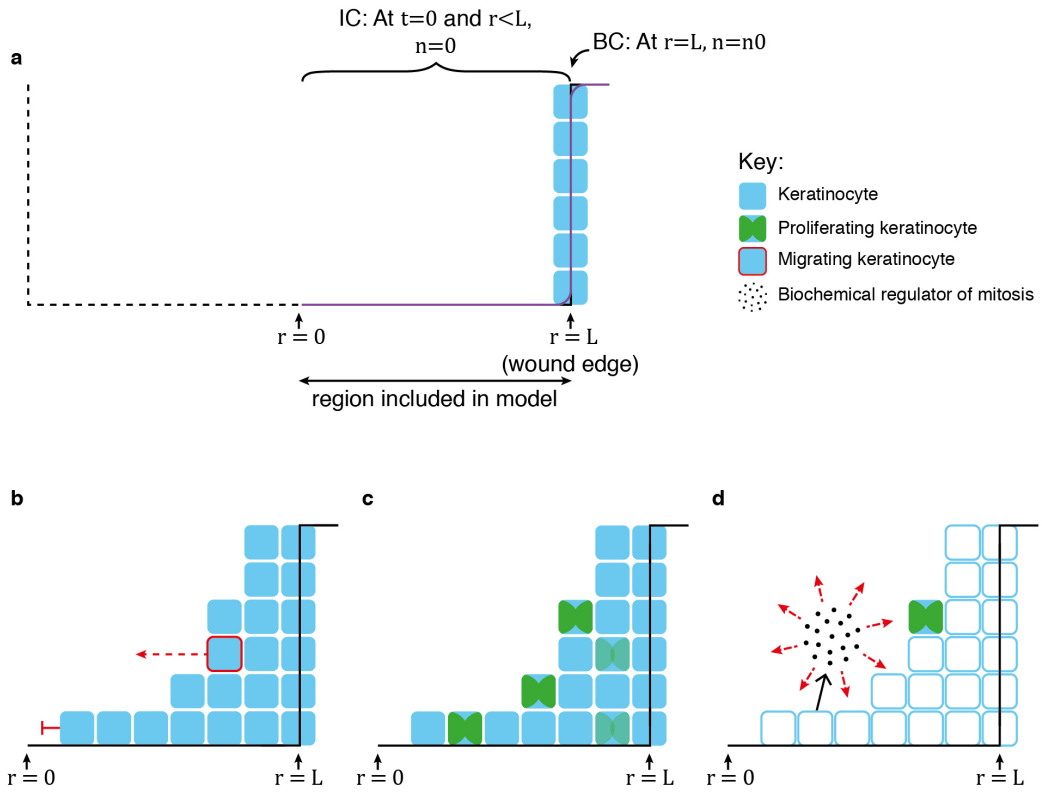

Figure 3.1: **The cellular processes included in a reaction-diffusion PDE model of epidermal repair (Sherratt and Murray, 1990 [87]).** (a) The wound space is considered two-dimensional and symmetric, with only one half of the wound included in the model domain (between $r = 0$ and $r = L$). The keratinocyte concentration at the boundary ($r = L$) is assumed to be equal to that of unwounded skin ($n = n_0$), and the initial condition (IC) states that there are no keratinocytes within the wound before re-epithelialisation begins ($n = 0$ at $t = 0$). (b) Migration is modelled using a non-linear diffusion term: keratinocytes in regions of high cell concentration diffuse into the wound space, whereas those in regions of low cell concentration undergo do not migrate, reflecting contact-controlled migration. (c) Keratinocyte proliferation is represented by a logistic growth model: mitosis occurs more frequently in areas of low or moderate cell concentration, but is constrained in areas of high cell concentration where there is limited space for new keratinocytes. (d) In an extension to the original model (a-c) the concentration of a biochemical regulator of mitosis is included. Keratinocytes produce a biochemical, which diffuses, enhances or inhibits (depending on the model formulation in question) the rate of keratinocyte mitosis, and decays linearly.

Table 3.3: **A description of the stages and implementation of an ABM modelling approach [75].**

Stage of the modelling process	**Implementation in Safferling et al., 2013** [75]
Selection of modelling approach based on the nature of the biological system	Creation and extension of the epidermal tongue are spatial processes so ODEs were inappropriate. Due to the low cell densities in the EET a discrete representation was chosen.
Identification of the populations and processes	Populations: fast dividing cells; basal cells; suprabasal cells; early suprabasal cells. Processes: proliferation; cell-cell adhesion; cell-substrate adhesion.
Formulation of model equations or computer simulations that best represent the known dynamics of the biological processes	An ABM was used to describe the positions of individual keratinocytes at the edge of and within a wound: fast dividing cells were given a fixed position. But increased proliferative activity; basal cells exerted the lowest adhesion forces, allowing migration to take place; supra-basal cells exerted high adhesion, inhibiting migration in the tissue surrounding the wound; early supra-basal cells represented a state between basal and supra-basal. Additionally, proliferating cells grow and increase the intercellular pressure of their neighbours. Distances between neighbouring cell centres were optimised based on intercellular pressure, cell-cell adhesion and adhesion to the basal membrane, leading to passive migration. Finally, the strength of cell-cell adhesions varied based on the cell types involved; the strength of cell-substrate adhesion varied depending on position (strong adhesion within the wound space impaired active migration).

Parameter estimation based on experimental data or model fitting	Bespoke experimental data was used to identify the relative sizes of parameters, but beyond that values were fairly arbitrary.
Comparison of model output with biological findings	A subset of basal cells were 'stained' and their locations at various timepoints compared with equivalent experimental staining, which were found to be qualitatively similar

Models formulated using differential equations (DEs) are based on different assumptions, and lead to very different outputs, than those of agent-based simulations. Both approaches have advantages and limitations, and the choice of most appropriate model technique should be informed by the characteristics of the biomedical system and the research question to be addressed. For example, standard DE approaches employ continuous descriptions of the populations involved, which allow the qualitative behaviour that results from cells moving in a continuum, subject to physical aspects such as flow and stress, to be investigated; ABMs are less amenable to including these mechanical and physical factors. However, continuous descriptions are most appropriate for continuous variables (such as the concentration of a chemoattractant) and for large populations of discrete entities (such as cells): solutions of DEs may not be biologically relevant when cell numbers or concentrations are low. By contrast, ABMs are formulated based on the properties of, and interactions between, individual agents within a biological system; this allows each agent to be described by a unique set of characteristics, which permits examination of heterogeneity in the overall population. Although it is possible to represent the parameters in DEs using distributions of values, this has not been applied in the DE models of epidermal healing developed thus far: instead their parameters and resulting solutions represent the average behaviour of each component of the system. This is reasonable when populations are fairly homogeneous and well-mixed but provides limited insight into the behaviour of individual cells or levels of variation across the population, which may become apparent when investigated using ABMs [200].

It is possible to describe heterogeneous populations in DE models by increasing the number of dependent variables: for example, a simple model with a single variable describing the number of keratinocytes may be extended to include separate variables for epidermal stem cells, transit amplifying cells recently progressed from stem cells, transit amplifying cells and quiescent cells [185]. Existing ODEs for epidermal healing also impose a homogenous spatial distribution which, if deemed inappropriate, may be overcome using a similar method: additional equations for populations in different spatial compartments, and terms stipulating

how biological components move between compartments may be included in a model. For example, separate equations could describe the keratinocytes within the wound space and those that make up the unwounded tissue at the periphery, with a transfer term allowing cells to migrate from the periphery to the wound space at a given rate. However, both these approaches require discrete categorisation of cell types and increased model complexity, making parameter estimation less manageable and increasing the computation time required to generate solutions [181]. Alternatively, spatial heterogeneity can be explicitly modelled using PDE approaches, which describe how the number or concentration of a biological component changes continuously over space and time, or ABMs that can include space, time and stochasticity.

Mathematical models of healing generally consider the wound as two-dimensional, asserting that the epidermis is sufficiently thin in comparison to wound diameter to neglect its depth, and axisymmetric, allowing the problem to be further simplified to one dimension [87]. An obvious extension, which might be more relevant to clinical scenarios, is to consider the effect of wound geometry on healing outcomes in either two or three dimensions. This may be achieved using PDEs or ABMs. For example, a PDE model for epidermal growth factor (EGF) stimulated keratinocyte migration and mitosis was established for arbitrary wound shapes, and demonstrated that the geometrical parameters of the model strongly influence the healing kinetics (healing was more readily initiated at regions with high curvature) [187]. This suggests that studies of axisymmetric wounds may be limited in their applicability to the irregular wound shapes more commonly observed in the clinic. ABMs, for example a study by Safferling et al. (2013) [75] that found essential elements of healing occurring in locations away from the frequently examined leading edge, have been used to investigate healing in three-dimensions, which is an area still under development for DEs. However, due to the low cell concentrations, continuous nature of signalling molecule gradients and spatial influences of the healing epidermis, it is likely that hybrid models (including both ABM and DE approaches) would be most instructive as studies move away from one- and two-dimensional abstractions (see Section 3.4) [75, 192].

A model component may describe a single biological entity, or a group of entities that have a similar action and effect. For example, Vermolen and Adam (2007) developed a PDE model in which growth factors produced by macrophages (termed MDGFs) stimulate keratinocyte mitosis [194]. MDGFs do not represent a specific signalling molecule, but instead describe a group of different biochemicals that collectively regulate the system, with inevitable redundancy and cross-talk between the individual components [201]. Modelling the generalised group of growth factors allows the overall function and consequences of

biochemical regulation to be determined, without requiring complex descriptions of complete signalling pathways to be incorporated. ODEs and PDEs can also be simplified by non-dimensionalisation; this introduces dimensionless parameters, each of which may include several biological phenomena, that allow for identification of competing effects and more efficient exploration of the parameter space.

Whereas it can be difficult to alter biological components in isolation without affecting other factors during wet-lab experiments, it is relatively straightforward to use the solutions of DE models to analyse the effect of an individual component on the system. By contrast, sophisticated techniques are required to identify the influence of a particular parameter or process on the behaviour and associated uncertainty of an ABM due to the size of the parameter space involved [202, 200]. Overall, the suitability of individual parameter perturbation as a technique for generating biological insights (for example to elucidate the role of an individual molecule on an overall process) is a controversial topic, with its application likely to be appropriate only in circumstances such as model scoping and simplification; whereas global sensitivity analysis, which allows a multidimensional parameter space to be explored, is a more powerful tool for identifying uncertainty in ABMs [203, 204].

Although computing capabilities have improved significantly, and continue to advance, the time taken to formulate a model system and generate its solutions is still an important consideration. ODE models are relatively simple to formulate and usually include fewer parameters than PDEs and ABMs; they are also the least computationally expensive approach due to the availability of established methods for generating analytical and numerical solutions. PDEs are moderately computationally expensive, due to the inclusion of spatial rates of change, and analytical solutions are less readily available. ABMs are generally more time consuming to formulate and require more computing power to implement than their DE equivalents, because agent-based approaches model large numbers of individual entities independently but concurrently [205]. Additionally, whilst DE models often aim for parsimony, the ability of ABMs to include large numbers of agents and interactions may lead to a capture problem, whereby it is difficult to identify the most appropriate biological processes to incorporate or exclude [206].

The form of model output produced can influence the perceived value of the findings and their accessibility to scientists and clinicians: ABM output is often considered more intuitive for clinicians and experimentalists to interpret than the DE equivalent, but analysing visualisations of a single ABM simulation run as representative of system behaviour may be misleading. The outputs of DEs can take the form of quantitative solutions, describ-

ing how the size of individual variables change over time and space, or qualitative output such as the shapes of solution profiles. Although such output may be initially unfamiliar to a biologist or clinician, and hence difficult to interpret, results of this form can provide novel insights and increased understanding of the system. In contrast, ABM outputs are often presented as visual illustrations of the position and characteristics of agents at specific timepoints within a single simulation (for example Safferling et al. (2013), Figures 8 and S4 [75]); and recent work allows simulation outputs to be represented in a similar format to results of experimental studies [207]. Such representation can be helpful in communicating details of the methodology and qualitative characteristics of the results to those without a computational background; however, due to the stochastic effects included in ABMs, the output of a single simulation run cannot be considered representative of the overall system behaviour or equivalent to a single *in vivo* experiment.

To fully exploit the potential of ABM output, quantitative measures of parameter sensitivity and uncertainty should be analysed: a computationally expensive process resulting in output that is no more intuitive for a non-specialist to interpret than that of DEs. Additionally, for large populations with limited variation, the time consuming process of running multiple stochastic ABM simulations and interpreting the model output may ultimately yield similar results to a simpler deterministic model [208]. With all modelling approaches, the ability to present and describe findings in an accessible manner, and promote engagement across disciplines, is of great importance to advance knowledge in the wider field; however, this must be balanced with the need to ensure that the data presented is fully representative of the simulated system behaviour, and can be effectively exploited to produce valuable mechanistic or clinical insights.

3.4 Extending and combining existing models

An advantage of computational models common to both DEs and ABMs is the ubiquity of the methods applied. Models can be applied to a wide range of scenarios from inflammatory bowel disease to corneal injury to chronic, non-healing wounds with only minor adjustments to the model formulation or parameter estimates [209]. This ease of adaptation also allows for basic models, which bear only a passing resemblance to the complex underlying biology, to be extended until they may produce clinically relevant outputs: although even the most recent models fail to encapsulate the full entanglement of pathways involved in the regulation of repair, there is plenty of scope for improvement in subsequent studies. For example, the simple model system described in Table 3.2 has limited clinical utility in its initial

form, but was extended to investigate the effect of wound geometry on healing time, thus increasing its biological relevance [190]. A further extension investigated the effects of topical application of mitotic regulators to the wound [191]. It was found that one-off application of a biochemical regulator had no significant effect on healing, regardless of the timing of application and chemical concentration; however, prolonged exposure to the biochemical did have an effect. The biochemical in question was abstract, with no specific treatment or its associated parameters specified, and results could only be compared to qualitative experimental measurements, representing significant limitations to the work. However, the study did illustrate the potential for basic models to be extended to investigate clinical interventions.

ABMs are well suited to modular organisation, allowing complex models to be progressively assembled to reflect changes in the biological knowledge base and increasing computational capabilities. For example, Sun et al. (2007) [193] undertook a study of keratinocyte colony formation which used an ABM to model keratinocytes in two dimensions and describe their basic cellular behaviours of proliferation, migration and differentiation. The authors classified keratinocytes as one of four cell types stem cells, transit amplifying cells, committed cells or corneocytes with rules governing cell behaviour and transition between the states. In a subsequent study, Sun et al. (2009) [192] extended the model in the context of epidermal healing by producing a three dimensional system that incorporated interactions between keratinocytes, the surface of the ECM and TGF-β1. Keratinocytes were modelled as non-deformable spheres that adhered to the same rule set as in the colony formation study, but with an additional physical condition to ensure cells did not overlap: repulsive forces proportional to the amount of overlap were applied (see Figure 3.2).

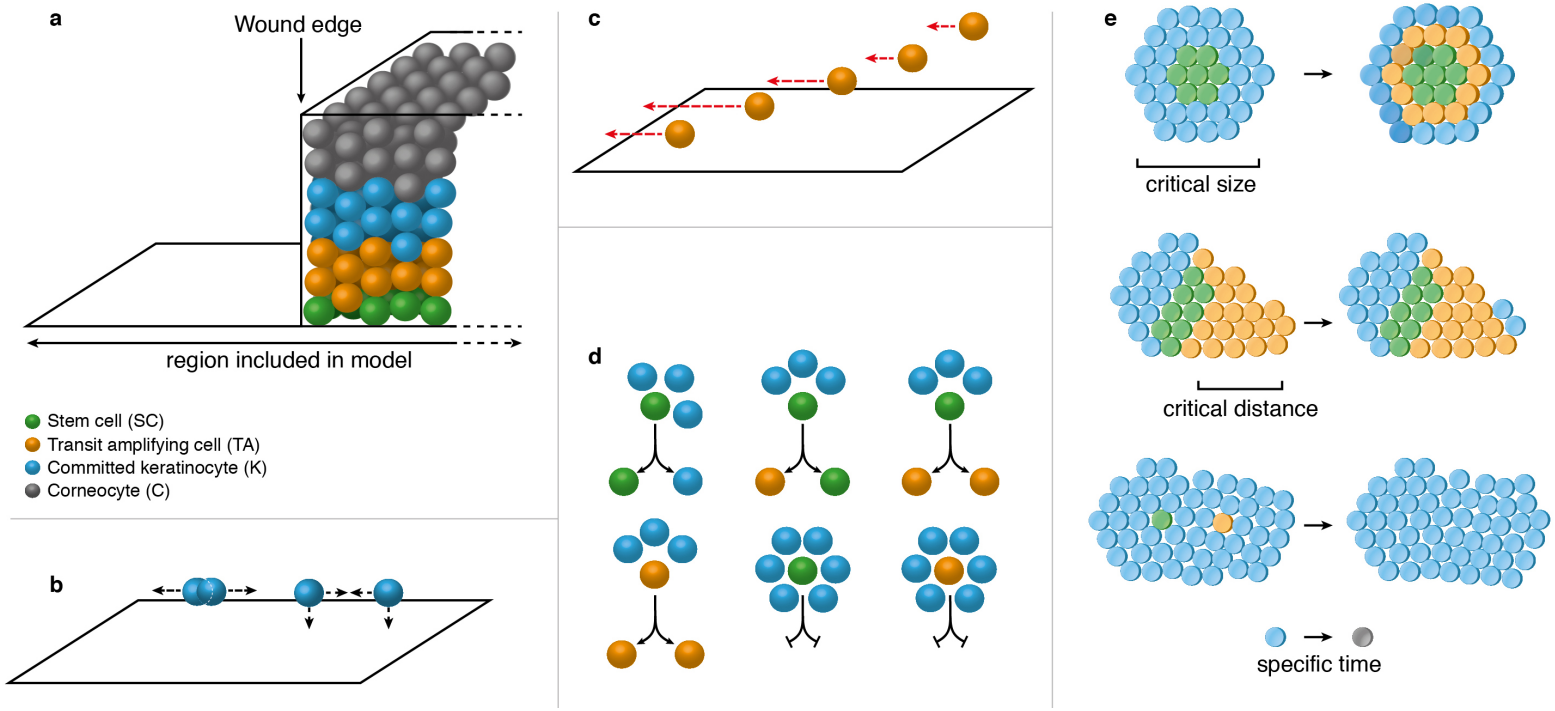

Figure 3.2: **The cellular processes included in an ABM of epidermal repair (Sun et al., 2009 [192]).** (a) A wound is modelled by removing all agents from a specified area of simulated epidermis. (b) A cell's migration speed depends on the strength of its adhesion to the substrate, which varies based on distance from the substrate. Intermediately adhesive cells migrate most quickly. (c) Repulsive forces proportional to the amount of cell overlap are applied; attractive forces occur between cells and their substrate when they are sufficiently close. (d) The types of daughter cells produced during mitosis depend on the parent cell type and the number of cells in its immediate environment. (e) A cell's propensity to differentiate is controlled by the cell types present in its local environment, except for committed keratinocytes which differentiate into corneocytes at a fixed rate.

Whilst extending existing models can be a valuable aspect of computational approaches, care must be taken when transferring assumptions from one model to the next. For example, Adam (1999) [182] extended the framework outlined in Table 3.2, using a PDE to describe both the wound space and surrounding tissue responsible for increased mitotic activity. Although the incorporation of tissue surrounding the wound may suggest increased biological relevance, it is unclear whether the model relates to healing of bone or skin. This is problematic as parameters estimated by Sherratt and Murray (1990) [87] in the context of epidermal healing were used to inform both Adam's initial model and its subsequent two-dimensional extension, which focuses only on bone repair [183]. It remains to be seen whether growth factor diffusion and decay rates are similar in bone and epidermis, but the failure to justify these assumptions is a significant limitation as resulting quantitative predictions may not be biologically relevant.

Extensions to models must also be treated with caution to ensure that additional equations and parameters are consistent with the established framework, and that the model is addressing a relevant biological question. For example, Vermolen and Adam (2007) [194] combined the model of epidermal healing described in Table 3.2 with models of dermal angiogenesis [195, 189] to formulate a system of PDEs describing dermal oxygen concentration, capillary density, keratinocyte concentration, the concentration of an autoregulator of keratinocyte mitosis and the concentration of growth factors produced by macrophages (termed MDGFs). Parameter values were taken from the two papers with no discussion of their relative magnitudes or relevance, representing a key limitation of the work. The system was coupled by assuming that the keratinocytes' mitotic rate is dependent on capillary density; however, no consideration was given to the direct effects of oxygen concentration or MDGFs on keratinocytes.

Although models that consider the actions of individual signalling molecules or pathways can explore biologically relevant hypotheses [192], the cumulative effects of the myriad growth factors involved should also be considered [201]. For example, the addition of a single mitotic regulator may have a large impact on the output of a simple model [191]; whereas, at specific timepoints, a complete biological system may actively compensate for such a change through alternative pathways [210, 56]. This feature is rarely included in mathematical models, for example the study by Vermolen and Adam (2007) [194] failed to take account of competing or overlapping effects of growth factors produced by keratinocytes and macrophages. However, this limitation is not unique to computational studies: *in vitro* and *in vivo* experiments commonly investigate the effects of changing individual growth factor concentrations in isolation [211, 212, 57] despite studies showing the more nuanced effects of manipulating

combinations of signalling molecules [213].

Hybrid model systems are a powerful approach to investigate complex systems, in which DEs and ABMs are employed concurrently with each describing biological or physical components to which their formulation is most suited [214, 192]. This may be particularly relevant when some components (e.g. growth factors or tissue mechanics) are best represented on a continuum, whereas others (such as cells) are best described as discrete entities. For example, Sun et al. (2009) [192] used an ODE model of TGF-β1 action (including activation of TGF-β1 promoter activity, induction of mRNA, and synthesis of TGF-β1 large latent complex) from a previous study [215], which was integrated into their existing ABM for cell and ECM behaviour [193] to produce a multiscale model. Thus TGF-β1 was represented on a continuum, keratinocytes were individual agents, and the underlying ECM was described using tile agents, which were larger than keratinocytes but still discrete entities. The production of TGF-β1 was influenced by the number and type of keratinocytes present, and was down-regulated in the presence of secondary ECM and basement membrane components. Concurrently, TGF-β1 promoted keratinocyte migration and inhibited cell proliferation. While the hybrid study successfully integrated multiple compartments and different scales, its output was used only to investigate the relative importance of parameters on model behaviour. Conclusions did not substantially improve understanding of epidermal healing, illustrating that hybrid models must be clearly justified and focused to be of additional value.

3.5 Using mathematical models to investigate biological hypotheses

Mathematical modelling can be a useful technique for investigating competing mechanistic hypotheses. For example, computational models may contribute to the debate surrounding the cellular mechanisms of epidermal healing by characterising the dynamics associated with each hypothesis; comparing the various model outputs to known biological results may then allow the most likely hypothesis to be identified. Both differential equation models and ABMs have been employed to this end, examples of which are discussed in this section.

Elucidating the process by which keratinocytes migrate across the granulation tissue is an open question in wound healing research [216, 217]. Vermolen and Javierre (2012) [218] formulated a PDE model for wound closure, which was based on previous reaction-diffusion systems [219] but extended to include additional equations for the dermal healing responses

of wound contraction, angiogenesis and dermal regeneration. The study confirmed the clinical observation that early epidermal closure uses a crawling and climbing mechanism, whilst a stratification process is employed at later stages. This is contrary to the findings of the ABM developed by Safferling et al. (2013) [75] that, combined with bespoke quantitative experiments, suggested a novel extending shield re-epithelialisation mechanism was responsible for keratinocyte migration. According to this hypothesis cells neither slide across the granulation tissue contiguously, nor do cells in supra-basal layers "leap-frog" over the keratinocytes adjacent to the basement membrane; instead, migrating keratinocytes "lift" cells ahead of them forming a multi-layered tongue close to the boundary of the wound. As new evidence comes to light, mathematical techniques are likely to have a key role in further clarifying the underlying processes of keratinocyte migration and examining their influence on overall healing outcomes.

3.6 Using mathematical models to inform clinical practice

Computational approaches can simulate new or incompletely understood treatment strategies in a non-invasive and inexpensive way. For example, a novel technique for treating severe burns involves collecting and culturing keratinocytes from a patient's healthy skin, which can then be sprayed onto the affected area to promote or accelerate healing. Although initial in vitro and in vivo studies demonstrated accelerated re-epithelialisation after treatment, the optimal cell distribution and concentration for spraying had not been established experimentally. A reaction-diffusion PDE system, based on the descriptive studies of Sherratt and Murray [87], was used to model growth patterns of cell colonies following aerosol application to predict changes in epidermal coverage over time [185].

Rather than assuming a homogenous population of keratinocytes, the model considered different levels of mitotic activity in separate equations: epidermal stem cells, transit amplifying cells recently progressed from stem cells, transit amplifying cells and quiescent cells were each represented by a separate variable. Parameters were experimentally determined, although using data from a different system to burn wounds. It was found that choosing initial positions of cell colonies from an approximately uniform distribution (which represents keratinocytes being sprayed from a distance) resulted in faster healing than when initial positions were chosen randomly from a normal distribution (which would occur when the spray nozzle is held close to the burn surface). The effects of increasing keratinocyte proliferation and migration rate, as well as altering the ratios of mitotic activity, were also investigated; however, these parameters are more difficult to manipulate during treatment

so the findings are less clinically relevant. Aspects for further exploration, for example the frequency of application, were also identified. This study has been highlighted as one of the first directly translational mathematical models of epidermal healing [220]; however, a period of examination and assessment will be required to determine how and where these advances in understanding may be applied.

Another clinically motivated study considered the process of surgical debridement: a procedure that is widely used to stimulate or expedite healing despite the limited clinical data available to support its benefits. A geometric model was formulated to fit ODEs to data on changes to wound size over time, but without incorporating any of the cellular mechanisms underpinning the process of healing [188]. Proportions of wound to slough area were predicted under a variety of conditions, including the timing of debridement and the amount of slough removed. The model identified timepoints at which debridement is most effective in forcing a non-healing wound to resume repair, although careful parameterisation would be required to move from the theoretical framework to a clinical recommendation. Questions that could be addressed by extending the model were also proposed, including identification of debridement strategies that would require the fewest number of surgical interventions, or would minimise the time required to complete healing. Despite neglecting to incorporate underlying biological processes, the study illustrates how simple mathematical models may describe clinically relevant scenarios and produce novel insights into potential interventions.

Another non-mechanistic approach was used in an early investigation of leg ulcer healing, which combined theoretical studies with clinical assessment to predict healing outcomes at early timepoints [196]. Instead of including mechanistic descriptions of the processes involved, the model predicted the evolution of an ulcer given its initial shape, producing a binary output designating the wound as healing or chronic. The model produced good spatial agreement between theoretical predictions and clinical observation, but gave limited information on the temporal dynamics of healing. If time evolution could be incorporated this may provide a valuable clinical tool to make early predictions of which wounds are likely to become chronic.

Models that are primarily designed to study biological hypotheses may be further exploited to investigate clinical scenarios. For example, the previously described hybrid model developed by Sun et al. (2009) [192] was also used to investigate healing in a large wound. Model output predicted that wounds above a certain size wound not heal regardless of the length of the time period simulated, which is a situation directly comparable to chronic wounds in the clinic. Model analysis suggested that auto-regulation of keratinocyte colony

formation promoted migrating keratinocytes to differentiate into committed cells and corneocytes before re-epithelialisation was complete, preventing the wound from fully healing: a novel and clinically applicable conclusion. However, to save computation time only small areas of epidermis were modelled, so a comparatively large wound in the simulation was not equivalent to a large wound in clinical practice. Thus the model provided some mechanistic evidence for the causes of non-healing wounds but the authors noted that it would require modification, in particular increasing the dimensions of the area of skin simulated, to draw clinically applicable conclusions [192].

Predicting outcomes and personalising treatment decisions based on characteristics of a patient and their wound would constitute an important improvement in the care of chronic wounds. A recent study used statistical methods to predict delayed wound healing [167]. Whilst not a mathematical model in the traditional sense of those described previously, the study applied computational approaches to a large dataset of information collected during routine wound care. 865 possible predictors of delayed healing were identified and a subset of data was used to develop a model of the predictors and their relevant importances. The model was then applied to the remaining data, and could predict which wounds would become chronic with reasonable reliability. Predictors with high importance could also be identified: these included patient age, wound dimensions and changes in wound size observed between assessments. Wound type and location had relatively little importance, suggesting that careful quantification and monitoring of changes to wound size over time should be prioritised soon after injury to identify indications of pathological healing. Results such as these could be used to recommend areas of clinical need, for example the development and evaluation of novel technologies to measure wounds accurately and non-invasively.

Diabetic wounds are known to exhibit non-healing pathologies, but our understanding of which cellular processes contribute to delayed repair is limited. A study by Bowden et al. (2014) [184] used an ODE model to describe healing of full-thickness wounds, incorporating equations for epidermal tissue undergoing cell migration and proliferation, dermal tissue undergoing contraction and growth, and the forces acting on the wound due to attachments between healthy tissue, granulation tissue and sub-dermal tissue. Model output suggested that growth in the dermis dominates healing and, when fitted to experimental data, identified a reduction in the rate of dermal tissue growth (as opposed to decreased levels of dermal contraction) to be the key difference between normal and diabetic healing. The ability of such a model to pinpoint aspects of the wound healing cascade for further study or clinical manipulation is a clear advantage of mathematical approaches.

One commonly proposed limitation of studies using mathematical models to inform treatment strategies is their failure to include every component and process of epidermal repair. Although it may be possible to formulate models that attempt to encompass the entire healing process, problems would occur due to the complexity of cellular processes and signals involved. Such models would suffer from reduced utility due to an increased number of unknown parameters, and coupling several subsystems can obscure the analysis of main healing processes. The studies described in this section show that, whilst mathematical methods are yet to unearth a novel strategy for the treatment of chronic wounds, they may be used to refine nascent procedures. One reason for the success of models investigating a particular treatment is that they focus on a specific subset of processes in the wound healing cascade, which may be studied in detail in the context of an intervention.

3.7 A marriage between experiments and theory: collaboration not competition

Computational models of healing cannot make significant advances in isolation from experimental studies, but together the two techniques represent a powerful approach for addressing open questions in epidermal repair. Models are often more successful in generating hypotheses than drawing firm conclusions; these hypotheses may be investigated experimentally and their findings then used to further update models in an iterative process that is more likely to yield novel and relevant results than experiments or modelling alone.

Another important link between theoretical studies and experiments is the reliance of computational models on parameter estimates derived from in vivo and in vitro work. Unreliable parameter estimation or misinterpretation of the underlying biology can be hugely detrimental, so models should be formulated in close collaboration with biologists and clinicians to identify uncertainties in processes and parameters from the outset. To facilitate this, when assessing the expense of conducting a computational study the additional costs associated with robust experimental derivation of parameter values should not be overlooked. Computational studies could be improved by noting the level of uncertainty associated with each experimentally determined parameter value: none of the studies described here list the confidence intervals of their parameters and, whilst some do carry out sensitivity analyses, a more explicit discussion of the potential estimation errors and their effects on model output would be a welcome addition. For example, Bayesian sensitivity analysis is a technique that has been implemented in models of electrical activation and recovery in cardiac cells, and

could also be applied to models of the healing epidermis [221].

When using models to investigate competing biological hypotheses, it is important that scientists and clinicians clearly communicate open questions that are not amenable to experimentation, and that theoreticians correctly interpret the associated hypotheses. For example, Sun et al. (2009) [192] claimed that experimental studies had purported increased mitotic activity in adjacent tissue as a possible stimulus for the onset of keratinocyte migration at the wound edge. However, the studies they cited in fact proposed that additional keratinocyte proliferation is not strictly required for migration, but increases the population of cells available to restore epidermal integrity [99]. Therefore, whilst the model output provided further evidence for this assertion it did not substantially increase understanding of the migratory stimulus. Closer collaboration between experimental and computational biologists will help ensure that theoretical work addresses relevant and open questions, thus increasing the value of modelling studies.

Conversely, clinicians and experimentalists should be open to the use of modelling as one of many important techniques for investigating biomedical systems. Wider understanding of the benefits and limitations of mathematical modelling, along with acknowledgement that all methodologies in vitro, in vivo, clinical and computational involve some degree of abstraction would help to achieve this. In particular, it should be recognised that models describing only a subset of the processes involved in healing may be equally if not more informative than those attempting to exhaustively investigate the entire system. Making model simplifications is a powerful tool that may enable a reduction of uncertainty in the model's processes and parameters, and therefore limit the noise associated with solution behaviour: balancing complexity and utility is of paramount importance. It is also important that clinicians and scientists engage with theoreticians at all stages of the modelling process to produce models that further the understanding of epidermal healing, and to ensure that theoretical results are presented in a form that is understandable to those without an extensive background in mathematical modelling. In particular model output should be considered carefully: quantifying the degree of injury and repair is of greatest relevance to healthcare practitioners but determining how best to extrapolate this from models on a cellular or mechanical level is non-trivial. Enabling scientists and clinicians without a mathematical background to evaluate models including making judgements on their confidence in the underlying biological assumptions, the suitability of the model formulation, and the usefulness of the model output is another challenge which has yet to be overcome.

Theoretical models of wound healing should not be considered as replacements for exper-

imental and clinical studies, but rather complementary techniques that play an important role in answering complex questions. Just as quantitative and qualitative insights from the wet-lab inform model development, the output of theoretical studies can be exploited to generate hypotheses that are testable using experimental techniques. Thus computational modelling can be used to organise complex biological data, connecting experimental results to fundamental biological principles in an iterative manner. Mathematical modelling of wound healing is an established field, but the scope for increased interaction with experiments and patients provides an exciting prospect for addressing biological unknowns and supporting personalised therapeutic decision making in epidermal repair.

Chapter 4

Models of epidermal healing

4.1 Introduction

The success of a mathematical model in providing mechanistic or clinically relevant insight depends on many factors; these include the selection of an appropriate modelling technique, the accuracy of parameter estimation, and the choice of approach for relating model output to relevant biological or clinical characteristics. Although the choice of modelling technique has a strong influence not only on the implementation but also the output of an *in silico* study, multiple modelling techniques have not been evaluated on the same biological system in the context of cutaneous wound healing.

Whilst qualitative experimental results can be used to inform the structure of a model and to identify interactions that should be included, quantitative data are necessary for parameter estimation. We therefore develop and test methods for ascertaining the population dynamics of epidermal cells from tissue histology experiments. We then apply three separate approaches – an ODE model, a PDE model and an ABM – to represent the basic cellular processes that underpin epidermal healing. This allows the impact of their implicit assumptions on the system's behaviour to be assessed.

4.2 Characterising wound healing in murine epidermis

Tissue histology is a commonly used technique in the study of murine cutaneous healing that allows the morphology of a wound and the position of different cell types relative to the wound space to be determined. Given that healing is an inherently spatial process, this

represents a significant advantage over non-spatial techniques such as flow cytometry and gene expression analyses (including microarrays and qPCR); however, quantitative results are infrequently derived from histological images, representing a key limitation. In this section we aim to use immunohistochemistry to systematically and quantitatively characterise properties of the healing murine epidermis.

4.2.1 Materials and methods

4.2.1.1 Mice

C57BL/6J and C57BL/6.RORγt$^{-/-}$ mice were bred in the Biological Services Facility at the University of York. In addition to exhibiting loss of lymph nodes and CD4^{+}CD8^{+} thymocytes [222], RORγt$^{-/-}$ mice are deficient in group 3 innate lymphoid cells (ILC3s) that have been implicated in the regulation of murine cutaneous healing [34]. B6;129S4-Gt(Rosa)26Sortm1(rtTA*M2)Jae Col1a1tm7(tetO-HIST1H2BJ/GFP)Jae/j mice (referred to as TetO-Hist GFP) were purchased from Charles River Laboratories. This is a knock-in strain that expresses Histone2B-GFP when induced by doxycycline, and was originally generated as shown in Figure 4.1.

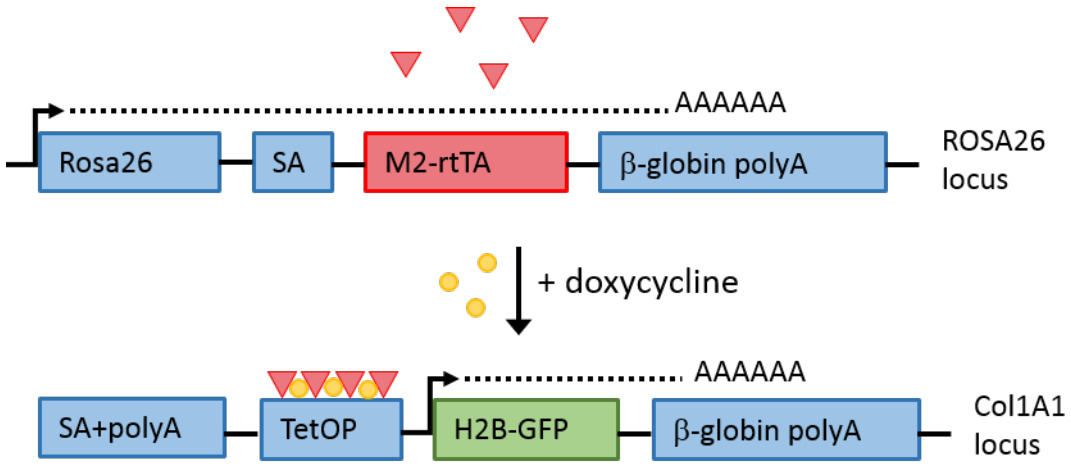

Figure 4.1: **Generation of TetO-Hist GFP mice.** Adapted from [223], Supplementary Figure 1.

All mice were maintained under specific pathogen free conditions at the University of York. Sentinel mice were housed with experimental mice and tested for pathogens every three months. Mice were housed in ventilated isolator cages under an artificial 12 hours

(7am/7pm) light/dark cycle, and given access to a standard irradiated rodent diet and autoclaved water *ad libitum*. All husbandry and experimental procedures were undertaken in accordance with United Kingdom Home Office requirements and granted local ethical approval.

4.2.1.2 Creating surgical wounds

Surgical wounds were created as described in Section 2.2.1.

4.2.1.3 3D image collection and wound size quantitation

3D images of murine dorsal wounds were collected and analysed as described in Section 2.2.2-2.2.3.

4.2.1.4 Tissue collection, preparation and frozen sectioning

An area of dorsal skin, approximately 3 cm in length and 1.5 cm in width, was removed using forceps and surgical scissors, and placed on nitrocellulose membrane (Protran, Whatman) with the epidermal surface upwards. Forceps were used to gently stretch the skin, ensuring it was positioned flat to the membrane. Wounds with 2-3 mm of surrounding tissue were excised using a scalpel: wounds from 4-8 dpw were excised in their entirety, whereas larger wounds from 0-3 dpw were first cut into two in an anterior-posterior direction. Tissue was transported in phospahte-buffered saline (PBS), unless green fluorescent protein (GFP) expression was expected in which case it was fixed in 4% paraformaldehyde (PFA), followed by a sucrose gradient. Samples were placed in a disposable vinyl specimen mold of appropriate size (Cryomold, Tissue-Tek) and covered with optimal cutting temperature (OCT) compound (Tissue-Tek). The sample was frozen on dry ice and stored at -80°C. Frozen sections were cut at a thickness of 8 µm at -18°C using a cryostat (Leica Microsystems), mounted on superfrost plus slides (Thermo Scientific) and air-dried for an hour before storing at -80°C.

4.2.1.5 Immunofluorescent staining of frozen tissue

Slides were defrosted and air dried for 30 mins, then fixed with 4% PFA for 15 mins. Sections were washed in PBS for 5 mins three times, allowed to air dry, and then encircled using a hydrophobic pen (Immedge, Fisher). Sections were blocked for 30 mins in a solution of PBS

Table 4.1: **Primary antibodies.**

	Clone	Host	Isotype	Manufacturer	Dilution
Integrin-α6	GoH3	Rat	IgG2A	Abcam	1:400
ki67	SP6	Rabbit	IgG	Abcam	1:200
GFP		Rabbit	IgG	Invitrogen	1:400

containing 0.5% bovine serum albumin (Sigma), 10% goat serum and 0.2% triton. Primary antibodies were diluted in blocking solution at the concentrations indicated in Table 4.1, added to the sections and incubated for 1 hour. Conjugated isotype controls were used to check for staining specificity. Slides were washed in PBS three times for 5 mins each, incubated with a secondary antibody AF 488, 594 or 647 (Invitrogen) at a dilution of 1:500 for 30 mins, then washed twice in PBS for 5 mins each. Secondary only controls were used to check for non-specific binding. Sections were then incubated for 10 mins with DAPI (Fisher) diluted 1:5000 in PBS, washed twice in PBS for 5 mins and gently blotted dry. All fixing, blocking, washing and incubation steps were carried out at room temperature in the dark. Slides were then mounted using antifade reagent (ProLong Gold, Fisher) and 22×50 mm #1.5 coverslips (VWR) and incubated overnight at 4°C. Clear nail varnish (Rimmel) was then used to seal the cover slips, and slides were stored at 4°C.

4.2.1.6 Confocal microscopy

Immunohistochemistry experiments were imaged using a Zeiss 710 or 880 laser scanning confocal microscope on an inverted base using Zen 2009 software. Skin sections were imaged using 20× and 40× objectives (Zeiss), at 1024×1024 pixels with averaging applied to reduce background where necessary. Tile scans were performed to image larger areas of skin. Relevant configurations of the microscope, filters and laser lines were used, which differ between experiments; however, for comparative studies of fluorescence intensity, laser power, detector gain voltage and digital offset gain were kept constant. Multi-track imaging was used to minimise bleedthrough.

Images were exported from the Zen 2009 software and further processed using Photoshop (Adobe CS4) to isolate the epidermis where necessary.

4.2.1.7 Quantitative image analysis

A CellProfiler pipeline [224] was developed to quantify cell numbers and positions of keratinocytes in murine skin. Separate pipelines were implemented for identifying DAPI+, GFP+ and ki67+ cells, but they do not differ in their basic format.

Images were manually manipulated in Photoshop to standardise their orientation and composition. First, images were rotated to ensure the intact portion of the epidermis was lying horizontally. Using integrin-α6 staining as a guide, the dermis was then blanked out, leaving only interfollicular epidermis, contiguous hair follicles and keratinocytes in the wound space. Brightness and contrast were left unaltered (but were adjusted in the images displayed in this chapter to enhance print quality).

Batches of images were imported into CellProfiler, and the following pipeline was then applied to each image in turn (Figure 4.2). The appropriate colour channel (chosen depending on whether DAPI+, GFP+ or ki67+ cells were to be counted) was first extracted (Figure 4.2a) and then the image converted to greyscale (Figure 4.2b). A Gaussian filter was applied to standardise the intensity of neighbouring pixels, thus smoothing the image and removing artefacts smaller than 1 µm in diameter (Figure 4.2c). For batches of large, tile scanned images, the size of individual images was reduced by half using a bilinear interpolation method to reduce processing time and memory requirements.

Cells were then identified, which comprises the main aspect of the pipeline (Figure 4.2d-e). Objects of diameter greater than 18 µm were discarded to exclude objects that are significantly larger than a keratinocyte nucleus. Intensity thresholding was then applied to determine whether each pixel should be considered part of the foreground (cell nuclei) or background. A single threshold value was calculated for each image by separating pixels into two classes (foreground and background) so as to minimise the variance within each class, and then setting the threshold in between. Clumps of objects were delineated based on their intensity; this was found to be more efficient than delineating based on shape despite the relative uniformity of nuclei intensities. The number of objects, and the coordinates of their centres were then output.

4.2.2 Evaluation of image analysis techniques

We first assess the suitability of the CellProfiler analysis pipeline to quantify nucleated keratinocyte numbers and positions in various areas of the healing epidermis. Two opera-

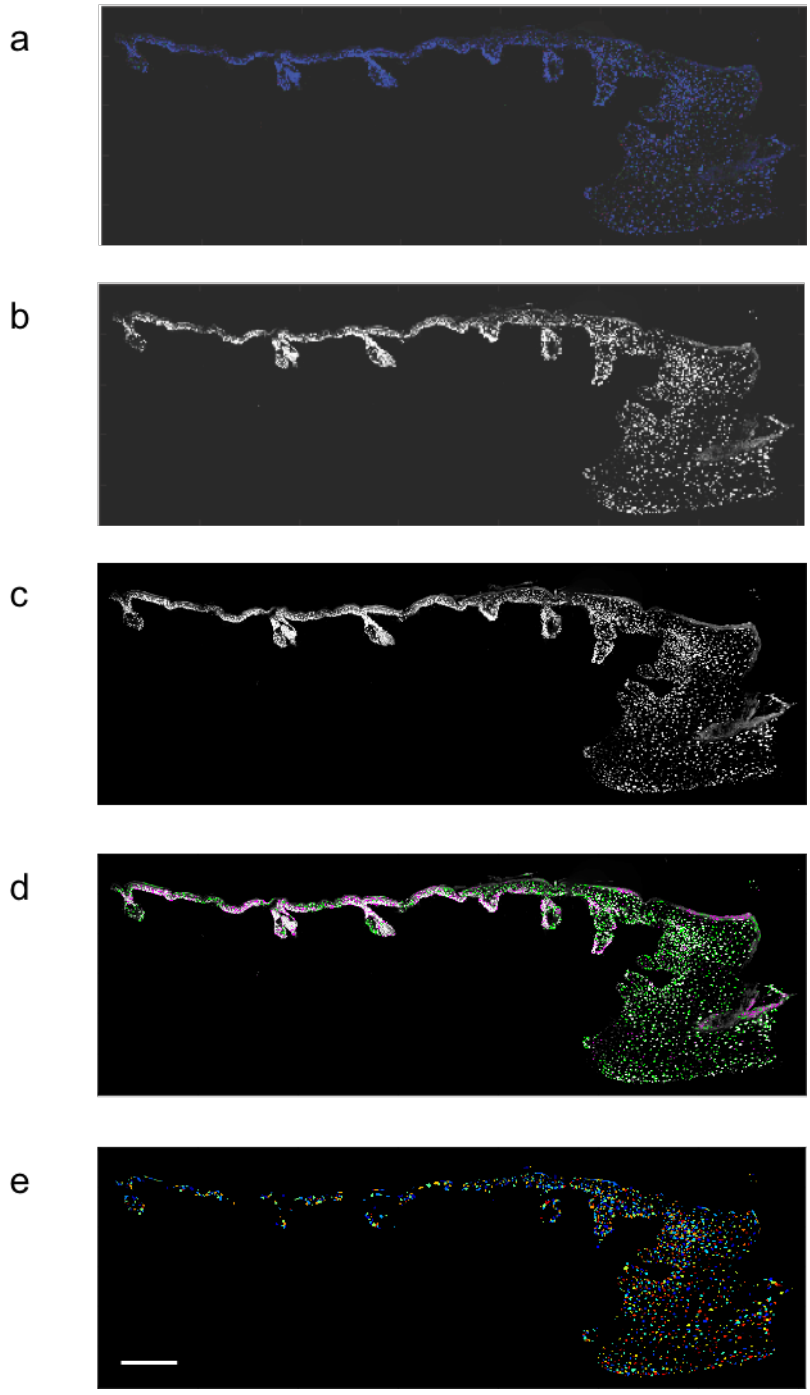

Figure 4.2: **Stages of the CellProfiler pipeline.** (a) The appropriate channel is extracted and (b) converted to greyscale. (c) Objects are smoothed to remove artifacts. (d-e) Nuclei are identified based on their size and intensity. Scale bar 200 µm

tors manually counted DAPI-stained keratinocytes in 5 images, and the same images were analysed by the semi-automated pipeline described previously. As shown in Figure 4.3a, no significant differences were found between the two operators or between operators and CellProfiler (rank ANOVA: F=2.06; d.f.=2,8 ; p= 0.190). However, we would also hope that counts would be well correlated between operators and CellProfiler, but this is not the case:

Figure 4.3b shows average operator counts plotted against CellProfiler's quantification, with a Spearman's rank correlation coefficient of 0.3.

To investigate whether differences in image size contribute to discrepancies in counting, interfollicular epidermis from single frames and tile scanned images of between 12 and 18 frames were analysed, and the number of keratinocytes per mm calculated. The means and distributions of cell concentrations did not significantly differ between the two image types (Figure 4.3c).

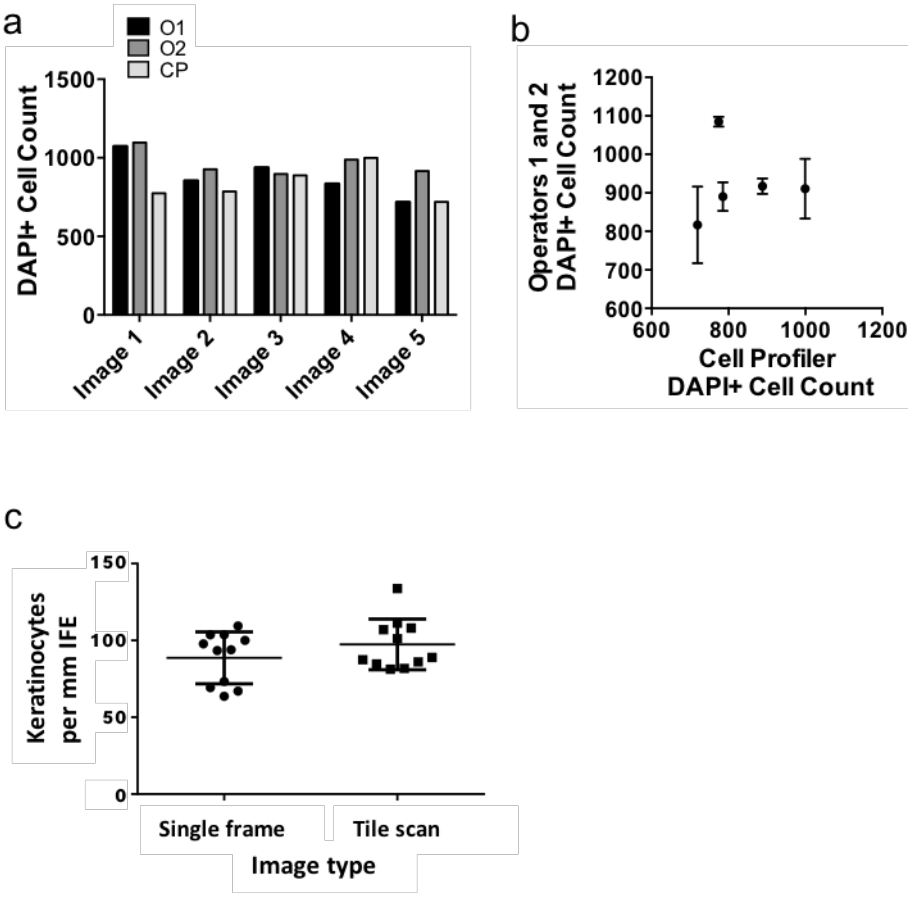

Figure 4.3: **Comparison of automated and manual DAPI+ cell counts.** (a) Comparison of DAPI+ cell counts in 5 images, collected by CellProfiler and two operators. (b) Automated and manual DAPI+ cell counts are not well correlated. Points – mean; bars – range. (c) DAPI+ cell counts per mm epidermis do not differ between small and large image areas. Error bars – mean and standard deviation.

CellProfiler can produce visual output highlighting which aspects of an image are considered positive objects (in this case DAPI+ cells) and which fail to meet the criteria set in the

pipeline. Analysing such images showed that the algorithm is good at identifying cells in the wound space and imediately adjacent epidermis (Figure 4.4a-b) but struggles to differentiate individual cells in hair follicles and areas of IFE away from the wound edge (Figure 4.4c-d). This may partly be due to the close packing of cells in these regions; however only a small proportion of cells in areas of high cell concentration in the wound space (right of centre in Figure 4.4b) are not recognised by CellProfiler.

Another likely cause is over-saturation of DAPI in certain areas of the image, which is a frequent problem in this context due to the relatively large sections of skin to be imaged. It is difficult to configure microscope settings such that the brightness of a large area of tissue will be consistent, and there may also be shifts in focus if the section is not placed perfectly flush to the slide. Of the 5 images inspected visually, all showed problems in CellProfiler's analysis of hair follicles and IFE in bright regions.

Analysing quantification methods before they are widely implemented is a key step in ensuring results are reliable and reproducible. Based on these findings, only keratinocyte concentration in the wound space will be quantified using the semi-automated pipeline, with IFE counts taken by hand.

4.2.3 The cellular composition of unwounded epidermis

The thickness and keratinocyte density of unwounded murine epidermis is known to vary with the age and sex of the mice. A study that measured murine skin depth and nucleated keratinocyte density by eye found that mice of 1, 6 and 27 months old had epidermal depths of 14, 12 and 8.4 µm respectively, and keratinocyte densities were 244, 208 and 165 cells/mm. [225]. Differences in thickness have been observed between male and female epidermis from the tail, abdomen and ear, but were not found in back skin [226]; a more recent study of mice aged between 3 and 4 months indicated that males have significantly thicker dermal layers, but that female epidermal thickness (13.3 µm) is greater than that of males (9.4 µm) [227].

As well as physiological differences in skin morphology, murine behaviour differs between male and female animals. In particular, males are more prone to fighting (a behaviour that is reduced but not eliminated when animals are housed with littermates) which may cause microabrasions to the dorsum. This may affect the cellular processes of seemingly intact skin, so where possible we used female animals. To mitigate age-related effects, tissue was collected from mice of between 6 and 9 weeks old.

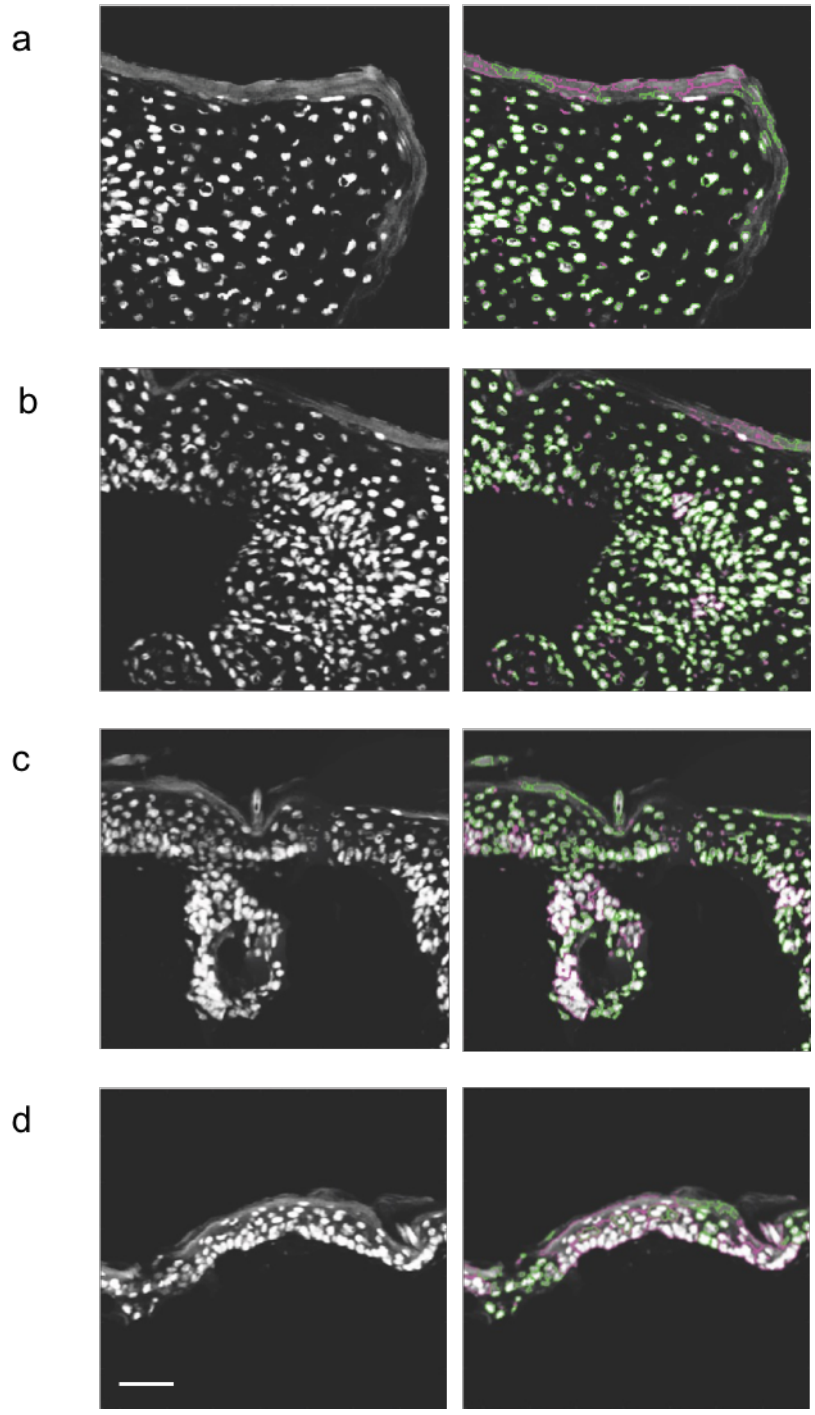

Figure 4.4: **Automated identification of nuclei in different epidermal regions.** (a) Wound edge, (b) wound space, (c) hair follicle, (d) interfollicular epidermis. Scale bar 50 µm.

To quantify the density of nucleated keratinocytes in unwounded skin, tissue from 5 female C57BL/6 mice and 5 female TetO-Hist GFP mice (all 7 weeks of age) was collected and stained with DAPI. DAPI+ nuclei of epidermal cells were counted by eye in three sections, each of 100 µm length, in each animal. Figure 4.5 shows that mean epidermal cell concen-

tration did not differ between the two strains, and was consistent with previously published results [225].

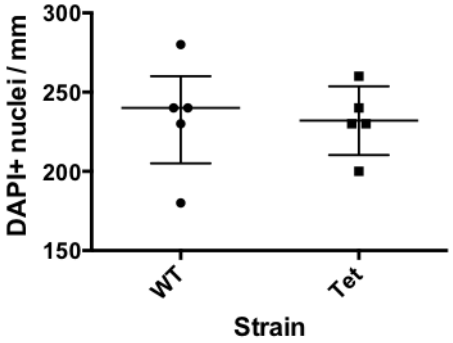

Figure 4.5: **Manual DAPI+ cell counts in interfollicular epidermis.** Comparing wild type (WT) and TetO-Hist GFP (Tet) strains. Error bars – median and interquartile range.

4.2.4 Cellular composition of the wound space

The semi-automated cell profiler pipeline was used to quantify the number of nucleated epidermal cells in the wound space of wild type mice at 1, 2, 4 and 5 dpw. All animals were female and aged between 6 and 9 weeks. Tissue was collected at the appropriate timepoint, sectioned and stained with DAPI. Nucleated keratinocytes in each half of the wound space were counted in 3 sections for each animal, and the mean value plotted in Figure 4.6a. Very few encroaching keratinocytes were observed at 1 and 2 dpw (medians 57 and 40 respectively), but the numbers increased at 4 dpw (median 316) and 5 dpw (969). The spread of data was also greater at 5 dpw, with two subsets of counts clustered around 500 and 1000 cells.

To investigate whether splitting the wound in half (which, at later timepoints, helps to ensure the entire image is in focus while not significantly increasing imaging time) had an effect of the results, counts from two halves of the same wound were summed and plotted in Figure 4.6b. This shows a similar spread of data at all timepoints (1 dpw is excluded as both counts were only available for one wound). Examining the histology images shows a range of wound space morphologies at 5 dpw (Figure 4.7). These include keratinocytes encroaching on the wound space but not forming a continuous layer across the wound bed (Figure 4.7a), a layer of keratinocytes one cell thick forming beneath the scab (Figure 4.7b), and can also take the form of a multi-layered structure (Figure 4.7c). Whilst care was

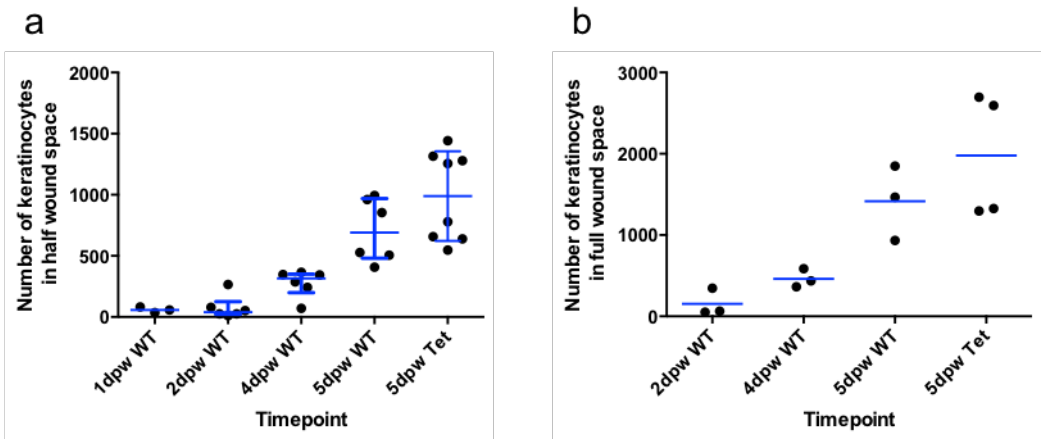

Figure 4.6: **Automated DAPI+ cell counts from within the wound space.** (a) Counts from half the wound space at various timepoints post healing, (b) counts from the full wound space at various timepoints post healing for wild type (WT) and TetO-Hist GFP (Tet) strains. Error bars – (a) median and interquartile range, (b) median.

taken to cut sections from the centre of the wound, it is possible that slight deviations to this were incorporated during freezing and sectioning the tissue. However, the similar wound diameters and marked differences in keratinocyte coverage suggest that the variation observed is a reliable representation of the biological variability.

4.2.5 Quantifying keratinocyte hyperproliferation during epidermal healing

Tissue samples were collected from 3 female wild type mice of between 6 and 9 weeks old at each of 2 dpw and 4 dpw, and from 4 mice at 5 dpw. Three sections from each wound were stained with ki67, a cell cycle marker; this enables visualisation of keratinocytes that were undergoing mitosis at the time that the tissue was collected. CellProfiler was used to quantify ki67+ cells in 5 images, and the results compared to the manual counts of 2 operators. As shown in Figure 4.8, no significant difference between the 3 counts were observed (rank ANOVA: $F=17.3$; d.f.$=2,8$; $p= 0.302$), and the manual counts showed a strong positive correlation with values output from the CellProfiler pipeline. This may be attributed to the relative sparsity of ki67+ cells compared to DAPI+ keratinocytes, and their more consitent level of brightness (an example of the staining is shown in Figure 4.9c).

Results were averaged across the three technical replicates, and are presented in Figure 4.9a. In the majority of wounds, no wound space keratinocytes were found to be ki67+ at 2

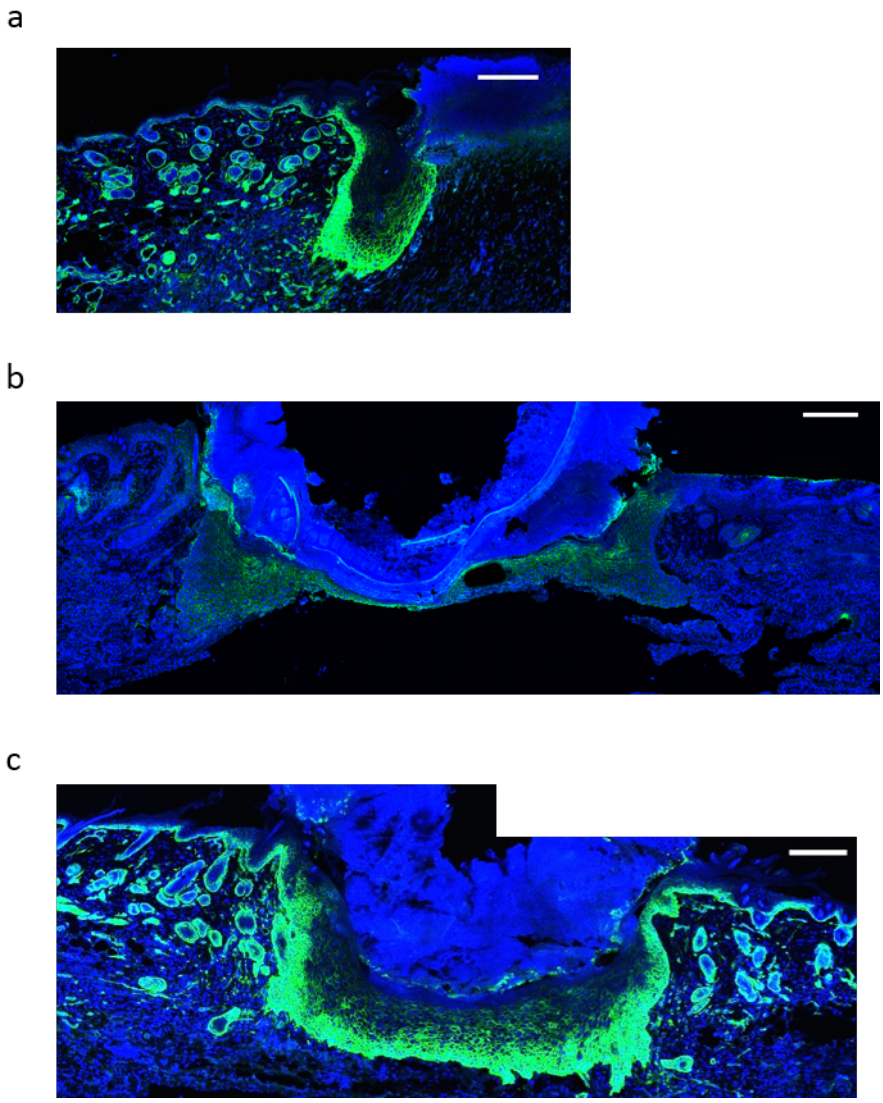

Figure 4.7: **Wound space morphology at 5 dpw.** Variations in keratinocyte infiltration of the wound space at 5 dpw. (a) Keratinocytes at the wound edge only, (b) a single continuous layer of keratinocytes across the wound space, (c) a multi-layered structure of keratinocytes. Sectioned stained for DAPI (blue) and integrin-α6 (green). Scale bars 200 µm.

dpw; at 4 dpw there were two distinct subsets – half of the wound edges had only 10-20 ki67+ keratinocytes whereas the others had between 50 and 100; a similar spread of counts was observed at 5 dpw, but with a higher mean. It is possible that the variation could be attributed to the wide range of total keratinocyte cell numbers in the wound space (as illustrated in Figure 4.7). To compensate for this, the number of ki67+ cells is represented as a percentage of DAPI+ cells in Figure 4.9b. This shows a much wider spread of percentages at 4 dpw, ranging from 5 to 31%, whereas at 5 dpw ki67+ keratinocytes make up 5-18% of epidermal cells in the wound space.

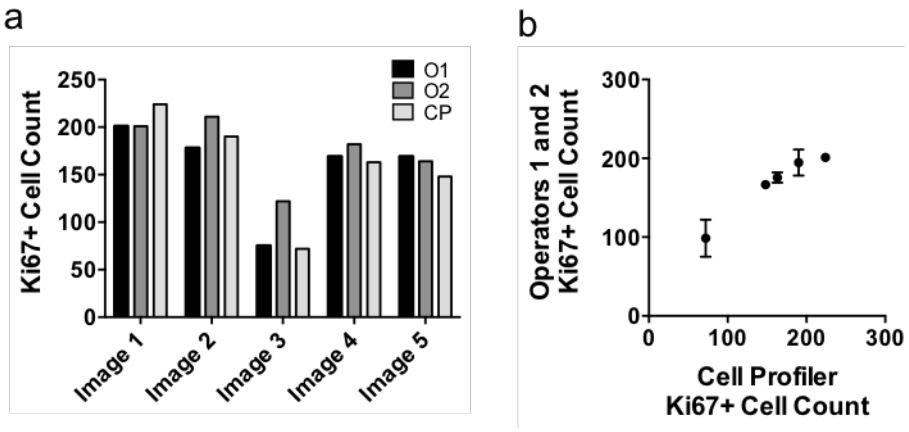

Figure 4.8: **Comparison of automated and manual ki67+ cell counts.** (a) Comparison of ki67+ cell counts in 5 images, collected by CellProfiler and two operators. (b) Automated and manual DAPI+ cell counts are well correlated. Error bars – mean and range.

A representative example of the location of ki67+ cells at 5 dpw is shown in Figure 4.9c: keratinocytes in cell cycle are clustered in a small region of epidermis adjacent to the wound space, and are also located in a wide band immediately within the wound space. Where a multi-layered population of keratinocytes has formed, some keratinocytes in the lower 2-3 layers (though predominantly in the lowest layer) are also ki67+, suggesting that after migrating into the wound space they take on a proiferative phenotype to contribute further to re-epithelialisation.

Staining with ki67 identifies keratinocytes that were in cell cycle at the time the tissue was collected, which can be used to give estimates of the probability that a cell is proliferating at any given timepoint. However, it does not provide reliable estimates of the overall proliferation rate, as no information is provided on how many rounds of division each cell has undergone. To investigate this we used TetO-Hist GFP mice, which have previously been used to quantify turnover of haematopoietic stem cells [223]. Doxycycline was first used to induce H2B-GFP expression in haematopoietic stem cells; then, during a chase period when doxycycline was no longer administered, cells lost GFP expression with each round of cell division they underwent. It was hoped that a similar system could be used to label epidermal keratinocytes, which would allow the number of divisions undergone by cells in various spatial locations to be estimated. However, the period of 3-6 weeks between pups being weaned onto a doxycycline-containing diet and mice being of the correct age for use in wounding studies was not sufficient to label keratinocytes in unwounded skin. Given the

age-associated differences in skin structure described previously, their putative effects on healing rates, and the effects of hair cycle stage on the healing response, it is important to standardise the age at which mice are used. Therefore it was not feasible to extend the doxycycline induction period to achieve the initial level of labelling required.

One possible reason for the labelling inefficiency is that GFP expression is thought to be induced in cells that divide during the induction period. Therefore we used the induction period to label cells that had divided at least once during the timeframe. 8 female mice between 6 and 9 weeks old were moved to a diet including 0.2 mg/g of doxycycline the day before wounding, and tissue was collected from each of two wounds on 4 animals at 2 dpw and a further 4 animals at 5 dpw. At 2 dpw the percentages of GFP+ cells were very variable, with between 47 and 93% of cells seeming to have undergone at least one round of division; at 5 dpw the percentages were more consistent, with a mean of 91% (Figure 4.10a).

To investigate whether variation in the percentage of GFP+ cells at 2 dpw could be attributed to varying numbers of keratinocytes in the wound space, the two variables were compared for each wound (Figure 4.10b). Wounds with higher DAPI+ cell counts showed a relatively low percentage of GFP+ cells, whereas those with a keratinocyte count that suggested significant wound space infiltration had not taken place showed a greater variety of expression levels. This could be a biological effect, where proliferation is less consistent during the early stages of keratinocyte migration into a wound, but may also be a technical issue: it is more difficult to determine where the wound space ends and intact epidermis begins when keratinocytes have not migrated as far as the wound bed. Nonetheless, the finding that the majority of keratinocytes have proliferated at least once during the 5 dpw period is novel, as ki67 staining suggests that only cells in certain spatial regions undergo hyperproliferation. Figure 4.10c shows that keratinocytes in all layers of the intact epidermis adjacent to the wound, and the majority of keratinocytes in the wound space (regardless of their proximity to the initial wound edge) had divided at least once within 5 days of a wound event. Whilst it is disappointing that the TetO-Hist GFP system is not well suited to continuous monitoring of keratinocyte proliferation rates in young mice, information on the spatial locations of previously-dividing cells may be valuable in the development of PDE models and ABMs.

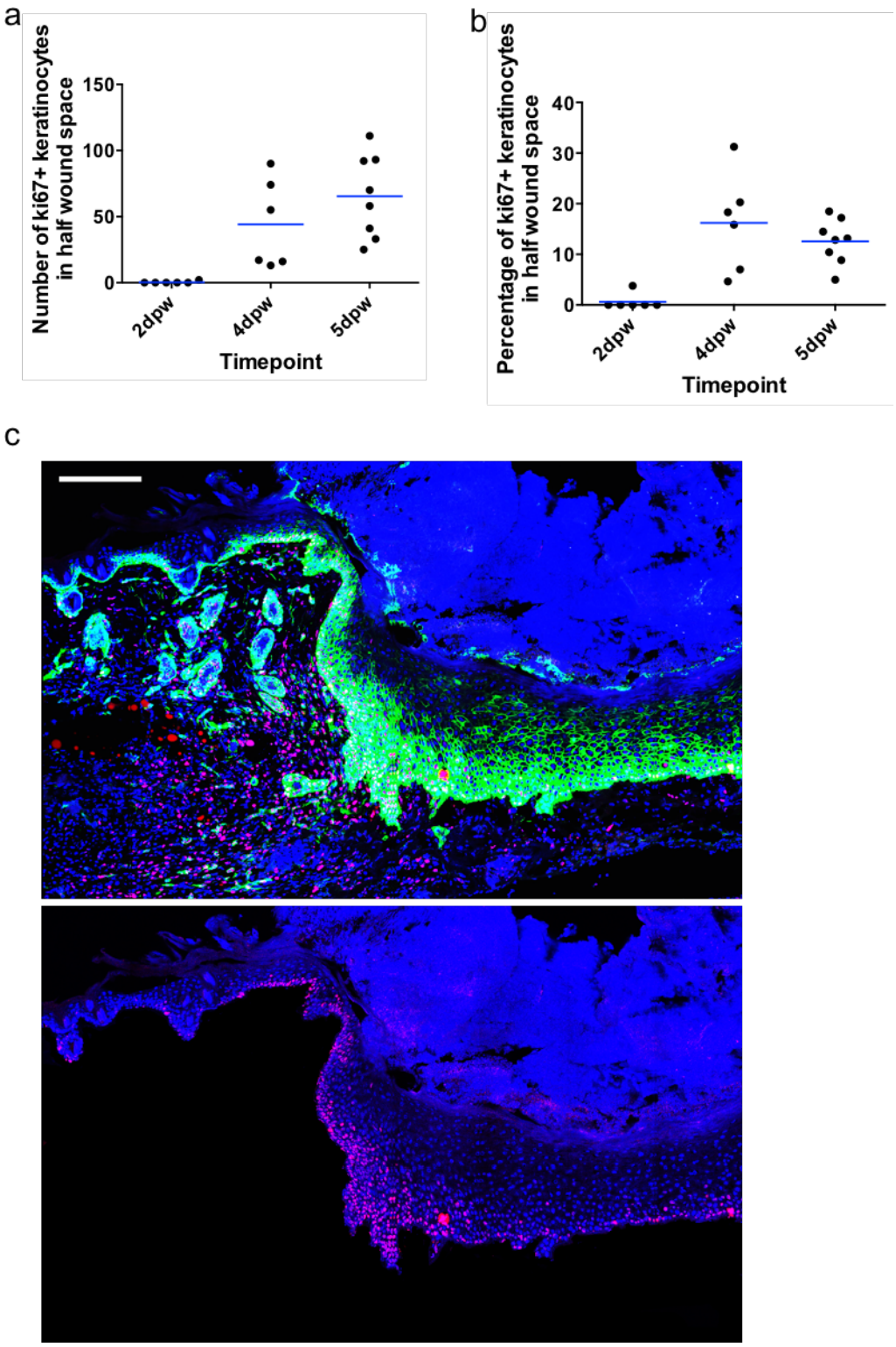

Figure 4.9: **Automated ki67+ cell counts and localisation within the wound space.** (a) Counts from half the wound space at various timepoints post healing, (b) counts from the full wound space at various timepoints post healing. (a-b) Bars – median. (c) ki67+ cells are localised towards the dermal-epidermal junction. Sectioned stained for DAPI (blue), integrin-α6 (green) and ki67 (red). Scale bar 200 µm.

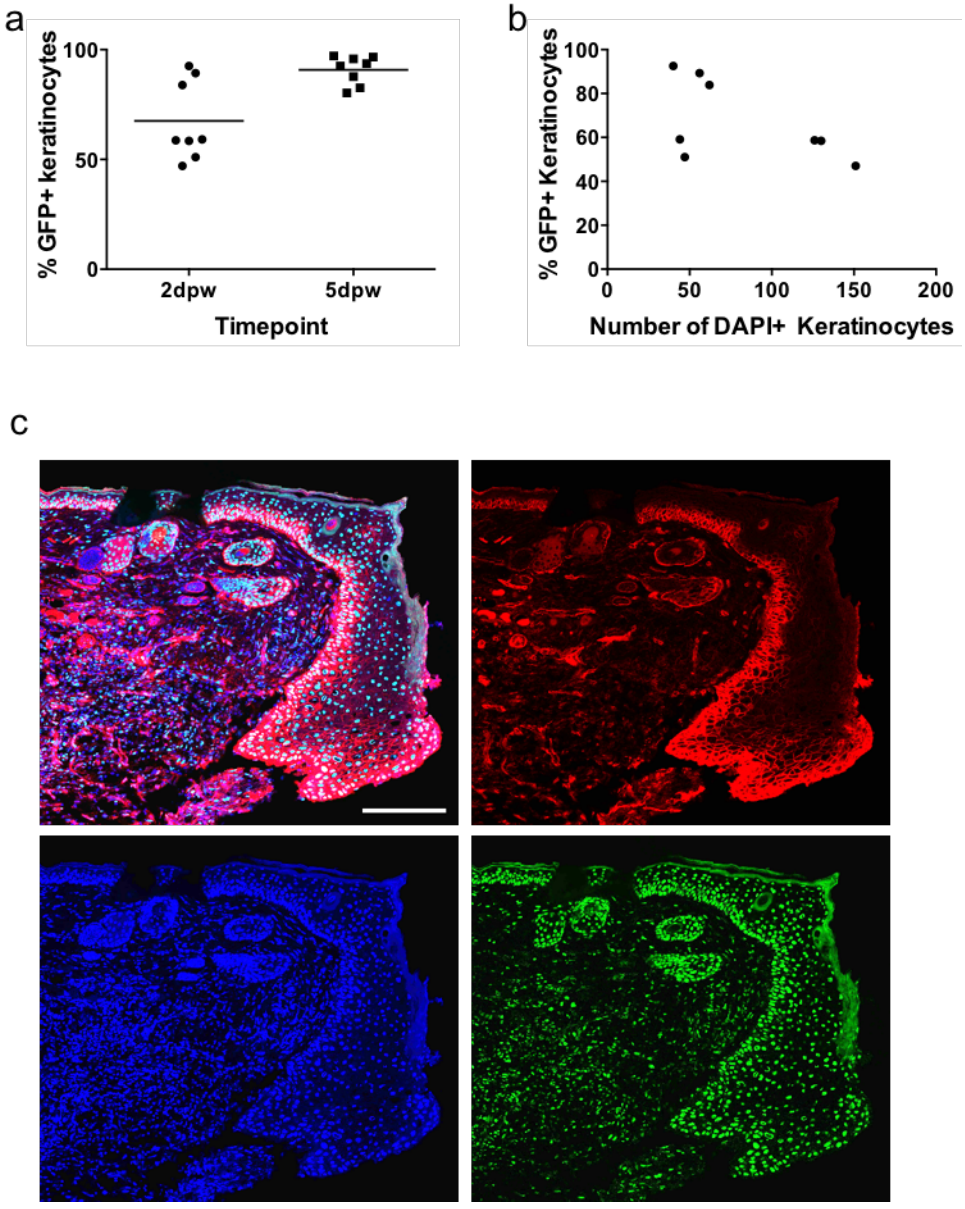

Figure 4.10: **Automated quantification of GFP+ cells within the wound space in TetO-Hist GFP mice.** (a) GFP+ cells as a percentage of DAPI+ cells within the wound space. Bars – mean. (b) Correlation between %GFP+ cells and total number of DAPI+ cells within the wound. (c) Cells in intact epidermis adjacent to the wound are also GFP+. Sectioned stained for DAPI (blue), integrin-α6 (red) and GFP (green). Scale bar 200 µm.

4.3 A semi-spatial ordinary differential equation model for epidermal healing

4.3.1 Formulating an ODE model of epidermal healing

An initial model of epidermal healing simulates the effects of immune cells, I, migratory keratinocytes, M, and proliferative keratinocytes, E, on the epidermal wound diameter, D. We consider a circular wound of initial diameter D_0, made in an area of skin of width L. The value of L is set sufficiently large so as to justify a two-dimensional abstraction, whereby wound depth is negligibly small compared the diameter of both the wound and surrounding intact skin. Additionally, given that murine epidermis can be as little as two nucleated cells thick, a sufficiently large tissue diameter is required to justify a homogenous, population-level approach. Limiting to perfectly circular geometries is restrictive as most clinical wounds will not take this form, and it is known that wound geometry has a significant effect on healing [228]. However, experimental studies in both mice and humans frequently use circular biopsy punches to create uniform wounds and, whilst there will be slight deviations from a perfect circle, the behaviour of these wounds may be reliably compared to model output. Modelling circular wounds also simplifies the problem due to symmetry, although the approach may be extended to consider other wound geometries. We abstract the cellular processes described in Section 1.3, and their effect on wound diameter, into the set of interactions illustrated in Figure 4.11.

We assume that the number of resident immune cells in unwounded skin is at steady state, with additional immune cells recruited following wounding. Therefore the immune cell population may be modelled using the equation

$$\frac{\mathrm{d}I}{\mathrm{d}t} = s_I L + D_0 m_I(t) - d_I I \ , \tag{4.1}$$

where the first and last terms represent the baseline diffusion of immune cells into and out of the epidermis occurring in normal, unwounded skin. The coefficient of the source term takes the form $s_I = d_I I_s$ where I_s is the available pool of immune cells (assumed to be large and constant) and d_I denotes the rate at which immune cells diffuse out of the epidermis. The initial wounding event induces immune cell recruitment to the skin surrounding the wound site, consisting of a peak in the number of immune cells shortly after wounding which then reduces gradually back towards baseline levels. This profile is simulated by solving

$$\frac{\mathrm{d}m_I}{\mathrm{d}t} = m_d \left(G(t-\tau) - d_m m_I \right) \ , \tag{4.2}$$

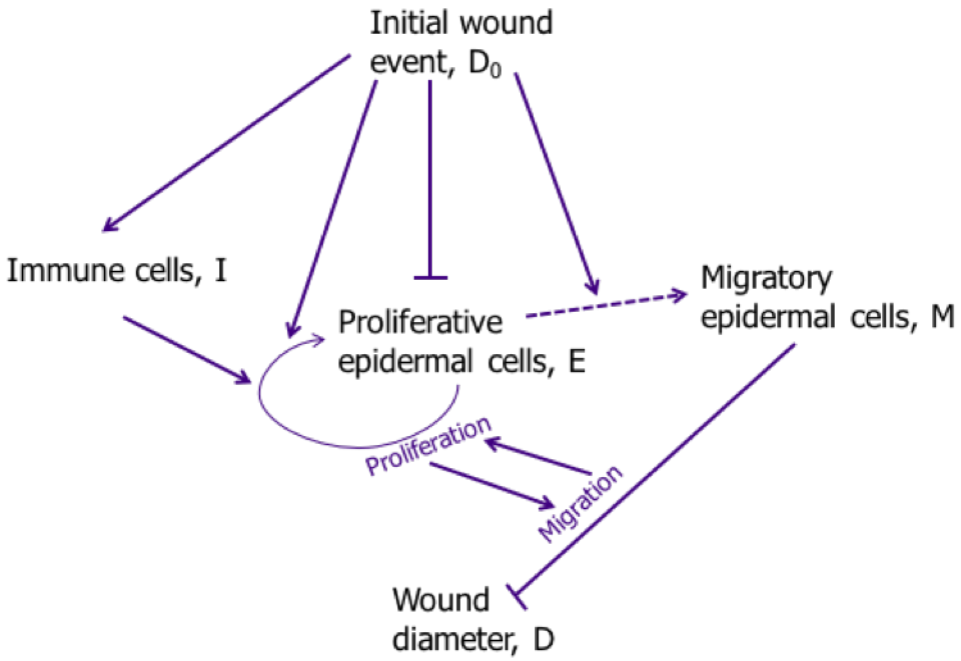

Figure 4.11: **Schematic of the biological interactions included in the ODE model (4.1)-(4.8).** The effect of proliferative, migratory and immune cell populations on each other and wound diameter during the healing process. Arrows denote increases, flat-headed arrows denote decreases, and dashed arrows denote transitions from one cell population to another.

where the additional decay rate of the signal is given by d_m, and m_d is a coefficient for the effect of initial wound size on the magnitude of the immune cell response. $G(t-\tau)$ is a sharp Gaussian curve given by

$$G(t-\tau) = \frac{1}{\sigma\sqrt{2\pi}} \exp\left\{\frac{-(t-\tau)^2}{2\sigma^2}\right\}, \tag{4.3}$$

where τ imposes the delay between the initial wound event and the onset of immune cell recruitment that occurs while the pre-repair processes of haemostasis and platelet degranulation take place. Plots of $G(t-\tau)$ and $m_I(t)$ against time are shown in Figure 4.12.

Many distinct populations of immune cells, including neutrophils, macrophages, ILC3s and Langerhans cells, contribute to the regulation of the cutaneous healing response; it may therefore be considered a weakness of the model to incorporate all immune cells into one variable. However, extensive redundancy in immune cell functions have been observed. In particular, animals deficient in specific immune populations have shown similar or acclerated healing rates compared to immunocompetent controls. Guinea pigs with depleted neutrophil populations showed no differences in cellularity, connective tissue formation or the extent

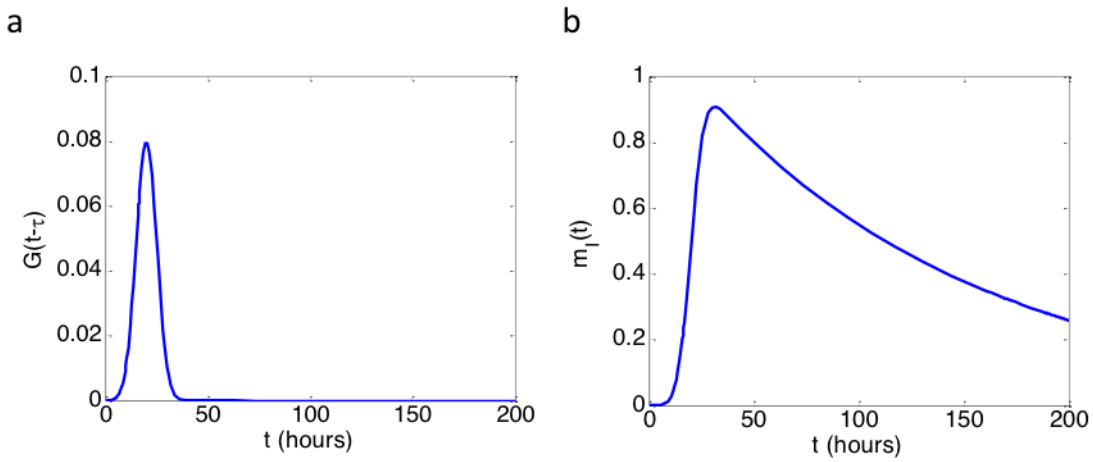

Figure 4.12: **Solutions to the time-dependent functions imposed to represent immune cell recruitment to the wound space.** (a) The steep Gaussian curve given by equation (4.3) for $\tau = 20$, $\sigma = 5$. (b) The solution of equation (4.2), which represents the dynamics of immune cell recruitment, for $\tau = 20$, $\sigma = 5$, $m_d = 50$, $d_m = 0.0075$, with $m_I(t = 0) = 0$.

of repair of sterile wounds compared to control animals [229], and more recent studies have found accelerated wound closure in neutropenic mice [230]. Neonatal PU.1 mice, which are deficient in both macrophages and functioning neutrophils, exhibited similar repair times to control animals [231]. As shown in Chapter 2, mice deficient in ILC3s exhibit larger wounds than wild type controls at 4-5 dpw, but this effect is not observed at earlier and later timepoints (Figure 2.11 and [34] Supplementary Figure 7e) suggesting that other cell populations can assume their regulatory functions, albeit after a short delay. These effects may be attributed to redundancies in the regulation of cellular processes underpinning the epidermal healing response, as discussed in Section 1.3.5.

Modelling immune cell recruitment simply as a time-dependent process is limited as it neglects the underlying signalling cascade that leads to an immune response. However, given the extensive redundancy in signalling that has been observed, using a time-dependent equation is reasonable as it captures the overall dynamics of the recruitment process and is more straightforward to formulate. Modelling m_I as an additional ODE increases the complexity of the model by introducing an extra equation; it may be possible to reproduce similar behaviour with an implicit formulation, although this could be less transparent.

Keratinocytes close to or inside a wound can take on one of two phenotypes: proliferative, whereby cells undergo mitosis to increase or maintain the cell population size; or migra-

tory, in which cells do not proliferate but can migrate into the wound space to achieve re-epithelialisation. Although there are several conflicting theories as to the precise mechanisms of re-epithelialisation (see Section 1.3), a common feature is that cells are either migratory or proliferative, and cannot carry out both functions simultaneously [104]. As such, these distinct groups will be considered as two separate cell populations, each modelled with its own differential equation. Using an ordinary differential equation approach means that we predict only the number of each type of cell, not their locations. Therefore, the model is not constrained to describe a specific re-epithelialisation mechanism, and can be considered a generalised representation of the system.

After wounding, cytokines are released by immune cells and damaged skin cells on the wound margin, which stimulate epidermal cells close to the wound edge to take on a migratory phenotype by dissolution of cell-cell and cell-substratum contacts [99, 100]. We assume that the strength of the biochemical signal is a function of the amount of initial damage, and hence the number of migratory cells will depend on the initial circumference of the wound. The location of the migratory layer (in terms of both proximity to the wound and epidermal layer) need not be specified in this non-spatial model, and hence it provides a generalised description of the various possible migratory mechanisms. Given the brief delays observed between initial wounding, release of stimulatory molecules and change to a migratory phenotype [86], we model the population of migratory epithelial cells as increasing with negative exponential growth,

$$\frac{\mathrm{d}M}{\mathrm{d}t} = \sigma_m \pi D_0 \left(1 - \frac{M}{M_E \pi D_0}\right) , \tag{4.4}$$

where the exponential growth rate of the population is given by $-\sigma_M = \frac{-\sigma_m}{M_E}$. The maximum number of cells per unit length in the migratory layer is denoted M_E, so $M_E \pi D_0$ is the maximum number of migratory cells that can be sustained by the initial wound. In reality the layer is unlikely to be uniform, however M_E can be considered as an average over the circumference of the wound.

We assume that the proliferating keratinocytes also follow a logistic growth model, up to some carrying capacity $K_E(D)$. The key resource limiting population growth is space, so the local carrying capacity is $K_{E_{local}} =$ number of keratinocytes/unit length^2, where both cell density and the depth of the skin are expected to remain broadly constant. When the epidermis is initially damaged the carrying capacity of the epithelial cell population reduces, as cells do not proliferate into completely empty space, but instead retain cell-cell contacts. However, migration of keratinocytes into the wounded area renders more space available for proliferation, and hence the total carrying capacity is dependent on the current wound size,

taking the form

$$K_E(D) = \frac{\pi}{4}(L^2 - D^2)K_{E_{local}} \ . \tag{4.5}$$

Then the equation for the rate of change of the number of proliferating epidermal cells is

$$\frac{\mathrm{d}E}{\mathrm{d}t} = \sigma_E(I)E\left(1 - \frac{E+M}{K_E(D)}\right) - \sigma_m \pi D_0 \left(1 - \frac{M}{M_E \pi D_0}\right) \ , \tag{4.6}$$

where the first term describes logistic growth within the proliferative population, and the second term accounts for the loss of cells which take on a migratory phenotype early in the healing process.

The rate of keratinocyte proliferation is hypothesised to increase once the level of immune cell signalling reaches some critical value, hence the growth rate $\sigma_E(I)$ is given by

$$\sigma_E(I) = \sigma_{E0} + \sigma_{EI}\widetilde{H_I}(I - I_{crit}) \ , \tag{4.7}$$

where σ_{E0} is the baseline proliferation rate, σ_{EI} is the additional proliferation induced by immune cells, I_{crit} is the threshold number of immune cells required for increased proliferation, and $\widetilde{H_I}$ is a smooth approximation to the Heaviside function given by $H_I(I - I_{crit}) = \frac{1}{2}\left(1 + \tanh(g_I(I - I_{crit}))\right)$. This formulation assumes that mitogenic immune cell signalling is linearly related to the number of immune cells present; this has not been investigated experimentally so the simplest relationship has been modelled.

Migratory cells reduce the amount of epidermal damage by encroaching on the wound space; however cell-cell contact must be maintained so, regardless of the proposed re-epithelialisation mechanism, migration cannot occur until the cell population is close to its carrying capacity [104, 107]. Therefore the rate of change of epidermal wound diameter is given by

$$\frac{\mathrm{d}D}{\mathrm{d}t} = -\alpha M \widetilde{H_D}(E + M - K_E + \upsilon)\widetilde{H_0}(D) \ , \tag{4.8}$$

where α is the speed at which a cell can migrate (which we assume to be constant, but can be considered an average over all migrating cells) and the smooth Heaviside function given by $\widetilde{H_D}(E + M - K_E + \upsilon) = \frac{1}{2}\left(1 + \tanh(g_D(E + M - K_E + \upsilon))\right)$, prevents loss of cell-cell contact. Once migrating cells from opposite sides of the wound come into contact, migration is halted as contact inhibition is re-established [86]. This is modelled by the smooth Heaviside function $\widetilde{H_0}(D) = \frac{1}{2}\left(1 + \tanh(g_0(D - \varepsilon))\right)$ for small ε.

4.3.2 Model output

The system of equations described in Section 4.3.1 can be solved using the MATLAB routine `ode23tb`, which runs a second-order implicit Runge-Kutta method that is well suited

Table 4.2: **Initial conditions used to simulate the system of ODEs described in Section 4.3.1.** Descriptions and initial conditions of the variables included in equations (4.1)-(4.8).

Variable	Description	Initial condition
I	Concentration of immune cells	$I_0 = 20$
m_I	Concentration of immune cells recruited per hour	$m_{I_0} = 0$
M	Concentration of migratory epidermal cells	$M_0 = 0$
E	Concentration of proliferative epidermal cells	$E_0 = \frac{\pi}{4}(L^2 - D_0^2)K_{E_{local}}$
D	Wound diameter	$D_0 = 4$

to stiff problems (TR-BDF2). The initial conditions and parameter set used are shown in Tables 4.2-4.3. Healing trajectories are simulated over an 8 day period, as shown in Figure 4.13. Solutions are generated using an adaptive timestep, so timepoints are more frequent in regions where the solution is changing rapidly .

The immune cell profile has been engineered to correspond to known dynamics of immune cell recruitment and up-regulation following wounding; this solution is not coupled to those for keratinocyte numbers or wound radius, being dependent only on time and initial wound size. This represents an abstraction, as it is likely that immune cells would respond dynamically to the progression of healing (or lack thereof), but the simplification is not unreasonable given that the model is formulated primarily to investigate keratinocytes' contribution to healthy healing.

A subset of epidermal cells rapidly switch phenotype to become migratory, reaching their maximum population size within the first two days and then remaining steady. This transformation is mirrored in the initial decrease in the number of proliferative epidermal cells. Hyperproliferation begins once the immune cell concentration reaches some critical value (here 25), leading to logistic growth of the population of proliferative cells, E. This is enhanced by cell migration, which reduces the wound diameter and provides space into which keratinocytes may proliferate.

Wound diameter decreases almost as a mirror of the number of proliferative cells: the lag phase corresponds to the time required for a subset of keratinocytes to adopt a migratory phenotype, and the delay before hyperproliferation begins. Previous studies and our own data have shown that wound diameter decreases with a concave profile (see [232] for ex-

Table 4.3: **Parameter values used to simulate the system of ODEs described in Section 4.3.1.** Descriptions, values and units of the parameters used to generate solutions to the system of equations (4.1)-(4.8).

Parameter	Description	Value	Units
s_I	Tissue-resident immune cell concentration	2.5	cells /mm·hour
L	Diameter of initially intact skin	8	mm
d_I	Rate of tissue-resident immune cell loss	2	hour^{-1}
m_d	Rate of immune cell recruitment	50	cells /mm·hour
d_m	Distance per recruited cell	0.0075	mm/cells
σ	Standard deviation of Gaussian curve $G(t-\tau)$	5	hours
τ	Time of maximal immune cell recruitment	20	hours
σ_M	Growth rate of the migratory cell population	0.107	hour^{-1}
M_E	Cell concentration in migratory layer	234	cells/mm
$K_{E_{local}}$	Local keratinocyte carrying capacity	10000	cells/mm^2
σ_{E0}	Baseline keratinocyte proliferation rate	$0.02\dot{6}$	hour^{-1}
σ_{EI}	Keratinocyte hyperproliferation rate	$0.10\dot{2}$	hour^{-1}
I_{crit}	Criterion for keratinocyte hyperproliferation	25	cells
α	Keratinocyte migration speed	0.0002	mm/cell·hour
υ	Carrying capacity correction for migration	930	cells

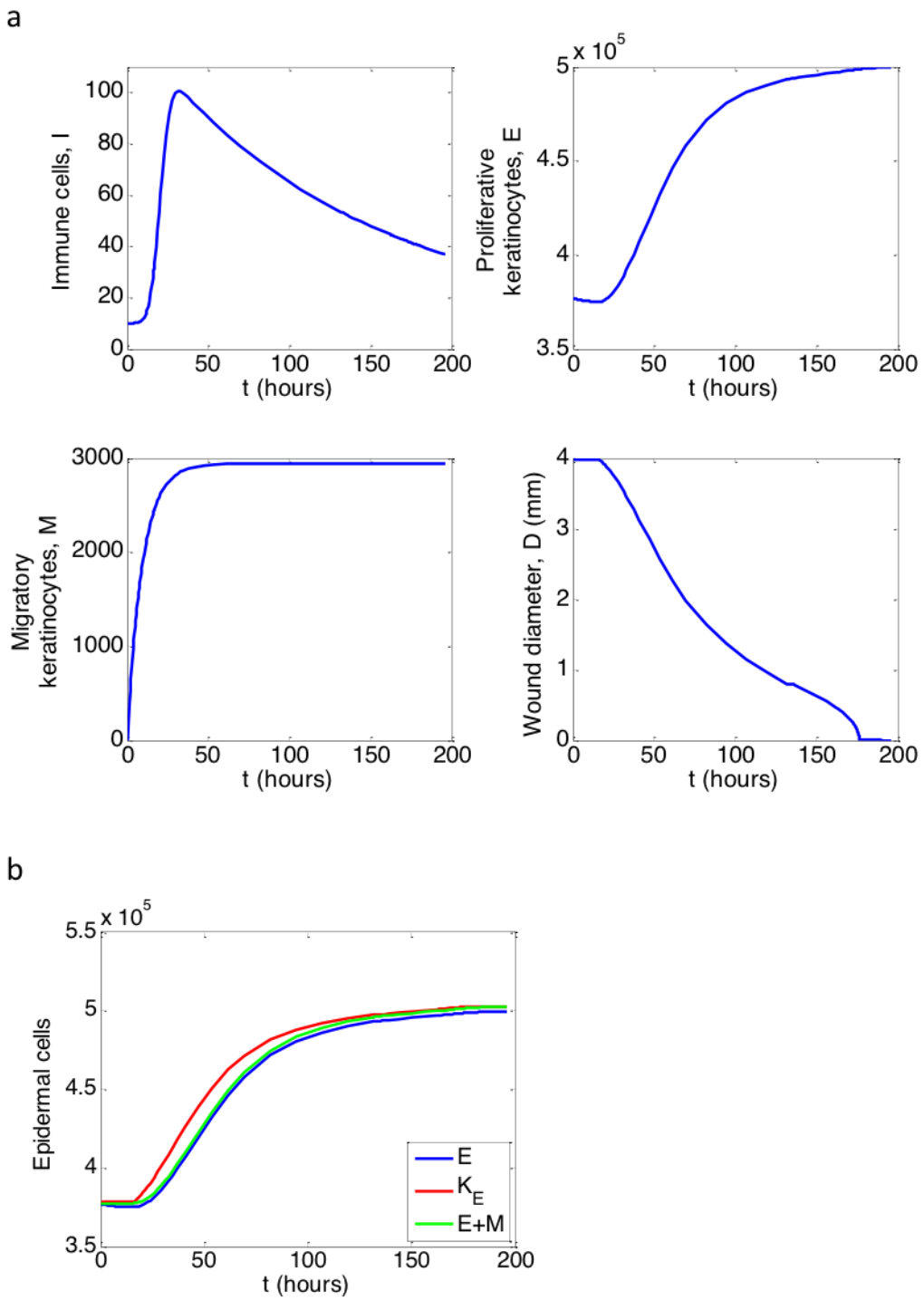

Figure 4.13: **Predictions of immunce cell and keratinocyte concentrations, and wound diameter during the first 8 days of the epidermal healing process.** (a) Solution curves for equations (4.1)-(4.8) generated using the initial conditions listed in Table 4.2, and parameter values listed in Table 4.3. (b) Changes to the concentrations of proliferative keratinocytes (blue) and all keratinocytes (green) over time, compared to their carrying capacity (red).

ample), which is consistent with the solution curve shown in Figure 4.13. However, the transition to $D = 0$ is very sharp as a result of the abrupt halt in migration caused by $\widetilde{H_0}(D)$. Physiologically, it is likely that migration slows down more gradually as cells get close to each other, which is not well represented by a Heaviside step function.

Heaviside step functions can also cause more general problems for numerical solvers, as even when smoothed they can change value rapidly over small timeframes. We have chosen the parameters g_I, g_D and g_0 such that a stiff solver with an adaptive timestep can compute reasonable numerical approximations. However, it would be advantageous if solutions could be generated analytically.

The use of a threshold value of immune cell density to regulate keratinocyte hyperproliferation was chosen in an absence of any biological insight as to the dynamics, and becuase it represented a simple interaction between the cell populations. It is possible that the dynamics may actually operate on a continuum, with increasing immune cell numbers causing increasing levels of keratinocyte hyperproliferation. This was implemented by altering the keratinocyte proliferation rate to

$$\sigma_E(I) = \sigma_{E0} + \sigma_{EI}\frac{I - 20}{100} \, . \tag{4.9}$$

The output (Figure 4.14) takes a very similar form to when a critical threshold is employed, suggesting that either a threshold or dynamic relationship can be employed so long as the sizes of the effects are comparable.

4.3.3 Model simplification

In order to explore the model behaviour analytically, we can reduce the system described previously down to two equations by generalising the behaviour of the other variables. In particular, M increases rapidly at early time points and quickly levels off at its limiting value of $M_E\pi D_0$. Therefore, when considering healing dynamics beyond 2 dpw, and with $\sigma_M > 0.1$, we can make the approximation $M = M_E\pi D_0$ and neglect the second term of equation (4.6), which describes the initial change from proliferative to migratory cells immediately after wounding. This simplification neglects to include the time delay involved in keratinocytes taking on a migratory phenotype; however as the focus of our analytical investigation is on the long term behaviour of the system then this is not an unreasonable approximation. In particular, D, I and the proliferation rate of E do not change substantially within the short timescale when M increases rapidly, so the simplification is not expected to alter the behaviour of the other variables as the timecourse proceeds.

The keratinocyte proliferation rate, $\sigma_E(I)$, is a function of the number of immune cells. Given that the solution for the number of immune cells is imposed – that is the equations for their dynamics are engineered to produce a solution of a particular form, which varies only with time and initial wound diameter – the effect of immune cells on proliferation rate can be simplified to a time-dependent effect. Setting $\sigma_E(I) = \sigma_E(t)$ allows equation (4.1) to be omitted entirely.

Making these substitutions and simplifications gives the system illustrated in Figure 4.15, which can be described by the following equations:

$$\frac{\mathrm{d}E}{\mathrm{d}t} = \sigma_E(t)E\left(1 - \frac{E + M_E\pi D_0}{K_E(D)}\right) , \tag{4.10}$$

$$\frac{\mathrm{d}D}{\mathrm{d}t} = -\alpha M_E\pi D_0\widetilde{H_D}(E + M_E\pi D_0 - K_E(D) + \upsilon) \text{ for } D > 0 , \tag{4.11}$$

where

$$K_E(D) = \frac{\pi}{4}(L^2 - D^2)K_{E_{local}} ,$$
$$\sigma_E(t) = \sigma_{E0} + \sigma_{EI}\widetilde{H_\sigma}(t - t_{crit}) .$$

The system can be non-dimensionalised by scaling the variables as follows:

$$E = \frac{\pi}{4}L^2K_{E_{local}}\hat{E} \quad , \quad D = L\hat{D} \quad , \quad t = \frac{\hat{t}}{\sigma_{E0}} \quad ,$$

which gives

$$\frac{\mathrm{d}\hat{E}}{\mathrm{d}\hat{t}} = \left(1 + \hat{\sigma}_d\widetilde{H_\sigma}(\hat{t} - \hat{t}_{crit})\right)\hat{E}\left(1 - \frac{\hat{E} + \hat{M}_d}{1 - \hat{D}^2}\right) , \tag{4.12}$$

$$\frac{\mathrm{d}\hat{D}}{\mathrm{d}\hat{t}} = -\hat{\alpha}_d\widetilde{H_D}\left(\hat{E} + \hat{M}_d - (1 - \hat{D}^2) + \hat{\upsilon}_d\right) , \tag{4.13}$$

where we introduce the dimensionless parameters

$$\hat{\sigma}_d = \frac{\sigma_{EI}}{\sigma_{E0}} \quad , \quad \hat{M}_d = \frac{4M_ED_0}{L^2K_{E_{local}}} \quad , \quad \hat{\alpha}_d = \frac{\alpha M_ED_0}{L\sigma_{E0}} \quad , \quad \hat{\upsilon}_d = \frac{4\upsilon}{\pi L^2K_{E_{local}}} . \tag{4.14}$$

The parameter $\hat{\sigma}_d$ represents the ratio of keratinocytes' wound-induced hyperproliferation rate to the proliferation rate in unwounded skin. These quantities are possible to measure *in vivo* as described in Section 4.2. $\hat{M}_d$ gives the ratio of migratory keratinocytes to proliferative keratinocytes, which is dependent on the length of unwounded skin included in the model. The rate of keratinocyte migration is contained in the parameter $\hat{\alpha}_d$, which compares the rate of migration to that of proliferation in unwounded skin. This is a key parameter, as changes in the balance between migration and proliferation are widely considered to drive healing and non-healing phenotypes [127]. We assume that migratory keratinocytes can encroach on the wound space when the total number of keratinocytes is close to carrying capacity;

the parameter υ represents how many cells fewer than carrying capacity the population can be to still acheive migration. Thus the dimensionless parameter $\hat{\upsilon}_d$ represents the ratio of υ to the maximum number of keratinocytes sustainable in the area of skin that is simulated.

4.3.4 Analysis of the simplified model

The reduced system of equations (4.12)-(4.13) may be investigated by considering its null clines and phase plane plot, which are useful for visualising the overall behaviour of a system of two ODEs. First the null clines are determined, which occur when the derivatives of each variable are equal to zero. Given that phase plots are less sensitive to rapid changes in solution than numerical methods, we need not use the smoothed Heaviside function in equation (4.13). Hence we solve (dropping the hats from equations (4.12)-(4.13) for notational simplicity)

$$\frac{\mathrm{d}E}{\mathrm{d}t} = (1 + \sigma_d H(t - t_{crit}))\, E \left(1 - \frac{E + M_d}{1 - D^2}\right) = 0 \,, \tag{4.15}$$

$$\frac{\mathrm{d}D}{\mathrm{d}t} = -\alpha_d H \left(E + M_d - (1 - D^2) + \upsilon_d\right) = 0 \,, \tag{4.16}$$

where H denotes the Heaviside step function.

Equation (4.15) gives the solutions $E = 0$ and $E = 1 - D^2 - M_d$, which are shown (for the parameter values listed in Table 4.3) by the blue lines depicting null clines in Figure 4.16. Equation (4.16) is satisfied when the Heaviside function is zero, hence we have the cutoff condition $E < 1 - D^2 - M_d - \upsilon_d$. The rest of the phase plot is produced by constructing the direction field, which shows the behaviour of the system subject to various initial conditions (Figure 4.16). The phase plot illustrates that when the number of proliferating epidermal cells is lower than the cutoff value, damage does not decrease. This reflects the biological assumption that migration does not occur until cells surrounding the wound are close to their carrying capacity, to prevent loss of contact inhibition between keratinocytes. When the number of epidermal cells is at or above the cutoff (analogous to being at or above their carrying capacity), migration can proceed and wound diameter reduces. The distance between the curves reflects the relatively small value of υ compared to the total carrying capacity of the keratinocyte population; however, as shown when the plot is zoomed in on smaller regions, the null cline lies consistently above the threshold curve, suggesting that wound diameter will always decrease to 0 in this parameter space.

This model does not take spatial aspects of wound closure into account, only the overall number of cells is considered; however, given that a consensus has not been reached as to

the spatial dynamics of re-epithelialisation, a more generalised model may be instructive. Additionally, the ODE system is relatively simple, computationally inexpensive and many parameters can be determined with *in vivo* experiments. Therefore the model provides a good starting point to investigate the mechanisms of re-epithelialisation, and can be built upon in subsequent studies to further improve agreement with biological observations.

Limitations of the model include the assumption that the keratinocyte migration rate is fixed, whereas it may vary with time and based on the location of the cell in question. It is difficult to track migration *in vivo*, so making α a function of time could allow various migratory dynamics to be investigated. However, given the inherently spatial nature of migration this may be better achieved using a PDE or ABM approach. This model also imposes a keratinocyte carrying capacity that does not vary with distance from the wound, but is averaged over the entire domain of interest taking the current wound size into account. This means that the effect of wound diameter reduction by keratinocyte migration is spread across all the intact tissue, rather than concentrated at the interface between the wound and skin.

Another shortcoming of this model is that it is not possible to quantify the number of cells in the wound space, only the diameter of the wound, which means the output cannot be directly compared to the experimental data presented in Figure 4.6. To assess whether a spatial description may be better placed to provide novel insight into the dynamics of healing, we next develop a PDE model of the same phenomena and investigate its output.

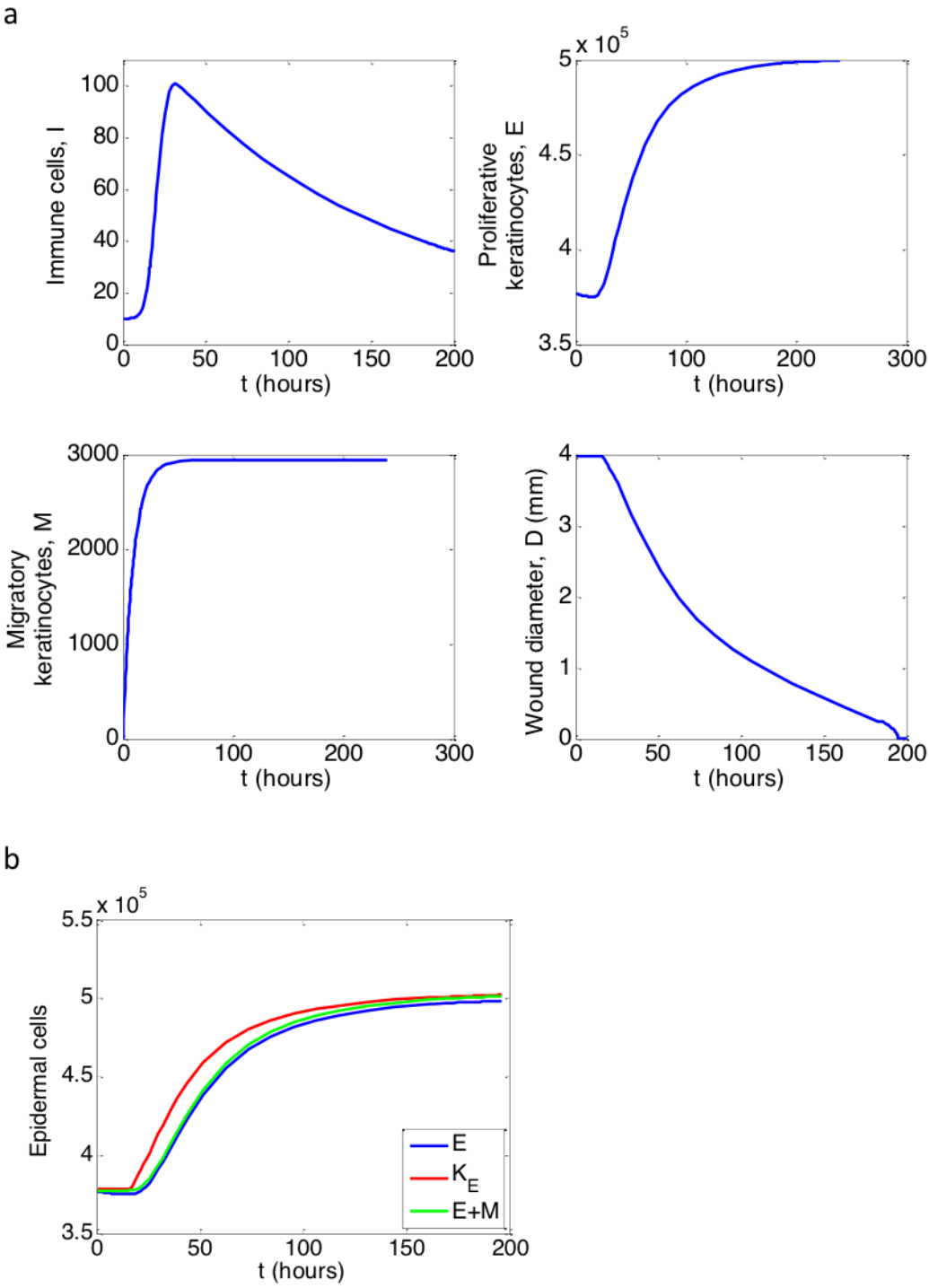

Figure 4.14: **Predictions of immunce cell and keratinocyte concentrations, and wound diameter when the keratinocyte hyperproliferation rate, σ_{EI}, changes dynamically with the concentration of immune cells.** (a) Solution curves for the system of equations (4.1)-(4.6), (4.8) and (4.9) for the initial conditions listed in Table 4.2, and parameter values listed in Table 4.3. (b) Changes to the concentrations of proliferative keratinocytes (blue) and all keratinocytes (green) over time, compared to their carrying capacity (red).

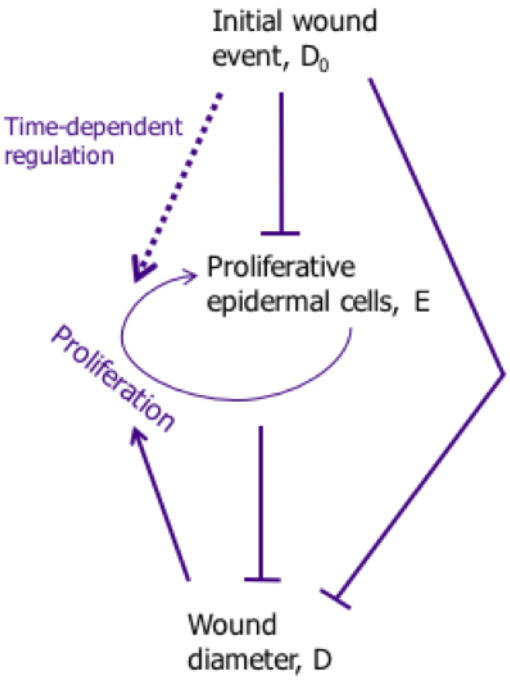

Figure 4.15: **Schematic of the biological interactions included in the simplified ODE model (4.10)-(4.11).** The effect of proliferative epidermal cells on wound diameter during the healing process. Arrows denote increases, flat-headed arrows denote decreases, and dotted arrows denote interactions that, instead of explicitly including multiple cell types, are modelled as time-dependent processes.

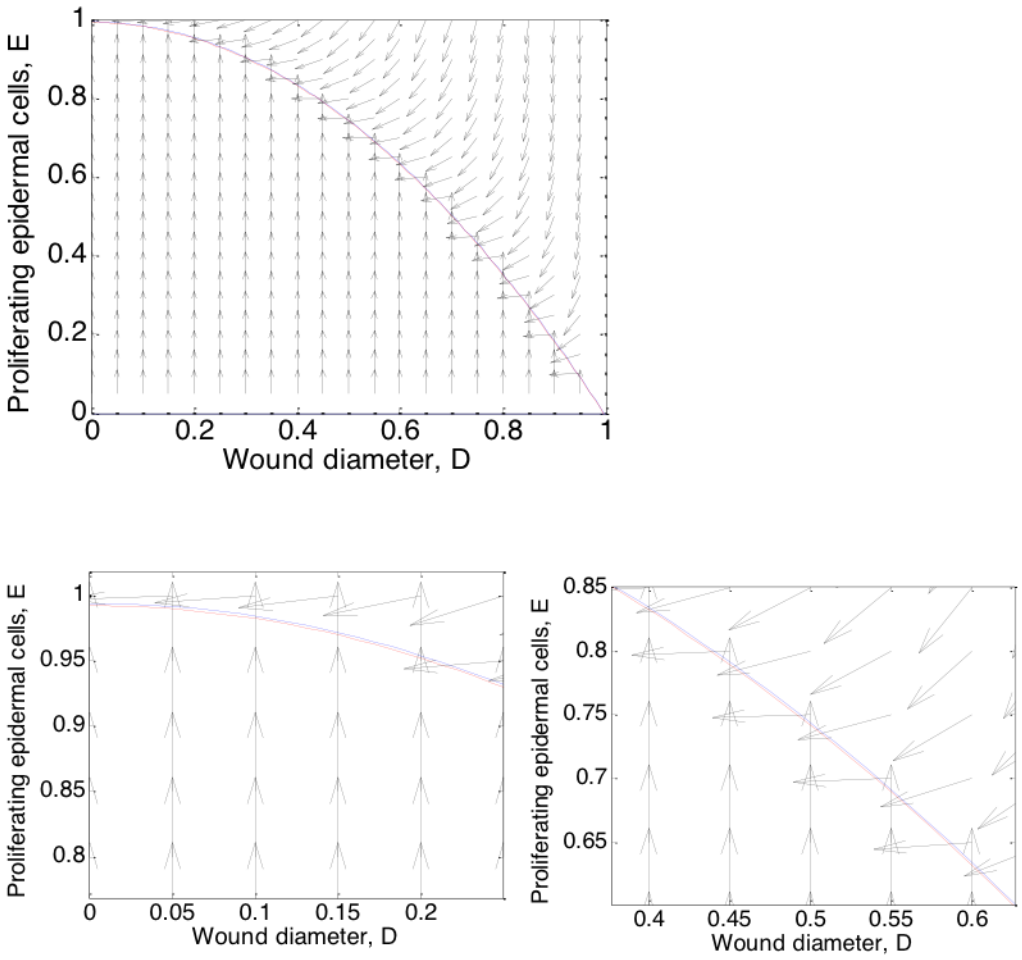

Figure 4.16: **Steady state solutions for proliferating epidermal cell concentration and wound diameter in a simplified system of ODEs.** Null cline (blue), cutoff line (red) and direction field (black) of the system (4.15)-(4.16) when non-dimensional parameters (4.14) are calculated from values in Table 4.3 (giving $\hat{\sigma}_d = 0.261$, $\hat{M}_d = 0.00585$, $\hat{\alpha}_d = 0.878$, $\hat{\upsilon}_d = 0.00185$).

4.4 An extended domain, partial differential equation model of epidermal healing

As discussed in Chapter 3, PDE models of epidermal healing have used reaction-diffusion systems to investigate the roles of biochemically regulated keratinocyte mitosis and migration in skin repair [87]. Whilst model output is reportedly consistent with experimental studies, the approach is limited by its representation of a homogeneous epidermis and failure to incorporate processes that occur in the adjacent unwounded skin. In this section we adapt the PDE model described in Chapter 3, Table 3.2 to reflect spatial heterogeneity of healing processes and epidermal structure, and extend the model's domain to include the surrounding, unwounded epidermis.

4.4.1 Formulating a PDE model of epidermal healing

In order to migrate, keratinocytes alter their phenotype by detaching from those around them and becoming elongated, which is not conducive to undergoing mitosis [99]. Therefore, we hypothesise that spatially separating proliferating and migrating cells may be advantageous. To model this, an extended domain can be considered where both the wound and surrounding unwounded skin are represented. We consider a section of skin of radius L, from which a wound is created of radius L_W with its centre at $r = 0$; cells close to the wound edge make up an area of width $L_M - L_W$, as illustrated in Figure 4.17.

We then include spatial control of mitosis and migration rates, using

$$\frac{\partial n}{\partial t} = \boldsymbol{\nabla} \cdot \left[D(r) \widetilde{H}(n) \boldsymbol{\nabla} n \right] + s(r) n \left(1 - \frac{n}{n_0} \right) , \tag{4.17}$$

where n is the number of keratinocytes, $D(r)$ is the diffusion rate, $s(r)$ is the proliferation rate and n_0 is the maximum number of keratinocytes that can be sustained by the healthy epidermis. Density-dependent diffusion is implemented using the heaviside function

$$\widetilde{H}(n) = \frac{1}{2} \left(\tanh \left(h_1 \left(\frac{n}{n_0} - h_2 \right) \right) + 1 \right) . \tag{4.18}$$

Within the wound space cells are expected to actively migrate, whereas in intact skin migration will be negligible except for a small amount of passive diffusion occurring as cells spread out after mitosis. We represent active migration by diffusion at a higher rate, which can be implemented as

$$D(r) = \begin{cases} D_w & \text{for} \quad r \leq L_W \\ \delta D_w & \text{for} \quad r > L_W \ , \end{cases} \tag{4.19}$$

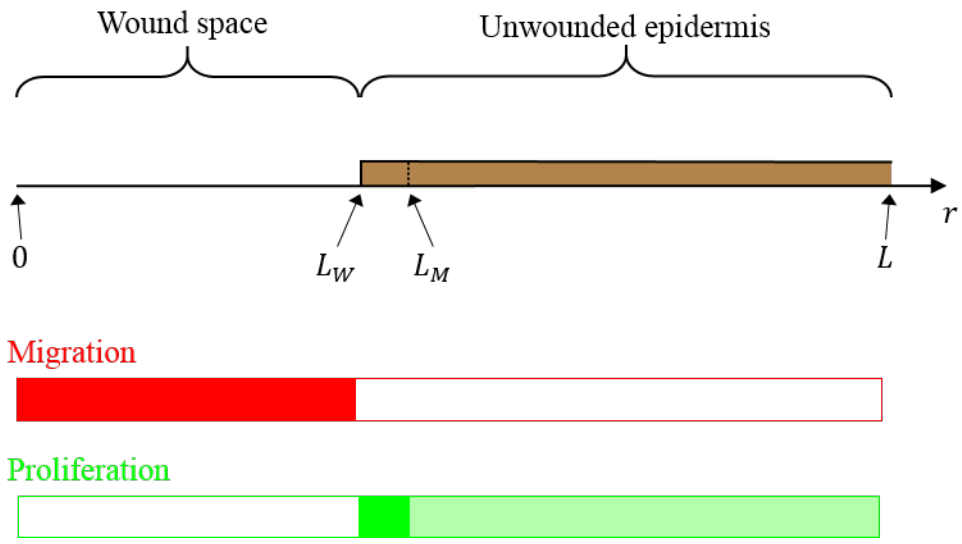

Figure 4.17: **Schematic of the extended-domain PDE model of epidermal healing described by equations (4.17)-(4.20).** The spatial organisation of an extended domain, showing regions of high keratinocyte migration rate (red), keratinocyte hyperproliferation (dark green), and keratinocyte proliferation at the same rate as in unwounded skin (light green).

where D_w is the migration rate within the wound and δ is small. Similarly, an increased mitotic rate in a layer close to the wound edge (between $r = L_W$ and $r = L_M$), can be modelled as

$$s(r) = \begin{cases} 0 & \text{for} \quad r \leq L_W \\ s_m & \text{for} \quad L_W < r \leq L_M \\ s_s & \text{for} \quad r > L_m \ , \end{cases} \tag{4.20}$$

where s_m is the mitotic rate in the band of cells close to the wound, and s_s is the mitotic rate in unwounded skin.

These equations can be solved subject to the conditions of no flux at the boundaries of the extended domain:

$$D(r = 0) \cdot \widetilde{H}(n(r = 0)) \cdot \boldsymbol{\nabla} n(r = 0) = 0 \ , \tag{4.21}$$

$$D(r = L) \cdot \widetilde{H}(n(r = L)) \cdot \boldsymbol{\nabla} n(r = L) = 0 \ , \tag{4.22}$$

for all times. We impose the intial condition illustrated in Figure 4.17 – that there are no cells within the wound space, and the cell concentration in the surrounding intact skin is that of unwounded skin – which can be expressed as

$$n(r, t = 0) = n_0 H(r - L_w) \ , \tag{4.23}$$

where $H()$ denotes a heaviside function.

4.4.2 Non-dimensionalisation

Equation 4.17 can be non-dimensionalised using the following scalings:

$$n = n_0\hat{n} \quad , \quad t = \frac{1}{s_s}\hat{t} \quad , \quad r = L_W\hat{r} \quad , \quad D = s_s L_W^2 \hat{D} \quad ,$$

which gives

$$\frac{\partial \hat{n}}{\partial \hat{t}} = \boldsymbol{\nabla} \cdot \left[\hat{D}(\hat{r})\widetilde{H}(\hat{n})\boldsymbol{\nabla}\hat{n}\right] + \hat{s}(\hat{r})\hat{n}\,(1-\hat{n}) \ , \tag{4.24}$$

with

$$\hat{D}(\hat{r}) = \begin{cases} \hat{D} & \text{for} \quad \hat{r} \leq 1 \\ \delta\hat{D} & \text{for} \quad \hat{r} > 1 \ , \end{cases} \tag{4.25}$$

$$\hat{s}(\hat{r}) = \begin{cases} 0 & \text{for} \quad \hat{r} \leq 1 \\ \sigma & \text{for} \quad 1 < \hat{r} \leq \lambda \\ 1 & \text{for} \quad \hat{r} > \lambda \ , \end{cases} \tag{4.26}$$

Boundary and initial conditions (4.21)-(4.23) are similarly non-dimensionalised, giving

$$\hat{D}(\hat{r}=0)\widetilde{H}(\hat{n}(\hat{r}=0))\boldsymbol{\nabla}n(r=0) = 0 \ , \tag{4.27}$$

$$\hat{D}(\hat{r}=\kappa)\widetilde{H}(\hat{n}(\hat{r}=\kappa))\boldsymbol{\nabla}\hat{n}(\hat{r}=\kappa) = 0 \ , \tag{4.28}$$

and

$$\hat{n}(\hat{r}, \hat{t}=0) = H(\hat{r}-1) \ , \tag{4.29}$$

where we introduce the non-dimensional parameters $\sigma = \frac{s_m}{s_s}$, $\lambda = \frac{L_M}{L_W}$ and $\kappa = \frac{L}{L_W}$. In the following sections we drop the hats for notational simplicity.

The number of non-dimensional parameters involved is smaller than for the ODE model, as space is represented as a variable. This is advantageous as parameter estimation and sensitivity analysis are more straightforward to conduct. However, there is no explicit description of wound size in this representation, so assumptions must be made as to which cell concentrations constitute "healed" epidermis. Previous studies have considered an area to be healed when its keratinocyte concentration exceeds 80% of the value in unwounded skin [87].

4.4.3 Numerical solutions

We solve equation 4.24 with a no-flux boundary condition at $r = 0$, and at $r = \frac{L}{L_W}$ the cell concentration is that of unwounded skin: $n = 1$. The initial condition is depicted in Figure 4.17, where $n = 0$ for $0 \leq r < 1$ and $n = 1$ for $r > 1$ which is smoothed for use in the numerical solver. Solutions are generated using the Matlab solver `pdepe` over the spatial domain $0 \leq r < 2$, using an adaptive timestep.

Substituting the values from Table 4.3 into the non-dimensional parameters gives $\sigma = 3.8\dot{3}$, $\lambda = 1.025$ and $\hat{D} = 0.00047$. We set $h_1 = 10$ and $h_2 = 0.6$ which allows keratinocytes in the migratory region to reach the maximum migration speed when their concentration exceeds $n = 0.8$, as depicted in Figure 4.18.

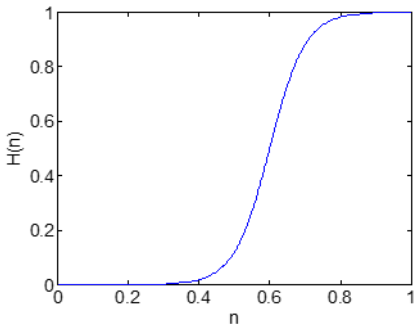

Figure 4.18: **Form of the Heaviside function $\widetilde{H}(n)$.** Solution of equation (4.18) for $h_1 = 10$, $h_2 = 0.6$.

Solutions to this system are shown in Figure 4.19a-b. Initially, the cell density at $r = 1$ decreases as cells at the wound edge diffuse into the wound space before hyperproliferation has counteracted the effect. Immediately following this, a steep front of cell concentration advances through the wound space, which is facilitated by migration in the wound region and increased mitosis in the unwounded layer. The form of solutions in this time period differ from those of limited domain models [87] in that the position at which cell concentration approaches its unwounded value of $n = 1$ does not advance along with the steep front (illustrated in Figure 4.19c). In the extended domain model, once the steep front reaches the centre of the wound ($r = 0$), the shape of the solution curves change to represent the dynamics as cell concentrations within the wound space gradually increase to their unwounded value.

Overall, this solution behaviour is more consistent with the results of histological experiments (for example Figure 4.7), where keratinocytes migrate to form an epithelial layer one or two cells thick, before a fully stratified epidermis is re-formed. The solution behaviour is also insensitive to small perturbations in non-dimensional parameter values (changing either σ or D by an order of magnitude does not cause qualitative changes to the solution curves), suggesting a robust as well as biologically consistent description of epidermal healing.

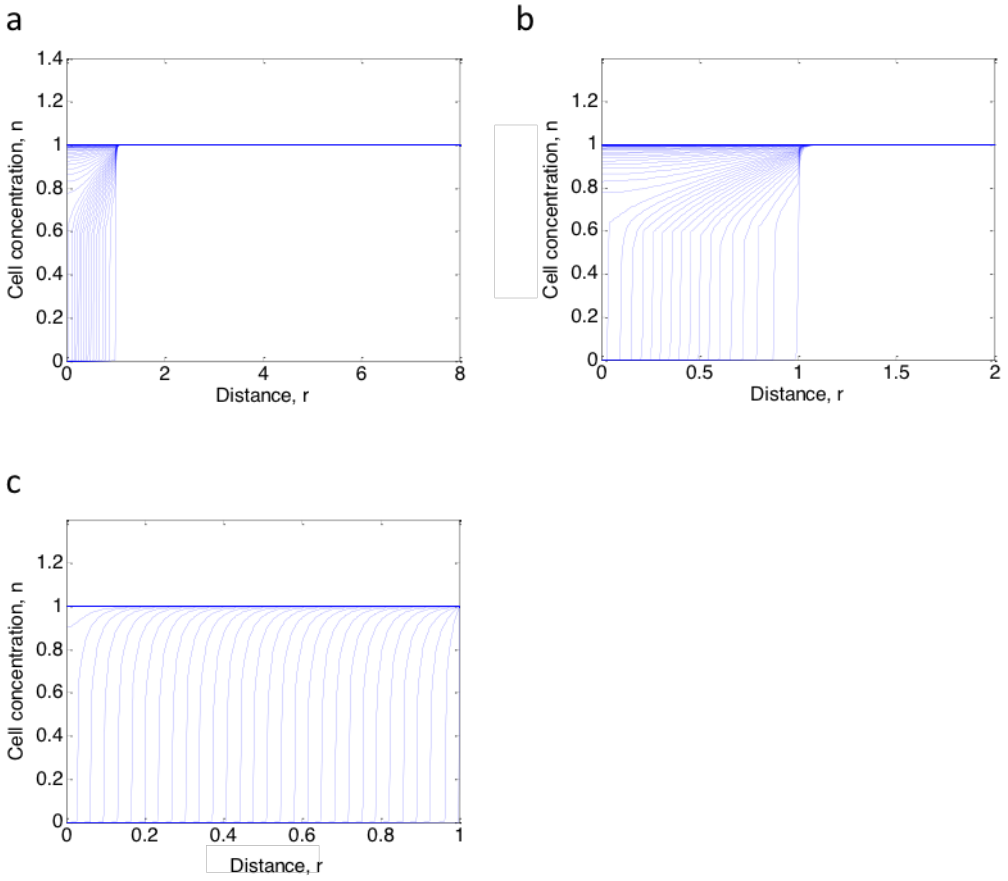

Figure 4.19: **Predictions of keratinocyte concentrations within and surrounding a wound during the healing process.** (a, b) Numerical solutions to equations (4.24)-(4.29), for parameter values $\sigma = 3.8\dot{3}$, $\lambda = 1.025$, $\hat{D} = 0.00047$, $h_1 = 10$ and $h_2 = 0.6$. All solutions were calculated over the entire domain $0 \leq r \leq 8$, but are presented for (a) the whole domain, and (b) the wound region and immediately adjacent skin. (c) Equivalent output for the limited domain model described in Table 3.2 [87]

Unlike the ODE model, there is no explicit description of the wound edge in this PDE representation. Although previous studies use a value of $n_{healed} = 0.8$ to denote areas of repaired epidermis, little justification has been provided for this choice [87]. Additionally,

given that healthy murine IFE is between 2 and 3 nucleated cells thick, a cell concentration of 0.8 may be non-physical for small spatial areas. The effect of varying the criterion for "healed" epidermis is shown in Figure 4.20. For the previously used value of $n_{healed} = 0.8$ (Figure 4.20b), after a brief lag phase wound size decreases linearly with time, followed by a rapid decrease to a wound diameter of 0 at $t = 159$; however, this does not correspond to the steep front of the solution curve, but rather to the sloping region. If the criterion for healing is reduced to $n_{healed} = 0.6$, the projected wound edge is consistent with the steep front of cells advancing through the wound space. The associated healing trajectory is shown in Figure 4.20a, and takes the form of a linear decrease in wound diameter.

The effects of increasing the cell concentration required for an area of the wound to be considered healed are shown in Figure 4.20c-e. As the required cell concentration increases, so does the initial lag phase of healing (during which wound diameter reduces very slowly). For $0.9 \leq n_{healed} \leq 0.99$ the subsequent wound size profile is convex, with the rate of change increasing as wound diameter approaches 0. When the cell concentration in the wound space is required to be equal to that of unwounded skin for the area to be considered healed, the wound radius is approximated as greater than that of the initial wound for the majority of the healing trajectory (Figure 4.20f). This is due to the initial decrease in cell concentration at the wound edge caused by early migration, as described previously. Therefore, $n_{healed} = 1$ appears to be an inappropriate criterion for estimating wound size, but it is unclear whether $n_{healed} = 0.8$ is an appropriate choice, as the qualitative form of the healing trajectory is strongly dependent on the criterion imposed. Whilst wound size is a biologically relevant and easy to understand measure of healing, representing each solution curve by a single number (wound diameter) reduces the information available and may result in misleading healing trajectories.

Making quantitative changes to the function $\widetilde{H}(n)$, which represents the effect of cell concentration on diffusion rate, can alter the height of the steep front of cell concentrations that advances through the wound space. For example, $h_2 = 0.8$ (compared to its previous value of 0.6) gives the solution profiles shown in Figure 4.21a. Healing proceeds more slowly as cells cannot migrate unless their concentration approaches that of unwounded skin. The shapes of the healing trajectories (Figure 4.21b-f) also differ when compared to those with $h_2 = 0.6$. A linear trajectory is now associated with the criterion $n_{healed} = 0.8$ (Figure 4.21b), and higher values of n_{healed} are required for the lag phase to be observed. Taking the steepest gradient of the solution curve as a determinant of the healed region could be used to correct for this parameter dependence; however the solutions would need to be qualitatively similar and an additional criterion to ensure that the position of the steepest gradient is not in an

area of low cell concentration (for example if h_2 were small) may also be required.

As shown in Figure 4.9c, hyperproliferation is not limited to the unwounded epidermis directly adjacent to the wound space, but also occurs within the wound. This can be incorporated into the PDE model by altering the form of the spatially-dependent mitosis rate to

$$\hat{s}(\hat{r}) = \begin{cases} 0 & \text{for} \quad \hat{r} \leq 1 \\ \sigma & \text{for} \quad \mu < \hat{r} \leq \lambda \\ 1 & \text{for} \quad \hat{r} > \lambda \, , \end{cases} \tag{4.30}$$

where $\mu < 1$ denotes the region within the wound where hyperproliferation occurs. Solutions for $\mu = 0.8$ and $\mu = 0.6$ are shown in Figure 4.22: the solutions curves do not differ qualitatively for those where $\mu = 1$, but the cell concentration increases far more quickly for smaller values of μ.

4.4.4 Incorporating epidermal stratification

Another aspect of the spatial organisation of the healing epidermis is the formation of distinct layers of keratinocytes. As discussed in Section 1.3.1, the epidermis is highly stratified with mitosis occurring predominantly in the basal layer. This may be represented by a system of PDEs, one representing nucleated cells in the basal layer (n_1) and another representing nucleated cells in the supra-basal layer(s) (n_2):

$$\frac{\partial n_1}{\partial t} = \boldsymbol{\nabla} \cdot \left[D_1(r) \left(\frac{n_1}{n_0} \right)^p \boldsymbol{\nabla} n_1 \right] + s_1(r) n_1 \left(1 - \frac{n_1}{n_0} \right) - f(n_1) \, , \tag{4.31}$$

$$\frac{\partial n_2}{\partial t} = \boldsymbol{\nabla} \cdot \left[D_2(r) \left(\frac{n_1 n_2}{n_0^2} \right)^p \boldsymbol{\nabla} n_2 \right] + s_2(r) n_2 \left(1 - \frac{n_2}{n_0} \right) + f(n_1) \, . \tag{4.32}$$

Equation (4.31) takes a similar form to the previous PDE representation (4.24) but with an additional term $f(n_1)$ that represents the transfer of keratinocytes from the basal to supra-basal layers. Equation (4.32) includes migration that is dependent on the local cell concentration, where the migration rate is controlled by the concentration in both layers. This incorporates the assumption that supra-basal cells cannot move into the wound space if there are no basal cells ahead of them over which to migrate.

This system can be solved subject to the boundary conditions of no flux in the centre of the wound for either layer:

$$D_1(r=0) \cdot \left(\frac{n_1(r=0)}{n_0} \right)^p \boldsymbol{\nabla} n_1(r=0) = 0 \, , \tag{4.33}$$

$$D_2(r=0) \cdot \left(\frac{n_1(r=0) \cdot n_2(r=0)}{n_0^2} \right)^p \boldsymbol{\nabla} n_2(r=0) = 0 \, , \tag{4.34}$$

and with cell concentration at its maximum value at the wound edge:

$$n_1(r = L_W) = n_0 \ , \tag{4.35}$$

$$n_2(r = L_W) = n_0 \ , \tag{4.36}$$

for all times. We impose the intial condition of no cells within the wound space in either layer, which can be expressed as

$$n_1(r, t = 0) = 0 \ , \tag{4.37}$$

$$n_2(r, t = 0) = 0 \ , \tag{4.38}$$

An example of the solution behaviour of this system, with no spatial control of proliferation or migration rates (i.e. $D_1(r) = D_1$, $D_2(r) = D_2$, $s_1(r) = s_1$ and $s_2(r) = s_2$), at early timepoints is shown in Figure 4.23. In this example the transfer term is linear, with $f(n_1) = fn_1$, but using a quadratic or sigmoidal representation does not qualitatively alter the output. Cells in the basal layer advance into the wound space ahead of the supra-basal keratinocytes above them; however, the dynamics of the system are driven by those of the basal layer, n_1. This is because there is no feedback from the supra-basal layers to the basal layer, so the system is not fully coupled. Additionally, the form of the cell concentration dependent migration in the supra-basal layer assumes that cells migrate as extending sheets; other migration mechanisms, for example the "leapfrog" or "extending epithelial shield" descriptions (see Section 1.3.6), are not well described by this model.

It would be possible to hybridise the system (4.31-4.32) with the spatially controlled migration and proliferation used previously (4.25-4.26), and to extend the domain to incorporate unwounded skin; however, the lack of feedback from supra-basal to basal cells is a significant limitation that would still be relevant in a hybrid system.

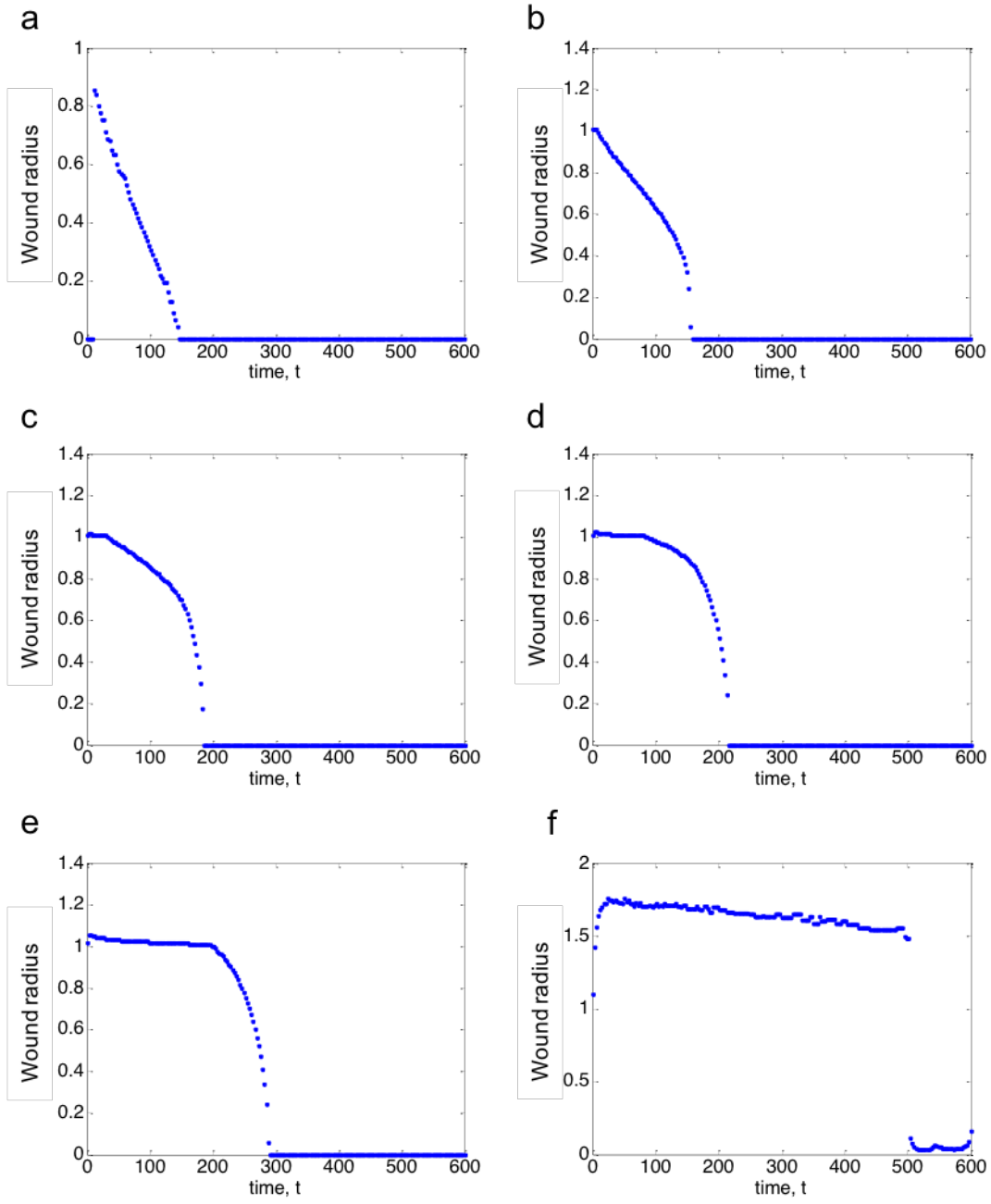

Figure 4.20: **Predictions of changes to wound radius during a healing timecourse.** Plots of the smallest value of r for which $n(r) \geq n_{healed}$ for the solutions presented in Figure 4.19. (a) $n_{healed} = 0.6$, (b) $n_{healed} = 0.8$, (c) $n_{healed} = 0.9$, (d) $n_{healed} = 0.95$, (e) $n_{healed} = 0.99$, (f) $n_{healed} = 1$.

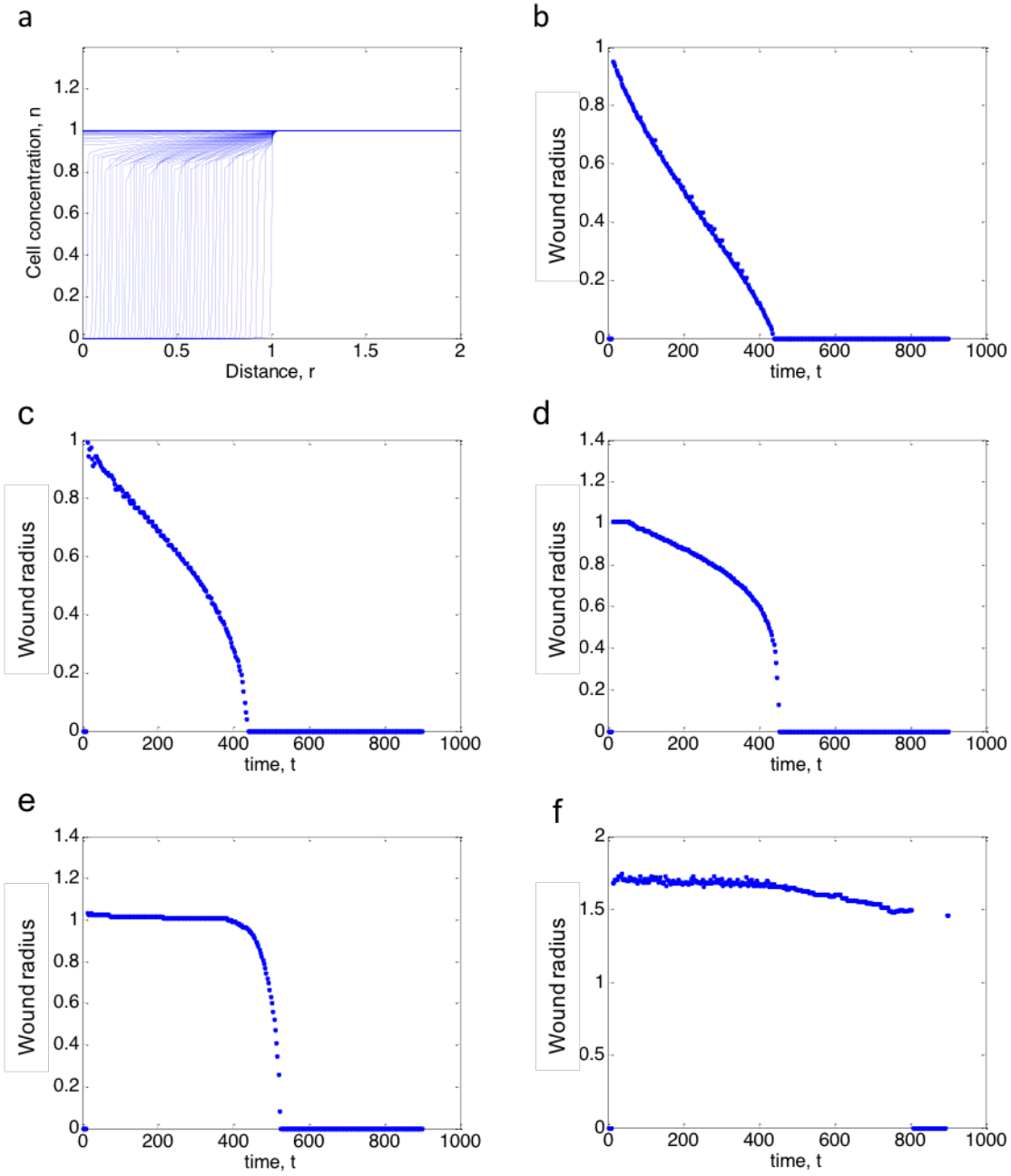

Figure 4.21: **Predictions of keratinocyte concentrations and wound radii during a healing timecourse, when a stricter density-dependent migration criterion is imposed.** (a) Numerical solutions to equations (4.24)-(4.29), for parameter values $\sigma = 3.8\dot{3}$, $\lambda = 1.025$, $\hat{D} = 0.00047$, $h_1 = 10$ and $h_2 = 0.8$. (b-f) Plots of wound radius when (b) $n_{healed} = 0.8$, (c) $n_{healed} = 0.9$, (d) $n_{healed} = 0.95$, (e) $n_{healed} = 0.99$, (f) $n_{healed} = 1$.

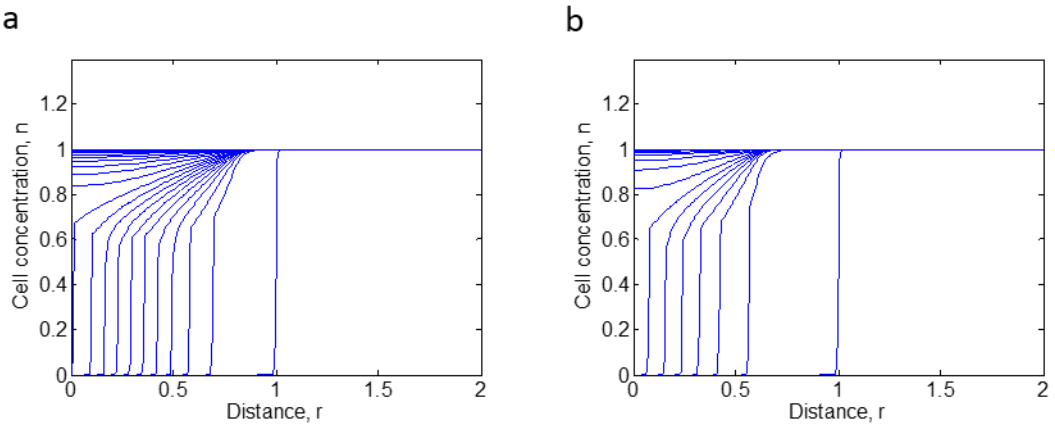

Figure 4.22: **Predictions of keratinocyte concentrations during a healing timecourse, with mitosis occuring within a portion of the wound space.** Numerical solutions to equations (4.24)-(4.25), (4.30) and (4.27)-(4.29) for $\sigma = 3.8\dot{3}$, $\lambda = 1.025$, $\hat{D} = 0.00047$, $h_1 = 10$, $h_2 = 0.6$ and (a) $\mu = 0.8$, (b) $\mu = 0.6$.

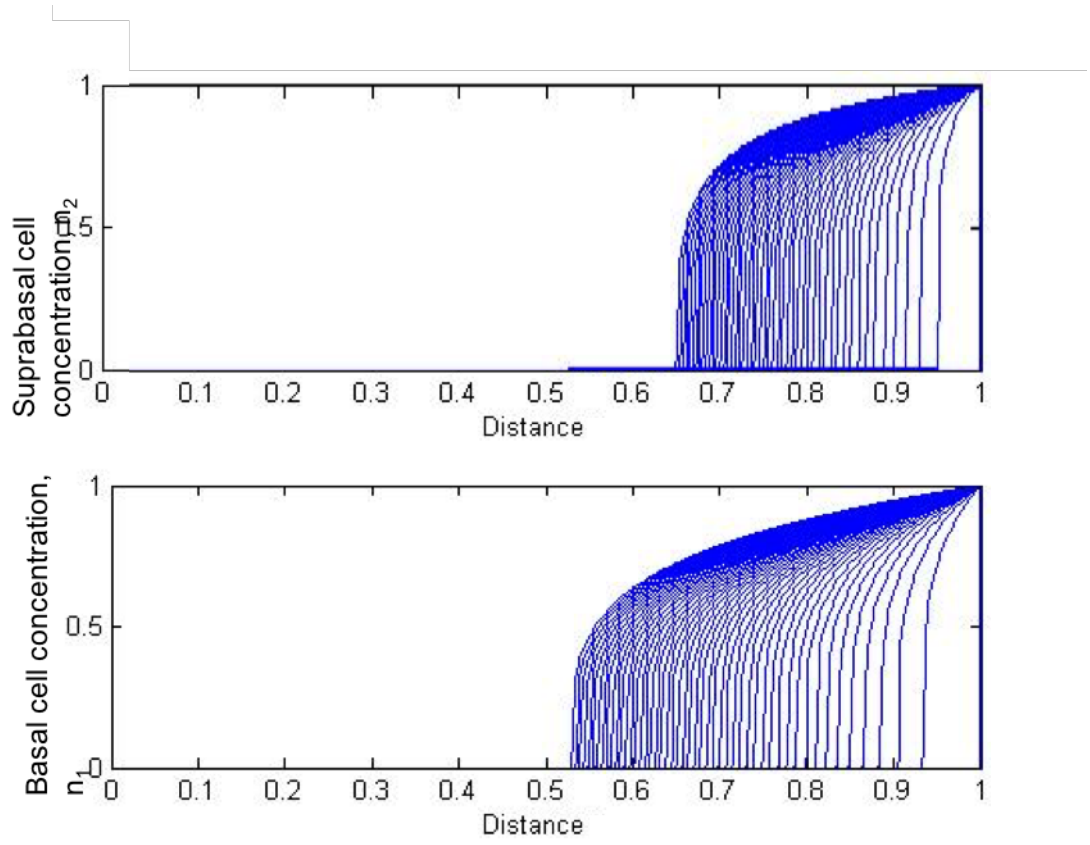

Figure 4.23: **Predictions of keratinocyte concentrations in the basal and suprabasal epidermal layers during a healing timecourse.** Numerical solutions to equations (4.31)-(4.38) with a linear transfer term, $f(n_1) = fn_1$, and parameter values $\hat{D}_1 = \hat{D}_2 = 10^{-3}$, $p = 1$, $s_1 = 10^{-5}$, $s_2 = 10^{-10}$, $f_1 = 10^{-5}$.

4.5 A discrete model of epidermal re-epithelialisation

4.5.1 Motivation for a discrete model

As discussed in Section 3.3, ABMs can represent cells as discrete entities whose behaviour is governed by a predetermined set of rules. Therefore, developing a discrete model of epidermal repair will allow the physical feedback between individual cells to be incorporated, such that the positions and space occupied by supra-basal cells can affect keratinocytes in the basal layer. If the stratification of the epidermis is considered to be an important aspect to include, then this may represent a significant advance over PDE systems.

Additionally, the model equations described in Section 4.4 use diffusive terms to represent the process of active migration, with the size of the diffusion coefficient increased in areas where cells migrate rapidly. We will use a discrete model to investigate whether passive diffusion is sufficient to replicate the dynamics of epidermal healing, or whether an explicit representation of active migration is required.

Although cells are represented as individual agents, it is possible to model their movement through continuous space using an agent based approach. Therefore a keratinocyte in our simulation can occupy any spatial location within the model's domain, and may increase in size by any increment. However, time is not modelled on a continuous scale; instead, the total simulation time is divided into discrete, fixed timesteps, with agents altering their position, size or state depending on the properties of other agents at the end of each timestep [206].

4.5.2 Passive cell movement

In this discrete model each cell, j, is represented as an individual entity described by the position of the cell's centre, $\mathbf{x}_j = (x_1, x_2, x_3)$, and its shape, which is assumed to take the form of an ellipsoid described by its semi-axis lengths $\mathbf{w} = (w_1, w_2, w_3)$. Changes to cell position and shape are caused by the forces exerted by other cells in the domain, which result from the relatively tight packing of keratinocytes in the epidermis. Cell position changes following the force-balance ODE

$$\alpha \dot{\mathbf{x}}_j = \sum_{k \neq j} \mathbf{F}_{jk} \ , \tag{4.39}$$

where the left hand side represents the persistence or "drag" that dampens the motion of cell j, and the right hand side describes the forces applied to cell j by all of the other cells in the domain. $\mathbf{F}_{jk}$ represents the forces exerted by two cells, j and k, as they resist overlapping each another, taking the form

$$\mathbf{F}_{jk} = \int_V (-\boldsymbol{\nabla}\phi_k)(\xi\phi_j) \, , \tag{4.40}$$

where ϕ_j and ϕ_k are the cell potentials, which describe the regions within and around a cell that may exert a physical effect on the cells surroundings, and $\xi\phi_j$ can be thought of as the density of cell j.

In its most basic form, the 3D potential of cell j is given by

$$\phi_j(\mathbf{x}) = b_1(x_1) + b_2(x_2) + b_3(x_3) \, , \tag{4.41}$$

where b is the bump function [233]

$$b(r; A, r_{min}, r_{max}) = \begin{cases} f(-r - r_{min}) & -r_{max} \leq r \leq -r_{min} \\ A & -r_{min} < r < r_{min} \\ f(r - r_{min}) & r_{min} \leq r \leq r_{max} \\ 0 & \text{otherwise} \, , \end{cases} \tag{4.42}$$

with parameters A, r_{min}, r_{max}, $T = r_{max} - r_{min}$ and

$$f(r) = \frac{2A}{T^3} r^2 \left(r - \frac{3T}{2} \right) + A \, . \tag{4.43}$$

The cell potential can be extended to 3D by allowing the parameters of the bump function to vary with spherical co-ordinates θ and ϕ. It is assumed that the surface of the cell is ellipsoidal and located at $r = r_{max}$, thus r_{max} is given by the polar form of an ellipsoid

$$E(\theta, \phi) = \frac{w_1 w_2 w_3}{\sqrt{{w_3}^2 \sin^2\phi({w_1}^2 \sin^2\theta + {w_2}^2 \cos^2\theta) + {w_1}^2 {w_2}^2 \cos^2\phi}} \, . \tag{4.44}$$

The parameter T is held fixed so that a region surrounding the cell's centre exerts a force on other cells.

Changes to a cell's shape occur as a result of squeezing as surrounding cells reposition, which is modelled analogously to [75] and [234] as

$$\mathbf{S}_j = -\sum_{k \neq j} \frac{\mathbf{x}_j - \mathbf{x}_k}{|\mathbf{x}_j - \mathbf{x}_k|} \circ \mathbf{F}_{jk} \, , \tag{4.45}$$

where the fractional part represents the direction from which the squeeze is being applied, the operator $\circ$ denotes elementwise multiplication, and $\mathbf{F}_{jk}$ gives a representation of the

distance over which the squeeze is acting. Cells are assumed to adopt a "natural" or optimal shape $\overline{\mathbf{w}} = (\overline{w}_1, \overline{w}_2, \overline{w}_3)$. The preference of cell j to adopt this natural shape, combined with the squeezing effects of other cells leads to an overall change of cell shape that is represented as

$$\dot{\mathbf{w}}_j = -\gamma(\mathbf{w}_j - \bar{\mathbf{w}}) + \beta \mathbf{S}_j - \mathbf{C} \,, \tag{4.46}$$

where γ is the rate at which cells adopt their preferred shape and $\mathbf{C}$ is a correction factor to conserve cell volume. We assume that cell volume grows according to

$$\dot{V} = f(V) = \dot{\mathbf{w}} \cdot \mathbf{N} \,, \tag{4.47}$$

where $V = \frac{4}{3}\pi w_1 w_2 w_3$ and $\mathbf{N} = \left(\frac{\partial V}{\partial w_1}, \frac{\partial V}{\partial w_2}, \frac{\partial V}{\partial w_3}\right) = (w_2 w_3, w_1 w_3, w_1 w_2)$. Substituting in the equation for the rate of change of cell shape (4.46) gives

$$\left(\gamma\left(\bar{\mathbf{w}} - \mathbf{w}_j\right) + \beta \mathbf{S}_j - \mathbf{C}\right) \cdot \mathbf{N} = f(V) \tag{4.48}$$

$$\implies \mathbf{C} \cdot \mathbf{N} = (\gamma(\bar{\mathbf{w}} - \mathbf{w}_j) + \beta \mathbf{S}) \cdot \mathbf{N} - f(V) \tag{4.49}$$

$$\implies \mathbf{C} = \frac{[(\gamma(\overline{\mathbf{w}} - \mathbf{w}_j) + \beta \mathbf{S}) \cdot \mathbf{N} - f(V)]\,\mathbf{N}}{|\mathbf{N}|^2} \tag{4.50}$$

4.5.3 Boundary effects

Corneocytes at the surface of the epidermis provide a strong but flexible barrier between the body and the outside world. Although corneocytes are not explicitly included in any of our representations of the epidermis, we model their effects on keratinocytes in this discrete representation. In particular, corneocytes that are positioned beyond the boundary of this model's domain will exert squeezing forces on keratinocytes. In our model, this will to some extent restrict the growth of the epidermis beyond it's usual limits, but it is important to allow for a degree of epidermal thickening that occurs during wound healing; therefore, squeezing from the boundary is modelled using a different method than squeezing by other cells.

For each cell j, if any part of the cell is positioned beyond the boundary of the model domain then boundary forces will be applied. Forces are applied to the cell in each direction, proportional to the distance between the cell's extremity and the boundary. In this way, cells overlapping the boundary are squeezed and translated away from the boundary, but some overlap is still possible when forces from within the epidermis are sufficiently strong.

4.5.4 Cell growth

We now assume that cell volume, $V = \frac{4}{3}\pi w_1 w_2 w_3$, grows logistically with some inhibition due to crowding. Thus the rate of change of volume of a cell j is given by

$$\dot{V} = f(V) = r\left(1 - \frac{V}{V_{max}}\right)\left(\left(1 - \frac{2\sum_{k\neq j}\mathbf{F}_{jk}}{1 + 2\sum_{k\neq j}\mathbf{F}_{jk}}\right)^5 - 0.01\right) , \tag{4.51}$$

where V_{max} is the the maximum volume of a cell.

4.5.5 Cell division

Cells are prohibited from undergoing division until their volume exceeds $\frac{9}{10}V_{max}$, after which at each timestep they may divide with probability given by

$$p(\text{division}) = \frac{1}{200}(V - 1800) . \tag{4.52}$$

4.5.6 Active migration

Cell migration speed is inversely proportional to the squeezing forces felt by the cell, thus a cell will move in the direction of the smallest squeezing force if that force is sufficiently small. This allows cells at the front of the advancing epidermis to migrate most quickly. The migration rate is also scaled by a cell's distance from $z = 0$, the base of the simulated area; this follows the formulation of previous models, wherein cells closer to the basement membrane are considered more likely to express the integrins required to facilitate active migration [192]. When the a cell's active migration speed is greater than zero its growth is inhibited, as it would be energetically unlikely that both growth and migration could be sustained simultaneously. This in turn reduces the likelihood of migrating cells undergoing division.

4.5.7 Initial conditions

Cell positions are initialised on a regular lattice with a small random perturbation applied to each coordinate. Cell shapes are similarly set to the "natural" shape $\bar{\mathbf{w}}$ with small random perturbations applied. A central subset of cells is then removed to produce a "wound" in the layer, and the processes of growth, division and migration described in the previous sections are applied.

4.5.8 The effect of active migration

To investigate the effect of active migration on the system output, the migration speed (before correcting for cell position and potential) was varied to simulate passive migration only, a low migration rate and a high migration rate. The results are shown in Figure 4.24, where the first column undergoes diffusion only, the second column includes active migration at a low rate and the third column is the result of a high rate of active migration. Each column provides a visualisation of an individual simulation run, which is representative of the output of three runs.

When only passive diffusion is included the front of cells advance as a block; this is similar to the output of the limited domain model described in Table 3.2 and shown in Figure 4.19. As the migration speed is increased, the output becomes qualitatively more similar to that of the extended domain PDE system (4.24-4.26), with cells first forming a single, intact layer over the basement membrane, before filling in the supra-basal layers above.

4.5.9 Further work

We have shown that, depending on the migration speed employed, a discrete model of epidermal re-epithelialisation gives output similar to that of PDE models on a limited or extended spatial domain. However, this is more of a proof-of-concept study as extensive further work would be required to enable biological conclusions to be drawn from the output of the discrete model. The stochastic elements of the the discrete model result in a slightly different output each time the simulation is run. Therefore, to truly understand its behaviour the model must be run numerous times and solution behaviour averaged over all of the simulations. This is why only qualitative results are presented in Figure 4.24: whilst it is possible to determine the locations, sizes and proliferation rates of the cells, the values from one simulation run cannot be used to predict the quantitative behaviour of the overall system.

The number of parameters included in the system is much greater than that of the ODE or PDE approaches described previously. Whilst some can be determined experimentally (for example proliferation rates and cell dimensions) many do not represent measurable quantities (for example the correction factor by which migration should be scaled based on location) so need to be fitted. The sensitivity of the model output to variations in parameter values should also be investigated.

Using this form of agent based approach also introduces an additional parameter: the fixed timestep (which determines the number of time intrevals into which the total simulation time is divided). In established ABM models, changing the size of the timestep has been found to affect model output. Larger timesteps are more computationally efficient but, for simulations where equivalent analytical results are available for verification, have been found to lead to errors in the solutions produced [235, 236]. Therefore, timestep should also be included in subsequent sensitivity analysis.

Another limitation is the size of the domain over which the simulation is run. The wound that is simulated is very small compared to the average cell diameter, and is certainly not representative of a murine experimental wound. Therefore, the behaviour shown can be considered indicative of the early time behaviour of the system, but the long time dynamics over a larger wound radius cannot be inferred. Increasing the size of the domain increases computation time, which is particularly disadvantageous for systems where extensive parameter fitting is required.

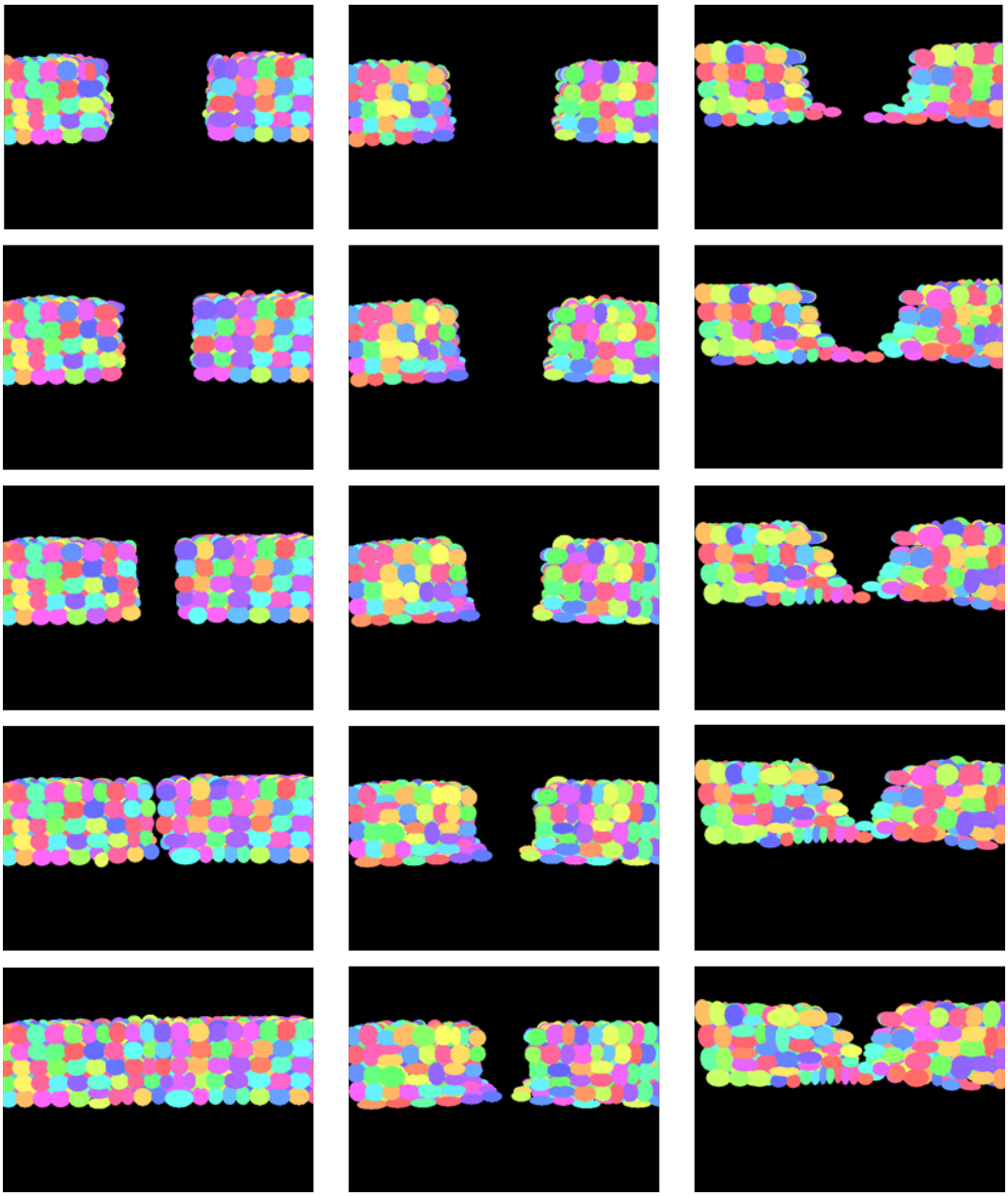

Figure 4.24: **The locations and dimensions of keratinocytes, as predicted by a discrete model of epidermal healing.** Qualitative output of the model described in Sections 4.5.2-4.5.7, for varying degrees of active migration: column 1 – diffusion only; column 2 – active migration at a low rate; column 3 – active migration at a high rate. Time increases from first to last row.

4.6 Discussion

Immunohistochemistry is a key technique used to investigate the effects of genetic variation and chemotherapeutic manipulation on epidermal healing dynamics [34, 237, 238, 239, 240]; however, such studies commonly collect data from a small number of experimental subjects at a limited number of timepoints. This is in part due to the limitations of murine cutaneous tissue histology, whereby multiple measurements of the same experimental subject cannot be made [241], but may also be attributed to the labour-intensive nature of manually quantifying cell numbers in stained tissue sections. We have developed and evaluated a semi-automated framework to expedite and standardise the process of quantification, and have proposed mathematical models that may be used to infer continuous healing dynamics from sparse data sets.

A previous study proposed a "medium throughput" method for quantifying epidermal re-epithelialisation and proliferation in *in vitro*, organotype cultures and use the resulting data to parameterise a computational model of healing [75]. We have developed a similar set of tools for use with *in vivo*, murine wounds. Neither quantification pipeline is fully automated, with both methodologies requiring manual extraction of the epidermal region; this represents a limitation in the size of datasets that can be analysed. However, compared with the time required to manually quantify the size of its various cell population (for example, as in [34]), determining the epidermal region is quick and straightforward as the staining provided clear delineation of the dermal-epidermal junction. This also reduces the level of subjectivity involved. Whilst the usage of organotype cultures is increasing [242, 243], mice are more commonly employed to study the cellular processes of epidermal repair [53, 145]; therefore the techniques that we have developed will provide a valuable addition to existing methodologies.

A significant limitation of our automated pipeline is its inability to successfully identify nuclei in large sections of healthy epidermis, both within hair follicles and IFE. In fact, that which makes the epidermis such a successful biological barrier – the tight packing of keratinocytes into cohesive layers – is partly responsible for its incompatibility with automated quantification of cell numbers. An additional problem is variations in brightness across large sections of tissue. These issues were not reported in the previous study, possibly because cell concentrations could be controlled in the organotype cultures [75].

Although we have focussed on determining the size of various keratinocyte populations, the set of images collected in this study could be used to quantify other features, for example

the thickness of the epidermis adjacent to the wound edge. Such measurements may be instructive in extending PDE models to include a spatially-varying keratinocyte carrying capacity. Given that integrin-α6 staining is not uniform across the epidermis (it is of higher intensity at the dermal-epidermal junction) this would be difficult to automate, but manual measurements could be taken at discrete spatial locations. Alternatively, a different epidermal marker may be more appropriate: for example, cytokeratin 14 and 10 could be used to stain basal and supra-basal keratinocytes respectively, which may lead to a more uniform fluorescence intensity [244].

It has been widely reported that keratinocyte proliferation occurs only in the intact skin surrounding a wound [102, 245, 246]; however, more recent data suggest that, whilst proliferation is initially confined to areas of intact skin, ki67 expression advances towards the centre of the wound as healing progresses, thus occurring in the extending epithelial tongue [75]. Our data support the latter claim, providing evidence using a transgenic approach that mitosis occurs within the wound.

Given that distributions of cell types within and around a wound cannot be established using non-invasive methods, and the ethical, financial and logistical considerations associated with *in vivo* studies, it is beneficial to develop methods that can predict intermediate points in the healing trajectory using relatively sparse experimental data sets [178]. We implemented three such methods: an ODE model, a PDE model and an ABM. The applications of multiple modelling approaches to the same biological system are rarely directly compared [247], and we have provided one such evaluation. Whilst the ODE model was the least computationally expensive to solve, its failure to explicitly include space in the model increased the number of parameters, particularly those that cannot be measured experimentally. This effect has been observed in ODE models of other spatial processes [248], and represents a significant limitation.

Murine experimental wounds of 4 mm diameter are useful tools for informing parameter estimation as experimental subjects are readily available [53], the surgical procedure is relatively straightforward to implement [241], and the epidermis is restored within 7 to 10 days so only short timecourses are required [107]. However, the fast rate of healing may contribute to the heterogeneity observed in healing outcomes, for example at 5 dpw (Figure 4.7). Averaging over multiple experimental subjects may mask extreme outcomes, especially where healing progression is so variable, so should be treated with caution when calculating parameter values and comparing output to experimental results. Models that do not use bespoke datasets to estimate parameters, but instead include values from different

areas of the literature, are even more susceptible to such heterogeneity [182, 183, 192]. In this study, we have illustrated the strength of conducting data collection alongside model formulation: an arrangement that is becoming more widespread [75, 249].

We observed similar descriptions of the locations of an advancing front of keratinocytes using both a limited-domain PDE [87], and an ABM in which cells migrate passively as a result of forces from other cells and the epidermal boundaries. This is not consistent with previously proposed ABM models, in which a thin epidermal "tongue is observed to extend into the wound space [192, 75]. However, our extended-domain PDE model produced output that was qualitatively distinct from that of limited-domain PDEs, and more in keeping with the results of previous ABMs and experimental studies [192, 75, 250]. Similar output was produced by an ABM in which cells at the wound edge could actively migrate; however, the active migration was not an emergent property of the ABM, but was instead imposed on the agents. Given that such a model cannot be implemented without making assumptions as to the mechanisms of migration, this represents a significant disadvantage of ABMs compared to the extended domain PDE. However, ABMs may be used to compare and contrast specific migratory mechanisms and test the assumptions underlying newly hypothesised cellular processes [75].

An aspect of healing that PDEs are not well placed to represent are spatial interactions between epidermal layers, particularly when there is no biological basis for feedback from supra-basal layers other than through volume-limiting effects on individual cells [92]. The discrete model that we have formulated is an advance over previous ABMs used to incorporate structure within the healing epidermis, as it represents cells as ellipsoids rather than non-deformable spheres [193]. This is particularly relevant in the upper layers of the epidermis and close to the wound edge, where cells become more flattened and elongated [216].

Implementing the ABM of epidermal repair is less straightforward than coding a PDE, and significant further work will be required to generate statistically robust output [202]. Both the PDE and ABM models presented do not give an explicit delineation of the wound edge, which must instead be inferred from cell concentrations. We have shown that the choice of threshold for what constitutes "healed" epidermis has a significant impact on the qualitative form of the healing trajectories. There is little biological consensus about when a re-forming epidermis is considered repaired: it could be when a single layer of keratinocytes forms an intact barrier, when a multi-layered structure is formed, or even when unviable corneocytes are first present in the wound space (indicating that the process of cell differentiation is

under way). Standardising the criterion across biological and computational studies would be advantageous for both experimentalists and theoreticians.

Chapter 5

A partial differential equation model of fibroblast and collagen orientation during dermal wound repair

5.1 Introduction and aims

Scar tissue formation is an important phase of the wound healing response, the results of which can have profound effects on the viability and functionality of the skin. The dermis is made up of an ECM composed primarily of collagen fibres, which are synthesised by fibroblasts – the predominant cell type of dermal tissue. After cutaneous wounding, fibroblasts infiltrate the wound area and produce collagen to restore tissue integrity. However, the structure and functionality of the scar tissue is quite different to that of healthy skin: scar tissue has fewer blood vessels [251] but increased numbers of microvessels [46]; denser, less elastic connective tissue [252]; greater collagen density with larger collagen fibres [253]; a different ratio of collagen types [254, 255]; a lack of sweat glands and hair follicles [256]; and increased collagen alignment compared to normal tissue [257, 258]. The latter is thought to be the most significant difference, which is primarily responsible for reduced functionality of scar tissue. Viable skin contains collagen in a mesh structure, whereas collagen in scar tissue is aligned in a more parallel fashion [258]. The processes of dermal healing directly affect the composition of scar tissue and orientation of its components, with dysregulation of these processes causing conditions such as keloids and hypertrophic scarring [259].

Several elements of the healing response affect the orientation of collagen fibres in scar tissue. Fibroblasts have been observed to deposit collagen fibres in the direction in which they are migrating [260], and also to reorient existing fibres towards a cell's trajectory [261]. Analogously, fibroblasts in culture tend to orient themselves in the direction of collagen alignment, an effect that may be ascribed to the comparative ease with which fibroblasts can migrate along fibres rather than through the surrounding ECM substrate [262]. Additionally, fibroblasts have been observed to align in the direction of chemoattractants known to be present in the wound space, predominantly PDGF but also including EGF, FGF, KGF and TGF-β [263]. Finally, tissue-wide deformation may result from initial wound edge retraction, movement-associated mechanics of the skin and surgical interventions such as suturing [264, 265]; such deformation will have a global influence on the orientation of the fibres and cells within a wound.

A range of modelling approaches have been employed to describe how the orientations of fibroblasts and collagen fibres evolve over space and time (see Section 5.2). Most previous studies have focussed on the predominant orientation of fibres at a particular point in space and time [266, 267, 268, 269]; however, whether fibres are parallel or perpendicular is a defining characteristic of scar versus normal tissue, and hence considering averages may be inappropriate. Probabilistic methods have also been used to characterise distributions of orientations using tensorial approaches, based on the fibres' predominant direction and its perpendicular counterpart [270, 271]. This limits the types of distributions that can be represented: in particular, non-symmetric (skewed) distributions are not possible under this framework. Additionally, fibroblasts are frequently represented as discrete points or discs; this allows their direction of movement to be represented, from which orientation can be inferred, but disregards the elongated morphology of individual cells [272, 267, 268, 269, 270]. We aim to formulate a probabilistic model for distributions of orientations of both collagen and fibroblasts, which may better describe the organisation of fibres in scar tissue and does not limit the shape of distribution that can be produced. We will propose methods for approximating solutions of the model, and will compare output for a range of parameter values. Finally, possible modifications of and extensions to the model will be suggested.

5.2 Models of collagen fibre orientation

A range of models have been previously used to investigate the orientation of ECM fibres in healthy and healing tissue, incorporating a variety of different components and modelling techniques. Early work modelled the effects of cells and fibres on ECM alignment using

reaction-diffusion equations. In particular, the proportions of fibres predominantly aligned parallel with and perpendicular to the plane of the skin were predicted, with fibres transitioning between the two directions in response to a flux of fibroblasts [266]. It was found that contact guidance of cells along fibres increased the speed of healing and the degree of fibre alignment. Restricting the model to two predominant angles made the solutions tractable, but less general than approaches that consider a continuous orientation space. A subsequent extension incorporated ECM alignment induced by tissue-wide mechanical stress in combination with the effects of cell flux, and included two types of ECM fibre with different alignment properties; however, interactions between the two fibre networks were not modelled [272]. Differences in micro- and macroscopic properties of the fibre alignment patterns were observed, indicating that models incorporating effects at both scales may be most relevant.

An alternative approach used integro-differential equations to describe interactions between cells and fibres, with fibre density determined over a continuum of angles from an arbitrary reference direction [273]. Feedback between collagen fibres and fibroblasts determined the orientation of fibres and the concentrations of fibres and cells. Steady states representing healthy and scar tissue were both found to be stable for the same parameters, with the initial conditions of fibre orientation determining which of the steady states formed. Further work modelled cells as discrete entities described by their paths, and fibres as a continuous vector field where the direction of the vector at a particular point in space and time represented the predominant fibre orientation [267]. The model considered the local effects of cell movement on ECM fibre orientation, with cell motility modelled as a balance between directional cues received from fibres and persistence in their own direction. The model output suggested cell flux as the most significant alignment mechanism, although cell speed, polarisation and concentration, as well as the initial alignment of fibres, were also influential.

A subsequent extension included spatial variation in the fibroblast population in two dimensions, and focused on the initial deposition of collagen in the wound space [268]. The model was used to investigate the effects of experimental interventions, including blocking fibroblast entry at the subcutaneous fascia, enhancing cell division and altering the collagen production and degradation rates; findings were used to hypothesise the mode of action of anti-scarring therapies, in particular TGF-β. However, all of these studies considered only solutions for the alignment of fibres taking the form of isolated peaks in orientation space, with spatial variation simply shifting the position of the peak.

A similar approach, based on a continuous vector field representation of ECM fibre ori-

entation and a discrete model of cell behaviour, was used to investigate the effects of a chemoattractant on ECM composition [269]. Cell migration paths were modelled as stochastic processes that respond to the gradient of a chemoattractant, which was modelled on a continuum. However, solutions were only calculated in the context of an intact ECM, and model equations were not used to explicitly represent processes occurring in a wound space.

The effect of the chemoattractant TGF-β was also considered in a six-species model, which included fibrin, collagen, macrophages, fibroblasts, TGF-β and tissue plasminogen activator (tPA) [270]. The orientation of a fibre network (made up of collagen and fibrin) was represented using a tensorial approach, and PDEs were used to model changes to their concentrations as a result of deposition by fibroblasts and degradation by tPA. Cells were represented as discrete individuals, but with ODEs modelling cellular processes such as cell receptor binding by cytokines and chemotactic bias. The dynamics of TGF-β and tPA were modelled using PDEs. This allowed an investigation of the effects of reducing TGF-β expression, TGF-β diffusion rate and the availability of cytokine receptors on fibroblasts on the rate of healing at various timepoints. The degree of scarring (determined by the degree of alignment of the fibre network) was also analysed, finding that stochastic effects on cell behaviour in the discrete portion of the model were more closely associated with overall alignment of the fibre network than effects such as TGF-β concentration and fibre density. When results were averaged over multiple simulations, collagen in healed tissue was found to be less aligned when the proportion of cytokine receptors on fibroblasts was reduced.

A similar tensorial approach was also used to investigate a scenario whereby a portion of newly produced collagen was deposited in alignment with fibroblast movement, and the rest was deposited by ratio in the direction of the present collagen bundles [271]. This allowed a degree of "persistence" of collagen alignment to be maintained explicitly, rather than indirectly through contact guidance between collagen and fibroblasts. The tissue-level effects of wound contraction were also incorporated, and the effects of collagen alignment on the bulk mechanical behaviour were ascertained, finding that the initial distribution of collagen bundles had the greatest impact on the wound shape and degree of contraction during healing.

Fibre orientation has also been represented using discrete models, whereby tissue structure is determined on individual grid spaces; these models can be combined with continuous descriptions of chemokine gradients and tissue mechanics but have only been applied to the study of myocardial infarcts, which operate in a very different geometry to cutaneous wounds [274, 275, 276].

Table 5.1: **Variables included in the model for dermal healing.**

Variable	Description
$\hat{\mathbf{p}} = \mathbf{p} = (\cos\theta, \sin\theta)$	Fibroblast orientation vector ($0 \leq \theta < 2\pi$)
$f = f(x, y, \theta, t)$	Fibroblast PDF over θ at position (x, y) and time t
$\dot{\mathbf{p}}$	Fibroblast mean rotational drift (torque balance)
$\hat{\mathbf{q}} = \mathbf{q} = (\cos\phi, \sin\phi)$	Collagen orientation vector ($0 \leq \phi < \pi$)
$g = g(x, y, \phi, t)$	Collagen PDF over ϕ at position (x, y) and time t
$\dot{\mathbf{q}}$	Collagen mean rotational drift (torque balance)

5.3 Equations for the orientations of fibroblasts and collagen in a dermal wound

Our model describes two aspects of collagen fibres and fibroblasts in and around the wound region: their orientation, given by a vector describing the angle between the component and the horizontal; and a probability density function (PDF) describing the probability of each component lying at any given angle, as a function of space and time (see Table 5.1.)

A Fokker-Planck equation is a PDE that represents the evolution of a PDF over time [277]; they are commonly used to describe and predict the properties of stochastic systems, such as the probability density of Brownian particles [278]. Whilst the Fokker-Planck equation does not well represent the behaviour of individual cells, it is useful in predicting the overall distribution of a cell population. In particular, Fokker-Planck equations have been applied to the study of cell migration in the context of swimming cells [279] and tissue-resident cells such as granulocytes [280]. The Fokker-Planck equation describing the PDF of orientations of fibroblasts, f, follows the general form [277]:

$$\frac{\partial f}{\partial t} + \boldsymbol{\nabla}_\theta \cdot (\dot{\mathbf{p}} f) = D_f \boldsymbol{\nabla}_\theta^2 f \ , \tag{5.1}$$

where the left hand side describes deterministic changes to orientation, for example as a result of chemotaxis or substrate rotation, and the right hand side represents stochastic changes.

The system we describe is written such that it can be generalised to three dimensions; however, when generating solutions we consider only the 2D case, with one angle describing the orientation of each cell or fibre. This is a similar approach to a study of gyrotactic micro-organisms, which considered motion only in a 2D vertical plane in order to reduce computation time and facilitate comparison between individual-based and population level models [281]. Simpler models investigating swimming cells have used a spherical polar coordinate system to represent orientation in three dimensions [279, 282, 283]; however, such models include only one species of cell and investigate how their swimming behaviour interacts with outside influences such as surrounding flows. The model we propose involves a set of coupled equations to describe fibroblasts and collagen fibres, with the two populations interacting with each other and their environment to determine their distributions of orientation. Simplifying to a 2D geometry allows analytical solutions for the resulting coupled coefficients to be generated, which would take a prohibitively large amount of computational time in the 3D case. 2D representations have also been justified by noting that the depth of a cutaneous wound is small compared to its diameter [35]. However, care should be taken when considering orientation space, as a cell or fibre affected by a 2D flow will have a non-zero probability of being oriented out of the plane of the flow [279]. Therefore, a significant limitation of our 2D simplification is that the effects of tissue mechanics, and in particular 2D shear, on cells and fibres may not be fully represented around a single axis of orientation.

The deterministic portion of the the Fokker-Planck equation depends on the mean rotational drift of a fibroblast, $\dot{\mathbf{p}}$, which is a unit vector that satisfies

$$\dot{\mathbf{p}} = \boldsymbol{\pi}_p \times \mathbf{p} \,, \tag{5.2}$$

where

$$\boldsymbol{\pi}_p = [\chi_p \boldsymbol{\nabla}\beta] \times \mathbf{p} + \frac{1}{2}(\boldsymbol{\nabla} \times \mathbf{v}) - \left[\left[\alpha_f \dot{\mathbf{E}} - \int_0^\pi k_f \frac{G}{G_0} g \mathbf{pp} \, \mathrm{d}\phi\right] \cdot \mathbf{p}\right] \times \mathbf{p} \,. \tag{5.3}$$

This equation takes essentially the same form as presented by Pedley and Kessler (1990) [284], which has subsequently been employed in the study of gyrotaxis in swimming cells [285, 286, 287, 288]. In this representation, the expression in brackets in the first term takes the form of a pendulum-like effective torque, the second term describes a constant rotational effect, whilst the inner bracket in the final term describes an effective rate of strain, following [284].

Regrouping the terms of $\boldsymbol{\pi}_p$ highlights their effect on the reorientation of a cell:

$$\boldsymbol{\pi}_p = k_f \frac{G}{G_0} \int_0^\pi \mathbf{R}_f \left(\mathbf{p}, \mathbf{q}\right) g \, \mathrm{d}\phi + \chi_p \left(\boldsymbol{\nabla}\beta \times \mathbf{p}\right) + \frac{1}{2}(\boldsymbol{\nabla} \times \mathbf{v}) - \alpha_f \left(\left(\dot{\mathbf{E}} \cdot \mathbf{p}\right) \times \mathbf{p}\right) \,. \tag{5.4}$$

The first term describes the tendency for fibroblasts to align with the collagen matrix, where k_f is the coefficient of contact guidance. G represents the concentration of collagen in the wound space. The maximum possible collagen concentration is given by G_0; multiplying by the pre-factor $\frac{G}{G_0}$ represents the assumption that higher collagen density leads to increased contact guidance. We assume that $\mathbf{R}_f(\mathbf{p},\mathbf{q})$ takes the form $(\mathbf{p}\cdot\mathbf{q})(\mathbf{p}\times\mathbf{q})$, where the dot product describes the magnitude of the effect, and the cross product between $\mathbf{p}$ and $\mathbf{q}$ describes the torque. Finally, we integrate over the entire distribution of collagen orientations so that the effects of all fibres (including those that are not aligned towards the predominant direction) still affect the orientation of fibroblasts. The second term represents the rotation of fibroblasts in response to a chemotactic gradient, $\boldsymbol{\nabla}\beta$, where χ_p is the coefficient of chemotactic rotation. The effect shearing forces (resulting from displacement) in the provisional ECM (pECM) are described by the third and fourth terms. Shear can be decomposed into a rotational effect and an effect of strain; the effect of the rotation on the alignment of fibroblasts is given by the third term, where $\mathbf{v}$ denotes the velocity of the pECM. The final term describes the effect of pECM strain, where $0 \leq \alpha_f < 1$ represents the cell eccentricity, given by the square of the third eccentricity $\alpha_f = \frac{b^2-a^2}{b^2+a^2}$ where a is the length of the semi-major axis, and b is the length of the semi-minor axis (giving $\alpha_f = 0$ for a spherical cell and $\alpha_f \to 1$ for very elongated cells). The local rate of strain tensor is given by $\dot{\mathbf{E}}$, and $(\dot{\mathbf{E}}\cdot\mathbf{p})$ describe the ideal directions of $\mathbf{p}$. This term is a leading order approximation; due to the elongated and asymmetric nature of fibroblasts other effects may also be present, however it is expected that these will be comparatively small.

Equations for collagen orientation are formulated similarly, with the PDF over orientation space satisfying the Fokker-Planck equation

$$\frac{\partial g}{\partial t} + \boldsymbol{\nabla}_\phi \cdot (\dot{\mathbf{q}} g) = D_g \boldsymbol{\nabla}_\phi^2 g \, . \tag{5.5}$$

The coefficient of stochastic diffusion of collagen, D_g, will be smaller than that of fibroblasts, D_f, as collagen fibres are more strongly fixed and don't survey their environment for directional cues as fibroblasts do. The mean rotational drift of a collagen fibre is given by $\dot{\mathbf{q}} = \boldsymbol{\pi}_q \times \mathbf{q}$, where

$$\boldsymbol{\pi}_q = k_g \frac{F}{F_0} \int_0^{2\pi} \mathbf{R}_f(\mathbf{q},\mathbf{p}) \; f \, \mathrm{d}\theta + \frac{1}{2}(\boldsymbol{\nabla}\times\mathbf{v}) - \alpha_g \left(\left(\dot{\mathbf{E}} \cdot \mathbf{q} \right) \times \mathbf{q} \right) \, . \tag{5.6}$$

This is analogous to equation (5.4) for the rotation of a fibroblast, except that collagen fibres do not respond to chemotactic gradients. The first term describes the active remodelling of collagen by fibroblasts, which is proportional to fibroblast density, F, (scaled by the maximum possible fibroblast density, F_0) but occurs at a slower rate than fibroblasts aligning with collagen, and hence $k_g << k_f$.

We aim to generate closed-form approximations of the PDFs f and g, which may be achieved by expressing the PDFs as Fourier series. This is an appropriate approach as we expect periodic solutions (between 0 and 2π for fibroblasts and 0 and π for collagen fibres), for which Fourier series provide a natural basis. This method is equivalent to the expansion in spherical harmonics that has previously been employed to generate solutions to the Fokker-Planck equation in a 3D geometry [279]. The Fourier series representations of the PDFs take the forms

$$f(\theta,t) = a_0(t) + \sum_{n=1}^{\infty} \left[a_n(t)\cos(n\theta) + b_n(t)\sin(n\theta)\right] \ , \tag{5.7}$$

$$g(\phi,t) = c_0(t) + \sum_{n=1}^{\infty} \left[c_{2n}(t)\cos(2n\phi) + d_{2n}(t)\sin(2n\phi)\right] \ . \tag{5.8}$$

The normalisation conditions, $\int_0^{2\pi} f(\theta)\,\mathrm{d}\theta = 1$ and $\int_0^{\pi} g(\phi)\,\mathrm{d}\phi = 1$, imply that $a_0(t) = a_0 = \frac{1}{2\pi}$ and $c_0(t) = c_0 = \frac{1}{\pi}$.

To evaluate the integrals in the first terms of equations (5.4) and (5.6) for the mean rotational drift of fibroblasts and collagen fibres, we substitute in the Fourier series for f and g and the definitions $\mathbf{p} = (\cos\theta, \sin\theta)$ and $\mathbf{q} = (\cos\phi, \sin\phi)$, which gives

$$I_f = \int_0^{\pi} (\mathbf{p}\cdot\mathbf{q})(\mathbf{p}\times\mathbf{q}) \times \mathbf{p}\, g\,\mathrm{d}\phi = \frac{\pi}{4}\left(d_2\cos(2\theta) - c_2\sin(2\theta)\right)\hat{\boldsymbol{\theta}}_p \ , \tag{5.9}$$

$$I_g = \int_0^{2\pi} (\mathbf{p}\cdot\mathbf{q})(\mathbf{q}\times\mathbf{p}) \times \mathbf{q}\, f\,\mathrm{d}\theta = \frac{\pi}{2}\left(b_2\cos(2\phi) - a_2\sin(2\phi)\right)\hat{\boldsymbol{\phi}}_q \ , \tag{5.10}$$

where $\hat{\boldsymbol{\theta}}_p = (-\sin\theta, \cos\theta)$ and $\hat{\boldsymbol{\phi}}_q = (-\sin\phi, \cos\phi)$.

We assume that the tissue undergoing strain effects is incompressible, which gives

$$\mathrm{Tr}(\dot{\mathbf{E}}) = 0 \ , \tag{5.11}$$

as the divergence of the tissue velocity is zero. The vectors $\mathbf{p}$ and $\mathbf{q}$ are of unit length with directions perpendicular to the unit circle, and hence $\boldsymbol{\nabla}_\theta s$ is perpendicular to $\mathbf{p}$ for any function $s = s(\mathbf{p})$, and equivalently for functions of $\mathbf{q}$. This gives

$$(\mathbf{p}\cdot\boldsymbol{\nabla}_\theta)s = 0 \quad \text{for } s = s(\mathbf{p}) \ , \tag{5.12}$$

$$(\mathbf{q}\cdot\boldsymbol{\nabla}_\theta)s = 0 \quad \text{for } s = s(\mathbf{q}) \ . \tag{5.13}$$

For a cylindrical system we also have, by direct calculation,

$$\boldsymbol{\nabla}_\theta\cdot\mathbf{p} = \boldsymbol{\nabla}_\theta\cdot\mathbf{q} = 1 \ , \tag{5.14}$$

$$\boldsymbol{\nabla}_\theta\mathbf{p} = \mathbf{I} - \mathbf{pp} \ , \tag{5.15}$$

$$\boldsymbol{\nabla}_\theta\mathbf{q} = \mathbf{I} - \mathbf{qq} \ , \tag{5.16}$$

$$\boldsymbol{\nabla}_\theta\times\mathbf{p} = \boldsymbol{\nabla}_\theta\times\mathbf{q} = 0 \ , \tag{5.17}$$

and we define

$$\chi_p \boldsymbol{\nabla}\beta \coloneqq B \begin{pmatrix} \cos(\theta_\beta) \\ \sin(\theta_\beta) \end{pmatrix} \ , \quad \boldsymbol{\nabla}_\theta \mathbf{v} \coloneqq \boldsymbol{\Omega} = \Omega \mathbf{k} \ ,$$

where θ_β represents the angle of the direction of chemoattractant from the horizontal axis.

Substituting these expressions into the second terms of the Fokker-Planck equations (5.1) and (5.5) gives:

$$\begin{aligned} \boldsymbol{\nabla}_\theta \cdot (\dot{\mathbf{p}} f) = \frac{\pi}{4} \frac{G}{G_0} k_f \left[\frac{\partial f}{\partial \theta} \left(d_2 \cos(2\theta) - c_2 \sin(2\theta) \right) - 2f \left(d_2 \sin(2\theta) + c_2 \cos(2\theta) \right) \right] \\ + B \left[\frac{\partial f}{\partial \theta} \left(-\cos(\theta_\beta)\sin(\theta) + \sin(\theta_\beta)\cos(\theta) \right) - f \left(\cos(\theta_\beta)\cos(\theta) + \sin(\theta_\beta)\sin(\theta) \right) \right] \\ + \frac{1}{2}\Omega \frac{\partial f}{\partial \theta} - \alpha_f \left[\frac{\partial f}{\partial \theta} \left(-\sin(2\theta) E_{11} + \cos(2\theta) E_{12} \right) - 2f \left(\cos(2\theta) E_{11} + \sin(2\theta) E_{12} \right) \right] , \end{aligned} \tag{5.18}$$

$$\begin{aligned} \boldsymbol{\nabla}_\phi \cdot (\dot{\mathbf{q}} g) = \frac{\pi}{2} \frac{F}{F_0} k_g \left[\frac{\partial g}{\partial \phi} \left(b_2 \cos(2\phi) - a_2 \sin(2\phi) \right) - 2g \left(a_2 \cos(2\phi) + b_2 \sin(2\phi) \right) \right] \\ + \frac{1}{2}\Omega \frac{\partial g}{\partial \phi} - \alpha_g \left[2g \left(\cos(2\phi) E_{11} + \sin(2\phi) E_{12} \right) - \frac{\partial g}{\partial \phi} \left(-E_{11} \sin(2\phi) + E_{12} \cos(2\phi) \right) \right] . \end{aligned} \tag{5.19}$$

The system is coupled by the second order Fourier coefficients, which are the only coefficients that remain when the integrations (5.9-5.10) are computed.

The movement and reorientation of fibroblasts occurs at a much faster rate than that of collagen fibres. *In vitro* experiments have shown that normal human dermal fibroblasts can migrate through collagen gels at a rate of $0.234 \pm 0.09\,\mu\text{m/min}$ [289], can reorient in response to collagen contact guidance within 12-48 hours (depending on the uniformity of the collagen distribution) [262], and can reorient in response to a chemoattractant within 36 hours [263]. By contrast, collagen displacement by fibroblasts occurs at a rate one order of magnitude lower, measured as $0.02 \pm 0.0035\,\mu\text{m/min}$ and $0.08 \pm 0.02\,\mu\text{m/min}$ in two independent studies [261, 290]. The speed of collagen reorientation has not been measured independently from displacement *in vitro*, but it is known that collagen reorientation occurs on a timescale of months in porcine skin [291]. Therefore, due to the differences in timescales we can consider the Fokker-Planck equation for fibroblast orientation (5.1) to be at steady state, and hence neglect its first term. The system (5.1, 5.5) then becomes

$$\boldsymbol{\nabla}_\theta \cdot (\dot{\mathbf{p}} f) = D_f \boldsymbol{\nabla}_\theta^2 f \ , \tag{5.20}$$

$$\frac{\partial g}{\partial t} + \boldsymbol{\nabla}_\phi \cdot (\dot{\mathbf{q}} g) = D_g \boldsymbol{\nabla}_\phi^2 g \ . \tag{5.21}$$

Substituting the expressions for the deterministic terms, (5.18) and (5.19), into the system (5.20-5.21) gives the Fokker-Planck equation for the probability density function of fibroblast

orientations as

$$\begin{aligned}
&\frac{\pi}{4}\frac{G}{G_0}k_f\left[\frac{\partial f}{\partial\theta}\left(d_2\cos(2\theta)-c_2\sin(2\theta)\right)-2f\left(d_2\sin(2\theta)+c_2\cos(2\theta)\right)\right]\\
&+B\left[\frac{\partial f}{\partial\theta}\left(-\cos(\theta_\beta)\sin(\theta)+\sin(\theta_\beta)\cos(\theta)\right)-f\left(\cos(\theta_\beta)\cos(\theta)+\sin(\theta_\beta)\sin(\theta)\right)\right]\\
&+\frac{1}{2}\Omega\frac{\partial f}{\partial\theta}-\alpha_f\left[\frac{\partial f}{\partial\theta}\left(-\sin(2\theta)E_{11}+\cos(2\theta)E_{12}\right)-2f\left(\cos(2\theta)E_{11}+\sin(2\theta)E_{12}\right)\right]\\
&=D_f\frac{\partial^2 f}{\partial\theta^2}\,,
\end{aligned}\tag{5.22}$$

and the Fokker-Planck equation for the probability density function of collagen orientations as

$$\begin{aligned}
&\frac{\partial g}{\partial t}+\frac{\pi}{2}\frac{F}{F_0}k_g\left[\frac{\partial g}{\partial\phi}\left(b_2\cos(2\phi)-a_2\sin(2\phi)\right)-2g\left(a_2\cos(2\phi)+b_2\sin(2\phi)\right)\right]\\
&+\frac{1}{2}\Omega\frac{\partial g}{\partial\phi}-\alpha_g\left[2g\left(\cos(2\phi)E_{11}+\sin(2\phi)E_{12}\right)-\frac{\partial g}{\partial\phi}\left(-E_{11}\sin(2\phi)+E_{12}\cos(2\phi)\right)\right]\\
&=D_g\frac{\partial^2 g}{\partial\theta^2}\,.
\end{aligned}\tag{5.23}$$

5.3.1 Non-dimensionalisation

Equations (5.22-5.23) can be non-dimensionalised to reduce the number of parameters involved and facilitate the analysis of changes to the ratios of competing effect sizes. Ω and $\dot{\mathbf{E}}$ are non-dimensionalised with respect to a typical voticity scale Ω_0, such that $\omega=\Omega/\Omega_0$ and $\mathbf{e}=\dot{\mathbf{E}}/\Omega_0$, giving

$$\begin{aligned}
&\frac{\pi}{4}\frac{G}{G_0}k_f\left[\frac{\partial f}{\partial\theta}\left(d_2\cos(2\theta)-c_2\sin(2\theta)\right)-2f\left(d_2\sin(2\theta)+c_2\cos(2\theta)\right)\right]\\
&+B\left[\frac{\partial f}{\partial\theta}\left(-\cos(\theta_\beta)\sin(\theta)+\sin(\theta_\beta)\cos(\theta)\right)-f\left(\cos(\theta_\beta)\cos(\theta)+\sin(\theta_\beta)\sin(\theta)\right)\right]\\
&+\frac{1}{2}\omega\Omega_0\frac{\partial f}{\partial\theta}-\alpha_f\Omega_0\left[\frac{\partial f}{\partial\theta}\left(-\sin(2\theta)e_{11}+\cos(2\theta)e_{12}\right)-2f\left(\cos(2\theta)e_{11}+\sin(2\theta)e_{12}\right)\right]\\
&=D_f\frac{\partial^2 f}{\partial\theta^2}\,.
\end{aligned}\tag{5.24}$$

Dividing through by the characteristic rate, which we take to be the rate at which fibroblasts align with collagen fibres, k_f, gives the non-dimensional equation

$$\begin{aligned}
&\gamma_f\left[\frac{\partial f}{\partial\theta}\left(d_2\cos(2\theta)-c_2\sin(2\theta)\right)-2f\left(d_2\sin(2\theta)+c_2\cos(2\theta)\right)\right]\\
&+\kappa_f\left[\frac{\partial f}{\partial\theta}\left(-\cos(\theta_\beta)\sin(\theta)+\sin(\theta_\beta)\cos(\theta)\right)-f\left(\cos(\theta_\beta)\cos(\theta)+\sin(\theta_\beta)\sin(\theta)\right)\right]\\
&+\omega\eta_f\frac{\partial f}{\partial\theta}-2\alpha_f\eta_f\left[\frac{\partial f}{\partial\theta}\left(-\sin(2\theta)e_{11}+\cos(2\theta)e_{12}\right)-2f\left(\cos(2\theta)e_{11}+\sin(2\theta)e_{12}\right)\right]\\
&=\lambda_f\frac{\partial^2 f}{\partial\theta^2}\,,
\end{aligned}\tag{5.25}$$

where

$$\gamma_f=\frac{\pi G}{4G_0},\quad \kappa_f=\frac{B}{k_f}\quad,\quad \eta_f=\frac{\Omega_0}{2k_f}\quad\text{and}\quad \lambda_f=\frac{D_f}{k_f}\,,\tag{5.26}$$

are dimensionless parameters. The parameter γ_f describes the concentration of collagen in the wound space compared to that of unwounded skin. This, along with the initial conditions, can be used to determine the phase of healing represented by the model. The ratio of rates of alignment with collagen and a chemoattractant is represented by κ_f, which is likely to be biologically relevant, particularly when comparing different biochemical signalling pathways. Similarly, λ_f represents the ratio of the stochastic reorientation rate and the rate of alignment with collagen; and η_f compares the rate of tissue rotation with that of alignment with collagen.

In the Fokker-Planck equation for collagen orientation, time is non-dimensionalised with respect to a typical timescale T, such that $\tau = t/T$. The other terms are manipulated analogously to those in equation (5.25), giving the non-dimensional Fokker-Planck equation for collagen orientation as

$$\psi_g \frac{\partial g}{\partial \tau} + \gamma_g \left[\frac{\partial g}{\partial \phi} \left(b_2 \cos(2\phi) - a_2 \sin(2\phi) \right) - 2g \left(a_2 \cos(2\phi) + b_2 \sin(2\phi) \right) \right] + \omega \eta_g \frac{\partial g}{\partial \phi}$$
$$-2\alpha_g \eta_g \left[2g \left(\cos(2\phi) e_{11} + \sin(2\phi) e_{12} \right) - \frac{\partial g}{\partial \phi} \left(-e_{11} \sin(2\phi) + e_{12} \cos(2\phi) \right) \right] = \lambda_g \frac{\partial^2 g}{\partial \phi^2} \, , \tag{5.27}$$

with dimensionless parameters

$$\psi_g = \frac{1}{k_g T}, \quad \gamma_g = \frac{\pi F}{2F_0}, \quad \eta_g = \frac{\Omega_0}{2k_g} \quad \text{and} \quad \lambda_g = \frac{D_g}{k_g} \, . \tag{5.28}$$

Time is scaled by the reciprocal of the rate at which fibroblasts reorient collagen, giving the parameter ψ_g. The other three parameters are equivalent to those for the fibroblast equation described previously (5.26), but scaled by the maximum concentration of fibroblasts and the rate at which fibroblasts reorient collagen.

5.4 Solutions to the steady state Fokker-Planck equation for fibroblast orientation

The non-dimensional steady state Fokker-Planck equation for fibroblast orientation given in (5.25) may be solved to give expressions for the Fourier coefficients a_n and b_n. The Fourier series representation of the PDF is truncated at a given value, producing a system of $2t_{order}$ equations which are used to approximate the Fokker-Planck equation. The solutions of these equations give expressions for a_n and b_n ($n = 1 \dots t_{order}$). A full description of the method employed is presented in Appendix 1.

These solutions can be used to investigate the effect of truncation order on the values of the Fourier coefficients, and to show how the PDF for fibroblast orientation f behaves under a range of parameter values.

5.4.1 Collagen contact guidance and stochastic reorientation

We first investigate solution behaviour where the only effects in the non-dimensional Fokker-Planck equation (5.25) are that of fibroblasts aligning themselves with collagen fibres and undergoing random reorientation; that is to say $\kappa_f = 0$ and $\eta_f = 0$ so that on the left hand side of equation (5.25) only the first term remains. Initially we assume that collagen is at its maximum density, so $\gamma_f = \frac{\pi}{4}$, and that collagen is distributed so that its mean orientation is towards $\phi = \frac{\pi}{8}$, which is achieved by setting $c_2 = d_2 = 0.2$. We generate solutions for the Fourier coefficients a_n and b_n for truncation orders from 2 to 8 and for values of λ_f from 0 to 1.

The odd Fourier coefficients a_1, a_3, a_5, a_7 and b_1, b_3, b_5, b_7, are zero for truncation orders up to 8 and with $0 \leq \lambda_f \leq 1$. At truncation orders 4 to 7 the coefficient a_4 is zero for $0 \leq \lambda_f \leq 1$; at truncation order 8 the order of magnitude of a_4 is 10^{-12}, so this coefficient may also be neglected. Additionally, for $\lambda_f > 0.075$ the coefficients a_6 and b_6 are of order 10^{-2}, and tend rapidly to zero with increasing λ_f (Figure 5.1c-d), suggesting that these coefficients may be omitted for all but very small values of λ_f. Coefficients a_2 and b_2 are equal because the collagen distribution with which the fibroblasts align is oriented such that $c_2 = d_2$; different predominant directions of collagen alignment would give $a_2 \neq b_2$. Figure 5.1a-b shows that the solutions for a_2, b_2 and b_4 at truncation order 4 provide good approximations to higher truncation orders for $\lambda_f > 0.075$. Additionally, for $\lambda_f > 0.2$ the coefficient b_4 is negligibly small, so can also be omitted (Figure 5.1b).

In summary, when fibroblast orientation is only affected by alignment with a distribution of collagen fibres and stochastic reorientation, the probability density function of the distribution of fibroblast orientations can be approximated as

$$f \approx \frac{1}{2\pi} + a_2 \cos(2\theta) + b_2 \sin(2\theta) + b_4 \sin(4\theta) \quad \text{when} \quad 0.075 < \lambda_f < 0.2 \,, \tag{5.29}$$

$$f \approx \frac{1}{2\pi} + a_2 \cos(2\theta) + b_2 \sin(2\theta) \quad \text{when} \quad \lambda_f > 0.2 \,, \tag{5.30}$$

for $a_2 = a_2(c_2, d_2)$, $b_2 = b_2(c_2, d_2)$ and $b_4 = b_4(c_2, d_2)$.

When the coefficients a_2, b_2 and b_4 are substituted into the Fourier expression for f (5.7) solutions for the PDF of fibroblast orientation are produced: Figure 5.2a shows Cartesian

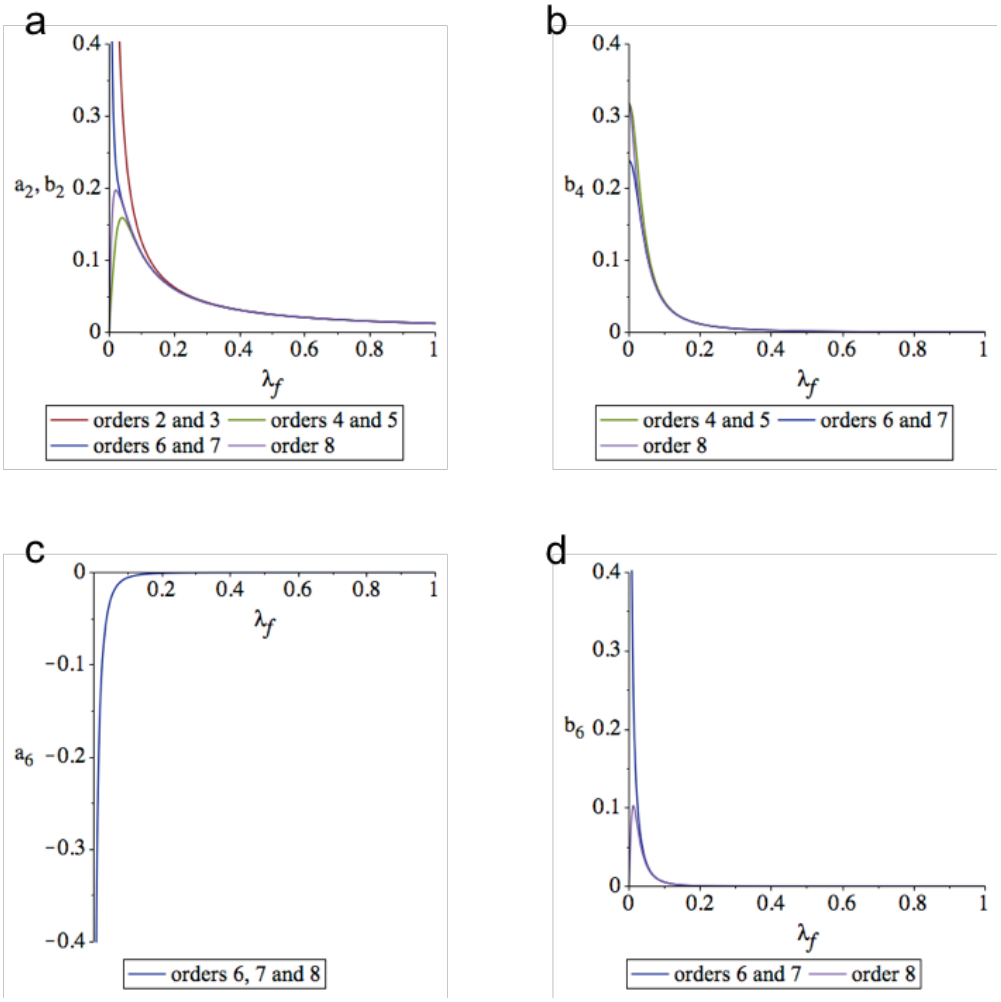

Figure 5.1: **Fourier coefficients when fibroblasts reorient to align with collagen.** (a-d) The effect of truncation order and the size of parameter λ_f on values of Fourier coefficients. For all graphs $\kappa_f = 0 = \eta_f$, $\gamma_f = \frac{\pi}{4}$ and $c_2 = d_2 = 0.2$.

and polar plots of f approximated at truncation order 4. For $\lambda_f = 0.05$ the probability density function drops below zero, which is biologically implausible; this is caused by a breakdown of the approximation employed, rather than by the properties of the full model. For $\lambda_f > 0.075$ the solutions are both biologically and mathematically sensible, and the shape of the distribution suggests that a higher truncation order would be required to represent the true solutions outside of this parameter space. As expected, fibroblasts align with the collagen fibres' predominant orientation, and as the size of λ_f increases the distributions of fibroblast orientations become more uniform.

When $\lambda_f > 0.2$, the PDF f can be represented by $f = \frac{1}{2\pi}\cos(2(\theta - \alpha))$, where $\alpha = \frac{1}{2}\arctan\left(\frac{b_2}{a_2}\right)$ gives the angle at which f is at its maximum. When the fixed collagen distribution is given by the parameters $c_2 = 0.2 = d_2$ then $\alpha = \frac{\pi}{8}$, which is also the predominant

direction of collagen orientation. If higher order terms are included, for example in the approximation (5.30), then the maximum can be determined by calculating the derivative $f'(\theta)$ given in equation (6.3), setting this equal to zero and solving for θ. For the parameter set used to generate Figure 5.2, the predominant direction is calculated as $\frac{\pi}{8}$ using either method for all values of λ_f listed; however, if the distribution were skewed then only the second method would be appropriate. Although the size of λ_f does not affect the predominant direction of orientation, it does alter the size of f in this direction. Figure 5.2b shows that small values of λ_f give a very peaked distribution, which becomes more uniform as λ_f increases.

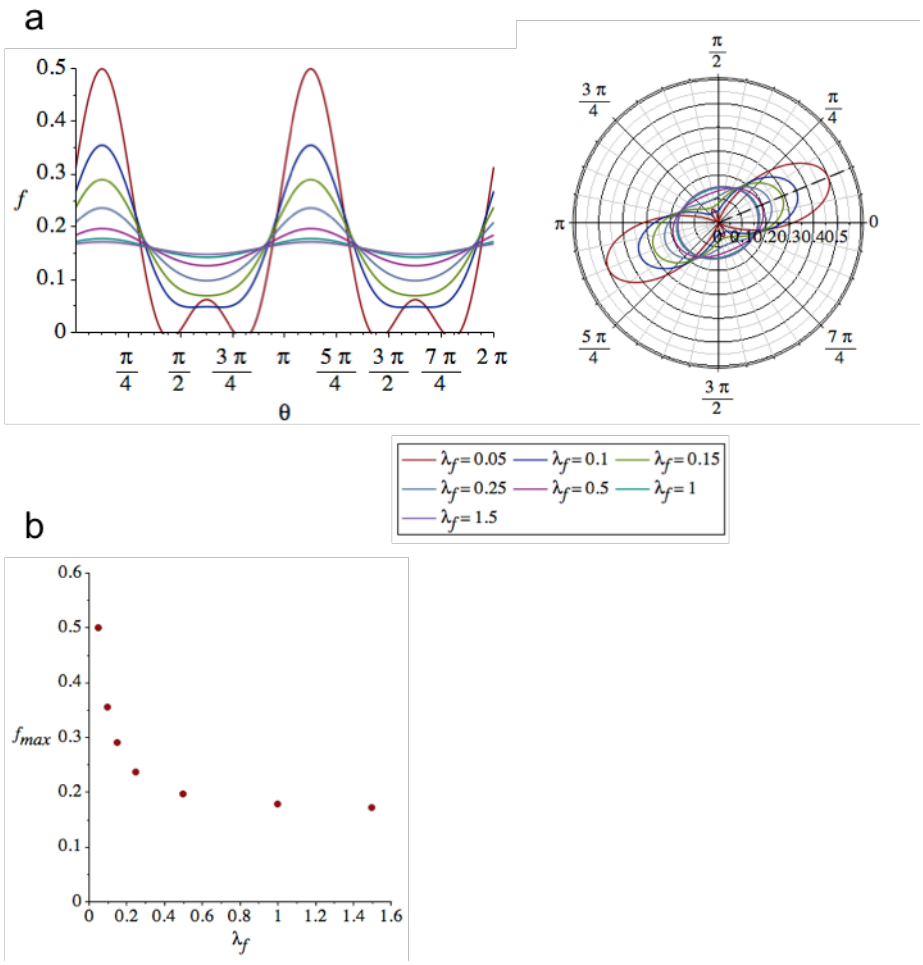

Figure 5.2: **Solution behaviour of f when fibroblasts reorient to align with collagen.** (a) The effect of changing the size of parameter λ_f on the PDF of fibroblast orientation, f. All solution curves are calculated at truncation order 4, with $\kappa_f = 0 = \eta_f$, $\gamma_f = \frac{\pi}{4}$ and $c_2 = d_2 = 0.2$. Dashed line denotes mean orientation. (b) The effect of the size of parameter λ_f on the maximum value of f.

5.4.2 Chemotaxis, collagen contact guidance and stochastic reorientation

An analogous investigation of solution behaviour can be conducted for the situation where fibroblasts reorient in response to a chemoattractant, rather than aligning with collagen fibres; this is implemented by setting $\gamma_f = 0$ and $\eta_f = 0$. We set $\theta_\beta = \frac{3\pi}{2}$, although analogous results are found for a chemoattractant located at any angle from the horizontal. In this case the odd Fourier coefficients of $\cos(n\theta)$ (namely a_1, a_3, a_5, a_7), and the even Fourier coefficients of $\sin(n\theta)$ (namely b_2, b_4 and b_6) are of order 10^{-10} so can be neglected. As shown in Figure 5.3a-d, the truncation order 4 solutions for b_1, a_2, b_3 and a_4 are reasonable approximations to higher truncation orders for $\kappa_{\lambda f} = \frac{\kappa_f}{\lambda_f} < 5$. The values of a_6, b_5 and b_7 are at least an order of magnitude smaller in this parameter space than the lower coefficients, so may be omitted for small values of $\kappa_{\lambda f}$ (Figure 5.3e-f). Therefore, when only chemotactic and stochastic effects are included, the PDF of fibroblast orientation can be approximated as

$$f \approx \frac{1}{2\pi} + b_1 \sin(\theta) + a_2 \cos(2\theta) + b_3 \sin(3\theta) + a_4 \cos(4\theta) \, . \tag{5.31}$$

It is also important to investigate solution behaviour under combinations of effects. For example, fibroblasts that reorient in response to both collagen fibres (at maximum density and predominantly aligned at $\phi = \frac{\pi}{8}$) and a chemoattractant (located at $\theta_\beta = \frac{3\pi}{2}$), as well as undergoing stochastic reorientation, can be simulated by setting $\gamma_f = \frac{\pi}{4}$, $c_2 = d_2 = 0.2$, $\theta_\beta = \frac{3\pi}{2}$, $\eta_f = 0$. In this case, the truncation order 4 solutions for a_1, b_2, a_3 and b_4 are good approximations to higher orders for $\kappa_{\lambda f} \leq 5$ (Figure 5.4a-d). The coefficients a_2, a_4, a_6 and b_1, b_3 and b_5 take the same form as when there is only chemotaxis (Figure 5.3a-f). Finally, a_5, a_7, b_6 and b_7 are at least an order of magnitude smaller than the earlier coefficients for $0 \leq \kappa_{\lambda f} \leq 5$, so may be omitted. Together this gives an approximation to f, when fibroblasts undergo alignment with collagen, chemotaxis and stochastic reorientation, of the form

$$f \approx \frac{1}{2\pi} + \sum_{n=1}^{4} a_n \cos(n\theta) + b_n \sin(n\theta) \, . \tag{5.32}$$

The expression (5.32) is computed from the values of its coefficients, and plots for various parameter sets are shown in Figures 5.5 and 5.6. For $\kappa_{\lambda f} > 2$, the probability density function drops below zero for some values of θ both when only chemotaxis is included, and when fibroblasts respond to a combination of chemotaxis and alignment with collagen (Figures 5.5a and 5.6a). Therefore, biologically and mathematically sensible solutions are only found for truncation order 4 when $\kappa_{\lambda f} \leq 2$. When chemotaxis is the only effect, the ratio $\frac{\kappa_f}{\lambda_f}$ determines how peaked the distribution is, with the mean direction always towards

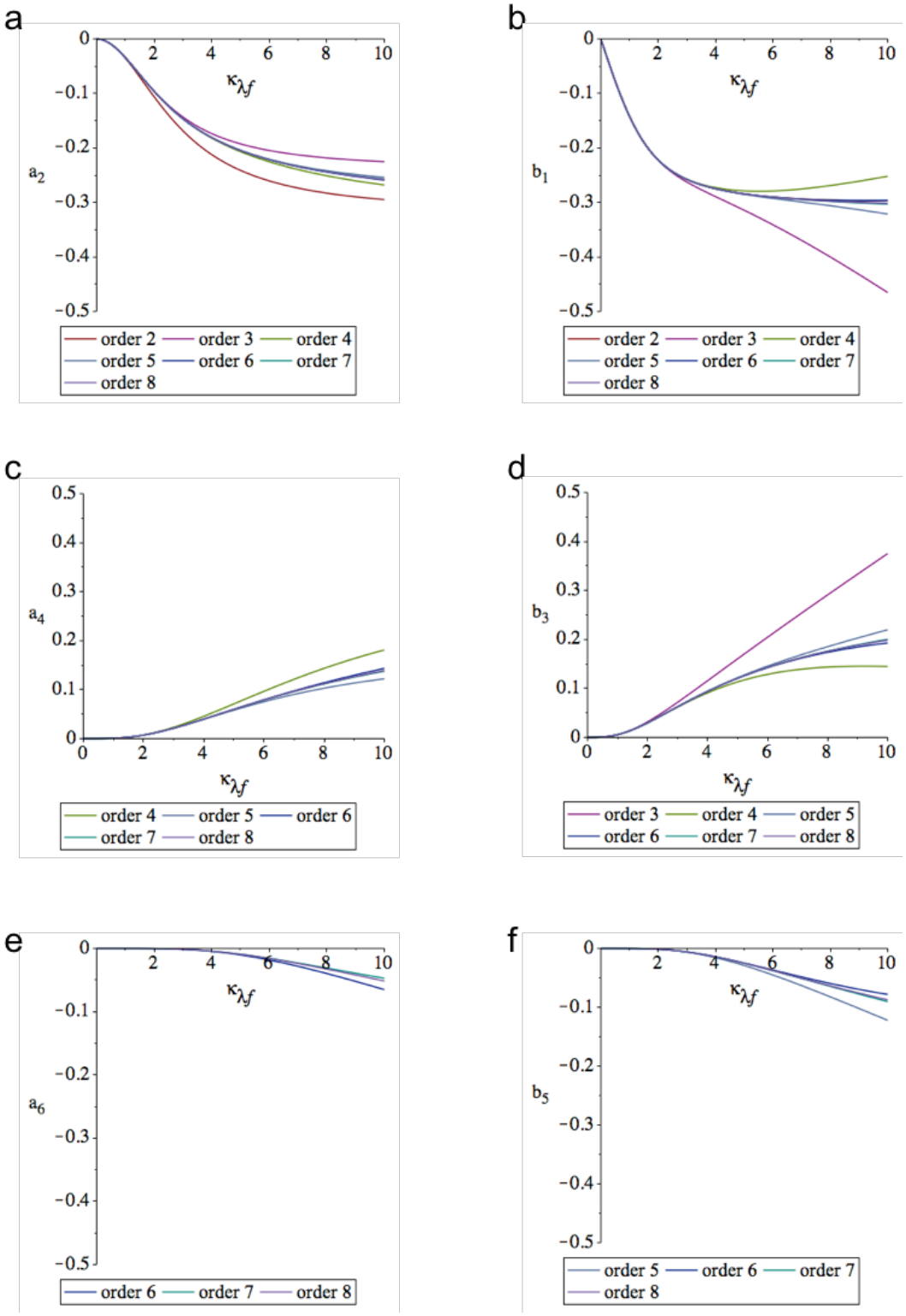

Figure 5.3: **Fourier coefficients of f when fibroblasts reorient to align with a chemoattractant.** (a-f) The effect of truncation order and the size of parameter $\kappa_{\lambda f} = \frac{\kappa_f}{\lambda_f}$ on values of Fourier coefficients when $\gamma_f = 0 = \eta_f$ and $\theta_\beta = \frac{3\pi}{2}$.

the location of the chemoattractant (Figure 5.5b, dashed line). However, as shown in Figure 5.6a-b, when collagen contact guidance is added there are three effects to be balanced:

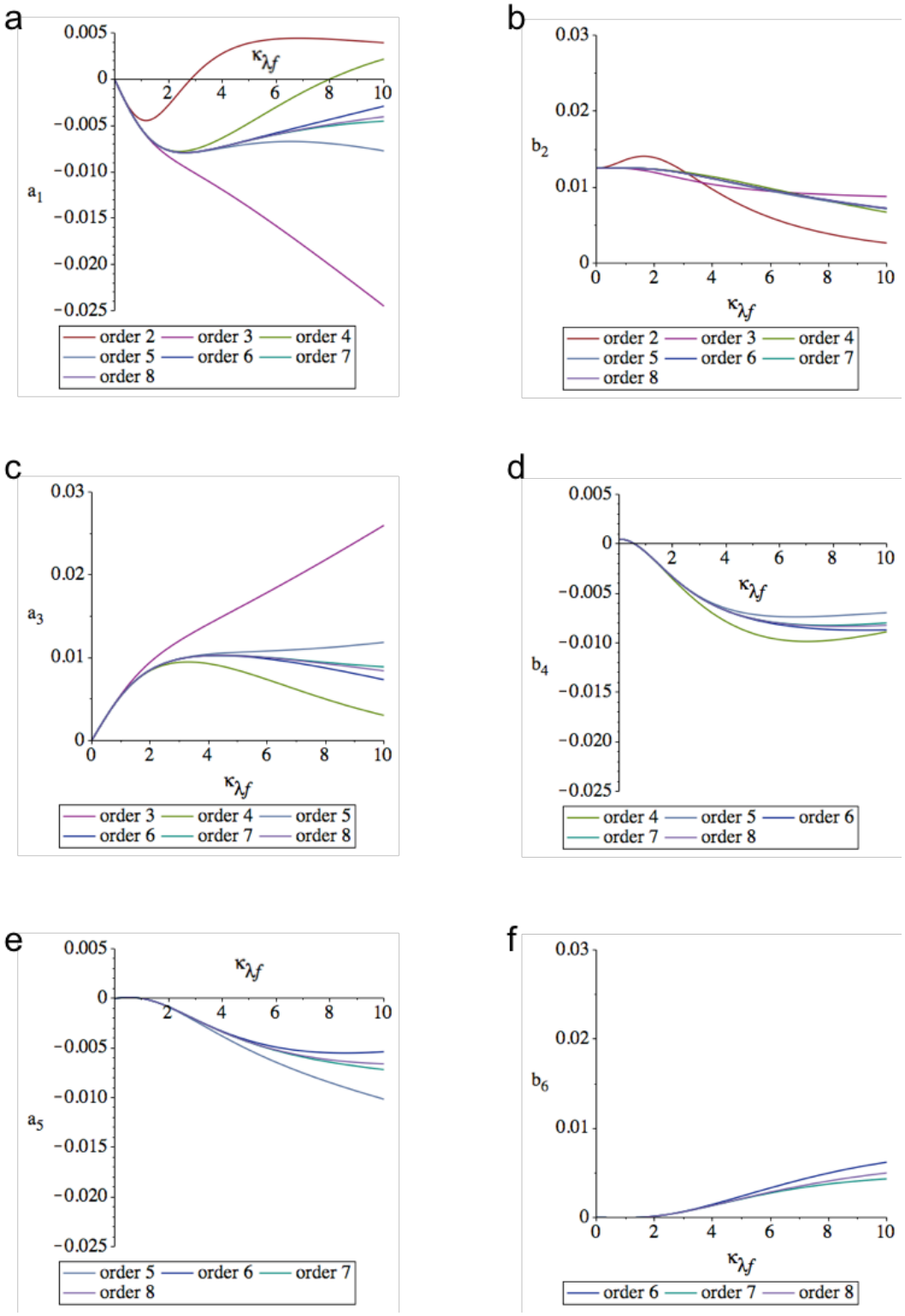

Figure 5.4: **Fourier coefficients of f when fibroblasts reorient towards a chemoattractant and align with collagen fibres.** (a-f) The effect of truncation order and the size of parameter $\kappa_{\lambda f} = \frac{\kappa_f}{\lambda_f}$ on values of Fourier coefficients when $\gamma_f = \frac{\pi}{4}$, $c_2 = d_2 = 0.2$, $\theta_\beta = \frac{3\pi}{2}$ and $\eta_f = 0$.

reorientation towards the chemoattractant, alignment with collagen and random reorientation. For $\kappa_{\lambda f} \geq 1$ the chemotaxis effect dominates; however, with $\kappa_{\lambda f} \leq 1$ chemotaxis and contact guidance both have a perceivable effect; the location of the steady state, and hence the mean orientation, is a compromise between their two directions (Figure 5.6c-d). This causes the distribution to be skewed for all but very small and very large values of $\kappa_{\lambda f}$.

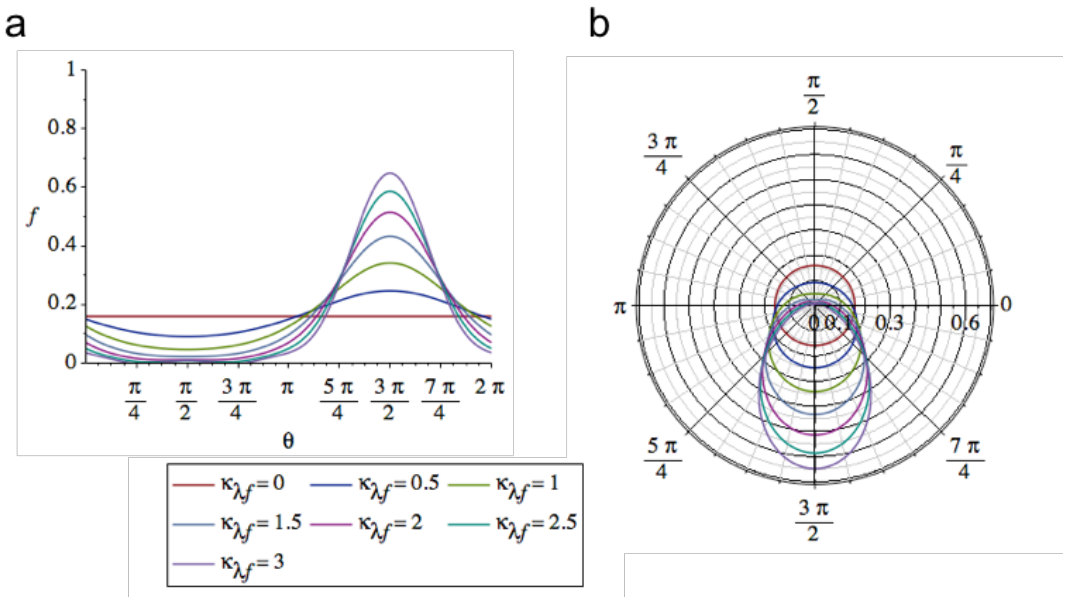

Figure 5.5: **Solution behaviour of f, the PDF of fibroblast orientation, when fibroblasts reorient towards a chemoattractant.** (a-b) The effect of the size of parameter $\kappa_{\lambda f} = \frac{\kappa_f}{\lambda_f}$ on the PDF f, when fibroblasts undergo stochastic reorientation and align with a chemoattractant of varying strength ($\gamma_f = 0 = \eta_f$, $\theta_\beta = \frac{3\pi}{2}$). Solutions are computed at truncation order 4.

5.4.3 ECM shear, chemotaxis, collagen contact guidance and stochastic reorientation

Next we consider the effects of fibroblasts aligning with collagen whilst undergoing rotation initiated by ECM movement. These rotational effects are greatest early in the wound healing process, so are likely to occur when collagen concentration has not reached its maximum. Therefore we set $\gamma_f = \frac{\pi}{16}$ (a quarter of its maximal value) but once again align the collagen predominantly towards $\phi = \frac{\pi}{8}$ by setting $c_2 = d_2 = 0.2$; $\kappa_f = 0$ ensures there is no chemotactic effect. The effect of the parameter $\xi_f = \frac{\omega \eta_f}{\lambda_f}$ on the values of the coefficients and the overall solution behaviour can then be investigated.

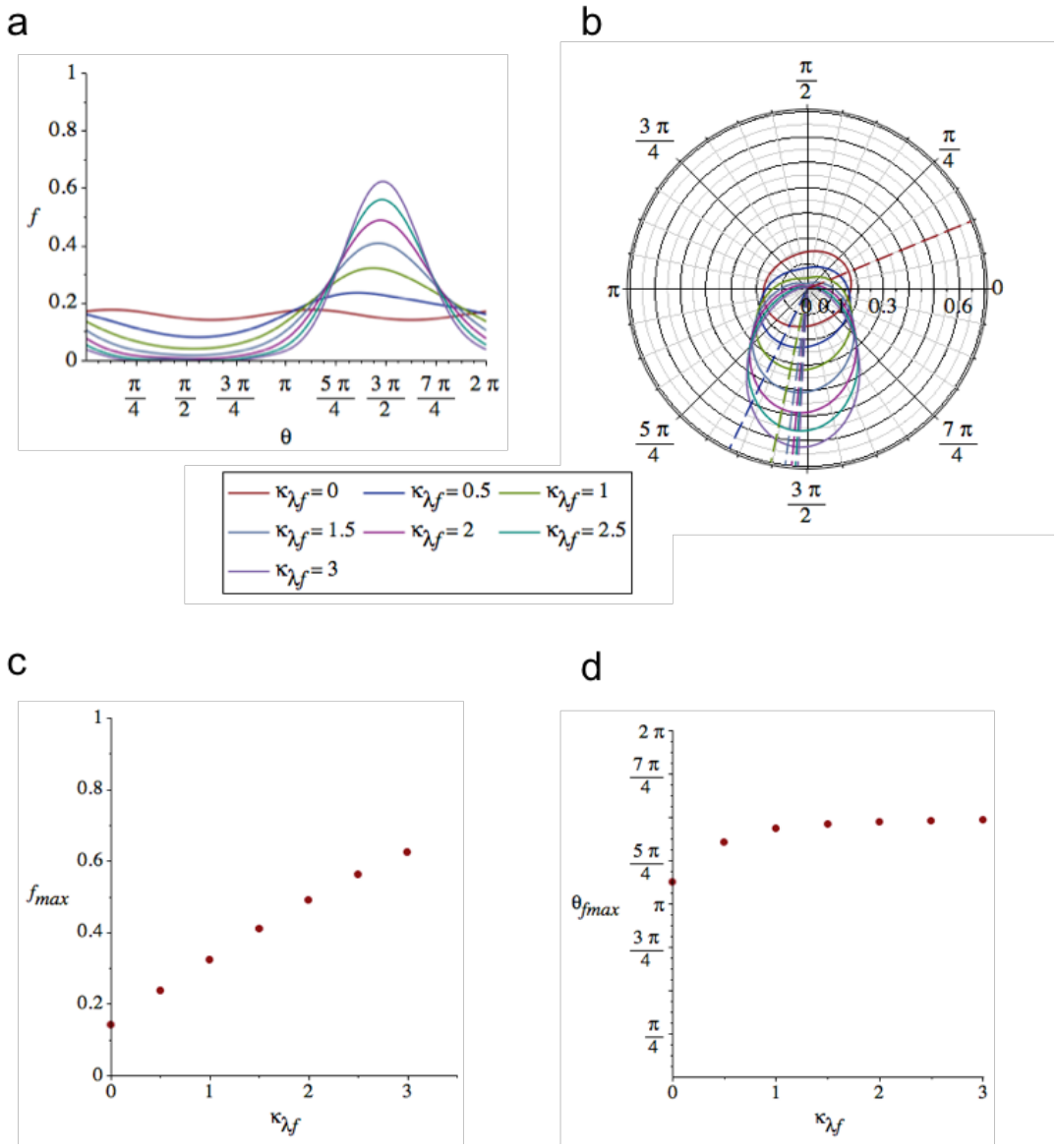

Figure 5.6: **Solution behaviour of f, the PDF of fibroblast orientation, when fibroblasts reorient towards a chemoattractant and align with collagen fibres.** (a-b) The effect of the size of parameter $\kappa_{\lambda f} = \frac{\kappa_f}{\lambda_f}$ on the PDF f, when fibroblasts undergo stochastic reorientation, respond to a chemoattractant and align with collagen fibres ($\gamma_f = \frac{\pi}{4}$, $c_2 = d_2 = 0.2$, $\theta_\beta = \frac{3\pi}{2}$ and $\eta_f = 0$). All solutions are computed at truncation order 4. (c-d) The effect of the size of parameter $\kappa_{\lambda f}$ on the maximum value of f and associated direction.

As in the case with collagen alignment only, the odd coefficients a_1, a_3, a_5, b_1, b_3 and b_5 are zero for $0 \leq \xi_f \leq 0.5$. Additionally, a_6 and b_6 are of the order 10^{-6} and a_4 is even smaller, so can be safely excluded from the Fourier series representation. In this parameter space b_4 is a constant, taking the value 5×10^{-4} for $0 \leq \xi_f \leq 0.5$. The expressions for a_2 and b_2 are more complicated than when only alignment with collagen and/or chemotaxis were included,

and terms including η_f^4 are involved. Given that the tissue-wide effects are expected to be relatively small compared to those of chemotaxis and contact guidance, terms involving higher orders of η_f could be neglected to simplify the solution. Figure 5.7a-b shows that truncating the Fourier series at orders 2 to 6 give identical results, and that taking linear approximations of a_2 and b_2 (calculated by Taylor expanding in η_f and discarding quadratic and higher polynomial terms) is reasonable. Substituting these coefficients into the Fourier expression for f gives the solutions shown in Figure 5.7c. As the amount of rotation (and hence the value of $\xi_f = \frac{\omega\eta_f}{\lambda_f}$) increases, the peaks of the PDF become offset from the predominant direction of the collagen: the mean directions are 0.393, 0.453 and 0.512 for $\kappa_{\lambda f} = 0$, 0.25 and 0.5 respectively. However, the overall shape of the function is preserved, with no skew observed.

Shear associated with movement of the ECM can be decomposed into rotation and strain; we now consider the strain element in isolation (so $\gamma_f = \kappa_f = \omega = 0$). As before, the odd Fourier coefficients are zero, and a_2, b_2, a_4 and b_4 can be simplified by taking a linear approximation of a low truncation order solution (Figure 5.8a-d). The effect of strain is equivalent to that of alignment with collagen (as highlighted in equation (5.3)): the fibroblasts will reorient towards a predominant direction, given by the choice of parameters. In this example we chose $e_{11} = 0$ and $e_{12} = 0.5$, corresponding to the strain component of the flow $\mathbf{v} = y\mathbf{i}$, in which fibroblasts orient predominantly towards $\frac{3\pi}{4}$ (Figure 5.8e).

For various combinations of reorientation effects the full solution for the PDF of fibroblast orientation, f, can be computed; truncation order 4 with a linear approximation to the shear terms has been found to provide a reasonable approximation to the full solution. Figure 5.9a shows solution behaviour for fibroblasts contained in an ECM that is undergoing shear from the flow $\mathbf{v} = y\mathbf{i}$; this is essentially a combination of the effects illustrated in Figure 5.7c and Figure 5.8e. The parameter α_f is a measure of cell eccentricity; estimates of the aspect ratio, a_r, of human dermal fibroblasts in fibrous scaffolds range from 3.5 to 12.0 [292]. Substituting these values into $\alpha_f = \sqrt{1 - \frac{1}{a_r^2}}$ gives $\alpha_f = 0.85$ and $\alpha_f = 0.99$ respectively, both of which represent elongated cell shapes: here we set $\alpha_f = 0.96$. The parameter $\eta_{\lambda f} = \frac{\eta_f}{\lambda_f}$ may then be varied, affecting the size of both the rotation and strain effects which represents increasing the overall shear effect.

Adding the effect of collagen contact guidance skews the PDF further, towards the direction of predominant collagen alignment (Figure 5.9b). For this parameter set, the effect of contact guidance is small because the collagen concentration is low; however, its inclusion is important because contact guidance will begin to outweigh the mechanical effects from

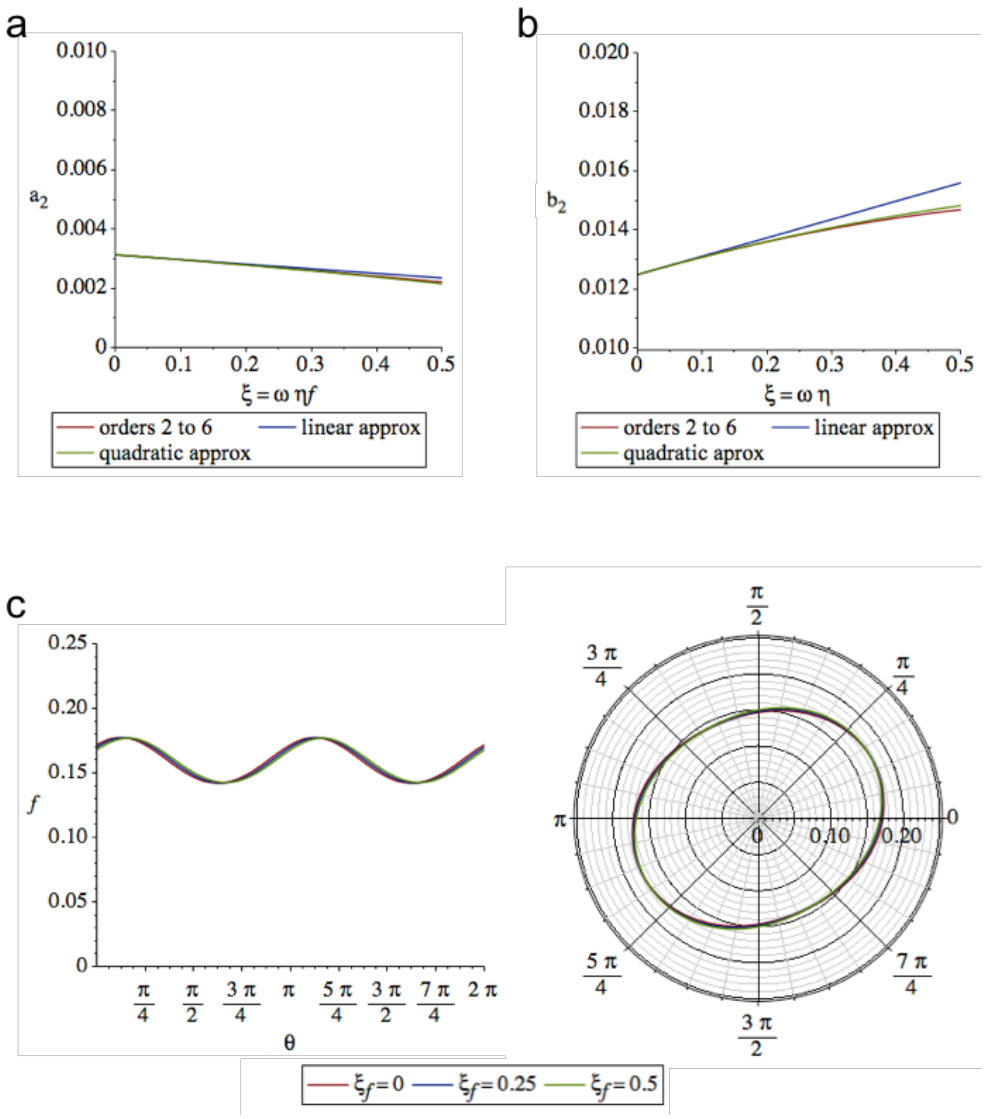

Figure 5.7: **Fourier coefficients and solution behaviour of f when fibroblasts are subject to rotation of the ECM and reorient to align with collagen.** (a-b) The effect of truncation order and taking Taylor approximations on the values of Fourier coefficients for a range of parameter values $\xi_f = \frac{\omega\eta_f}{\lambda_f}$. (c) The effect of changing the size of parameter ξ_f on the PDF of fibroblast orientation f at truncation order 4. For all graphs $\gamma_f = \frac{\pi}{16}$, $c_2 = d_2 = 0.2$ and $\kappa_f = 0$.

the ECM as the collagen concentration increases later in the healing process. As expected, the effect of increasing $\eta_{\lambda f}$ on the mean direction of fibroblasts is greater when both shear and collagen contact guidance are included (Figure 5.9c-d).

The final stimulus of fibroblast reorientation to be incorporated is chemotaxis. Early in the healing process this has a large effect due to the high concentration of chemoattractant in the wound space, which is simulated by setting $\kappa_{\lambda f} = 1$. Although the chemotactic effect

dominates, at higher values of $\eta_{\lambda f}$ ECM mechanics also contribute, causing the PDF of fibroblast distribution to be both peaked and skewed (Figure 5.10a). The mean orientation and maximum value of the distribution do not alter substantially when $\eta_{\lambda f}$ is varied in the interval $0 \leq \eta_{\lambda f} \leq 0.5$ (Figure 5.10b); however the skewness of the PDF increases with increasing $\eta_{\lambda f}$. This illustrates why solving the Fokker-Planck equation using Fourier series rather than elliptical equations is necessary, and highlights a limitation of previously implemented tensorial approaches [270].

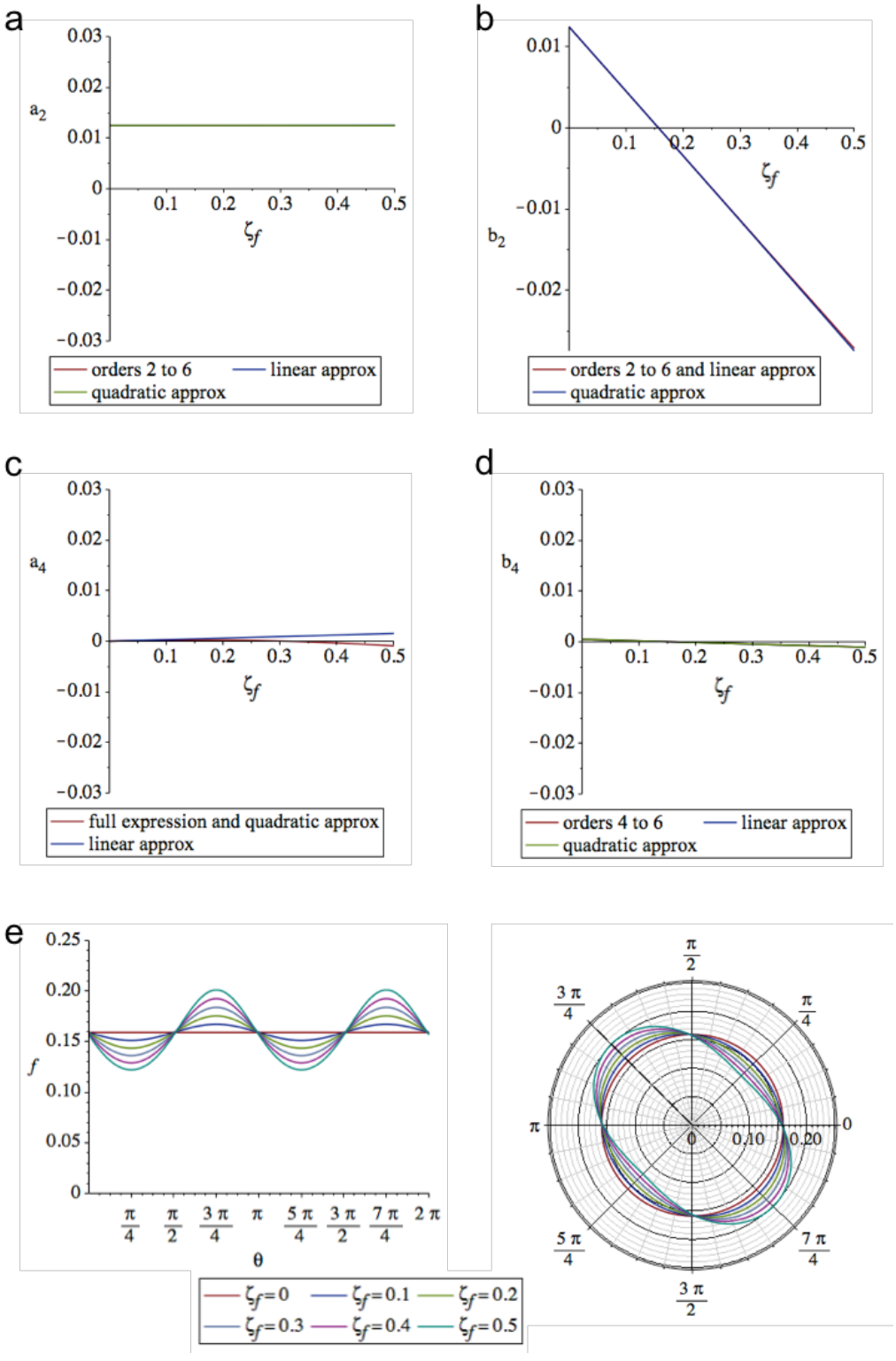

Figure 5.8: **Fourier coefficients and solution behaviour of f when fibroblasts are subject to ECM strain.** (a-d) The effect of truncation order, taking Taylor approximations and the parameter $\zeta_f = \frac{\alpha_f \eta_f}{\lambda_f}$ on Fourier coefficients. (c) The effect of ζ_f on the PDF of fibroblast orientation f at truncation order 4. Dashed line shows mean orientation. For all graphs $e_{11} = 0$, $e_{12} = 0.5$, $\gamma_f = 0$, $\kappa_f = 0$ and $\omega = 0$.

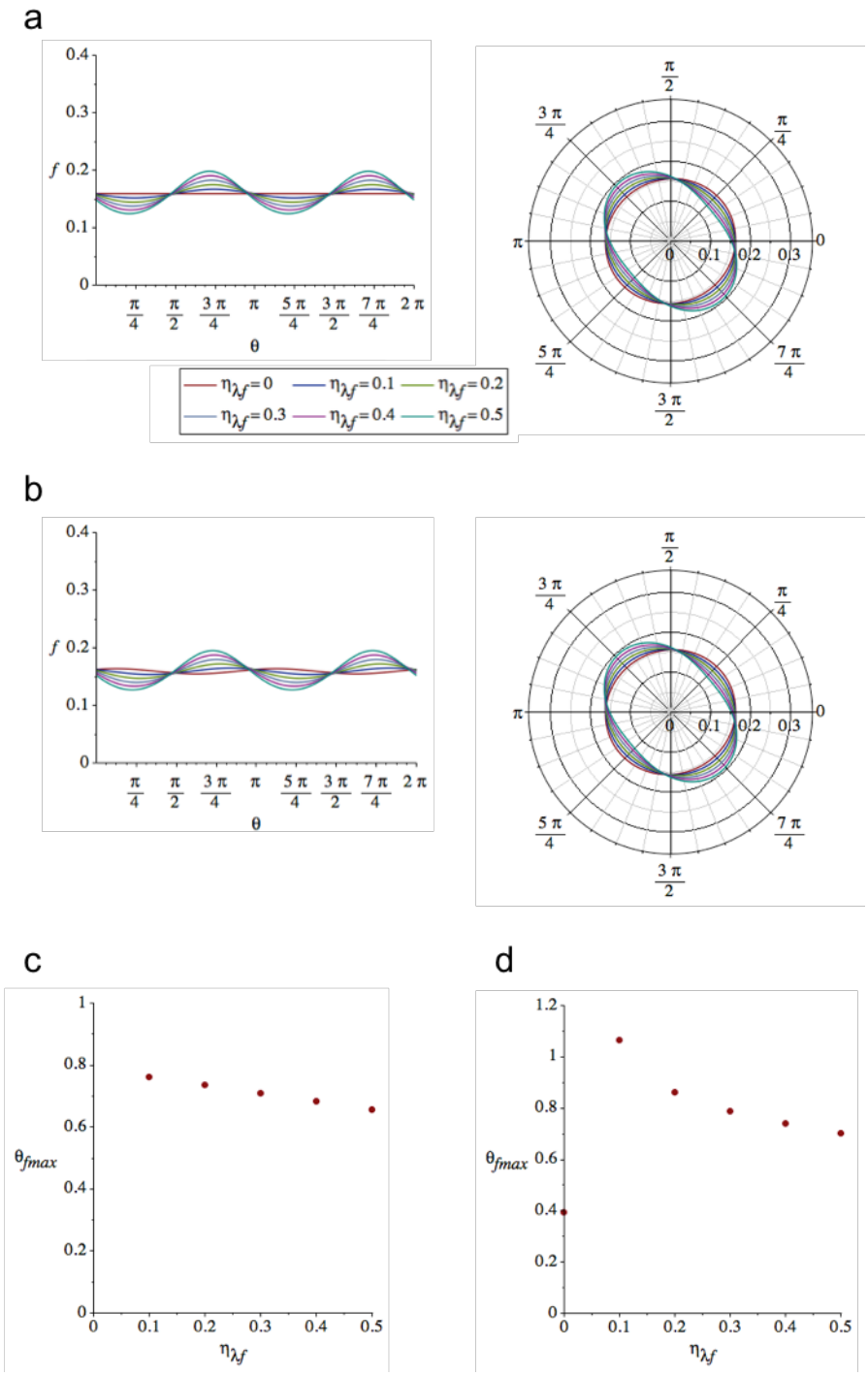

Figure 5.9: **Solution behaviour of f when fibroblasts are subject to collagen contact guidance and ECM shear.** Solution behaviour for various values of $\eta_{\lambda f} = \frac{\eta_f}{\lambda_f}$ when: (a) fibroblasts are affected by ECM shear ($\gamma_f = 0$, $\kappa_{\lambda f} = 0$, $\omega = -1$, $\alpha_f = 0.96$, $e_{11} = 0$, $e_{12} = 0.5$); (b) fibroblasts are affected by ECM shear and collagen contact guidance (as (a) but with $\gamma_f = \frac{\pi}{16}$, $c_2 = d_2 = 0.2$). (c-d) Effect of $\eta_{\lambda f}$ on the maximum value of f and its associate direction θ.

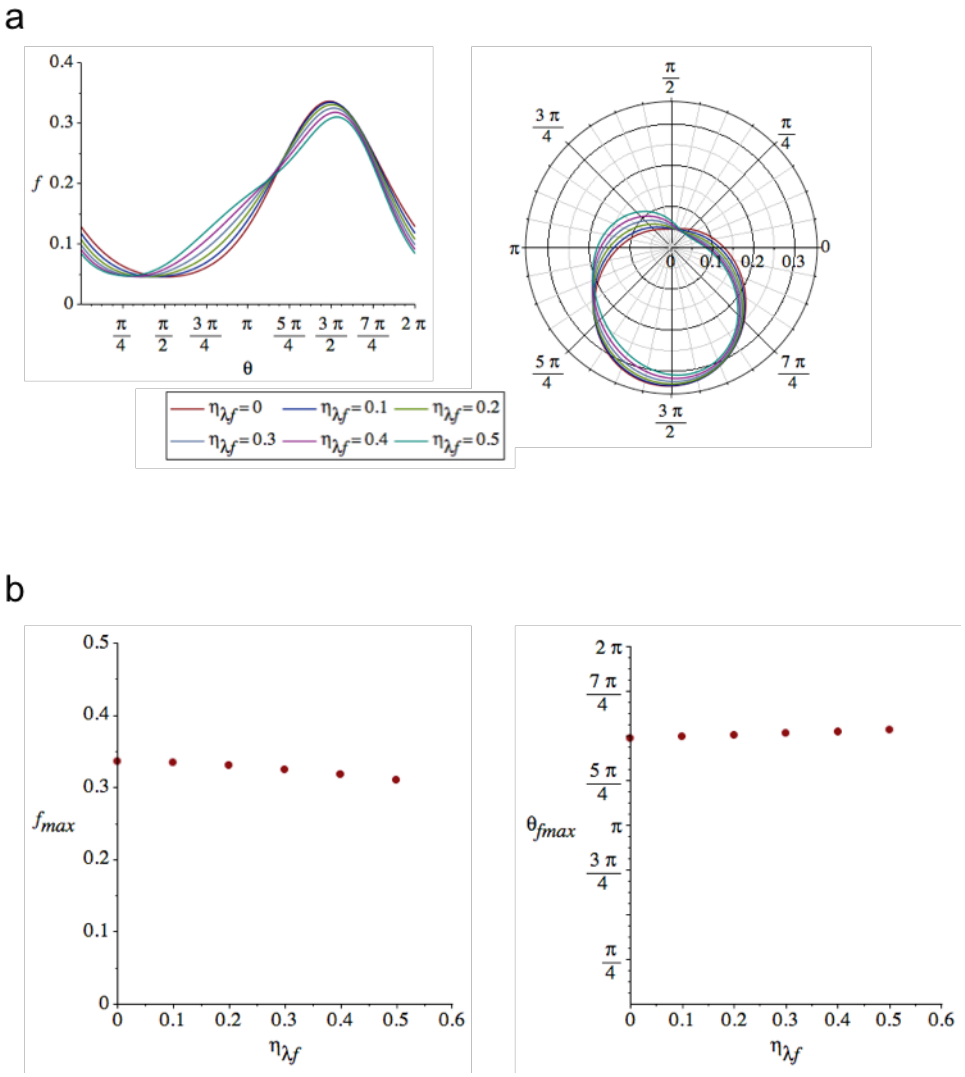

Figure 5.10: **Solution behaviour of f when fibroblasts are subject to collagen contact guidance, chemotaxis, and ECM rotation and strain.** (a) Solution behaviour for various values of $\eta_{\lambda f} = \frac{\eta_f}{\lambda_f}$ for $\gamma_f = \frac{\pi}{16}$, $c_2 = d_2 = 0.2$, $\kappa_{\lambda f} = 1$, $\theta_\beta = \frac{3\pi}{2}$, $\omega = -1$, $\alpha_f = 0.96$, $e_{11} = 0$, $e_{12} = 0.5$. (b) Effect of $\eta_{\lambda f}$ on the maximum value of f and its associated direction θ.

5.5 Time-dependent solutions for collagen orientation

5.5.1 Collagen remodelling

We now consider the PDF of collagen orientation, which can be described by the Fourier series

$$g(\phi,t) = c_0 + \sum_{n=1}^{\infty} \left[c_{2n}(t)\cos(2n\phi) + d_{2n}(t)\sin(2n\phi)\right] := \sum_{n=0}^{\infty} G_{2n} \ , \tag{5.33}$$

with derivatives

$$g'(\phi,t) = \sum_{n=1}^{\infty} \left[-2nc_{2n}(t)\sin(2n\phi) + 2nd_{2n}(t)\cos(2n\phi)\right] := \sum_{n=0}^{\infty} G'_{2n} \ , \tag{5.34}$$

$$g''(\phi,t) = \sum_{n=1}^{\infty} \left[-4n^2c_{2n}(t)\cos(2n\phi) - 4n^2d_{2n}(t)\sin(2n\phi)\right] := \sum_{n=0}^{\infty} -4n^2G_{2n} \ , \tag{5.35}$$

$$\dot{g}(\phi,t) = \sum_{n=0}^{\infty} \dot{c}_{2n}(t)\cos(2n\phi) + \dot{d}_{2n}(t)\sin(2n\phi) \ , \tag{5.36}$$

where

$$G_{2n} := c_{2n}(t)C_{2n} + d_{2n}(t)S_{2n} \ . \tag{5.37}$$

Substituting these expressions into the Fokker-Planck equation (5.27) gives

$$\begin{aligned}\sum_{n=0}^{\infty} \Big\{ \psi_g \left[\dot{c}_{2n}(t)C_{2n} + \dot{d}_{2n}S_{2n}\right] + \gamma_g \left[G'_{2n}(a_2S_2 - b_2C_2) + 2G_{2n}(a_2C_2 + b_2S_2)\right] \\ + \omega\eta_g G'_{2n} - 2\alpha_g\eta_g \left[2G_{2n}(e_{11}C_2 + e_{12}S_2 - G'_{2n}(e_{12}C_2 - e_{11}S_2)\right] \\ + 4n^2\lambda_g G_{2n}\Big\} = 0 \ .\end{aligned} \tag{5.38}$$

We use a method analogous that described in Section 5.4: substitute in the operators (6.5-6.8), truncate the Fourier series representation of the probability density function of collagen orientation at $2n = 4$th order and, by grouping coefficients, generate a system of four ODEs from which approximations to the full solution can be computed. These ODEs take the form

$$\frac{\psi_g}{2}\frac{\mathrm{d}}{\mathrm{d}t}c_2(t) = \frac{\gamma_g a_2}{\pi} + \frac{2\alpha_g\eta_g e_{12}}{\pi} - \omega\eta_g d_2(t) - \alpha_g\eta_g(e_{11}c_4(t) + e_{12}d_4(t)) - 2\lambda_g c_2(t) \ , \tag{5.39}$$

$$\frac{\psi_g}{2}\frac{\mathrm{d}}{\mathrm{d}t}d_2(t) = \frac{\gamma_g b_2}{\pi} + \frac{2\alpha_g\eta_g e_{11}}{\pi} - \omega\eta_g c_2(t) - \alpha_g\eta_g(-e_{11}d_4(t) + e_{12}c_4(t)) - 2\lambda_g d_2(t) \ , \tag{5.40}$$

$$\psi_g\frac{\mathrm{d}}{\mathrm{d}t}c_4(t) = 4\alpha_g\eta_g(e_{11}c_2(t) - e_{12}d_2(t)) - 4\omega\eta_g d_4(t) - 16\lambda_g c_4(t) + 3\gamma_g(a_2c_2(t) - b_2d_2(t)) \ , \tag{5.41}$$

$$\psi_g\frac{\mathrm{d}}{\mathrm{d}t}d_4(t) = 4\alpha_g\eta_g(e_{11}d_2(t) + e_{12}c_2(t)) + 4\omega\eta_g d_4(t) - 16\lambda_g d_4(t) + 3\gamma_g(a_2d_2(t) + b_2c_2(t)) \ . \tag{5.42}$$

Generating analytical solutions of this system was infeasible in a reasonable amount of computational time; however, a simplified system is tractable. We consider the parameter space where $\eta_g = 0$, which represents the remodelling of collagen by fibroblasts in the absence of rotation or strain, and assume that the distribution of fibroblasts is fixed – hence a_2 and b_2 are constants and the equation is uncoupled to that for the fibroblast distribution (5.25). This gives the following system of equations

$$\frac{\psi_g}{2}\frac{\mathrm{d}}{\mathrm{d}t}c_2(t) = \frac{\gamma_g a_2}{\pi} - 2\lambda_g c_2(t)\ , \tag{5.43}$$

$$\frac{\psi_g}{2}\frac{\mathrm{d}}{\mathrm{d}t}d_2(t) = \frac{\gamma_g b_2}{\pi} - 2\lambda_g d_2(t)\ , \tag{5.44}$$

$$\psi_g\frac{\mathrm{d}}{\mathrm{d}t}c_4(t) = 3\gamma_g(a_2c_2(t) - b_2d_2(t)) - 16\lambda_g c_4(t)\ , \tag{5.45}$$

$$\psi_g\frac{\mathrm{d}}{\mathrm{d}t}d_4(t) = 3\gamma_g(a_2d_2(t) + b_2c_2(t)) - 16\lambda_g d_4(t)\ , \tag{5.46}$$

which can be solved analytically to give the following expressions for the Fourier coefficients

$$c_2(t) = \frac{-1}{\pi\lambda_g}b_2\gamma_g\left(e^{-\rho t} - 1\right)\ , \tag{5.47}$$

$$d_2(t) = \frac{-1}{\pi\lambda_g}b_2\gamma_g\left(e^{-\rho t} - 1\right)\ , \tag{5.48}$$

$$c_4(t) = \frac{-\gamma_g^2}{32\pi\lambda_g}(a_2^2 - b_2^2)\left(4e^{-\rho t} - e^{-4\rho t} - 3\right)\ , \tag{5.49}$$

$$d_4(t) = \frac{-\gamma_g^2}{16\pi\lambda_g}a_2b_2\left(4e^{-\rho t} - e^{-4\rho t} - 3\right)\ , \tag{5.50}$$

where $\rho = \frac{4\lambda_g}{\psi_g}$. These take the form of exponential curves that either increase or decrease to a steady state, depending on the parameters and initial conditions imposed, as illustrated in Figure 5.11a for $\psi_g = 1$, $\gamma_g = \frac{\pi}{2}$, $a_2 = 0.1$, $b_2 = 0.2$ and $\lambda_g = 0.1$. It is also possible to solve the system of equations numerically for a given set of parameters, the solutions generated using a 5th order Runge-Kutte solver are presented in Figure 5.11b, showing agreement with the analytical solutions. Solutions to the full system are computed using the numerical method, as analytical solutions take an excessive length of computational time to produce.

Coefficients calculated for specific parameter sets can be substituted back into the Fourier expression for $g(\theta, t)$ (5.33) to determine how the PDF of collagen orientation changes over time. Due to the similarities between the equations for fibroblasts and collagen, the steady state solutions for collagen alignment are qualitatively similar to those presented in Section 5.4 where the chemotactic effect is omitted. We therefore concentrate on the transient behaviour of $g(\theta, t)$.

We first consider collagen being reoriented by the movement of fibroblasts, but not undergoing any mechanical effects from the wider tissue (represented by $\eta_g = 0$). Computing numerical solutions for the parameter set $\psi_g = 10$, $a_2 = 0.2$, $b_2 = 0.2$, $\gamma_g = \frac{\pi}{16}$ and $\lambda_g = 0.3$

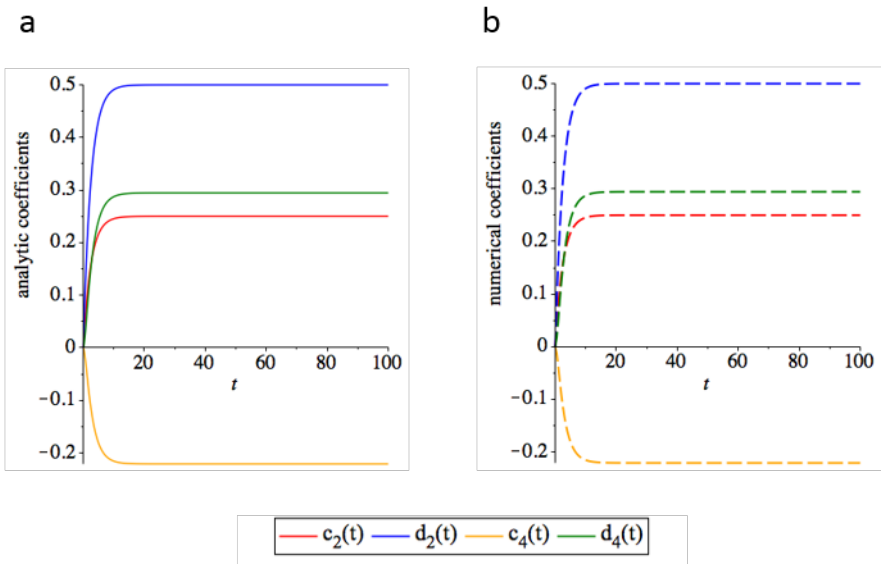

Figure 5.11: **Time dependent Fourier coefficients of $g(t)$ when collagen is remodelled by fibroblasts.** Coefficients calculated for the parameter set $\psi_g = 1$, $\gamma_g = \frac{\pi}{2}$, $a_2 = 0.1$, $b_2 = 0.2$ and $\lambda_g = 0.1$ using (a) analytic and (b) numerical methods.

(which represents a fibroblast population at one quarter of its maximal concentration) leads to the distributions shown in Figure 5.12. Solution profiles differ based on the initial conditions imposed: when collagen orientation is initially uniformly distributed, the effect of remodelling by fibroblasts results in a peaked distribution in the direction of predominant fibroblast orientation (Figure 5.12a); however, when collagen orientation is initially biased towards the horizontal, solutions move towards a more uniform distribution, presumably due to the stochastic effects on fibres (Figure 5.12b). For both initial conditions, the predominant orientation of collagen matches that of the fixed fibroblast population.

Holding the concentration of fibroblasts fixed over time is reasonable during the late phases of healing as the population is likely to be relatively stable. However, the concentration of fibroblasts will increase during the first few weeks of healing, as cells are recruited and proliferate. We investigate the effect of increasing fibroblast concentration linearly with time, and following a sigmoidal profile, in Figure 5.13. The resulting collagen distributions are still peaked at a direction corresponding to the predominant direction of fibroblasts; however, the region of orientation space in which few or no collagen fibres are distributed is much wider at later timepoints. Again, the choice of initial conditions has an effect on the distributions at later timepoints. It is likely that the dynamics of the fibroblast population will be more complex than just linear or sigmoidal growth, as discussed in Section 5.7, but Figure 5.13 illustrates how such an extension may be implemented.

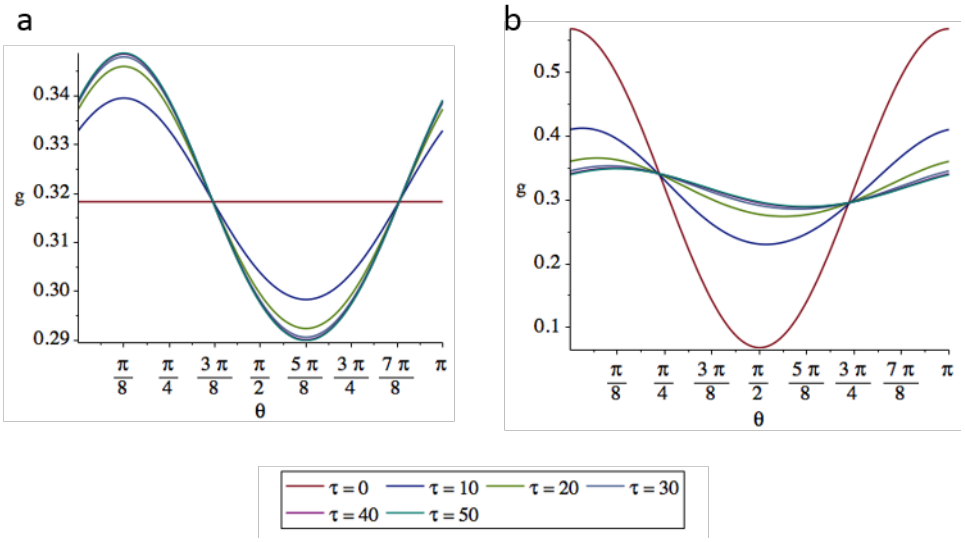

Figure 5.12: **Solution behaviour of $g(t)$ when collagen is remodelled by fibroblasts.** Time-dependent solutions of the PDF of collagen orientation, where $\psi_g = 10$, $a_2 = 0.2$, $b_2 = 0.2$, $\gamma_g = \frac{\pi}{16}$, $\lambda_g = 0.3$ and $\eta_g = 0$. Initial conditions (a) $c_2 = d_2 = 0$, (b) $c_2 = 0.25$, $d_2 = 0$.

Adding the effect of ECM shear shifts the peak away from the predominant direction of the fibroblasts (Figure 5.14a); when this effect is combined with a dynamic concentration of fibroblasts (increasing sigmoidally with time, as shown in Figure 5.12b) the shear forces have less of an effect at later timpoints, when fibroblast concentration approaches its carrying capacity (Figure 5.14b). However, the shape of the solution at later timepoints between $\theta = \frac{\pi}{2}$ and $\theta = \pi$ suggests that the approximation used to convert the PDE (5.38) into a system of ODEs is not appropriate across the entire domain. This illustrates that if more sophisticated descriptions of the dynamics of the fibroblast concentration are to be included (see Figure 5.7), the suitability of the approximation scheme should be assessed across the range of possible values, with the truncation order increased as appropriate.

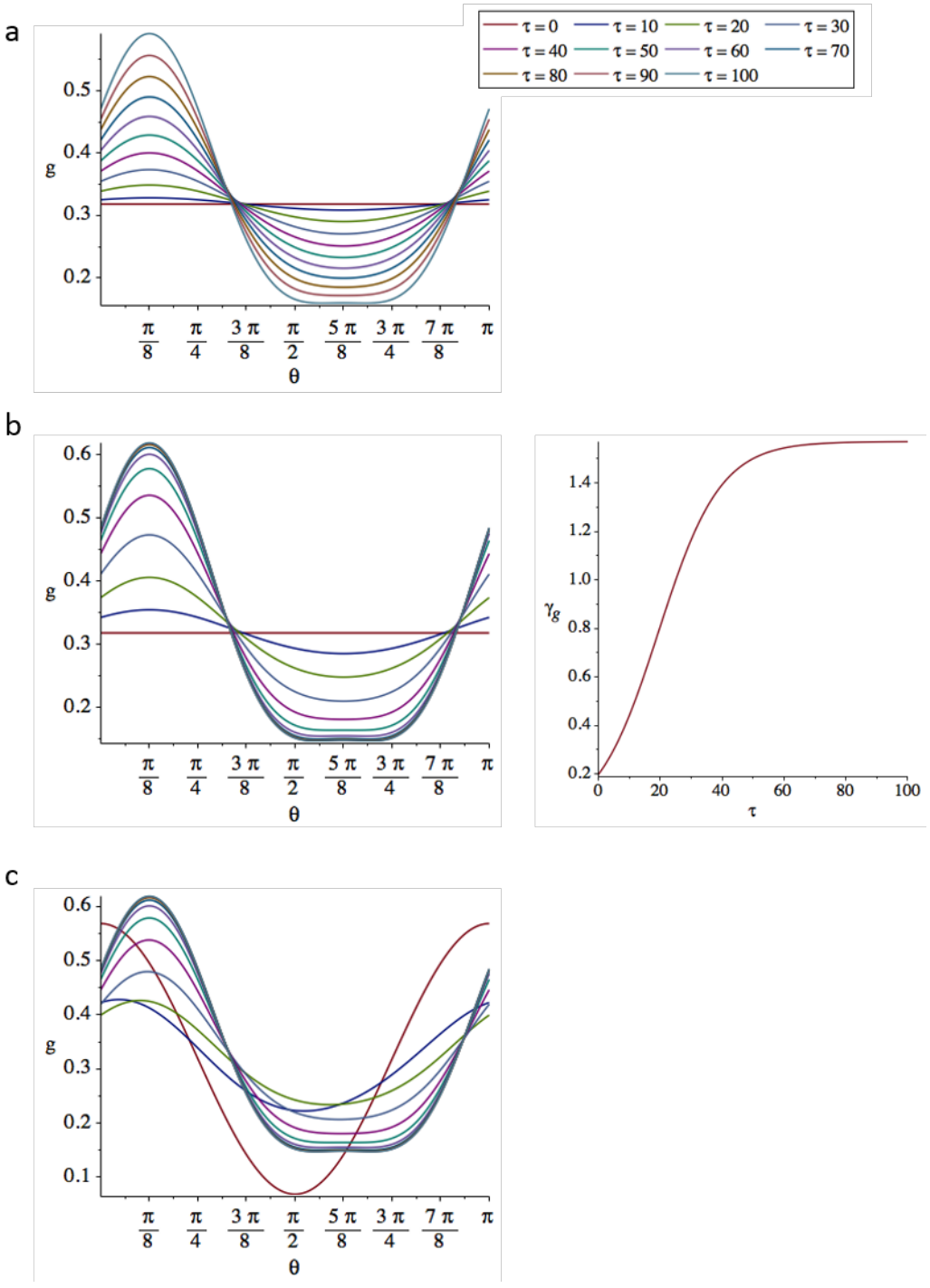

Figure 5.13: **The effect of fibroblast population dynamics of the form of the time dependent PDF of collagen orientation.** Solution curves of $g(t)$ where $\psi_g = 10$, $a_2 = 0.2$, $b_2 = 0.2$, $\lambda_g = 0.3$ and $\eta_g = 0$. The parameter describing the concentration of fibroblasts, γ_g varied with time in a (a) linear and (b) sigmoidal profile. Initial conditions: (a,b) $c_2 = d_2 = 0$, (c) $c_2 = 0.25$, $d_2 = 0$.

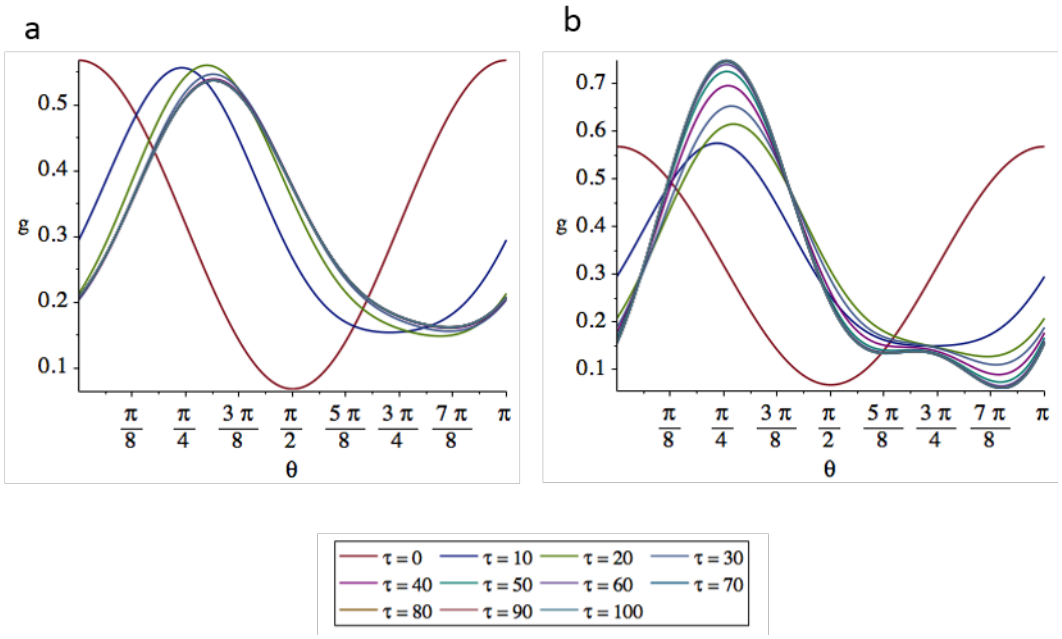

Figure 5.14: **The effect of ECM shear on the form of the time dependent PDF of collagen orientation.** Solution curves of $g(t)$ where $\psi_g = 10$, $a_2 = 0.2$, $b_2 = 0.2$, $\lambda_g = 0.3$, $\eta_g = 0.4$, $\omega = 1$. Initial conditions: $c_2 = 0.25$, $d_2 = 0$. (a) Constant concentration of fibroblasts: $\gamma_g = \frac{\pi}{16}$, (b) concentration of fibroblasts increases sigmoidally with time.

5.6 Solutions to the fully coupled system for fibroblast and collagen orientation

Collagen and fibroblast reorientation are dynamic processes that interact to alter the properties of scar tissue. Therefore, the full system is coupled so that both processes are time dependent, as $f = f(g(t))$ and $g = g(f, t)$. This can be achieved by substituting the analytic expressions for Fourier coefficients of the PDF for fibroblast orientation, a_2 and b_2, into the system of ODEs (5.39-5.42). Solution profiles are qualitatively similar to those of the uncoupled systems, but the fibroblast PDF varies with time. An example of the solutions computed when fibroblasts undergo contact guidance and chemotaxis, and collagen is remodelled by fibroblasts, is shown in Figure 5.15a-b. The peaked distribution of collagen fibres rapidly becomes more uniform, before beginning to realign towards the direction of fibroblast orientation. The wide distribution of fibroblast orientations also changes slightly in response to the direction of the collagen; however, the effect of chemotaxis dominates. When the effect of ECM shear is incorporated, the transient behaviour of the collagen PDF does not go through a uniform distribution of orientations; instead the position of the distribution's peak shifts (Figure 5.15c-d). This sort of solution behaviour could be captured with a simpler model [268], so it is possible that using Fourier approximations rather than full solutions is unnecessary in certain parameter spaces.

However, as shown in Figure 5.16, there are regions of parameter space where the PDF of collagen orientation does not take such a simple form. When the degree of ECM shear is increased, a skewed distribution is produced that could not be fully described using tensorial or predominant direction approaches. High levels of shear are likely to be present in incisional wounds, as their slit shape is more amenable to deformation that circular wounds. Procedures such as suturing can also cause strong shear forces, so the model's ability to represent distributions resulting from these effects will be advantageous for investigating the outcomes of interventions.

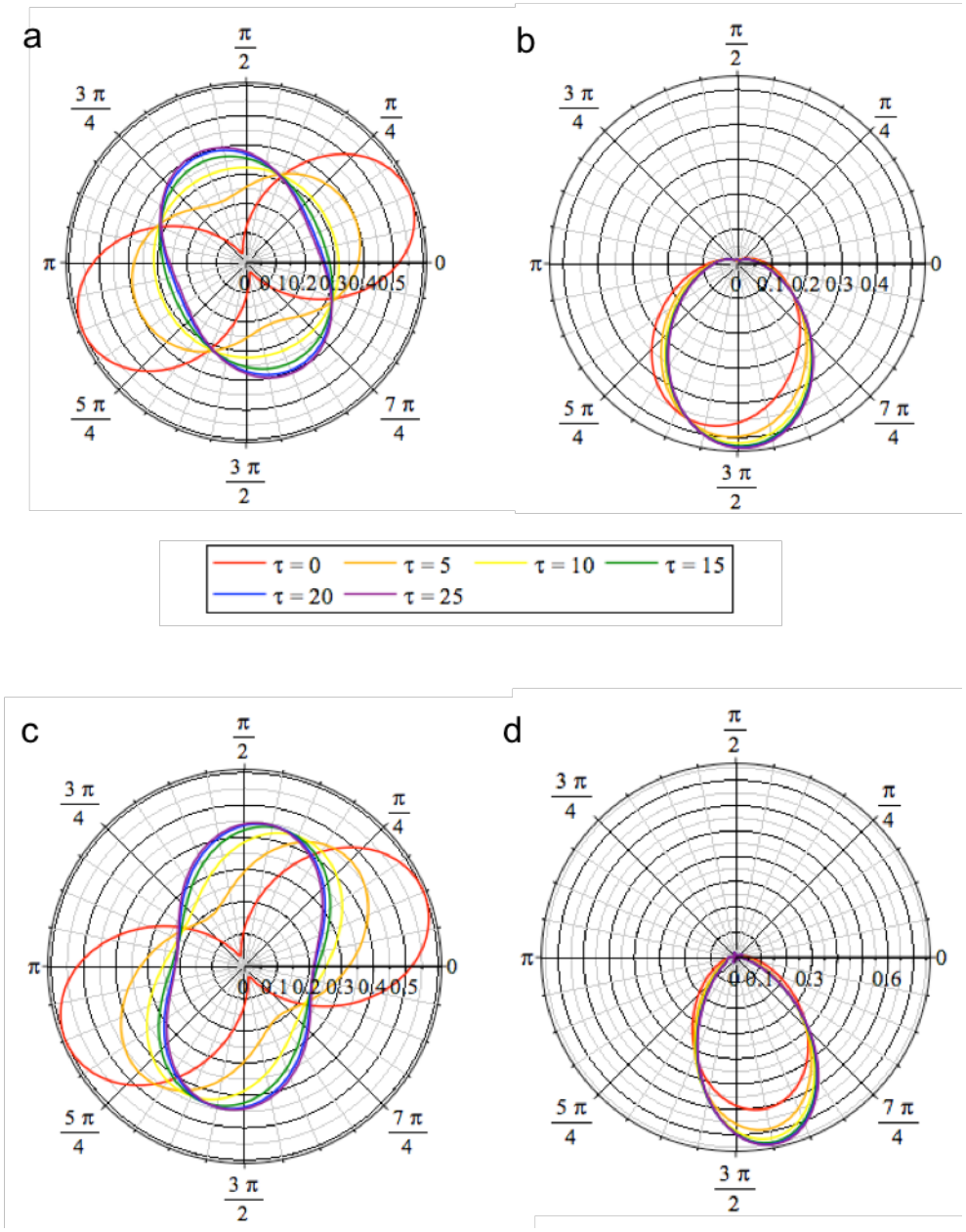

Figure 5.15: **Solutions to the fully-coupled dermal PDF system.** (a-b) Solution curves for collagen and fibroblasts reorienting in response to contact guidance, a chemoattractant and fibroblast-induced collagen remodelling ($\gamma_f = \frac{\pi}{2}$, $\gamma_g = \frac{\pi}{4}$, $\kappa_f = 1$, $\theta_\beta = \frac{3\pi}{2}$, $\psi_g = 10$, $\lambda_f = 0.5$, $\lambda_g = 0.25$, $\eta_f = 0$ and $\eta_g = 0$) for (a) the PDF of collagen orientations and (b) the PDF of fibroblast orientations. (c-d) Solution curves for collagen and fibroblasts reorienting in response to contact guidance, a chemoattractant, fibroblast-induced collagen remodelling and ECM shear ($\gamma_f = \frac{\pi}{2}$, $\gamma_g = \frac{\pi}{4}$, $\kappa_f = 1$, $\theta_\beta = \frac{3\pi}{2}$, $\psi_g = 10$, $\lambda_f = 0.5$, $\lambda_g = 0.25$, $\eta_f = 0.2$, $\eta_g = 0.4$, $\alpha_f = 0.96$, $\alpha_g = 0.99$, $e_{11} = 0$ and $e_{12} = 0.5$) for (a) the PDF of collagen orientations and (b) the PDF of fibroblast orientations. (a-d) Initial conditions: $c_2 = 0.25$, $d_2 = 0$.

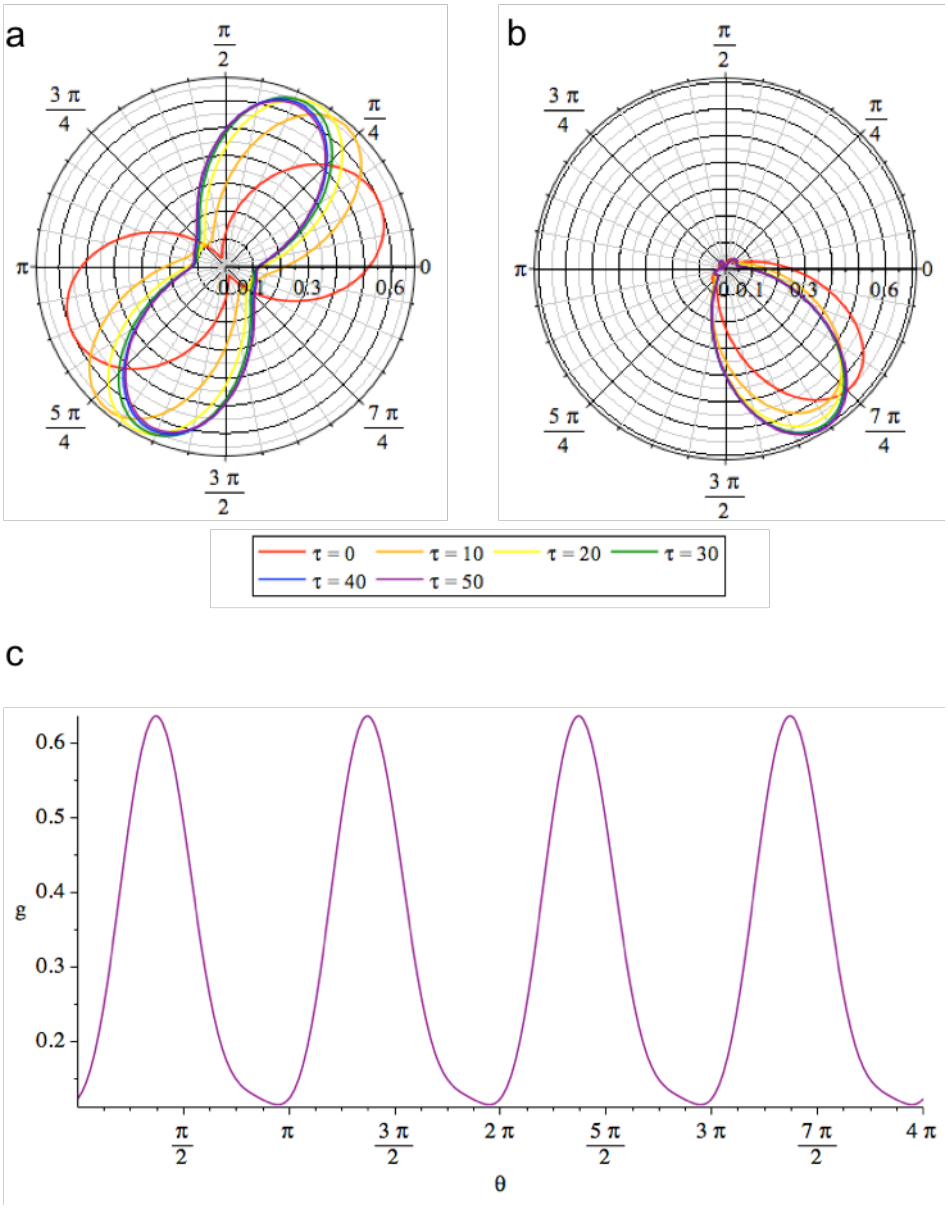

Figure 5.16: **Skewed distributions resulting from to the fully-coupled dermal PDF system.** Solution curves for (a,c) collagen and (b) fibroblasts reorienting in response to contact guidance, a chemoattractant and fibroblast-induced collagen remodelling ($\gamma_f = \frac{\pi}{2}$, $\gamma_g = \frac{\pi}{4}$, $\kappa_f = 1$, $\theta_\beta = \frac{3\pi}{2}$, $\psi_g = 10$, $\lambda_f = 0.5$, $\lambda_g = 0.25$, $\eta_f = 1$, $\eta_g = 1$, $\alpha_f = 0.96$, $\alpha_g = 0.99$, $e_{11} = 0$ and $e_{12} = 0.5$). Initial conditions: $c_2 = 0.25$, $d_2 = 0$.

5.7 Discussion and further work

In this study we have formulated a model for the distributions of orientations of scar tissue components that represents the underlying biological processes, and is versatile to different distribution shapes. Given that the functional properties of the ECM are strongly influ-

enced by the structure of its collagen matrix [258], it is important that models do not merely represent the predominant direction of collagen orientation, but also the distribution of orientations. Our framework allows both the predominant directions and overall distributions to be elucidated. We have shown that some parameter spaces produced markedly skewed distributions of orientations, which cannot be accurately represented by tensorial approaches [270]. However, it is difficult to quantify the degree of skew of a particular distribution, which could be a useful metric when comparing predicted properties of scar tissue [293]. Approaches exploiting the diffusion tensor to provide information on the amount of skew were unsuccessful, so further work to develop a suitable metric is required.

Previous studies have used hybrid model frameworks, whereby cells are modelled as discrete entities that interact with fibres whose properties are represented on a continuum [294]. Our approach also represents fibroblast orientation on a continuum for a population of cells, and allows closed-form analytic solutions to be generated. Although determining the expressions for Fourier coefficients is computationally expensive, particularly at high truncation order, the subsequent process of computing solutions for a particular parameter set is straightforward and quick to implement. It may be possible to further simplify the analytical expressions for fibroblast Fourier coefficients to expedite the generation of numerical solutions for collagen coefficients [279]. This is not particularly necessary for the truncation order 4 results presented here, as solutions are computed relatively quickly. However, if scenarios such as that in Figure 5.14 are to be investigated, higher truncation order approximations will be required and simplification will prove a valuable tool.

A limitation of our modelling framework is that initial conditions for the distribution of fibroblast orientations cannot be explicitly implemented: instead, the initial distribution of fibroblast orientations is computed from the imposed initial collagen distribution, and the chemotactic and mechanical effects. This limits the range of initial conditions that can be simulated, and couples the collagen and fibroblast distributions from the outset, which is not the case for discrete models. Given that we and other groups have shown that initial conditions of the collagen distribution have a big impact on the qualitative and quantitative properties of the model output [295, 273], it is plausible that the initial distribution of fibroblasts could have a similarly significant effect that cannot be elucidated using our framework.

We have investigated the effects of dynamically varying the fibroblast concentration using simple linear and sigmoid representations. Whilst these were instructive in highlighting the effects of gradually increasing fibroblast concentrations, they do not well represent the

underlying stimuli for fibroblast recruitment and tissue residence. We propose the following system of equations, adapted from [294], that can be coupled to the orientation model to simulate changes to the concentrations of fibroblasts, collagen fibres and chemoattractant.

$$\frac{\partial F}{\partial t} + \boldsymbol{\nabla} \cdot [F\mathbf{v} + Fv_s\bar{\mathbf{p}} - \mathbf{D} \cdot \boldsymbol{\nabla} F] = (1 + \alpha_{n\beta}\beta)\, F\, (r - \delta_{nn} F) \ . \tag{5.51}$$

$F\mathbf{v}$ denotes the effect of ECM advection on fibroblast movement, $Fv_s\bar{\mathbf{p}}$ denotes the active movement of a fibroblast where v_s is fibroblast speed, and $\mathbf{D} \cdot \boldsymbol{\nabla} F$ is fibroblast diffusion. The right hand side of the equation describes logistic growth of the fibroblast population, where proliferation has an intrinsic rate, r, but is further stimulated by a growth factor β. δ_{nn} describes the limiting of proliferation when crowding of fibroblasts occurs.

Collagen does not undergo active movement, only ECM-mediated advection, so a possible equation for collagen concentration is

$$\frac{\partial G}{\partial t} + \boldsymbol{\nabla} \cdot (G\mathbf{v}) = \sigma(1 + b_c\beta)F \left(1 - \frac{G}{K_G}\right) \ . \tag{5.52}$$

The right hand side describes collagen production by fibroblasts, which follows logistic growth characterised by a production rate σ. Collagen production increases in the presence of growth factor up to a carrying capacity K_G.

The growth factor is produced by fibroblasts, moves through the dermis and decays, so can be modelled with the equation

$$\frac{\partial \beta}{\partial t} + \boldsymbol{\nabla} \cdot (\beta\mathbf{v}) = D_\beta \nabla^2 \beta - k_1 \beta + \frac{\alpha_\beta F}{1 + b_\beta \beta} \ , \tag{5.53}$$

where the left hand side denotes advection by the ECM. On the right hand side the first term describes growth factor diffusion, the second term describes its linear decay, and the final term denotes production by fibroblasts at a rate α_β and with half-maximal rate of production b_β.

Similarly, the mechanics of the ECM, which in this model are represented by a simple flow, could be explicitly modelled in a system that would be coupled to those of orientations and concentrations. Substantial further work would be required to develop such a model, test it in isolation, incorporate it into the wider system and robustly evaluate the complex output that would result. However this constitutes an exciting future prospect in predicting and understanding the composition of scar tissue in a variety of healing pathologies.

Chapter 6

Discussion

6.1 Summary of findings

Throughout this thesis, methods to enable the study of cutaneous wound healing on a more continuous scale have been developed, implemented and evaluated. The approaches proposed are diverse, including non-invasive wound measurement, the generation of temporally continuous predictions of cellular behaviour from sparse histological datasets, and modelling cell and fibre orientations over an angular continuum.

Imaging wounds photographically to record their morphological properties has been applied to both clinical and experimental studies involving rodents and humans. Recent advances have introduced 3D imaging techniques that allow volumetric quantification of wound sizes, one of which we assessed in the context of murine excisional wound healing. It was found that the camera system generated more reliable wound measurements for 2D metrics (perimeter and diameter) than those computed in 3D (volume and depth). Multiple measurements of the same photograph were also less consistent at later timepoints, indicating a reduction in measurement reliability as healing progresses. Whilst this could not be attributed exclusively to either reducing wound size or healing time, it is likely that both effects act together to the detriment of measurement consistency.

A clear advantage of the LifeViz system is separating the image collection phase from that of wound measurement, which reduces disturbance of the mice and allows multiple measurements to be taken from the same photograph, and by different operators if necessary. We found a good degree of inter-operator consistency, suggesting that multiple operators could work on portions of the same dataset; however, we suggest that measurements are

normalised to those from 0 dpw collected by the same operator to mitigate any systematic over- or under-estimation. In tests for accuracy, the 3D camera system was found to underestimate the volume of indents, with the most notable effect associated with cylindrical indents. Wounds are most likely to take on this geometry at 0 dpw, which could be problematic if other measurements are normalised to this timepoint. We instead recommend that measurements are normalised to those from 3 hours post wounding, which allows mice to fully recover from anaesthesia (so they will not be in a prone position) and allows the wound edge to retract, forming a more concave wound space.

Ultimately, the greatest advantage of the LifeViz system is the projection system that standardises the distance and angle from the wound at which photographs are taken. This, combined with the more reliable 2D measurements of perimeter and diameter, represents a significant advance over using a standard digital camera for murine wound size quantification.

Although non-invasive imaging can quantify healing outcomes, and therefore elucidate the effects of genetic or chemotherapeutic modification of cutaneous repair processes, it does not provide information on the mechanisms underlying changes to wound size. Tissue histology is a useful, but invasive technique for establishing the cellular composition of a wound space; however, the temporal resolution of data collected cannot match that of non-invasive imaging. We propose a pipeline to quantify cell populations in histological images, the results of which may be used to inform the formulation and parameterisation of computational models to "interpolate" between histological data points.

Through comparing three modelling techniques – ODEs, PDEs and ABMs – we have assessed their utility in the context of cutaneous healing. Semi-spatial ODEs can require more parameters than spatially-explicit PDEs in order to encode a representation of space into equations that are only time-dependent. We have shown that PDE models including only diffusion and proliferation can nonetheless replicate the dynamics of cells that actively migrate, through spatial control of the density-dependent diffusion rate. Conversely, the discrete model of epidermal healing that we implemented could only replicate the qualitative behaviour observed in histological experiments (whereby a single layer of keratinocytes covers the wound space, before increasing to a multi-layer barrier) when active migration was explicitly coded into cell behaviour. Active migration was enabled based on the position and microenvironment of each agent: those with space to one side of them and relatively close to the basement membrane could actively migrate most quickly, which could occur at any location in the spatial domain. By contrast, the PDE model hard-coded the locations

of subpopulations of keratinocytes, assigning fixed diffusion rates to each spatial area. Ultimately, a lack of robust experimental data on the stimulus and mechanisms of keratinocyte migration in response to wound events limits the insight that can be applied to choices of models, so a general description is likely to be appropriate for investigating most biological hypotheses.

Time is not the only aspect of wound healing that operates on a continuum; the angles at which cells and fibres are aligned also exist in continuous orientation space. We developed a modelling framework that allows both fibroblasts and collagen fibres to be represented as elongated entities that take on a particular direction, and calculated PDFs for their distribution over continuous orientation space. It was found that both collagen and fibroblast distributions can take on skewed distributions both transiently during reorientation and at steady state, which cannot be represented if only the predominant direction of orientation or distributions based on probabilities at two perpendicular directions are represented in the model framework.

In agreement with previous studies [273, 271], we found that the initial conditions of orientation were influential in determining the transient behaviour and steady state locations of the PDF solutions. This suggests that extending the model to include concentrations of cells and fibres may be integral to fully representing the dynamics of scar tissue composition; we propose a system that could be implemented to achieve this, but which would require careful parameterisation. The underlying orientation model does not restrict model output to a particular distribution shape, thus providing a robust framework on which to build complexity.

6.2 Limitations and future directions

6.2.1 Comparison of wound measurement techniques

The camera system that was evaluated in Chapter 2 was tested in isolation. It may be instructive to directly compare the merits and shortcomings of the 3D imaging technique to other commonly used methods, for example calliper measurement or standard 2D photography. Given the variation in healing responses observed, this would be preferable to comparing results from separate studies. Additionally, the reliability and accuracy of calliper and 2D photography methods have not been investigated in detail, so a comparative study would also provide useful additional information on individual techniques.

An advantage of the LifeViz camera system is that it standardises the distance and angle from the wound at which images are taken. This is achieved by projecting light onto the surface that, when the camera is positioned correctly, are circular and completely overlapping. This is relatively easy to achieve on flat surfaces, but may be more difficult on areas of high curvature (such as a murine dorsum). It would be helpful to investigate whether operators can reliably position the camera with respect to curved surfaces, which could be achieved using indents of known dimensions on surfaces of increasing curvature.

6.2.2 Automated extraction of epidermal region from tissue histology images

A drawback of the cell quantification pipeline is its inability to automate the process of extracting the epidermal region from histological images. This could potentially be overcome if an H&E staining was used instead of immunohistochemistry, as epidermal cells are more consistently labelled. However, this approach would suffer from limitations including a lack of clarity of nuclear staining compared to the background (CellProfiler performs best on images with distinct RGB channels). Additionally, such a method could only be used to determine the number and position of keratinocytes, and would be incompatible with staining for cell markers such as ki67.

6.2.3 Quantifying the number of proliferation events undergone by each cell

It is disappointing that doxycycline-induced labelling of Tet0-Hist GFP mice was not sufficient to quantify the proliferation rate of keratinocytes, as this would provide important additional information to inform the parameterisation of models of epidermal healing. However, only one method of doxycycline induction – using feed containing doxycycline – was tested in the context of epidermal labelling. Previous attempts to introduce doxycycline through the animals water supply had been unsuccessful; injection would be an alternative approach, that it may be possible to commence earlier after birth than weaning.

6.2.4 Uncertainty of parameter estimates

Given the variation observed in healing outcomes, particularly at 5 dpw, it would be advantageous to expand the number of datapoints used to estimate model parameters. The

low n numbers presented were in part due to implementing study designs focussed on the methodological analyses, but were also a result of the time-consuming nature of histology and subsequent quantification protocols. However, now that a robust framework has been developed, we are well placed to increase the level of throughput. It is also advantageous that measurements of multiple wound characteristics (including spatial morphology and effects of wounding on adjacent intact skin) can be taken from the existing dataset, which may be further exploited in the future.

6.2.5 Quantitative evaluation of ABM output

As discussed in Section 4.5.9, extensive additional work is required to establish the sensitivity of the ABM to differing combinations of parameters. This analysis was beyond the scope of the current study, but is of paramount importance if quantitative predictions are to be extracted from the behaviour of the ABM system. Additionally, the model domain should be extended to include a biologically realistic spatial region. This is a significant computational undertaking, highlighting the time-consuming process of ABM formulation and output analysis.

6.2.6 Investigating hybrid models

Whilst we have shown the limitations of ODEs in representing spatial processes, their limitations as single models do not necessarily render the approach inappropriate in a hybrid system. In particular, ODEs could be used to represent non-spatial elements of healing, such as receptor binding, or to simplify aspects of the model that are found to be spatially homogenous. Assessing the benefits and shortcomings of ODEs, PDEs and ABMs individually was instructive in identifying to which types of system they can be most successfully applied, but failed to highlight their strengths in hybrid models. It is likely that their individual attributes would also hold in a more complex model, but an analysis of methods for combining distinct model approaches, and the consequences of doing so, would be a valuable piece of further work.

6.2.7 Parameterisation of the model for scar tissue composition

We have explored the parameter space associated with our model for scar tissue composition, using values from the literature and comparisons of expected effect sizes to inform the re-

gions under consideration. However, parameter estimation using experimental methods has not been accomplished. An experimental system was established whereby fibroblasts were imaged within a collagen gel, with the aim of providing data on the rates of the reorientation and migration of human dermal fibroblasts. In the absence of a chemoattractant fibroblast motility could not be observed; this may be attributed to effects from fibroblast labelling or the composition of the collagen gel. Further work would be required to develop the system such that effects of collagen guidance can be distinguished from those of a chemoattractant.

6.2.8 Investigating healing disorders

The models and experimental techniques presented all focus on investigating healthy healing in wild-type mice. However, the ultimate aim of such approaches should be to provide insight into the mechanisms underpinning healthy healing, and how these differ when healing disorders occur. Estimating parameters using data from mice with known healing impairments can provide insight into the dynamics associated with dysregulation of the repair response, so may be very valuable. However, if it is changes to the mechanisms that underlie aberrant healing responses, then alterations to the model formulation may need to be considered. Whilst this is a more lengthy process, the parameter space of an aberrant healing model may then be explored to investigate whether healthy healing dynamics can be recapitulated by altering specific aspects of the healing response.

In conclusion, this study provides a suite of computational approaches, that together constitute a powerful set of tools with which the mechanisms of cutaneous wound healing can be investigated, quantified and elucidated.

Appendix

Generating solutions to the steady state Fokker-Planck equation for fibroblast orientation

The non-dimensional steady state Fokker-Planck equation for fibroblast orientation given in (5.25) may be written as

$$\begin{aligned} f'\left[\gamma_f\left(d_2\cos(2\theta)-c_2\sin(2\theta)\right)+\kappa_f\left(-\cos(\theta_\beta)\sin(\theta)+\sin(\theta_\beta)\cos(\theta)\right)+\omega\eta_f\right. \\ \left.-2\alpha_f\eta_f\left(-\sin(2\theta)e_{11}+\cos(2\theta)e_{12}\right)\right] \\ +f\left[-2\gamma_f\left(d_2\sin(2\theta)+c_2\cos(2\theta)\right)-\kappa_f\left(\cos(\theta_\beta)\cos(\theta)+\sin(\theta_\beta)\sin(\theta)\right)\right. \\ \left.+4\alpha_f\eta_f\left(\cos(2\theta)e_{11}+\sin(2\theta)e_{12}\right)\right] \\ =\lambda_f f''\ , \end{aligned} \tag{6.1}$$

where primes denote differentiation with respect to θ in cylindrical coordinates, and so the associated derivatives f' and f'' take the form

$$f'(\theta)=\sum_{n=1}^{\infty} n\left[-a_n\sin(n\theta)+b_n\cos(n\theta)\right]\ , \tag{6.2}$$

$$f''(\theta)=\sum_{n=1}^{\infty} n^2\left[-a_n\cos(n\theta)-b_n\sin(n\theta)\right]\ . \tag{6.3}$$

For notational simplicity we define the following:

$$C_n := \cos(n\theta)\ ,$$

$$S_n := \sin(n\theta)\ ,$$

$$F_n := a_nC_n+b_nS_n\ ,$$

so that

$$\begin{aligned}\sum_{n=0}^{\infty} F_n =& f(\theta) \ , \\ \sum_{n=0}^{\infty} F_n' =& f'(\theta) \ , \\ \sum_{n=0}^{\infty} F_n'' =& -\sum_{n=0}^{\infty} n^2 F_n = f''(\theta) \ .\end{aligned}$$

Then the Fokker-Planck equation (6.1) can be written as

$$\begin{aligned}\sum_{n=0}^{\infty} \big\{ F_n' \left[\gamma_f \left(d_2 C_2 - c_2 S_2\right) + \kappa_f \left(-\cos(\theta_\beta) S_1 + \sin(\theta_\beta) C_1\right) - 2\alpha_f \eta_f \left(-S_2 e_{11} + C_2 e_{12}\right)\right. \\ \left. + \omega \eta_f \right] + F_n \left[-2\gamma \left(d_2 S_2 + c_2 C_2\right) - \kappa_f \left(\cos(\theta_\beta) C_1 + \sin(\theta_\beta) S_1\right)\right. \\ \left. + 4\alpha_f \eta_f \left(C_2 e_{11} + S_2 e_{12}\right)\right] + \lambda_f n^2 F_n \big\} = 0 \ .\end{aligned} \tag{6.4}$$

For $m = 1, 2$ and $n \geq 2$ we define a set of operators acting on C_n and S_n:

$$\begin{aligned}\chi_C(C_n, m) &:= \frac{1}{2}(C_{n-m} + C_{n+m}) \ , \\ \chi_S(C_n, m) &:= \frac{1}{2}(S_{n+m} - S_{n-m}) \ , \\ \chi_C(S_n, m) &:= \frac{1}{2}(S_{n+m} + S_{n-m}) \ , \\ \chi_S(S_n, m) &:= \frac{1}{2}(C_{n-m} - C_{n+m}) \ ,\end{aligned}$$

$$\begin{aligned}\chi_{Cp}(C_n, m) &:= \frac{-1}{2} n (S_{n+m} + S_{n-m}) \ , \\ \chi_{Sp}(C_n, m) &:= \frac{-1}{2} n (C_{n-m} - C_{n+m}) \ , \\ \chi_{Cp}(S_n, m) &:= \frac{1}{2} n (C_{n-m} + C_{n+m}) \ , \\ \chi_{Sp}(S_n, m) &:= \frac{1}{2} n (S_{n+m} - S_{n-m}) \ .\end{aligned} \tag{6.5}$$

The operators with $n = 1$, $m = 2$ also take the form (6.5). However for $n = 1$, $m = 1$ we

have

$$\begin{aligned}
\chi_C(C_1,1) &:= \frac{1}{2}(1+C_2)\ ,\\
\chi_S(C_1,1) &:= \frac{1}{2}S_2\ ,\\
\chi_C(S_1,1) &:= \frac{1}{2}S_2\ ,\\
\chi_S(S_1,1) &:= \frac{1}{2}(1-C_2)\ ,
\end{aligned}$$

$$\begin{aligned}
\chi_{Cp}(C_1,1) &:= \frac{-1}{2}S_2\ ,\\
\chi_{Sp}(C_1,1) &:= \frac{-1}{2}(1-C_2)\ ,\\
\chi_{Cp}(S_1,1) &:= \frac{1}{2}(1+C_2)\ ,\\
\chi_{Sp}(S_1,1) &:= \frac{1}{2}S_2\ ,
\end{aligned} \tag{6.6}$$

and for $n=0$, $m=1,2$ the operators take the form

$$\begin{aligned}
\chi_C(C_0,m) &= \frac{1}{2}(C_{-1}+C_1) = C_m\ ,\\
\chi_S(C_0,m) &= \frac{1}{2}(S_1-S_{-1}) = S_m\ ,\\
\chi_C(S_0,m) &= \frac{1}{2}(S_1+S_{-1}) = 0\ ,\\
\chi_S(S_0,m) &= \frac{1}{2}(C_{-1}-C_1) = 0\ ,\\
\chi_{Cp}(C_0,m) = \chi_{Sp}(C_0,m) &= \chi_{Cp}(S_0,m) = \chi_{Sp}(S_0,m) = 0\ .
\end{aligned} \tag{6.7}$$

Evaluating products of C_m, S_m with F, F' shows that

$$\begin{aligned}
C_mF_n =& \frac{a_n}{2}(C_{n-m}+C_{n+m}) + \frac{b_n}{2}(S_{n+m}+S_{n-m}) = a_n\chi_C(C_n,m) + b_n\chi_C(S_n,m)\ ,\\
S_mF_n =& \frac{a_n}{2}(S_{n+m}-S_{n-m}) + \frac{b_n}{2}(C_{n-m}-C_{n+m}) = a_n\chi_S(C_n,m) + b_n\chi_S(S_n,m)\ ,\\
C_mF_n' =& \frac{-na_n}{2}(S_{n+m}+S_{n-m}) + \frac{nb_n}{2}(C_{n-m}+C_{n+m})\\
=& a_n\chi_{Cp}(C_n,m) + b_n\chi_{Cp}(S_n,m)\ ,\\
S_mF_n' =& \frac{-na_n}{2}(C_{n-m}-C_{n+m}) + \frac{nb_n}{2}(S_{n+m}-S_{n-m})\\
=& a_n\chi_{Sp}(C_n,m) + b_n\chi_{Sp}(S_n,m)\ .
\end{aligned} \tag{6.8}$$

Substituting these operators into the Fokker-Planck equation (6.4) gives a system of algebraic equations for the Fourier coefficients a_n and b_n. For example, if we consider the case where fibroblast orientation is affected only by the presence of a chemoattractant (so $\gamma_f = 0$ as there is no contact guidance from collagen, and $\eta_f = 0$ as there are no mechanical effects

from the wider ECM) then the Fokker-Planck equation (6.4) becomes

$$\sum_{n=0}^{\infty} \left\{ F_n' \left[\kappa_f \left(-\cos(\theta_\beta) S_1 + \sin(\theta_\beta) C_1 \right) \right] - F_n \left[\kappa_f \left(\cos(\theta_\beta) C_1 + \sin(\theta_\beta) S_1 \right) \right] + \lambda_f n^2 F_n \right\} = 0 \, . \tag{6.9}$$

Using the operators defined previously (6.5-6.8) this can be written as

$$\begin{aligned} -\kappa_f \Bigg[\sum_{n=2}^{\infty} \{ & a_n \left(\cos(\theta_\beta)(\chi_{Sp}(C_n, 1) + \chi_C(C_n, 1)) + \sin(\theta_\beta)(-\chi_{Cp}(C_n, 1) + \chi_S(C_n, 1)) \right) \\ & + b_n \left(\cos(\theta_\beta)(\chi_{Sp}(S_n, 1) + \chi_c(S_n, 1)) + \sin(\theta_\beta)(-\chi_{Cp}(S_n, 1) + \chi_S(S_n, 1)) \right) \} \\ & + a_1 (C_2 \cos(\theta_\beta) + S_2 \sin(\theta_\beta)) + b_1 (S_2 \cos(\theta_\beta) - C_2 \sin(\theta_\beta)) \\ & a_0 (C_1 \cos(\theta_\beta) + S_1 \sin(\theta_\beta)) \Bigg] + \lambda_f \sum_{n=0}^{\infty} n^2 (a_n C_n + b_n S_n) = 0 \, . \end{aligned} \tag{6.10}$$

This enables coefficients of $\cos(n\theta)$ and $\sin(n\theta)$ to be grouped, giving as a system of algebraic equations. For example, at truncation order 2 the Fokker-Planck equation for fibroblast orientation (6.4) can be approximated by the following system:

$$\begin{aligned} \omega \eta_f b_1 + \alpha_f \eta_f (e_{11} a_1 + e_{12} b_1) + \frac{1}{2} \kappa_f ((a_2 - 2a_0) \cos(\theta_\beta) + b_2 \sin(\theta\beta)) + \lambda_f a_1 \\ - \frac{1}{2} \gamma_f (d_2 b_1 + c_2 a_1) = 0 \, , \end{aligned} \tag{6.11}$$

$$\begin{aligned} -\omega \eta_f a_1 - \alpha_f \eta_f (e_{11} b_1 + e_{12} a_1) + \frac{1}{2} \kappa_f (b_2 \cos(\theta_\beta) - (a_2 + 2a_0) \sin(\theta\beta)) + \lambda_f b_1 \\ + \frac{1}{2} \gamma_f (c_2 b_1 - d_2 a_1) = 0 \, , \end{aligned} \tag{6.12}$$

$$4\alpha_f \eta_f e_{11} a_0 + 2\omega \eta_f b_2 + 4\lambda_f a_2 + \kappa_f (b_1 \sin(\theta_\beta) - a_1 \cos(\theta_\beta)) - 2\gamma_f c_2 a_0 = 0 \, , \tag{6.13}$$

$$4\alpha_f \eta_f e_{12} a_0 - 2\omega \eta_f a_2 + 4\lambda_f a_2 - \kappa_f (a_1 \sin(\theta_\beta) + b_1 \cos(\theta_\beta)) - 2\gamma_f d_2 a_0 = 0 \, . \tag{6.14}$$

Solving these equations gives expressions for the Fourier coefficients a_1, b_1, a_2 and b_2. For any given truncation order t_{order}, a system of $2t_{order}$ equations is used to approximate the Fokker-Planck equation, giving expressions for a_n and b_n ($n = 1 \ldots t_{order}$).

Abbreviations

Abbreviation	Definition
ABM	Agent-based model
dpw	Days post wounding
ECM	Extracellular matrix
EPC	Epidermal progenitor cell
FGF	Fibroblast growth factor
GFP	Green fluorescent protein
GM-CSF	Granulocyte macrophage colony-stimulating factor
HB-EGF	Heparin binding epidermal growth factor
hpw	Hours post wounding
IFE	Inter-follicular epidermis
IL-6	Interleukin-6
ILC	Innate lymphoid cell
KGF	Keratinocyte growth factor
OCT	Optimal cutting temperature
ODE	Ordinary differential equation
PBS	Phosphate buffered saline
PDE	Partial differential equation
PDF	Probability density function
PDGF	Platelet-derived growth factor
pECM	Provisional extracellular matrix
PFA	Paraformaldehyde
TGF	Transforming growth factor
tPA	Tissue plasminogen activator

Bibliography

[1] Di Meglio, P., Perera, G. K., and Nestle, F. O. The multitasking organ: recent insights into skin immune function. *Immunity*, 35(6):857–69, 2011.

[2] Yamaguchi, Y. and Yoshikawa, K. Cutaneous wound healing: an update. *The Journal of Dermatology*, 28(10):521–534, 2001.

[3] Izadi, K. and Ganchi, P. Chronic Wounds. *Clinics in Plastic Surgery*, 32(2):209–222, 2005.

[4] Trace, A. P., Enos, C. W., Mantel, A., and Harvey, V. M. Keloids and hypertrophic scars: a spectrum of clinical challenges. *American Journal of Clinical Dermatology*, 17(3):201–223, 2016.

[5] Werdin, F., Tennenhaus, M., Schaller, H.-E., and Rennekampff, H.-O. Evidence-based management strategies for treatment of chronic wounds. *Eplasty*, 9:e19, 2009.

[6] Bjarnsholt, T., Kirketerp-Møller, K., Jensen, P. Ø., Madsen, K. G., Phipps, R., Krogfelt, K., Høiby, N., and Givskov, M. Why chronic wounds will not heal: a novel hypothesis. *Wound Repair and Regeneration*, 16(1):2–10, 2008.

[7] Drew, P., Posnett, J., and Rusling, L. The cost of wound care for a local population in England. *International Wound Journal*, 4(2):149–155, 2007.

[8] Graham, I. D., Harrison, M. B., Nelson, E. A., Lorimer, K., and Fisher, A. Prevalence of lower-limb ulceration: a systematic review of prevalence studies. *Advances in Skin & Wound Care*, 16(6):305–16, 2003.

[9] Gauglitz, G. G., Korting, H. C., Pavicic, T., Ruzicka, T., and Jeschke, M. G. Hypertrophic scarring and keloids: pathomechanisms and current and emerging treatment strategies. *Molecular Medicine*, 17(1-2):113–25, 2011.

[10] Shaw, T. J., Kishi, K., and Mori, R. Wound-associated skin fibrosis: mechanisms and treatments based on modulating the inflammatory response. *Endocrine, Metabolic & Immune Disorders Drug Targets*, 10(4):320–30, 2010.

[11] Finnerty, C. C., Jeschke, M. G., Branski, L. K., Barret, J. P., Dziewulski, P., and Herndon, D. N. Hypertrophic scarring: the greatest unmet challenge after burn injury. *The Lancet*, 388(10052):1427–1436, 2016.

[12] Shih, B. and Bayat, A. Genetics of keloid scarring. *Archives of Dermatological Research*, 302(5):319–339, 2010.

[13] Jumper, N., Paus, R., and Bayat, A. Functional histopathology of keloid disease. *Histology and Histopathology*, 30(9):1033–57, 2015.

[14] Serra, R., Grande, R., Butrico, L., Rossi, A., Settimio, U. F., Caroleo, B., Amato, B., Gallelli, L., and de Franciscis, S. Chronic wound infections: the role of Pseudomonas aeruginosa and Staphylococcus aureus. *Expert Review of Anti-infective Therapy*, 13(5):605–613, 2015.

[15] Madsen, S. M., Westh, H., Danielsen, L., and Rosdahl, V. T. Bacterial colonization and healing of venous leg ulcers. *APMIS : Acta Pathologica, Microbiologica, et Immunologica Scandinavica*, 104(12):895–9, 1996.

[16] Hirsch, T., Spielmann, M., Zuhaili, B., Koehler, T., Fossum, M., Steinau, H.-U., Yao, F., Steinstraesser, L., Onderdonk, A. B., Eriksson, E., Ferringer, T., Miller, F., Jude, E., Abbott, C., Young, M., Anderson, S., Douglas, J., Boulton, A., Jeffcoate, W., Harding, K., Ferguson, M., Herrick, S., Spencer, M., Shaw, J., Boulton, A., Sloan, P., Delamaire, M., Maugendre, D., Moreno, M., Goff, M. L., Allannic, H., Genetet, B., Wysocki, J., Wierusz-Wysocka, B., Wykretowicz, A., Wysocki, H., Goldstein, E., Citron, D., Nesbit, C., Steinstraesser, L., Tack, B., Waring, A., Hong, T., Boo, L., Fan, M., Remick, D., Su, G., Lehrer, R., Wang, S., Fridkin, S., Hageman, J., Morrison, M., Sanza, L., Como-Sabetti, K., Jernigan, J., Harriman, K., Harrison, L., Lynfield, R., Farley, M., Chambers, H., Cosgrove, S., Sakoulas, G., Perencevich, E., Schwaber, M., Karchmer, A., Carmeli, Y., Archer, G., Grundmann, H., Aires-de Sousa, M., Boyce, J., Tiemersma, E., Diekema, D., Pfaller, M., Schmitz, F., Smayevsky, J., Bell, J., Jones, R., Beach, M., Clark, N., Weigel, L., Patel, J., Tenover, F., Chen, C., Schultz, G., Bloch, M., Edwards, P., Tebes, S., Mast, B., Wang, J., Olson, M., Reno, C., Wright, J., Hart, D., Vardaxis, N., Brans, T., Boon, M., Kreis, R., Marres, L., Montagna, W., Yun, J., Sullivan, T., Eaglstein, W., Davis, S., Mertz, P., Singer, A., McClain, S., Breuing, K., Kaplan, S., Liu, P., Onderdonk, A., Eriksson, E., Steinstraesser,

L., Vranckx, J., Mohammadi-Tabrisi, A., Jacobsen, F., Mittler, D., Lehnhardt, M., Langer, S., Kuhnen, C., Gatermann, S., Steinau, H., Eriksson, E., Onderdonk, A., Dvorak, A., Cisneros, R., McLeod, R., Antionoli, D., Silen, W., Blair, J., Monahan-Earley, R., Cullen, J., Cohen, Z., O'Meara, S., Nelson, E., Golder, S., Dalton, J., Craig, D., Iglesias, C., Robson, M., Mannari, R., Smith, P., Payne, W., Sharma, S., Verma, K., Schubert, S., Heesemann, J., Blakytny, R., Jude, E., Spravchikov, N., Sizyakov, G., Gartsbein, M., Accili, D., Tennenbaum, T., Wertheimer, E., Perschel, W., Langefeld, T., Federlin, K., Armstrong, D., and Frykberg, R. Enhanced susceptibility to infections in a diabetic wound healing model. *BMC Surgery*, 8(1):5, 2008.

[17] Posnett, J., Gottrup, F., Lundgren, H., and Saal, G. The resource impact of wounds on health-care providers in Europe. *Journal of Wound Care*, 18(4):154–161, 2009.

[18] Sen, C. K., Gordillo, G. M., Roy, S., Kirsner, R., Lambert, L., Hunt, T. K., Gottrup, F., Gurtner, G. C., and Longaker, M. T. Human skin wounds: a major and snowballing threat to public health and the economy. *Wound Repair and Regeneration*, 17(6):763–71, 2009.

[19] Franks, P. J. and Morgan, P. A. Health-related quality of life with chronic leg ulceration. *Expert Review of Pharmacoeconomics & Outcomes Research*, 3(5):611–22, 2003.

[20] Posnett, J. and Franks, P. The burden of chronic wounds in the UK. *Nursing Times*, 104(3):44–45, 2008.

[21] Furtado, F., Hochman, B., Ferrara, S. F., Dini, G. M., Nunes, J. M. C., Juliano, Y., and Ferreira, L. M. What factors affect the quality of life of patients with keloids? *Revista da Associacao Medica Brasileira*, 55(6):700–4, 2009.

[22] Bock, O., Schmid-Ott, G., Malewski, P., and Mrowietz, U. Quality of life of patients with keloid and hypertrophic scarring. *Archives of Dermatological Research*, 297(10):433–8, 2006.

[23] Stojadinovic, O., Brem, H., Vouthounis, C., Lee, B., Fallon, J., Stallcup, M., Merchant, A., Galiano, R. D., and Tomic-Canic, M. Molecular pathogenesis of chronic wounds: the role of beta-catenin and c-myc in the inhibition of epithelialization and wound healing. *The American Journal of Pathology*, 167(1):59–69, 2005.

[24] Shih, B., Sultan, M. J., Chaudhry, I. H., Tan, K. T., Johal, K. S., Marstan, A., Tsai, M., Baguneid, M., and Bayat, A. Identification of biomarkers in sequential

biopsies of patients with chronic wounds receiving simultaneous acute wounds: a genetic, histological, and noninvasive imaging study. *Wound Repair and Regeneration*, 20(5):757–69, 2012.

[25] Bagabir, R., Byers, R. J., Chaudhry, I. H., Müller, W., Paus, R., and Bayat, A. Site-specific immunophenotyping of keloid disease demonstrates immune upregulation and the presence of lymphoid aggregates. *The British Journal of Dermatology*, 167(5):1053–66, 2012.

[26] Wilhelm, K.-P., Wilhelm, D., and Bielfeldt, S. Models of wound healing: an emphasis on clinical studies. *Skin Research and Technology*, 0:1–10, 2016.

[27] Lademann, J., Jacobi, U., Surber, C., Weigmann, H.-J., and Fluhr, J. The tape stripping procedure evaluation of some critical parameters. *European Journal of Pharmaceutics and Biopharmaceutics*, 72(2):317–323, 2009.

[28] Kottner, J., Hillmann, K., Fimmel, S., Seité, S., and Blume-Peytavi, U. Characterisation of epidermal regeneration in vivo: a 60-day follow-up study. *Journal of Wound Care*, 22(8):395–400, 2013.

[29] Wigger-Alberti, W., Kuhlmann, M., Ekanayake, S., and Wilhelm, D. Using a novel wound model to investigate the healing properties of products for superficial wounds. *Journal of Wound Care*, 18(3):123–28, 131, 2009.

[30] Cohen, I. K., Crossland, M. C., Garrett, A., and Diegelmann, R. F. Topical application of epidermal growth factor onto partial-thickness wounds in human volunteers does not enhance reepithelialization. *Plastic and Reconstructive Surgery*, 96(2):251–4, 1995.

[31] Khan, A. A., Banwell, P. E., Bakker, M. C., Gillespie, P. G., McGrouther, D. A., and Roberts, A. H. N. Topical radiant heating in wound healing: an experimental study in a donor site wound model. *International Wound Journal*, 1(4):233–40, 2004.

[32] Greco, J. A., Pollins, A. C., Boone, B. E., Levy, S. E., and Nanney, L. B. A microarray analysis of temporal gene expression profiles in thermally injured human skin. *Burns*, 36(2):192–204, 2010.

[33] Ud-Din, S., Greaves, N. S., Sebastian, A., Baguneid, M., and Bayat, A. Noninvasive device readouts validated by immunohistochemical analysis enable objective quantitative assessment of acute wound healing in human skin. *Wound Repair and Regeneration*, 23(6):901–14, 2015.

[34] Li, Z., Hodgkinson, T., Gothard, E. J., Boroumand, S., Lamb, R., Cummins, I., Narang, P., Sawtell, A., Coles, J., Leonov, G., Reboldi, A., Buckley, C. D., Cupedo,

T., Siebel, C., Bayat, A., Coles, M. C., and Ambler, C. A. Epidermal Notch1 recruits RORγ+ group 3 innate lymphoid cells to orchestrate normal skin repair. *Nature Communications*, 7:11394, 2016.

[35] Bon, F. X., Briand, E., Guichard, S., Couturaud, B., Revol, M., Servant, J. M., and Dubertret, L. Quantitative and kinetic evolution of wound healing through image analysis. *IEEE Transactions on Medical Imaging*, 19(7):767–72, 2000.

[36] Gethin, G. The importance of continuous wound measuring. *Wounds UK*, 2(2):60–68, 2006.

[37] Robson, M. C., Hill, D. P., Woodske, M. E., and Steed, D. L. Wound healing trajectories as predictors of effectiveness of therapeutic agents. *Archives of Surgery*, 135(7):773–7, 2000.

[38] Franz, M. G., Kuhn, M. A., Wright, T. E., Wachtel, T. L., and Robson, M. C. Use of the wound healing trajectory as an outcome determinant for acute wound healing. *Wound Repair and Regeneration*, 8(6):511–516, 2000.

[39] Johnson, M. and Miller, R. Measuring healing in leg ulcers: practice considerations. *Applied Nursing Research*, 9(4):204–8, 1996.

[40] Flanagan, M. Wound measurement: can it help us to monitor progression to healing? *Journal of Wound Care*, 12(5):189–94, 2003.

[41] van de Kerkhof, P. C., de Mare, S., Arnold, W. P., and van Erp, P. E. Epidermal regeneration and occlusion. *Acta Dermato-venereologica*, 75(1):6–8, 1995.

[42] Wigger-Alberti, W., Stauss-Grabo, M., Grigo, K., Atiye, S., Williams, R., and Korting, H. C. Efficacy of a tyrothricin-containing wound gel in an abrasive wound model for superficial wounds. *Skin Pharmacology and Physiology*, 26(1):52–6, 2013.

[43] Pereira, G. G., Guterres, S. S., Balducci, A. G., Colombo, P., and Sonvico, F. Polymeric films loaded with vitamin E and aloe vera for topical application in the treatment of burn wounds. *BioMed Research International*, 2014:641590, 2014.

[44] Hartel, M., Illing, P., Mercer, J. B., Lademann, J., Daeschlein, G., and Hoffmann, G. Therapy of acute wounds with water-filtered infrared-A (wIRA). *GMS Krankenhaushygiene Interdisziplinar*, 2(2), 2007.

[45] Myers, S. R., Leigh, I. M., and Navsaria, H. Epidermal repair results from activation of follicular and epidermal progenitor keratinocytes mediated by a growth factor cascade. *Wound Repair and Regeneration*, 15(5):693–701, 2007.

[46] Brown, N. J., Smyth, E. A. E., Cross, S. S., and Reed, M. W. R. Angiogenesis induction and regression in human surgical wounds. *Wound Repair and Regeneration*, 10(4):245–251, 2002.

[47] Ehrlich, H. P. and Freedman, B. M. Topical platelet-derived growth factor in patients enhances wound closure in the absence of wound contraction. *Cytokines, Cellular & Molecular Therapy*, 7(3):85–90, 2002.

[48] Nuutila, K., Siltanen, A., Peura, M., Bizik, J., Kaartinen, I., Kuokkanen, H., Nieminen, T., Harjula, A., Aarnio, P., Vuola, J., and Kankuri, E. Human skin transcriptome during superficial cutaneous wound healing. *Wound Repair and Regeneration*, 20(6):830–839, 2012.

[49] Razzell, W., Wood, W., and Martin, P. Swatting flies: modelling wound healing and inflammation in Drosophila. *Disease Models & Mechanisms*, 4(5), 2011.

[50] Richardson, R., Slanchev, K., Kraus, C., Knyphausen, P., Eming, S., and Hammerschmidt, M. Adult zebrafish as a model system for cutaneous wound-healing research. *The Journal of Investigative Dermatology*, 133(6):1655–65, 2013.

[51] Ansell, D. M., Holden, K. A., and Hardman, M. J. Animal models of wound repair: Are they cutting it? *Experimental Dermatology*, 21(8):581–585, 2012.

[52] Nunan, R., Harding, K. G., and Martin, P. Clinical challenges of chronic wounds: searching for an optimal animal model to recapitulate their complexity. *Disease Models & Mechanisms*, 7(11):1205–13, 2014.

[53] Grose, R. and Werner, S. Wound-healing studies in transgenic and knockout mice. *Molecular Biotechnology*, 28(2):147–166, 2004.

[54] Scheid, A., Meuli, M., Gassmann, M., and Wenger, R. H. Genetically modified mouse models in studies on cutaneous wound healing. *Experimental Physiology*, 85(6):687–704, 2000.

[55] McFarland-Mancini, M. M., Funk, H. M., Paluch, A. M., Zhou, M., Giridhar, P. V., Mercer, C. A., Kozma, S. C., and Drew, A. F. Differences in wound healing in mice with deficiency of IL-6 versus IL-6 receptor. *The Journal of Immunology*, 184(12):7219–28, 2010.

[56] Guo, L., Degenstein, L., and Fuchs, E. Keratinocyte growth factor is required for hair development but not for wound healing. *Genes & Development*, 10(2):165–75, 1996.

[57] Werner, S., Smola, H., Liao, X., Longaker, M., Krieg, T., Hofschneider, P., and Williams, L. The function of KGF in morphogenesis of epithelium and reepithelialization of wounds. *Science*, 266(5186):819–822, 1994.

[58] Liu, Z., Xu, Y., Chen, L., Xie, J., Tang, J., Zhao, J., Shu, B., Qi, S., Chen, J., Liang, G., Luo, G., Wu, J., He, W., and Liu, X. Dendritic epidermal T cells facilitate wound healing in diabetic mice. *American Journal of Translational Research*, 8(5):2375–84, 2016.

[59] Fang, Y., Shen, J., Yao, M., Beagley, K. W., Hambly, B. D., and Bao, S. Granulocyte-macrophage colony-stimulating factor enhances wound healing in diabetes via upregulation of proinflammatory cytokines. *The British journal of dermatology*, 162(3):478–86, 2010.

[60] Huang, C., Orbay, H., Tobita, M., Miyamoto, M., Tabata, Y., Hyakusoku, H., and Mizuno, H. Proapoptotic effect of control-released basic fibroblast growth factor on skin wound healing in a diabetic mouse model. *Wound Repair and Regeneration*, 24(1):65–74, 2016.

[61] Zhao, G., Hochwalt, P. C., Usui, M. L., Underwood, R. A., Singh, P. K., James, G. A., Stewart, P. S., Fleckman, P., and Olerud, J. E. Delayed wound healing in diabetic (db/db) mice with Pseudomonas aeruginosa biofilm challenge: a model for the study of chronic wounds. *Wound Repair and Regeneration*, 18(5):467–477, 2010.

[62] Wosgrau, A. C. C., Jeremias, T. d. S., Leonardi, D. F., Pereima, M. J., Di Giunta, G., and Trentin, A. G. Comparative experimental study of wound healing in mice: Pelnac versus Integra. *PloS One*, 10(3):e0120322, 2015.

[63] Mao, Z., Wu, J. H., Dong, T., Wu, M. X., Al-Watban, F., Zhang, X., Andres, L., Beckmann, H., Meyer-Hamme, G., Schröder, S., Singh, N., Armstrong, D., Lipsky, A., Schultz, S., Richard, J., Sotto, A., Lavigne, J., Moulik, P., Mtonga, R., Gill, G., Driver, V. R., Fabbi, M., Lavery, L. A., Gibbons, G., Eells, J. T., Dungel, P., Kim, W.-S., Calderhead, R. G., Posten, W., Chaves, A., Piancastelli, A. C. C., Silveira, P., Crane, F. L., Ernster, L., Dallner, G., Kohli, Y., Bentinger, M., Choi, B. S., Watanabe, S., Salic, A., Mitchison, T. J., Bordiuk, O. L., Smith, K., Morin, P. J., Semenov, M. V., Zhang, Q., Zhou, C., Hamblin, M. R., Wu, M. X., Flegg, J., Byrne, H. M., Flegg, M. B., McElwain, D. L. S., LoGerfo, F. W., Faglia, E., O'Reilly, D., O'Reilly, D., Dancakova, L., Dong, T., Zhang, Q., Hamblin, , Michael, R., Wu, M. X., Lamson, D. W., Plaza, S. M., Senel, O., Cetinkale, O., Ozbay, G., Ahçiolu, F., Bulan, R., Panchatcharam, M., Miriyala, S., Gayathri, V. S., Suguna, L., Hodgson, J. M.,

Watts, G. F., Playford, D. a., Burke, V., Croft, K. D., and Jameie, S. B. Additive enhancement of wound healing in diabetic mice by low level light and topical CoQ10. *Scientific Reports*, 6:20084, 2016.

[64] Zhang, X., Xu, R., Hu, X., Luo, G., Wu, J., He, W., Bi, H., Jin, Y., Queen, D., Gaylor, J., Evans, J., Courtney, J., Reid, W., Hinman, C., Maibach, H., Wang, X., Ge, J., Tredget, E., Wu, Y., Davidson, J., Galiano, R., Michaels, J., Dobryansky, M., Levine, J., Gurtner, G., Ma, L., Shi, Y., Chen, Y., Zhao, H., Gao, C., Han, C., Yusof, N., Wee, A., Lim, L., Khor, E., Luo, Y., Diao, H., Xia, S., Dong, L., Chen, J., Zhang, J., Schunck, M., Neumann, C., Proksch, E., Xu, R., Luo, G., Xia, H., He, W., Zhao, J., Liu, B., Zhang, Y., Ruan, J., Xiao, R., Zhang, Q., Huang, Y., Eming, S., Werner, S., Bugnon, P., Wickenhauser, C., Siewe, L., Utermohlen, O., Bedossa, P., Dargere, D., Paradis, V., Manousou, P., Burroughs, A., Tsochatzis, E., Isgro, G., Hall, A., Green, A., Standish, R., Cholongitas, E., Dhillon, A., Burroughs, A., Dhillon, A., Volk, S., Bohling, M., Atiyeh, B., Ioannovich, J., Al-Amm, C., El-Musa, K., Miller, M., Svensjo, T., Pomahac, B., Yao, F., Slama, J., Eriksson, E., Gilliver, S., Ashworth, J., Mills, S., Hardman, M., and Ashcroft, G. A systematic and quantitative method for wound-dressing evaluation. *Burns & Trauma*, 3(1):15, 2015.

[65] Pasparakis, M., Haase, I., and Nestle, F. O. Mechanisms regulating skin immunity and inflammation. *Nature Reviews Immunology*, 14(5):289–301, 2014.

[66] Rittié, L. Cellular mechanisms of skin repair in humans and other mammals. *Journal of Cell Communication and Signaling*, 10(2):103–120, 2016.

[67] Chen, L., Mirza, R., Kwon, Y., DiPietro, L. A., and Koh, T. J. The murine excisional wound model: Contraction revisited. *Wound Repair and Regeneration*, 23(6):874–7, 2015.

[68] Summerfield, A. and Ricklin, M. E. The immunology of the porcine skin and its value as a model for human skin. *Molecular Immunology*, 66(1):14–21, 2015.

[69] Watson, S. A. J. and Moore, G. P. M. Postnatal development of the hair cycle in the domestic pig. *Journal of Anatomy*, 170:1–9, 1990.

[70] Bowes, L. E., Jimenez, M. C., Hiester, E. D., Sacks, M. S., Brahmatewari, J., Mertz, P., and Eaglstein, W. H. Collagen fiber orientation as quantified by small angle light scattering in wounds treated with transforming growth factor-beta2 and its neutalizing antibody. *Wound Repair and Regeneration*, 7(3):179–186, 1999.

[71] Hebda, P. A., Klingbeil, C. K., Abraham, J. A., and Fiddes, J. C. Basic fibroblast growth factor stimulation of epidermal wound healing in pigs. *The Journal of Investigative Dermatology*, 95(6):626–31, 1990.

[72] Kiwanuka, E., Hackl, F., Philip, J., Caterson, E. J., Junker, J. P. E., and Eriksson, E. Comparison of healing parameters in porcine full-thickness wounds transplanted with skin micrografts, split-thickness skin grafts, and cultured keratinocytes. *Journal of the American College of Surgeons*, 213(6):728–35, 2011.

[73] Shen, Y.-I., Song, H.-H. G., Papa, A. E., Burke, J. A., Volk, S. W., and Gerecht, S. Acellular hydrogels for regenerative burn wound healing: translation from a porcine model. *The Journal of Investigative Dermatology*, 135(10):2519–29, 2015.

[74] Harding, A. C., Gil, J., Valdes, J., Solis, M., and Davis, S. C. Efficacy of a bio-electric dressing in healing deep, partial-thickness wounds using a porcine model. *Ostomy Wound Management*, 58(9):50–5, 2012.

[75] Safferling, K., Sütterlin, T., Westphal, K., Ernst, C., Breuhahn, K., James, M., Jäger, D., Halama, N., and Grabe, N. Wound healing revised: A novel reepithelialization mechanism revealed by in vitro and in silico models. *The Journal of Cell Biology*, 203(4):691–709, 2013.

[76] Liang, C.-C., Park, A. Y., and Guan, J.-L. In vitro scratch assay: a convenient and inexpensive method for analysis of cell migration in vitro. *Nature Protocols*, 2(2):329–333, 2007.

[77] Stamm, A., Reimers, K., Strauß, S., Vogt, P., Scheper, T., and Pepelanova, I. In vitro wound healing assays state of the art. *BioNanoMaterials*, 17(1-2):79–87, 2016.

[78] Johnston, S. T., Ross, J. V., Binder, B. J., Sean McElwain, D., Haridas, P., and Simpson, M. J. Quantifying the effect of experimental design choices for in vitro scratch assays. *Journal of Theoretical Biology*, 400:19–31, 2016.

[79] Pampaloni, F., Reynaud, E. G., and Stelzer, E. H. K. The third dimension bridges the gap between cell culture and live tissue. *Nature Reviews Molecular Cell Biology*, 8(10):839–845, 2007.

[80] Groeber, F., Holeiter, M., Hampel, M., Hinderer, S., and Schenke-Layland, K. Skin tissue engineering in vivo and in vitro applications. *Advanced Drug Delivery Reviews*, 63(4):352–366, 2011.

[81] Maarof, M., Law, J. X., Chowdhury, S. R., Khairoji, K. A., Saim, A. B., and Idrus, R. B. H. Secretion of wound healing mediators by single and bi-layer skin substitutes. *Cytotechnology*, 68(5):1873–1884, 2016.

[82] Sherratt, J. A. and Dallon, J. C. Theoretical models of wound healing: past successes and future challenges. *Comptes Rendus Biologies*, 325:557–564, 2002.

[83] Vedula, S. R. K., Hirata, H., Nai, M. H., Brugués, A., Toyama, Y., Trepat, X., Lim, C. T., and Ladoux, B. Epithelial bridges maintain tissue integrity during collective cell migration. *Nature Materials*, 13(1):87–96, 2014.

[84] Orazov, M., Sakiyama, Y., and Graves, D. B. Wound healing modeling: investigating ambient gas plasma treatment efficacy. *Journal of Physics D: Applied Physics*, 45(44):445201, 2012.

[85] Andriessen, M. P., van Bergen, B. H., Spruijt, K. I., Go, I. H., Schalkwijk, J., and van de Kerkhof, P. C. Epidermal proliferation is not impaired in chronic venous ulcers. *Acta Dermato-venereologica*, 75(6):459–62, 1995.

[86] Woodley, D. T. Reepithelialisation. In Clark, R. A. F. (editor), *The Molecular and Cellular Biology of Wound Repair*. Plenum Press, New York, 1996.

[87] Sherratt, J. A. and Murray, J. D. Models of epidermal wound healing. *Proceedings of the Royal Society B*, 241:29–36, 1990.

[88] A., H., A., S. G., and A., H. K. Structure and function of the skin: overview of the epidermis and dermis. In K., F. R. and T., W. D. (editors), *The Biology of the Skin*. Taylor and Francis, New York, 2001.

[89] Wickett, R. R. and Visscher, M. O. Structure and function of the epidermal barrier. *American Journal of Infection Control*, 34(10):S98–S110, 2006.

[90] Baroni, A., Buommino, E., De Gregorio, V., Ruocco, E., Ruocco, V., and Wolf, R. Structure and function of the epidermis related to barrier properties. *Clinics in Dermatology*, 30(3):257–62, 2012.

[91] Blanpain, C. and Fuchs, E. Epidermal stem cells of the skin. *Annual Review of Cell and Developmental Biology*, 22:339–73, 2006.

[92] Clayton, E., Doupé, D. P., Klein, A. M., Winton, D. J., Simons, B. D., and Jones, P. H. A single type of progenitor cell maintains normal epidermis. *Nature*, 446(7132):185–9, 2007.

[93] Lippens, S., Denecker, G., Ovaere, P., Vandenabeele, P., and Declercq, W. Death penalty for keratinocytes: apoptosis versus cornification. *Cell Death and Differentiation*, 12:1497–1508, 2005.

[94] Borradori, L. and Sonnenberg, A. Structure and function of hemidesmosomes: more than simple adhesion complexes. *The Journal of Investigative Dermatology*, 112(4):411–8, 1999.

[95] Ovaere, P., Lippens, S., Vandenabeele, P., and Declercq, W. The emerging roles of serine protease cascades in the epidermis. *Trends in Biochemical Sciences*, 34(9):453–63, 2009.

[96] Webb, A., Li, A., and Kaur, P. Location and phenotype of human adult keratinocyte stem cells of the skin. *Differentiation; Research in Biological Diversity*, 72(8):387–95, 2004.

[97] Kenny, F. N. and Connelly, J. T. Integrin-mediated adhesion and mechano-sensing in cutaneous wound healing. *Cell and Tissue Research*, 360(3):571–582, 2015.

[98] Sivamani, R. K., Garcia, M. S., and Isseroff, R. R. Wound re-epithelialization: modulating keratinocyte migration in wound healing. *Frontiers in Bioscience*, 12:2849–2868, 2007.

[99] Martin, P. Wound healing - aiming for perfect skin regeneration. *Science*, 276(5309):75–81, 1997.

[100] Regan, M. and Barbul, A. The cellular biology of wound healing. In Schlag, G. and Redl, H. (editors), *Wound Healing*. Springer-Verlag, Heidelberg, 1994.

[101] Ito, M., Liu, Y., Yang, Z., Nguyen, J., Liang, F., Morris, R. J., and Cotsarelis, G. Stem cells in the hair follicle bulge contribute to wound repair but not to homeostasis of the epidermis. *Nature Medicine*, 11(12):1351–1354, 2005.

[102] Pastar, I., Stojadinovic, O., Yin, N. C., Ramirez, H., Nusbaum, A. G., Sawaya, A., Patel, S. B., Khalid, L., Isseroff, R. R., and Tomic-Canic, M. Epithelialization in wound healing: a comprehensive review. *Advances in Wound Care*, 3(7):445–464, 2014.

[103] Krawczyk, W. S. A pattern of epidermal cell migration during wound healing. *The Journal of Cell Biology*, 49(2):247–263, 1971.

[104] Garlick, J. A. and Taichman, L. B. Fate of human keratinocytes during reepithelialization in an organotypic culture model. *Laboratory Investigation; a Journal of Technical Methods and Pathology*, 70(6):916–24, 1994.

[105] Potten, C. S., Barthel, D., Li, Y. Q., Ohlrich, R., Matthé, B., and Loeffler, M. Proliferation in murine epidermis after minor mechanical stimulation. Part 1. Sustained increase in keratinocyte production and migration. *Cell Proliferation*, 33(4):231–46, 2000.

[106] Roshan, A., Murai, K., Fowler, J., Simons, B. D., Nikolaidou-Neokosmidou, V., and Jones, P. H. Human keratinocytes have two interconvertible modes of proliferation. *Nature Cell Biology*, 18(2):145–156, 2015.

[107] Santoro, M. M. and Gaudino, G. Cellular and molecular facets of keratinocyte reepithelization during wound healing. *Experimental Cell Research*, 304(1):274–86, 2005.

[108] Takazawa, Y., Ogawa, E., Saito, R., Uchiyama, R., Ikawa, S., Uhara, H., and Okuyama, R. Notch down-regulation in regenerated epidermis contributes to enhanced expression of interleukin-36α and suppression of keratinocyte differentiation during wound healing. *Journal of Dermatological Science*, 79(1):10–19, 2015.

[109] Cheng, F., Shen, Y., Mohanasundaram, P., Lindström, M., Ivaska, J., Ny, T., and Eriksson, J. E. Vimentin coordinates fibroblast proliferation and keratinocyte differentiation in wound healing via TGF-βSlug signaling. *Proceedings of the National Academy of Sciences*, 113(30):E4320–E4327, 2016.

[110] Wikramanayake, T. C., Stojadinovic, O., and Tomic-Canic, M. Epidermal differentiation in barrier maintenance and wound healing. *Advances in Wound Care*, 3(3):272–280, 2014.

[111] Gillitzer, R. and Goebeler, M. Chemokines in cutaneous wound healing. *Journal of Leukocyte Biology*, 69(4):513–21, 2001.

[112] Werner, S. and Grose, R. Regulation of wound healing by growth factors and cytokines. *Physiol Rev*, 83(3):835–870, 2003.

[113] Delavary, B. M., van der Veer, W. M., van Egmond, M., Niessen, F. B., and Beelen, R. H. J. Macrophages in skin injury and repair. *Immunobiology*, 216(7):753–62, 2011.

[114] Willenborg, S. and Eming, S. A. Macrophages - sensors and effectors coordinating skin damage and repair. *Journal of the German Society of Dermatology*, 12(3):214–21, 214–23, 2014.

[115] Mann, G. B., Fowler, K. J., Gabriel, A., Nice, E. C., Williams, R. L., and Dunn, A. R. Mice with a null mutation of the TGF alpha gene have abnormal skin architecture, wavy hair, and curly whiskers and often develop corneal inflammation. *Cell*, 73(2):249–61, 1993.

[116] Luetteke, N. C., Qiu, T. H., Peiffer, R. L., Oliver, P., Smithies, O., and Lee, D. C. TGF alpha deficiency results in hair follicle and eye abnormalities in targeted and waved-1 mice. *Cell*, 73(2):263–78, 1993.

[117] Ortega, S., Ittmann, M., Tsang, S. H., Ehrlich, M., and Basilico, C. Neuronal defects and delayed wound healing in mice lacking fibroblast growth factor 2. *Proceedings of the National Academy of Sciences*, 95(10):5672–7, 1998.

[118] Johnson, F. R. and McMinn, R. M. H. The cytology of wound healing of body surfaces in mammals. *Biological Reviews*, 35(3):364–410, 1960.

[119] Paladini, R. D. Onset of re-epithelialization after skin injury correlates with a reorganization of keratin filaments in wound edge keratinocytes: defining a potential role for keratin 16. *The Journal of Cell Biology*, 132(3):381–397, 1996.

[120] Usui, M. L., Underwood, R. A., Mansbridge, J. N., Muffley, L. A., Carter, W. G., and Olerud, J. E. Morphological evidence for the role of suprabasal keratinocytes in wound reepithelialization. *Wound Repair and Regeneration*, 13(5):468–79, 2005.

[121] Lau, K., Paus, R., Tiede, S., Day, P., and Bayat, A. Exploring the role of stem cells in cutaneous wound healing. *Experimental Dermatology*, 18(11):921–933, 2009.

[122] Gustafsson, E. and Fässler, R. Insights into extracellular matrix functions from mutant mouse models. *Experimental Cell Research*, 261(1):52–68, 2000.

[123] Sriram, G., Bigliardi, P. L., and Bigliardi-Qi, M. Fibroblast heterogeneity and its implications for engineering organotypic skin models in vitro. *European Journal of Cell Biology*, 94(11):483–512, 2015.

[124] Bernabei, P., Rigamonti, L., Ariotti, S., Stella, M., Castagnoli, C., and Novelli, F. Functional analysis of T lymphocytes infiltrating the dermis and epidermis of post-burn hypertrophic scar tissues. *Burns*, 25(1):43–48, 1999.

[125] Gersch, C., Dewald, O., Zoerlein, M., Michael, L. H., Entman, M. L., and Frangogiannis, N. G. Mast cells and macrophages in normal C57/BL/6 mice. *Histochemistry and Cell Biology*, 118(1):41–9, 2002.

[126] Pool, J. G. Normal hemostatic mechanisms: a review. *The American Journal of Medical Technology*, 43(8):776–80, 1977.

[127] Velnar, T., Bailey, T., and Smrkolj, V. The wound healing process: an overview of the cellular and molecular mechanisms. *Journal of International Medical Research*, 37(5):1528–1542, 2009.

[128] Golebiewska, E. M. and Poole, A. W. Platelet secretion: from haemostasis to wound healing and beyond. *Blood Reviews*, 29(3):153–162, 2015.

[129] Numata, Y., Terui, T., Okuyama, R., Hirasawa, N., Sugiura, Y., Miyoshi, I., Watanabe, T., Kuramasu, A., Tagami, H., and Ohtsu, H. The accelerating effect of histamine on the cutaneous wound-healing process through the action of basic fibroblast growth factor. *Journal of Investigative Dermatology*, 126(6):1403–1409, 2006.

[130] Gethin, G. Understanding the inflammatory process in wound healing. *British Journal of Community Nursing*, Suppl:S17–8, S20, S22, 2012.

[131] Koh, T. J. and DiPietro, L. A. Inflammation and wound healing: the role of the macrophage. *Expert Reviews in Molecular Medicine*, 13:e23, 2011.

[132] Rajan, V. and Murray, R. Z. The duplicitous nature of inflammation in wound repair. *Wound Practice and Research*, 16(3):122–129, 2008.

[133] Dvorak, H. F. Tumors: wounds that do not heal. Similarities between tumor stroma generation and wound healing. *The New England Journal of Medicine*, 315(26):1650–9, 1986.

[134] Gabbiani, G., Lous, M. L., Bailey, A. J., Bazin, S., and Delaunay, A. Collagen and myofibroblasts of granulation tissue. A chemical, ultrastructural and immunologic study. *Virchows Archiv B*, 21(1):133–145, 1976.

[135] Olczyk, P., Mencner, Ł., and Komosinska-Vassev, K. The role of the extracellular matrix components in cutaneous wound healing. *BioMed Research International*, 2014:747584, 2014.

[136] Li, J., Zhang, Y.-P., and Kirsner, R. S. Angiogenesis in wound repair: angiogenic growth factors and the extracellular matrix. *Microscopy Research and Technique*, 60:107–114, 2003.

[137] Velazquez, O. C. Angiogenesis and vasculogenesis: inducing the growth of new blood vessels and wound healing by stimulation of bone marrow-derived progenitor cell mobilization and homing. *Journal of Vascular Surgery*, 45(Suppl A):A39–47, 2007.

[138] Thannickal, V. J., Lee, D. Y., White, E. S., Cui, Z., Larios, J. M., Chacon, R., Horowitz, J. C., Day, R. M., and Thomas, P. E. Myofibroblast differentiation by transforming growth factor-1 is dependent on cell adhesion and integrin signaling via focal adhesion kinase. *Journal of Biological Chemistry*, 278(14):12384–12389, 2003.

[139] Chan, M. W. C., Chaudary, F., Lee, W., Copeland, J. W., and McCulloch, C. A. Force-induced myofibroblast differentiation through collagen receptors is dependent on mammalian diaphanous (mDia). *Journal of Biological Chemistry*, 285(12):9273–9281, 2010.

[140] Wang, J., Chen, H., Seth, A., and McCulloch, C. A. Mechanical force regulation of myofibroblast differentiation in cardiac fibroblasts. *American Journal of Physiology - Heart and Circulatory Physiology*, 285(5):H1871–H1881, 2003.

[141] Gabbiani, G., Hirschel, B. J., Ryan, G. B., Statkov, P. R., and Majno, G. Granulation tissue as a contractile organ. A study of structure and function. *The Journal of Experimental Medicine*, 135(4):719–34, 1972.

[142] Ibrahim, M. M., Chen, L., Bond, J. E., Medina, M. A., Ren, L., Kokosis, G., Selim, A. M., and Levinson, H. Myofibroblasts contribute to but are not necessary for wound contraction. *Laboratory Investigation*, 95(12):1429–1438, 2015.

[143] Xue, M. and Jackson, C. J. Extracellular matrix reorganization during wound healing and its impact on abnormal scarring. *Advances in Wound Care*, 4(3):119–136, 2015.

[144] Shah, J. M. Y., Omar, E., Pai, D. R., and Sood, S. Cellular events and biomarkers of wound healing. *Indian Journal of Plastic Surgery*, 45(2):220–8, 2012.

[145] Ansell, D. M., Campbell, L., Thomason, H. A., Brass, A., and Hardman, M. J. A statistical analysis of murine incisional and excisional acute wound models. *Wound Repair and Regeneration*, 22(2):281–7, 2014.

[146] Canesso, M. C. C., Vieira, A. T., Castro, T. B. R., Schirmer, B. G. A., Cisalpino, D., Martins, F. S., Rachid, M. A., Nicoli, J. R., Teixeira, M. M., and Barcelos, L. S. Skin wound healing is accelerated and scarless in the absence of commensal microbiota. *The Journal of Immunology*, 193(10):5171–5180, 2016.

[147] Hamblin, M. R., Zahra, T., Contag, C. H., McManus, A. T., and Hasan, T. Optical monitoring and treatment of potentially lethal wound infections in vivo. *The Journal of Infectious Diseases*, 187(11):1717–1726, 2003.

[148] Holcomb, V. B., Keck, V. A., Barrett, J. C., Hong, J., Libutti, S. K., and Nunez, N. P. Obesity impairs wound healing in ovariectomized female mice. *In Vivo*, 23(4):515–8, 2009.

[149] Liu, M., Saeki, K., Matsunobu, T., Okuno, T., Koga, T., Sugimoto, Y., Yokoyama, C., Nakamizo, S., Kabashima, K., Narumiya, S., Shimizu, T., and Yokomizo, T. 12-hydroxyheptadecatrienoic acid promotes epidermal wound healing by accelerating keratinocyte migration via the BLT2 receptor. *The Journal of Experimental Medicine*, 211(6):1063–1078, 2014.

[150] Rønø, B., Engelholm, L. H., Lund, L. R., Hald, A., Schuster, V., Hugle, B., Tefs, K., Mehta, R., Shapiro, A., Bugge, T., Flick, M., Daugherty, C., Degen, J., Hald, A., Rono, B., Melander, M., Ding, M., Holck, S., Romer, J., Bugge, T., Pyke, C., Lund, L., Flick, M., Schuster, V., Seregard, S., Ploplis, V., French, E., Carmeliet, P., Collen, D., Plow, E., Gong, Y., Hart, E., Shchurin, A., Hoover-Plow, J., McColl, B., Baldwin, M., Roufail, S., Freeman, C., Moritz, R., Heissig, B., Lund, L., Akiyama, H., Ohki, M., Morita, Y., Lund, L., Green, K., Stoop, A., Ploug, M., Almholt, K., Lund, L., Romer, J., Bugge, T., Nielsen, B., Frandsen, T., Egeblad, M., Werb, Z., Hald, A., Rono, B., Lund, L., Egerod, K., McMahon, B., Kwaan, H., Dano, K., Behrendt, N., Hoyer-Hansen, G., Johnsen, M., Lund, L., Palumbo, J., Talmage, K., Liu, H., Jeunesse, C. L., Witte, D., Green, K., Almholt, K., Ploug, M., Rono, B., Castellino, F., Bugge, T., Flick, M., Danton, M., Daugherty, C., Romer, J., Jogi, A., Pass, J., Hoyer-Hansen, G., Lund, L., Nielsen, B., Lund, I., Jogi, A., Rono, B., Rasch, M., Lund, L., Larmann, J., Frenzel, T., Hahnenkamp, A., Herzog, C., Lorenz, A., Lund, L., Bjorn, S., Sternlicht, M., Nielsen, B., Solberg, H., Green, K., Nielsen, B., Castellino, F., Romer, J., Lund, L., Bugge, T., Kombrinck, K., Flick, M., Daugherty, C., Danton, M., Ashcroft, G., Mills, S., Lei, K., Gibbons, L., Jeong, M., Feng, X., Clark, R., Galanakis, D., Tonnesen, M., Hattori, N., Mochizuki, S., Kishi, K., Nakajima, T., Takaishi, H., Binder, B., Mihaly, J., Prager, G., Ploplis, V., Carmeliet, P., Vazirzadeh, S., Vlaenderen, I. V., Moons, L., Swaisgood, C., French, E., Noga, C., Simon, R., Ploplis, V., Arumugam, S., Jang, Y., Chen-Jensen, C., Gibran, N., Isik, F., Frossing, S., Rono, B., Hald, A., Romer, J., Lund, L., Bator, J., Cohen, R., Chambers, D., Island, E., Wu, H., Warburton, D., Anderson, K., Tuan, T., Weckroth, M., Vaheri, A., Virolainen, S., Saarialho-Kere, U., Jahkola, T., Murphy, G., Stanton, H., Cowell, S., Butler, G., Knauper, V., Juncker-Jensen, A., Lund, L., Velnar, T., Bailey, T., Smrkolj, V., Gilliver, S., Hotary, K., Yana, I., Sabeh, F., Li, X., Holmbeck, K., Grandas, O., Mountain, D., Kirkpatrick, S., Cassada, D., Stevens, S., Campbell, L., Emmerson, E., Davies, F., Gilliver, S., Krust, A., Azzi, L., El-Alfy, M.,

Martel, C., Labrie, F., Shuster, S., Black, M., McVitie, E., Pins, G., Collins-Pavao, M., Water, L. V. D., Yarmush, M., and Morgan, J. Gender affects skin wound healing in plasminogen deficient mice. *PLoS One*, 8(3):e59942, 2013.

[151] Thuraisingam, T., Sam, H., Moisan, J., Zhang, Y., Ding, A., and Radzioch, D. Delayed cutaneous wound healing in mice lacking solute carrier 11a1 (formerly Nramp1): correlation with decreased expression of secretory leukocyte protease inhibitor. *Journal of Investigative Dermatology*, 126(4):890–901, 2006.

[152] Jørgensen, L. B., Sørensen, J. A., Jemec, G. B., and Yderstraede, K. B. Methods to assess area and volume of wounds - a systematic review. *International Wound Journal*, 13(4):540–553, 2016.

[153] Gethin, G. and Cowman, S. Wound measurement comparing the use of acetate tracings and VisitrakTM digital planimetry. *Journal of Clinical Nursing*, 15(4):422–427, 2006.

[154] Shaw, J., Hughes, C. M., Lagan, K. M., Bell, P. M., and Stevenson, M. R. An evaluation of three wound measurement techniques in diabetic foot wounds. *Diabetes Care*, 30(10):2641–2, 2007.

[155] Hoeffelin, H., Jacquemin, D., Defaweux, V., and Nizet, J. L. A methodological evaluation of volumetric measurement techniques including three-dimensional imaging in breast surgery. *BioMed Research International*, 573249, 2014.

[156] Ceinos, R., Tardivo, D., Bertrand, M.-F., and Lupi-Pegurier, L. Inter- and intra-operator reliability of facial and dental measurements using 3D-stereophotogrammetry. *Journal of Esthetic and Restorative Dentistry*, 28(3):178–189, 2016.

[157] Skvara, H., Burnett, P., Jones, J., Duschek, N., Plassmann, P., and Thirion, J.-P. Quantification of skin lesions with a 3D stereovision camera system: validation and clinical applications. *Skin Research and Technology*, 19(1):e182–90, 2013.

[158] Stockton, K., McMillan, C., Storey, K., David, M., and Kimble, R. 3D photography is as accurate as digital planimetry tracing in determining burn wound area. *Burns*, 41(1):80–84, 2015.

[159] Gee Kee, E., Kimble, R., and Stockton, K. 3D photography is a reliable burn wound area assessment tool compared to digital planimetry in very young children. *Burns*, 41(6):1286–1290, 2015.

[160] Hamilton, E., Howard, A., and Potten, C. S. Cell kinetics in the sebaceous glands of the mouse. II. The glands during hair growth. *Cell and Tissue Kinetics*, 7(4):399–405, 1974.

[161] Engel, O., Kolodziej, S., Dirnagl, U., and Prinz, V. Modeling stroke in mice - middle cerebral artery occlusion with the filament model. *JoVE - Journal of Visualized Experiments*, 47:e2423, 2011.

[162] R Core Team, . *R: a language and environment for statistical computing*. R Foundation for Statistical Computing, Vienna, Austria, 2015.

[163] Rogers, L. C., Bevilacqua, N. J., Armstrong, D. G., and Andros, G. Digital planimetry results in more accurate wound measurements: a comparison to standard ruler measurements. *Journal of Diabetes Science and Technology*, 4(4), 2010.

[164] Shetty, R., Sreekar, H., Lamba, S., and Gupta, A. K. A novel and accurate technique of photographic wound measurement. *Indian Journal of Plastic Surgery*, 45(2):425–9, 2012.

[165] Kantor, J. M. and Margolis, D. J. Efficacy and prognostic value of simple wound measurements. *Archives of Dermatology*, 134(12):438–1574, 1998.

[166] Bowling, F. L., King, L., Fadavi, H., Paterson, J. A., Preece, K., Daniel, R. W., Matthews, D. J., and Boulton, A. J. M. An assessment of the accuracy and usability of a novel optical wound measurement system. *Diabetic Medicine*, 26(1):93–96, 2009.

[167] Jung, K., Covington, S., Sen, C. K., Januszyk, M., Kirsner, R. S., Gurtner, G. C., and Shah, N. H. Rapid identification of slow healing wounds. *Wound Repair and Regeneration*, 24(1):181–188, 2015.

[168] Bhedi, A., Saxena, A. K., Gadani, R., and Patel, R. Digital photography and transparency-based methods for measuring wound surface area. *The Indian Journal of Surgery*, 75(2):111–4, 2013.

[169] Langemo, D. K., Melland, H., Hanson, D., Olson, B., Hunter, S., and Henly, S. J. Two-dimensional wound measurement: comparison of 4 techniques. *Advances in Wound Care*, 11(7):337–43, 1998.

[170] Baron, M., Chung, L., Gyger, G., Hummers, L., Khanna, D., Mayes, M. D., Pope, J. E., Shah, A. A., Steen, V. D., Steele, R., Tatibouet, S., Herrick, A., Müller-Ladner, U., and Hudson, M. Consensus opinion of a North American Working Group regarding the classification of digital ulcers in systemic sclerosis. *Clinical Rheumatology*, 33(2):207–214, 2014.

[171] Okon, L. and Werth, V. P. Challenges in measuring outcomes: Size assessment of an individual cutaneous lesion. *Journal of the American Academy of Dermatology*, 71(2):402–404, 2014.

[172] Garrod, D. R., Berika, M. Y., Bardsley, W. F., Holmes, D., and Tabernero, L. Hyper-adhesion in desmosomes: its regulation in wound healing and possible relationship to cadherin crystal structure. *Journal of Cell Science*, 118(24):5743–54, 2005.

[173] Hopkinson, S. B., Hamill, K. J., Wu, Y., Eisenberg, J. L., Hiroyasu, S., and Jones, J. C. R. Focal contact and hemidesmosomal proteins in keratinocyte migration and wound repair. *Advances in Wound Care*, 3(3):247–263, 2014.

[174] Li, J., Chen, J., and Kirsner, R. Pathophysiology of acute wound healing. *Clinics in Dermatology*, 25(1):9–18, 2007.

[175] Shaw, T. J. and Martin, P. Wound repair at a glance. *Journal of Cell Science*, 122(18):3209–13, 2009.

[176] Guest, J. F., Ayoub, N., McIlwraith, T., Uchegbu, I., Gerrish, A., Weidlich, D., Vowden, K., and Vowden, P. Health economic burden that wounds impose on the National Health Service in the UK. *BMJ Open*, 5(12):e009283, 2015.

[177] Tricco, A. C., Cogo, E., Isaranuwatchai, W., Khan, P. A., Sanmugalingham, G., Antony, J., Hoch, J. S., Straus, S. E., Mustoe, T., O'Shaughnessy, K., Kloeters, O., Gottrup, F., Sen, C., Gordillo, G., Roy, S., Kirsner, R., Lambert, L., Hunt, T., Swanson, L., Miller, P., Jull, A., Rodgers, A., Walker, N., Lazarus, G., Cooper, D., Knighton, D., Percoraro, R., Rodeheaver, G., Robson, M., Werdin, F., Tennenhaus, M., Schaller, H., Rennekampff, H., Sampson, M., McGowan, J., Cogo, E., Grimshaw, J., Moher, D., Lefebvre, C., Stone, P., Black, W., Drummond, M., Augustin, M., Siegel, A., Heuser, A., Vanscheidt, W., DePalma, R., Kowallek, D., Spence, R., Caprini, J., Nehler, M., Jensen, J., Glinski, W., Chodynicka, B., Roszkiewicz, J., Bogdanowski, T., Lecewicz-Torun, B., Kaszuba, A., Gordon, L., Edwards, H., Courtney, M., Finlayson, K., Shuter, P., Lindsay, E., Guest, J., Taylor, R., Vowden, K., Vowden, P., Iglesias, C., Claxton, K., Iglesias, C., Nelson, E., Cullum, N., Torgerson, D., Jull, A., Walker, N., Parag, V., Molan, P., Rodgers, A., Junger, M., Arnold, A., Zuder, D., Stahl, H., Heising, S., Kerstein, M., Gahtan, V., Kikta, M., Schuler, J., Meyer, J., Durham, J., Eldrup-Jorgensen, J., Schwarcz, T., Michaels, J., Campbell, W., King, B., Macintyre, J., Palfreyman, S., Shackley, P., Morrell, C., Walters, S., Dixon, S., Collins, K., Brereton, L., Peters, J., O'Brien, J., Grace, P., Perry, I., Hannigan, A., Moloney, M. C., Burke, P., Oien, R., Hakansson, A., Ahnlide, I., Bjellerup,

M., Hansen, B., Borgquist, L., Sibbald, R., Torrance, G., Walker, V., Attard, C., MacNeil, P., Taylor, A., Taylor, R., Marcuson, R., Ukat, A., Konig, M., Vanscheidt, W., Munter, K., Watson, J., Kang'ombe, A., Soares, M., Chuang, L., Worthy, G., Bland, J., Pham, B., Harrison, M., Chen, M., Carley, M., Schonfeld, W., Villa, K., Fastenau, J., Mazonson, P., Falanga, V., Simon, D., Freak, L., Kinsella, A., Walsh, J., Lane, C., Groarke, L., Carr, L., Phillips, Z., Posnett, J., Guest, J., Nagy, E., Sladkevicius, E., Vowden, P., Price, P., Dumville, J., Worthy, G., Soares, M., Bland, J., Cullum, N., Dowson, C., Ohlsson, P., Larsson, K., Lindholm, C., Moller, M., Abidia, A., Laden, G., Kuhan, G., Johnson, B., Wilkinson, A., Renwick, P., Apelqvist, J., Ragnarson, T., Edmonds, M., Gough, A., Solovera, J., Standaert, B., Guo, S., Counte, M., Gillespie, K., Schmitz, H., Habacher, W., Rakovac, I., Gorzer, E., Haas, W., Gfrerer, R., Wach, P., Horswell, R., Birke, J., Patout, C., Jansen, J., Kumar, R., Carmeli, Y., Jeffcoate, W., Price, P., Phillips, C., Game, F., Mudge, E., Davies, S., McKinnon, P., Paladino, J., Grayson, M., Gibbons, G., Karchmer, A., Persson, U., Willis, M., Odegaard, K., Apelqvist, J., Piaggesi, A., Macchiarini, S., Rizzo, L., Palumbo, F., Tedeschi, A., Nobili, L., Redekop, W., McDonnel, J., Verboom, P., Lovas, K., Kalo, Z., Allenet, B., Paree, F., Lebrun, T., Carr, L., Posnett, J., Martinin, J., Ghatnekar, O., Willis, M., Persson, U., Ghatnekar, O., Persson, U., Willis, M., Odegaard, K., Hailey, D., Jacobs, P., Perry, D., Chuck, A., Morrison, A., Boudreau, R., Branom, R., Rappl, L., Burgos, A., Gimenez, J., Moreno, E., Lamberto, E., Utrera, M., Urraca, E., Chang, K., Alsagoff, S., Ong, K., Sim, P., Chuangsuwanich, A., Charnsanti, O., Lohsiriwat, V., Kangwanpoom, C., Thong-In, N., Ferrell, B., Keeler, E., Siu, A., Ahn, S., Osterweil, D., Foglia, E., Restelli, U., Napoletano, A., Coclite, D., Porazzi, E., Bonfanti, M., Graumlich, J., Blough, L., McLaughlin, R., Milbrandt, J., Calderon, C., Agha, S., Muller, E., Leen, M., Bergemann, R., Narayanan, S., Vleet, J., Strunk, B., Ross, R., Gray, M., Payne, W., Posnett, J., Alvarez, O., Brown-Etris, M., Jameson, G., Wolcott, R., Robson, M., Hill, D., Smith, P., Wang, X., Meyer-Siegler, K., Ko, F., Sanada, H., Nakagami, G., Mizokami, Y., Minami, Y., Yamamoto, A., Oe, M., Xakellis, G., Chrischilles, E., Sebern, M., Bale, S., Hagelstein, S., Banks, V., Harding, K., Terry, M., Halstead, L., O'Hare, P., Gaskill, C., Ho, P., Obecny, J., Vu, T., Harris, A., Duncan, G., Sussman, G., Sebern, M., Chuck, A., Hailey, D., Jacobs, P., and Perry, D. A systematic review of cost-effectiveness analyses of complex wound interventions reveals optimal treatments for specific wound types. *BMC Medicine*, 13(1):90, 2015.

[178] Geris, L., Gerisch, A., and Schugart, R. C. Mathematical modeling in wound healing, bone regeneration and tissue engineering. *Acta Biotheoretica*, 58(4):355–67, 2010.

[179] Geris, L., Schugart, R., and Van Oosterwyck, H. In silico design of treatment strategies

in wound healing and bone fracture healing. *Philosophical Transactions, Series A: Mathematical, Physical, and Engineering Sciences*, 368:2683–706, 2010.

[180] Smallwood, R. Computational modeling of epithelial tissues. *Wiley interdisciplinary reviews: Systems Biology and Medicine*, 1(2):191–201, 2009.

[181] Maclaren, O. J., Fletcher, A. G., Byrne, H. M., and Maini, P. K. Models, measurement and inference in epithelial tissue dynamics. *Mathematical Biosciences and Engineering*, 12(6):1321–1340, 2015.

[182] Adam, J. A simplified model of wound healing (with particular reference to the critical size defect). *Mathematical and Computer Modelling*, 30:23–32, 1999.

[183] Arnold, J. and Adam, J. A simplified model of wound healing II: The critical size defect in two dimensions. *Mathematical and Computer Modelling*, 30(11-12):47–60, 1999.

[184] Bowden, L. G., Maini, P. K., Moulton, D. E., Tang, J. B., Wang, X. T., Liu, P. Y., and Byrne, H. M. An ordinary differential equation model for full thickness wounds and the effects of diabetes. *Journal of Theoretical Biology*, 361:87–100, 2014.

[185] Denman, P. K., McElwain, D. L. S., Harkin, D. G., and Upton, Z. Mathematical modelling of aerosolised skin grafts incorporating keratinocyte clonal subtypes. *Bulletin of Mathematical Biology*, 69(1):157–79, 2007.

[186] Maini, P. K., McElwain, D. L. S., and Leavesley, D. I. Traveling wave model to interpret a wound-healing cell migration assay for human peritoneal mesothelial cells. *Tissue Engineering*, 10(3-4):475–82, 2004.

[187] Javierre, E., Moreo, P., Doblaré, M., and García-Aznar, J. Numerical modeling of a mechano-chemical theory for wound contraction analysis. *International Journal of Solids and Structures*, 46(20):3597–3606, 2009.

[188] Jones, M., Song, B., and Thomas, D. Controlling wound healing through debridement. *Mathematical and Computer Modelling*, 40(9-10):1057–1064, 2004.

[189] Maggelakis, S. A. A mathematical model of tissue replacement during epidermal wound healing. *Applied Mathematical Modelling*, 27(3):189–196, 2003.

[190] Sherratt, J. A. and Murray, J. D. Epidermal wound healing; a theoretical approach. *Comments on Theoretical Biology*, 2:315–333, 1992.

[191] Sherratt, J. A. and Murray, J. D. Epidermal wound healing: the clinical implications of a simple mathematical model. *Cell Transplant*, 1:365–371, 1992.

[192] Sun, T., Adra, S., Smallwood, R., Holcombe, M., and MacNeil, S. Exploring hypotheses of the actions of TGF-beta1 in epidermal wound healing using a 3D computational multiscale model of the human epidermis. *PloS One*, 4(12):e8515, 2009.

[193] Sun, T., McMinn, P., Coakley, S., Holcombe, M., Smallwood, R., and Macneil, S. An integrated systems biology approach to understanding the rules of keratinocyte colony formation. *Journal of the Royal Society Interface*, 4(17):1077–92, 2007.

[194] Vermolen, F. J. and Adam, J. A. A finite element model for epidermal wound healing. In Shi, Y., van Albada, G. D., Dongarra, J., and Sloot, P. M. A. (editors), *Computational Science - ICCS 2007*, pages 70–77. Springer Berlin Heidelberg, 2007.

[195] Gaffney, E. A., Pugh, K., Maini, P. K., and Arnold, F. Investigating a simple model of cutaneous wound healing angiogenesis. *Journal of Mathematical Biology*, 45:337–374, 2002.

[196] Zahouani, H., Assoul, M., Janod, P., and Mignot, J. Theoretical and experimental study of wound healing: Application to leg ulcers. *Medical & Biological Engineering & Computing*, 30(2):234–239, 1992.

[197] Buganza Tepole, A. and Kuhl, E. Systems-based approaches toward wound healing. *Pediatric Research*, 73(4):553–563, 2013.

[198] Dunster, J. L. The macrophage and its role in inflammation and tissue repair: mathematical and systems biology approaches. *Wiley Interdisciplinary Reviews: Systems Biology and Medicine*, 8(1):87–99, 2016.

[199] Macleod, A. S. and Mansbridge, J. N. The innate immune system in acute and chronic wounds. *Advances in Wound Care*, 5(2):65–78, 2016.

[200] Bauer, A. L., Beauchemin, C. A. A., and Perelson, A. S. Agent-based modeling of host-pathogen systems: The successes and challenges. *Information Sciences*, 179(10):1379–1389, 2009.

[201] Barrientos, S., Stojadinovic, O., Golinko, M. S., Brem, H., and Tomic-Canic, M. Growth factors and cytokines in wound healing. *Wound Repair and Regeneration*, 16(5):585–601, 2008.

[202] Alden, K., Read, M., Timmis, J., Andrews, P. S., Veiga-Fernandes, H., and Coles, M. Spartan: a comprehensive tool for understanding uncertainty in simulations of biological systems. *PLoS Computational Biology*, 9(2):e1002916, 2013.

[203] Marino, S., Hogue, I. B., Ray, C. J., and Kirschner, D. E. A methodology for performing global uncertainty and sensitivity analysis in systems biology. *Journal of Theoretical Biology*, 254(1):178–96, 2008.

[204] Read, M., Andrews, P. S., Timmis, J., and Kumar, V. Techniques for grounding agent-based simulations in the real domain: a case study in experimental autoimmune encephalomyelitis. *Mathematical and Computer Modelling of Dynamical Systems*, 18(1):67–86, 2012.

[205] An, G., Mi, Q., Dutta-Moscato, J., and Vodovotz, Y. Agent-based models in translational systems biology. *Wiley Interdisciplinary Reviews: Systems Biology and Medicine*, 1(2):159–71, 2009.

[206] Cosgrove, J., Butler, J., Alden, K., Read, M., Kumar, V., Cucurull-Sanchez, L., Timmis, J., and Coles, M. Agent-based modeling in systems pharmacology. *CPT Pharmacometrics & Systems Pharmacology*, 4(11):615–29, 2015.

[207] Butler, J., Alden, K., Fernandes, H., Timmis, J., and Coles, M. Novel approaches to the visualization and quantification of biological simulations by emulating experimental techniques. In *Artificial Life 14: Proceedings of the Fourteenth International Conference on the Synthesis and Simulation of Living Systems*, volume 14, pages 614–621. The MIT Press, 2014.

[208] Figueredo, G. P., Siebers, P.-O., and Aickelin, U. Investigating mathematical models of immuno-interactions with early-stage cancer under an agent-based modelling perspective. *BMC Bioinformatics*, 14(Suppl 6):S6, 2013.

[209] Stern, J. R., Christley, S., Zaborina, O., Alverdy, J. C., and An, G. Integration of TGF-β- and EGFR-based signaling pathways using an agent-based model of epithelial restitution. *Wound Repair and Regeneration*, 20(6):862–71, 2012.

[210] Brown, R. L., Ormsby, I., Doetschman, T. C., and Greenhalgh, D. G. Wound healing in the transforming growth factor-beta-deficient mouse. *Wound Repair and Regeneration*, 3(1):25–36, 1995.

[211] Jimenez, P. A. and Rampy, M. A. Keratinocyte growth factor-2 accelerates wound healing in incisional wounds. *The Journal of Surgical Research*, 81(2):238–42, 1999.

[212] Jones, S. C., Curtsinger, L. J., Whalen, J. D., Pietsch, J. D., Ackerman, D., Brown, G. L., and Schultz, G. S. Effect of topical recombinant TGF-beta on healing of partial thickness injuries. *The Journal of Surgical Research*, 51(4):344–52, 1991.

[213] Lynch, S. E., Colvin, R. B., and Antoniades, H. N. Growth factors in wound healing: Single and synergistic effects on partial thickness porcine skin wounds. *The Journal of Clinical Investigation*, 84(2):640–6, 1989.

[214] Adra, S., Sun, T., MacNeil, S., Holcombe, M., and Smallwood, R. Development of a three dimensional multiscale computational model of the human epidermis. *PloS One*, 5(1):e8511, 2010.

[215] Vilar, J. M. G., Jansen, R., and Sander, C. Signal processing in the TGF-beta superfamily ligand-receptor network. *PLoS Computational Biology*, 2(1):e3, 2006.

[216] Kirfel, G. and Herzog, V. Migration of epidermal keratinocytes: mechanisms, regulation, and biological significance. *Protoplasma*, 223:67–78, 2004.

[217] Woodley, D. T., Wysong, A., DeClerck, B., Chen, M., and Li, W. Keratinocyte migration and a hypothetical new role for extracellular heat shock protein 90 alpha in orchestrating skin wound healing. *Advances in Wound Care*, 4(4):203–212, 2015.

[218] Vermolen, F. J. and Javierre, E. A finite-element model for healing of cutaneous wounds combining contraction, angiogenesis and closure. *Journal of Mathematical Biology*, 65(5):967–96, 2012.

[219] Sherratt, J. A. and Murray, J. D. Mathematical analysis of a basic model for epidermal wound healing. *Journal of Mathematical Biology*, 29(5):389–404, 1991.

[220] An, G., Faeder, J., and Vodovotz, Y. Translational systems biology: introduction of an engineering approach to the pathophysiology of the burn patient. *Journal of Burn Care and Research*, 29(2):277–285, 2008.

[221] Chang, E. T., Strong, M., and Clayton, R. H. Bayesian sensitivity analysis of a cardiac cell model using a gaussian process emulator. *PLoS One*, 10(6):e0130252, 2015.

[222] Sun, Z., Unutmaz, D., Zou, Y.-R., Sunshine, M. J., Pierani, A., Brenner-Morton, S., Mebius, R. E., and Littman, D. R. Requirement for RORgamma in Thymocyte Survival and Lymphoid Organ Development. *Science*, 288(5475):2369–2373, 2000.

[223] Foudi, A., Hochedlinger, K., Van Buren, D., Schindler, J. W., Jaenisch, R., Carey, V., and Hock, H. Analysis of histone 2B-GFP retention reveals slowly cycling hematopoietic stem cells. *Nature Biotechnology*, 27(1):84–90, 2009.

[224] Carpenter, A. E., Jones, T. R., Lamprecht, M. R., Clarke, C., Kang, I., Friman, O., Guertin, D. A., Chang, J., Lindquist, R. A., Moffat, J., Golland, P., Sabatini, D. M., Moffat, J., Grueneberg, D., Yang, X., Kim, S., Kloepfer, A., Hinkle, G., Piqani, B.,

Eisenhaure, T., Luo, B., Grenier, J., Dasgupta, R., Perrimon, N., Carpenter, A., Sabatini, D., Vanhecke, D., Janitz, M., Echeverri, C., Perrimon, N., Kiger, A., Baum, B., Jones, S., Jones, M., Coulson, A., Echeverri, C., Perrimon, N., Kim, J., Gabel, H., Kamath, R., Tewari, M., Pasquinelli, A., Rual, J., Kennedy, S., Dybbs, M., Bertin, N., Kaplan, J., Mitchison, T., Perlman, Z., Mitchison, T., Mayer, T., Perlman, Z., Slack, M., Feng, Y., Mitchison, T., Wu, L., Altschuler, S., Taylor, D., Giuliano, K., Abraham, V., Taylor, D., Haskins, J., Bjorklund, M., Taipale, M., Varjosalo, M., Saharinen, J., Lahdenpera, J., Taipale, J., Ohya, Y., Sese, J., Yukawa, M., Sano, F., Nakatani, Y., Saito, T., Saka, A., Fukuda, T., Ishihara, S., Oka, S., Levsky, J., Singer, R., Sachs, K., Perez, O., Pe'er, D., Lauffenburger, D., Nolan, G., Gil, J., Wu, H., Wang, B., Chen, X., Murphy, R., Doudkine, A., Macaulay, C., Poulin, N., Palcic, B., Guillaud, M., Adler-Storthz, K., Malpica, A., Staerkel, G., Matisic, J., Niekirk, D. V., Cox, D., Poulin, N., Follen, M., Macaulay, C., Abramoff, M., Magalhaes, P., Ram, S., Zhou, X., Cao, X., Perlman, Z., Wong, S., Lindblad, J., Wahlby, C., Bengtsson, E., Zaltsman, A., Garippa, R., Harada, J., Bower, K., Orth, A., Callaway, S., Nelson, C., Laris, C., Hogenesch, J., Vogt, P., Chanda, S., Wheeler, D., Bailey, S., Guertin, D., Carpenter, A., Higgins, C., Sabatini, D., Armknecht, S., Boutros, M., Kiger, A., Nybakken, K., Mathey-Prevot, B., Perrimon, N., Price, J., Goodacre, A., Hahn, K., Hodgson, L., Hunter, E., Krajewski, S., Murphy, R., Rabinovich, A., Reed, J., Heynen, S., Eggert, U., Mitchison, T., Murphy, R., Meijering, E., Danuser, G., Jones, T., Carpenter, A., Sabatini, D., Golland, P., Wahlby, C., Malpica, N., de Solorzano, C., Vaquero, J., Santos, A., Vallcorba, I., Garcia-Sagredo, J., del Pozo, F., Wahlby, C., Sintorn, I., Erlandsson, F., Borgefors, G., Bengtsson, E., de Solorzano, C. O., Rodriguez, E., Jones, A., Pinkel, D., Gray, J., Sudar, D., Lockett, S., Meyer, F., Beucher, S., Jones, T., Carpenter, A., Golland, P., Boland, M., Murphy, R., Rodenacker, K., Bengtsson, E., Boland, M., Markey, M., Murphy, R., Haralick, R., Shanmuga, K., Dinstein, I., Gabor, D., Turner, M., Zhou, X., Liu, K., Bradley, P., Perrimon, N., Wong, S., Lockett, S., Jacobson, K., Herman, B., Poulin, N., Matthews, J., Skov, K., Palcic, B., Bailey, S., Ali, S., Carpenter, A., Higgins, C., Sabatini, D., Porter, K., Ravkin, I., Temov, V., Sigal, A., Milo, R., Cohen, A., Geva-Zatorsky, N., Klein, Y., Alaluf, I., Swerdlin, N., Perzov, N., Danon, T., Liron, Y., Philips, J., Rubin, E., Perrimon, N., Flockhart, I., Booker, M., Kiger, A., Boutros, M., Armknecht, S., Ramadan, N., Richardson, K., Xu, A., Perrimon, N., Mathey-Prevot, B., Swedlow, J., Goldberg, I., Brauner, E., Sorger, P., Stevens, B., Alvarez, C., Bohman, R., O'Connor, J., Zhang, J., Chung, T., Oldenburg, K., Ravkin, I., Ravkin, I., Temov, V., Nelson, A., Zarowitz, M., Hoopes, M., Verhovsky, Y., Ascue, G., Goldbard, S., Beske, O., and Bhagwat, B.

CellProfiler: image analysis software for identifying and quantifying cell phenotypes. *Genome Biology*, 7(10):R100, 2006.

[225] Bhattacharyya, T. K. and Thomas, J. R. Histomorphologic changes in aging skin. *Archives of Facial Plastic Surgery*, 6(1):21, 2004.

[226] Kietzmann, M., Lubach, D., and Heeren, H. J. The mouse epidermis as a model in skin pharmacology: influence of age and sex on epidermal metabolic reactions and their circadian rhythms. *Laboratory Animals*, 24(4):321–7, 1990.

[227] Azzi, L., El-Alfy, M., Martel, C., and Labrie, F. Gender differences in mouse skin morphology and specific effects of sex steroids and dehydroepiandrosterone. *The Journal of Investigative Dermatology*, 124(1):22–7, 2005.

[228] Fitzgerald, R. H. The relationship of wound shape to wound healing. *Podiatry Management*, 28(9):102, 2009.

[229] Simpson, D. M. and Ross, R. The neutrophilic leukocyte in wound repair. *Journal of Clinical Investigation*, 51(8):2009–2023, 1972.

[230] Dovi, J. V., He, L.-k., and Dipietro, L. A. Accelerated wound closure in neutrophil-depleted mice. *Journal of Leukocyte Biology*, 73(4):448–455, 2003.

[231] Martin, P., D'Souza, D., Martin, J., Grose, R., Cooper, L., Maki, R., and McKercher, S. R. Wound healing in the PU.1 null mouse–tissue repair is not dependent on inflammatory cells. *Current Biology*, 13(13):1122–8, 2003.

[232] Kim, Y. S., Lew, D. H., Tark, K. C., Rah, D. K., and Hong, J. P. Effect of recombinant human epidermal growth factor against cutaneous scar formation in murine full-thickness wound healing. *Journal of Korean Medical Science*, 25(4):589–96, 2010.

[233] Lindemann, S. R. and Lavalle, S. M. Simple and efficient algorithms for computing smooth, collision-free feedback laws over given cell decompositions. *The International Journal of Robotics Research*, 28(5):600–621, 2009.

[234] Van Liedekerke, P., Palm, M. M., Jagiella, N., and Drasdo, D. Simulating tissue mechanics with agent-based models: concepts, perspectives and some novel results. *Computational Particle Mechanics*, 2(4):401–444, 2015.

[235] Fennell, P. G., Melnik, S., and Gleeson, J. P. Limitations of discrete-time approaches to continuous-time contagion dynamics. *Physical Review E*, 94(5):052125, 2016.

[236] Buss, A. and Rowaei, A. A. A comparison of the accuracy of discrete event and discrete time. In *Proceedings of the 2010 Winter Simulation Conference*, pages 1468–1477. IEEE, 2010.

[237] Salathia, N. S., Shi, J., Zhang, J., and Glynne, R. J. An in vivo screen of secreted proteins identifies adiponectin as a regulator of murine cutaneous wound healing. *The Journal of Investigative Dermatology*, 133(3):812–21, 2013.

[238] Liang, X., Bhattacharya, S., Bajaj, G., Guha, G., Wang, Z., Jang, H.-S., Leid, M., Indra, A. K., and Ganguli-Indra, G. Delayed cutaneous wound healing and aberrant expression of hair follicle stem cell markers in mice selectively lacking Ctip2 in epidermis. *PloS One*, 7(2):e29999, 2012.

[239] Florin, L., Knebel, J., Zigrino, P., Vonderstrass, B., Mauch, C., Schorpp-Kistner, M., Szabowski, A., and Angel, P. Delayed wound healing and epidermal hyperproliferation in mice lacking JunB in the skin. *The Journal of Investigative Dermatology*, 126(4):902–11, 2006.

[240] Yang, L., Chan, T., Demare, J., Iwashina, T., Ghahary, A., Scott, P. G., and Tredget, E. E. Healing of burn wounds in transgenic mice overexpressing transforming growth factor-beta 1 in the epidermis. *The American Journal of Pathology*, 159(6):2147–57, 2001.

[241] Wong, V. W., Sorkin, M., Glotzbach, J. P., Longaker, M. T., and Gurtner, G. C. Surgical approaches to create murine models of human wound healing. *Journal of biomedicine & biotechnology*, page 969618, 2011.

[242] Kandyba, E., Hodgins, M., and Martin, P. A versatile murine 3D organotypic model to evaluate aspects of wound healing and epidermal organisation. *Methods in Molecular Biology*, 585:303–312, 2010.

[243] Bagabir, R., Syed, F., Paus, R., and Bayat, A. Long-term organ culture of keloid disease tissue. *Experimental dermatology*, 21(5):376–81, 2012.

[244] Meruvia-Pastor, O. E., Soh, J., Schmidt, E. J., Boughner, J. C., Xiao, M., Jamniczky, H. A., Hallgrímsson, B., and Sensen, C. W. Estimating cell count and distribution in labeled histological samples using incremental cell search. *International journal of biomedical imaging*, 2011:874702, 2011.

[245] Amar, M. B. and Wu, M. Re-epithelialization : advancing epithelium frontier during wound healing. *Journal of the Royal Society Interface*, 11(93), 2014.

[246] Morasso, M. I. and Tomic-Canic, M. Epidermal stem cells: the cradle of epidermal determination, differentiation and wound healing. *Biology of the Cell*, 97(3):173–183, 2005.

[247] Figueredo, G. P., Siebers, P.-O., Owen, M. R., Reps, J., and Aickelin, U. Comparing stochastic differential equations and agent-based modelling and simulation for early-stage cancer. *PloS one*, 9(4):e95150, 2014.

[248] Cowan, A. E., Moraru, I. I., Schaff, J. C., Slepchenko, B. M., and Loew, L. M. Spatial modeling of cell signaling networks. *Methods in Cell Biology*, 110:195–221, 2012.

[249] Weavers, H., Liepe, J., Sim, A., Wood, W., Martin, P., and Stumpf, M. P. H. Systems Analysis of the Dynamic Inflammatory Response to Tissue Damage Reveals Spatiotemporal Properties of the Wound Attractant Gradient. *Current Biology*, 26(15):1975–1989, 2016.

[250] Das, T., Safferling, K., Rausch, S., Grabe, N., Boehm, H., and Spatz, J. P. A molecular mechanotransduction pathway regulates collective migration of epithelial cells. *Nature Cell Biology*, 17(3):276–287, 2015.

[251] Arnold, F. and West, D. C. Angiogenesis in wound healing. *Pharmacology & Therapeutics*, 52(3):407–422, 1991.

[252] Roten, S. V., Bhat, S., and Bhawan, J. Elastic fibers in scar tissue. *Journal of Cutaneous Pathology*, 23(1):37–42, 1996.

[253] Stewart, K. J. A quantitative ultrastructural study of collagen fibrils in human skin normal scars, and hypertrophic scars. *Clinical Anatomy*, 8(5):334–338, 1995.

[254] Barnes, M. J., Morton, L. F., Bennett, R. C., Bailey, A. J., and Sims, T. J. Presence of type III collagen in guinea-pig dermal scar. *Biochemical Journal*, 157(1), 1976.

[255] Betz, P., Nerlich, A., Wilske, J., Tbel, J., Penning, R., and Eisenmenger, W. Analysis of the immunohistochemical localization of collagen type III and V for the time-estimation of human skin wounds. *International Journal of Legal Medicine*, 105(6):329–332, 1993.

[256] Gurtner, G. C., Werner, S., Barrandon, Y., and Longaker, M. T. Wound repair and regeneration. *Nature*, 453(7193):314–21, 2008.

[257] Hunter, J. A. A. and Finlay, J. B. Scanning electron microscopy of normal human scar tissue and keloids. *British Journal of Surgery*, 63(10):826–830, 1976.

[258] van Zuijlen, P. P. M., Ruurda, J. J. B., van Veen, H. A., van Marle, J., van Trier, A. J. M., Groenevelt, F., Kreis, R. W., and Middelkoop, E. Collagen morphology in human skin and scar tissue: no adaptations in response to mechanical loading at joints. *Burns*, 29(5):423–31, 2003.

[259] Verhaegen, P. D. H. M., van Zuijlen, P. P. M., Pennings, N. M., van Marle, J., Niessen, F. B., van der Horst, C. M. A. M., and Middelkoop, E. Differences in collagen architecture between keloid, hypertrophic scar, normotrophic scar, and normal skin: An objective histopathological analysis. *Wound Repair and Regeneration*, 17(5):649–656, 2009.

[260] Wang, J. H.-C., Jia, F., Gilbert, T. W., and Woo, S. L.-Y. Cell orientation determines the alignment of cell-produced collagenous matrix. *Journal of Biomechanics*, 36(1):97–102, 2003.

[261] Tamariz, E. and Grinnell, F. Modulation of fibroblast morphology and adhesion during collagen matrix remodeling. *Molecular Biology of the Cell*, 13(11):3915–29, 2002.

[262] Guido, S. and Tranquillo, R. T. A methodology for the systematic and quantitative study of cell contact guidance in oriented collagen gels. Correlation of fibroblast orientation and gel birefringence. *Journal of Cell Science*, 105:317–31, 1993.

[263] Shreiber, D. I., Enever, P. A., and Tranquillo, R. T. Effects of PDGF-BB on rat dermal fibroblast behavior in mechanically stressed and unstressed collagen and fibrin gels. *Experimental Cell Research*, 266(1):155–66, 2001.

[264] Robinson, J. K., Hanke, C. W. C. W., Siegel, D. M. D. M., Fratila, A., Bhatia, A., and Rohrer, T. E. *Surgery of the Skin: Procedural Dermatology*. Saunders, 3 edition, 2015.

[265] Rosińczuk, J., Taradaj, J., Dymarek, R., Sopel, M., Sopel, M., and Aw, . Mechanoregulation of wound healing and skin homeostasis. *BioMed Research International*, 2016:1–13, 2016.

[266] Olsen, L., Maini, P. K., Sherratt, J. A., and Marchant, B. Simple modelling of extracellular matrix alignment in dermal wound healing I. Cell flux induced alignment. *Journal of Theoretical Medicine*, 1(3):175–192, 1998.

[267] Dallon, J. C., Sherratt, J. A., and Maini, P. K. Mathematical modelling of extracellular matrix dynamics using discrete cells: fiber orientation and tissue regeneration. *Journal of Theoretical Biology*, 199(4):449–71, 1999.

[268] Dallon, J., Sherratt, J., Maini, P., and Ferguson, M. Biological implications of a discrete mathematical model for collagen deposition and alignment in dermal wound repair. *IMA Journal of Mathematics Applied in Medicine and Biology*, 17(4):379–93, 2000.

[269] Groh, A. and Louis, A. K. Stochastic modelling of biased cell migration and collagen matrix modification. *Journal of Mathematical Biology*, 61(5):617–47, 2010.

[270] Cumming, B. D., McElwain, D. L. S., and Upton, Z. A mathematical model of wound healing and subsequent scarring. *Journal of the Royal Society, Interface*, 7(42):19–34, 2010.

[271] Koppenol, D. C., Vermolen, F. J., Niessen, F. B., van Zuijlen, P. P. M., and Vuik, K. A biomechanical mathematical model for the collagen bundle distribution-dependent contraction and subsequent retraction of healing dermal wounds. *Biomechanics and Modeling in Mechanobiology*, pages 1–17, 2016.

[272] Olsen, L., Maini, P. K., Sherratt, J. A., and Dallon, J. Mathematical modelling of anisotropy in fibrous connective tissue. *Mathematical Biosciences*, 158(2):145–170, 1999.

[273] Dallon, J. and Sherratt, J. A. A mathematical model for fibroblast and collagen orientation. *Bulletin of Mathematical Biology*, 60(1):101–129, 1998.

[274] Rouillard, A. D. and Holmes, J. W. Mechanical regulation of fibroblast migration and collagen remodelling in healing myocardial infarcts. *The Journal of Physiology*, 590(18):4585–4602, 2012.

[275] Rouillard, A. D. and Holmes, J. W. Mechanical boundary conditions bias fibroblast invasion in a collagen-fibrin wound model. *Biophysical Journal*, 106(4):932–43, 2014.

[276] Richardson, W. and Holmes, J. Emergence of collagen orientation heterogeneity in healing infarcts and an agent-based model. *Biophysical Journal*, 110(10):2266–2277, 2016.

[277] Risken, H. H. *The Fokker-Planck equation: methods of solution and applications*. Springer-Verlag, 2nd ed. edition, 1989.

[278] Schweitzer, F. *Brownian agents and active particles: collective dynamics in the natural and social sciences*. Springer, 2003.

[279] Bees, M. A., Hill, N. A., and Pedley, T. J. Analytical approximations for the orientation distribution of small dipolar particles in steady shear flows. *Journal of Mathematical Biology*, 36(3):269–298, 1998.

[280] Schienbein, M. and Gruler, H. Langevin equation, Fokker-Planck equation and cell migration. *Bulletin of Mathematical Biology*, 55(3):585–608, 1993.

[281] Bearon, R. N., Hazel, A. L., and Thorn, G. J. The spatial distribution of gyrotactic swimming micro-organisms in laminar flow fields. *Journal of Fluid Mechanics*, 680:602–635, 2011.

[282] Lewis, D. M. The orientation of gyrotactic spheroidal micro-organisms in a homogeneous isotropic turbulent flow. *Proceedings: Mathematical, Physical and Engineering Sciences*, 459(2033):1293–1323, 2003.

[283] Bearon, R. N., Bees, M. A., and Croze, O. A. Biased swimming cells do not disperse in pipes as tracers: A population model based on microscale behaviour. *Physics of Fluids*, 24(12), 2012.

[284] Pedley, T. J. and Kessler, J. O. A new continuum model for suspensions of gyrotactic micro-organisms. *Journal of Fluid Mechanics*, 212:155–182, 1990.

[285] Williams, C. R. and Bees, M. A. Photo-gyrotactic bioconvection. *Journal of Fluid Mechanics*, 1(46), 2011.

[286] O'Malley, S. and Bees, M. A. The orientation of swimming biflagellates in shear flows. *Bulletin of Mathematical Biology*, 74(1):232–255, 2012.

[287] Croze, O. A., Sardina, G., Ahmed, M., Bees, M. A., and Brandt, L. Dispersion of swimming algae in laminar and turbulent channel flows: consequences for photobioreactors. *Journal of The Royal Society Interface*, 10(81), 2013.

[288] Cencini, M., Franchino, M., Santamaria, F., and Boffetta, G. Centripetal focusing of gyrotactic phytoplankton in solid-body rotation. *Journal of Theoretical Biology*, 399:62–70, 2015.

[289] Liu, Y.-J., Le Berre, M., Lautenschlaeger, F., Maiuri, P., Callan-Jones, A., Heuzé, M., Takaki, T., Voituriez, R., and Piel, M. Confinement and low adhesion induce fast amoeboid migration of slow mesenchymal cells. *Cell*, 160(4):659–672, 2015.

[290] Sawhney, R. K. and Howard, J. Slow local movements of collagen fibers by fibroblasts drive the rapid global self-organization of collagen gels. *The Journal of Cell Biology*, 157(6), 2002.

[291] Laufer, M., Ashkenazi, C., Katz, D., and Wolman, M. Orientation of collagen in wound healing. *British Journal of Experimental Pathology*, 55(3):233–6, 1974.

[292] Liu, Y., Ji, Y., Ghosh, K., Clark, R. A. F., Huang, L., and Rafailovich, M. H. Effects of fiber orientation and diameter on the behavior of human dermal fibroblasts on electrospun PMMA scaffolds. *Journal of Biomedical Materials Research Part A*, 90A(4):1092–1106, 2008.

[293] Mostaço-Guidolin, L. B., Ko, A. C.-T., Wang, F., Xiang, B., Hewko, M., Tian, G., Major, A., Shiomi, M., and Sowa, M. G. Collagen morphology and texture analysis: from statistics to classification. *Scientific Reports*, 3:2190, 2013.

[294] Murphy, K. E., Hall, C. L., Maini, P. K., McCue, S. W., and McElwain, D. L. S. A fibrocontractive mechanochemical model of dermal wound closure incorporating realistic growth factor kinetics. *Bulletin of Mathematical Biology*, 74(5):1143–70, 2012.

[295] Olsen, L., Sherratt, J. a., and Maini, P. K. A mathematical model for fibro-proliferative wound healing disorders. *Bulletin of Mathematical Biology*, 58(4):787–808, 1996.